



Università degli Studi di Roma “La Sapienza”

Doctorate in Biochemistry
XXX Cycle (A.Y. 2014-2017)

**Ferritin engineering by chemical
modification for bioimaging and drug
delivery**

PhD Student

Irene Benni

Tutor

Prof. Francesco Malatesta

Coordinator

Prof. Francesco Malatesta

Cotutor

Prof. Alberto Boffi

December 2017

Ai miei genitori e a nonna Elena

ACKNOWLEDGEMENTS

Three years have passed quickly, and everything I learned and achieved during my PhD would have never been possible without the knowledge, the guidance and the support of the people listed below.

First of all I am thankful to Prof. Francesco Malatesta and Prof. Alberto Boffi for giving me the chance to work on such a challenging and exciting project despite the fact that I had absolutely no experience in biochemistry and for making me progress as a researcher with their motivation and enthusiasm.

The most special thanks cannot go to anyone else other than Dr. Paola Baiocco, for introducing me to the world of biochemistry, for patiently teaching me everything, and for always supporting me inside and outside the lab. Her guidance and friendship throughout all these years are invaluable.

A second huge thanks goes to Matilde Trabuco for the help with the small everyday issues, for sharing every joy and sorrow with me, for being kind with my “craziness” and for making the lab such a great and friendly place.

I also wish to thank Prof. Alessandra Bonamore, Dr. Alberto Macone and Lorenzo Calisti from the Sapienza lab and Dr. Valeria de Turrís, Dr. Simone de Panfilis, Dr. Giovanna Peruzzi from the IIT labs for their help throughout all these years. I would have never been able to carry out so many experiments or achieve such nice results without their help and their amazing instruments. I would also like to thank everyone else at IIT for being a welcoming family. It was such a great, multidisciplinary and collaborative place to work.

I also wish to thank all the PhD students, past and present, who shared this pathway with me, for making the department such an enjoyable, helpful and inclusive place to work, even for an outsider like me.

I also want to thank Dr. Jamie Baker, for being so kind to accept my request to join his group for a while and for his constant support and enthusiasm, for all the chats that motivated me and inspired me. A big thanks goes also to Nafsika, Mauricio and everyone in the KLB lab for being so welcoming and nice.

Finally, I thank my parents, for the support, confidence and strength they gave me despite the fact that they didn't have a clue about what I was doing. I thank Alessandro for his infinite support, for knowing what I am not capable of writing down in words, and "so much more"! A huge thanks to all my friends, my second family, for being still here enjoying every weekend and every holiday together despite the months abroad everywhere in Europe, the jobs and life in general. We are definitely the best!

INDEX

ABBREVIATIONS

1.	INTRODUCTION	1
1.1	Chemical modification of proteins.....	1
1.1.1	Selective chemical modification of proteins.....	2
1.1.2	Lysine modification.....	4
1.1.3	Cysteine modification.....	5
1.1.3.1	Maleimides	7
1.1.3.2	Next generation maleimides	9
1.1.3.3	α -Halocarbonyls.....	10
1.1.3.4	Disulfides.....	11
1.2	Ferritins.....	12
1.2.1	Ferritin uptake	15
1.2.2	Ferritin structure and assembly	18
1.2.2.1	<i>Archaeoglobus fulgidus</i> ferritin structure and assembly	22
1.2.3	Ferritin in drug delivery and imaging.....	25
2.	AIM	29
3.	MATERIALS AND METHODS	31
3.1	Ferritin production and characterization	31
3.1.1	<i>Pyrococcus furiosus</i> ferritin	31
3.1.2	<i>Archaeoglobus fulgidus</i> ferritin.....	32
3.1.3	<i>Humanized Archaeoglobus fulgidus</i> ferritin.....	34
3.1.3.1	Self-assembly assessment	35
3.1.4	Ellman's assay.....	36

3.2	Archaea ferritin permeation study	37
3.2.1	DTNB-ferritin labelling reaction	37
3.2.2	TNB-labelled ferritin mass spectrometry analysis .	37
3.2.3	Stopped-flow experiments.....	38
3.3	Azobenzene-ferritin conjugate for self-assembly photocontrol.....	39
3.3.1	4,4'-Dichloroacetamido-azobenzene synthesis	39
3.3.2	Azobenzene-labelled ferritin preparation	42
3.3.3	Azobenzene-labelled ferritin mass spectrometry analysis	42
3.3.4	Photoinduced isomerization reaction	43
3.4	Pyrene-ferritin conjugate for protein oligomerization study and imaging in living cells	44
3.4.1	Pyrene-labelled ferritin preparation.....	44
3.4.2	Pyrene-labelled ferritin mass spectrometry analysis	45
3.4.3	Dynamic light scattering measurements.....	46
3.4.4	Fluorescence spectroscopy measurements	46
3.4.5	Stopped-flow measurements	47
3.4.6	FITC-labelled ferritin preparation	47
3.4.7	FITC-labelled ferritin internalization and visualization into HeLa cells	49
3.4.7.1	Flow cytometry analysis	49
3.4.7.2	Confocal microscopy measurements	50
3.4.7.3	TfR1 silencing in HeLa cells	51
3.4.8	Two-photon fluorescence spectroscopy measurements	51

3.4.8.1	Excitation.....	51
3.4.8.2	Emission	52
3.4.9	TRITC-labelled pyrene-ferritin preparation.....	53
3.4.10	Pyrene-Humanized ferritin internalization and visualization into HeLa cells	53
3.5	DNA encapsulation into Humanized ferritin.....	55
3.5.1	DNA-labelled Humanized ferritin preparation.....	55
3.5.2	DNA-labelled Humanized ferritin mass spectrometry analysis	56
3.5.3	DNA-labelled FITC-Humanized ferritin preparation.....	57
3.5.4	DNA-labelled FITC-Humanized ferritin cellular uptake	57
4.	RESULTS AND DISCUSSION.....	58
4.1	Archaea ferritin permeation study	58
4.1.1	Archaea ferritin mutants design	60
4.1.2	DTNB-ferritin reaction.....	62
4.1.3	Kinetics of DTNB binding	63
4.1.4	DTNB entrance route	66
4.2	Azobenzene-ferritin conjugate for self-assembly photocontrol.....	69
4.2.1	Ferritin mutant design	73
4.2.2	Azobenzene derivative synthesis.....	77
4.2.3	Azobenzene-labelled ferritin preparation.....	78
4.2.4	Photoinduced isomerization	81
4.2.5	Conclusion and future perspectives.....	83

4.3	Pyrene-ferritin conjugate for protein oligomerization study and imaging in living cells	84
4.3.1	Humanized archaea ferritin design.....	87
4.3.2	Pyrene-ferritin conjugate design	89
4.3.3	Pyrene-ferritin conjugate preparation.....	91
4.3.4	Ferritin assembly assessment by DLS.....	93
4.3.5	Ferritin assembly/disassembly assessment by fluorescence spectroscopy	95
4.3.6	Ferritin assembly/disassembly kinetics	102
4.3.7	Humanized ferritin cellular uptake.....	106
4.3.7.1	Flow cytometry analysis	107
4.3.7.2	Confocal microscopy measurements	108
4.3.8	Two-photon absorption and emission spectroscopy measurements on pyrene-HumAfFt	109
4.3.9	Pyrene-HumAfFt cellular uptake and visualization by two-photon fluorescence microscopy.....	112
4.4	DNA encapsulation into Humanized ferritin.....	114
4.4.1	DNA-labelled Humanized ferritin preparation.....	115
4.4.2	DNA-labelled Humanized ferritin cellular uptake	120
4.4.3	DNA encapsulation by electrostatic interaction...	121
4.4.4	Conclusion and future perspectives.....	122
5.	CONCLUSIONS	123
	REFERENCES	126
	ATTACHMENTS	137

ABBREVIATIONS

µg	microgram
µl	microliter
µm	micrometre
µM	micromolar
µmol	micromole
A	alanine
Å	ångström
ADC	antibody-drug conjugate
AfFt	<i>Archaeoglobus fulgidus</i> ferritin
Ala	alanine
Arg	arginine
Asn	asparagine
Asp	aspartic acid
ATP	adenosine triphosphate
AUC	area under the curve
b.m.	before mixing
BBB	blood brain barrier
BM(PEG)₂	1,8-bismaleimido-diethyleneglycol
C	cysteine
C2	2-fold symmetry axis
C3	3-fold symmetry axis
C4	4-fold symmetry axis
CCD	charge-coupled device
CD	circular dichroism
cm	centimetre
Cys	cysteine
D	aspartic acid

d	doublet
Da	Dalton
dd	double doublet
DIC	differential interference contrast
DLS	dynamic light scattering
DMEM	dulbecco's modified eagle medium
DMF	dimethyl formamide
DMSO	dimethyl sulfoxide
DNA	deoxyribonucleic acid
DTME	dithiobismaleimidoethane
DTNB	5,5-dithiobis(2-nitrobenzoic acid)
E	entgegen (<i>trans</i>)
E	glutamic acid
<i>E. coli</i>	Escherichia coli
e/m	excimer/monomer ratio
EDTA	ethylenediaminetetraacetic acid
eq.	equivalent
ES	electrospray
Et₂O	diethyl ether
Et₃N	trimethylamine
EWG	electron withdrawing group
ε	molar extinction coefficient
F	phenylalanine
FA	formic acid
FACS	fluorescence-activated cell sorting
FBS	fetal bovine serum
FITC	fluorescein isothiocyanate
FRET	Förster resonance energy transfer
G	glycine

GC-MS	gas chromatography–mass spectrometry
Glu	glutamic acid
H	heavy
H	histidine
h	hour
He	helium
HEPES	4-(2-hydroxyethyl)-1-piperazineethanesulfonic acid
His	histidine
HOMO	highest occupied molecular orbital
HuHF	human H-ferritin
HumAfFt	humanized <i>Archaeoglobus fulgidus</i> ferritin
I	isoleucine
IIT	Italian Institute of Technology
IPTG	isopropyl β -D-1-thiogalactopyranoside
IR	infrared
J	Joule
K	lysine
kDa	kiloDalton
k_{obs}	observed constant
kV	kiloVolt
L	light
l	litre
LB	Luria broth
LC-MS	liquid chromatography-mass spectrometry
LD	laser diode
LUMO	lowest unoccupied molecular orbital
Lys	lysine
M	methionine
M	molar

m/z	mass per charge
MALDI	matrix assisted laser desorption ionization
MeCN	acetonitrile
MEM	minimum essential medium
mg	milligram
Mg	magnesium
MgCl₂	magnesium chloride
MHz	megaHertz
min	minute
ml	millilitre
mm	millimetre
mM	millimolar
Mn	manganese
MRI	magnetic resonance imaging
MS	mass
mW	milliWatt
MWCO	molecular weight cut off
NA	numerical aperture
NaCl	sodium chloride
NAEM	N-(2-aminoethyl)maleimide
Ne	neon
NGM	next generation maleimide
NHS	N-hydroxysuccinimide
nm	nanometre
NMM	N-methylmaleimide
NMR	nuclear magnetic resonance
NPM	N-(1-pyrenyl)maleimide
ns	nanoseconds
OD	optical density

P	proline
PBS	phosphate buffered saline
PCR	polymerase chain reaction
PDB	protein data bank
PET	positron emission tomography
PfFt	<i>Pyrococcus furiosus</i> ferritin
Phe	phenylalanine
PMT	photomultiplier
ppm	parts per million
PTM	post-translational modification
R	arginine
r.t.	room temperature
RFP	red fluorescence protein
RNA	ribonucleic acid
Ro	rhodamine
ROS	reactive oxygen species
rpm	rotation per minute
s	second
SA	sinapinic acid
SAXS	small angle X-ray scattering
SCARA-5	scavenger receptor class A member 5
scr	scrambled
SDS-PAGE	sodium dodecyl sulphate polyacrylamide gel electrophoresis
SEC	size exclusion chromatography
siRNA	silencing ribonucleic acid
SN2	nucleophilic substitution 2
SPR	sulfhydryl per protein ratio
Tb	terbium

TB	trypan blue
TCEP	tris(2-carboxyethyl)phosphine
Tf	transferrin
TFA	trifluoroacetic acid
TfR1	transferrin receptor-1
THF	tetrahydrofuran
TIM-2	mouse T-cell immunoglobulin and mucin domain-2
TmFt	<i>Thermotoga maritima</i> ferritin
TNB	2-nitro-5-thiobenzoate
TOF	time of flight
TPFM	two-photon fluorescence microscopy
TRIS	tris(hydroxymethyl)aminomethane
TRITC	tetramethylrhodamine
Tyr	tyrosine
UPLC	ultra performance liquid chromatography
UV-Vis	ultraviolet-visible
V	Volt
v/v	volume per volume
W	Watt
Xe	xenon
Z	zusammen (<i>cis</i>)
Zn	zinc

1. INTRODUCTION

1.1 Chemical modification of proteins

In the last decades, owing to the improved understanding of biological processes and to the development of innovative chemical techniques, a new science field at the interface between biology and chemistry has emerged. This novel and expanding research area has the aim to investigate biological processes through a chemical approach via innovative bioconjugation techniques, a set of methods capable of site-specifically creating a covalent link between a biomolecule and a small molecule, a polymer or another biomolecule^{1,2}. The importance of such modifications can be easily understood by observing any natural biochemical reaction. Chemical modification of proteins is a key step in most biological processes, is common in all cellular events and has the aim to alter and modulate protein structure and function. Examples of post-translational modifications (PTMs), chemical alterations taking place following the ribosomal synthesis, include amino acid phosphorylation, acetylation, methylation, formylation, glycosylation, hydroxylation, ubiquitination, etc^{3,4}. The improved understanding of these *in vivo* modifications has opened the possibility to mimic and possibly expand nature's ability *in vitro*, disclosing a vast area of ongoing research. Since its discovery, chemical modification of proteins has been used for a variety of purposes: from the design of novel protein based therapeutics⁵ to the improvement of their pharmacokinetic and pharmacodynamic properties⁶, from the introduction of fluorescent tags for cell imaging⁷ to the employment of radionuclides⁸ and to FRET-based

structural studies⁹, from the creation of new affinity tags to the immobilization of proteins¹⁰, etc.

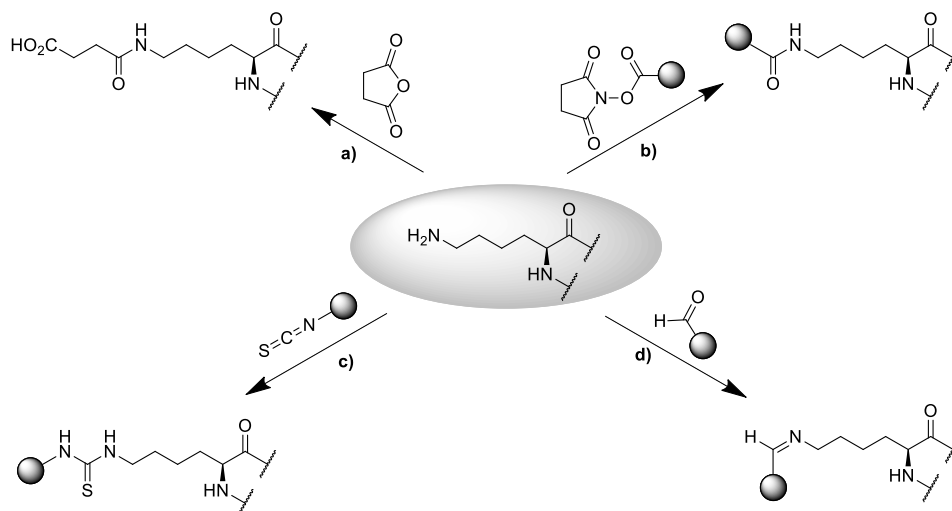
1.1.1 Selective chemical modification of proteins

Nature's selectivity in chemical modification is not always an easy task to reproduce in the laboratory. Poor control over the reaction often results in therapeutic conjugates with loss of their biological function¹¹. Consequently, the biggest challenge in the field is the selective and controlled labelling of only one amino acid among a sea of many others. However, in order to site-selectively modify a protein, many requirements need to be fulfilled. The chosen amino acid has to be accessible, exposed to the solvent, in order to react quickly and to be targeted in preference to the other amino acids around it. The reaction has to be biocompatible with the fragile nature of the protein to ensure its stability and the retention of its activity. Thus, the temperature has to remain under 37 °C, the pH has to be neutral and the reaction has to take place in an aqueous media with a minimum amount of organic solvents and in the presence of salts and surfactants that are often needed for protein's stability. In addition, high concentrations of reactant must be avoided not to waste precious starting material and not to induce cell stress^{2,12,13}. All these combined requirements strongly hinder the development of new methods but, despite the numerous challenges, after decades of research, a good variety of bioconjugation techniques is now available. Selectivity is commonly achieved via two main strategies: either the reaction is carefully tuned to be selective for a single natural amino acid or an unnatural amino acid with unique reactivity is incorporated into the protein of interest. This latter method inserts moieties such as amino acid analogues with a peculiar side

chain that will solely react with the labelling reagent¹⁴. The first method, instead, focuses on the labelling of the 20 available natural amino acids that are, therefore, immediately accessible without the need of additional modifications or specific techniques. Among the 20 natural amino acids only a few can actually be the target of bioconjugation techniques, and are the ones that present an intrinsic reactivity, often a nucleophilic site that can be modified with an electrophilic reagent. To this end, the methodology used is selected accordingly to the intrinsic reactivity of the targeted amino acid residue, depending on its acidity/basicity, electrophilicity/nucleophilicity, redox characteristics and its peculiar environment and hydrophobicity¹³. In this context, the reactivity of most hydrophilic residues has been exploited, and suitable reagents for selective protein modification have been developed for residues such as arginine^{15,16}, aspartic acid¹⁷, cysteine^{2,18}, glutamic acid¹⁹, histidine²⁰, lysine²¹, tyrosine²². Among these reactions, the most exploited modifications have been on cysteine and lysine residues. This success is a consequence of the high nucleophilicity of their side chains, which can offer higher selectivity and reactivity compared to others amino acids. Only a selection of the most common chemical modifications will be discussed below as this dissertation has not the aim of developing new bioconjugation techniques but rather the aim to use these techniques in order to test hypothesis, develop versatile nanodevices and exploit them from a biochemical point of view. Nonetheless, in order to control and correctly use bioconjugation reactions, a profound understanding of the chemistry of protein modification is required.

1.1.2 Lysine modification

Lysine is an amino acid bearing a primary amine on its side chain, which is commonly protonated under physiological pH, although it acts as strong nucleophile when deprotonated. The most common lysine labelling techniques, as shown in Scheme 1, include acylation with anhydrides²³ (a), acylation with activated esters like N-Hydroxysuccinimide (NHS) esters²⁴ (b), acylation with isothiocyanates²⁵ (c) and reductive amination of aldehydes^{26,27} (d). A common drawback of this set of reagents is the alkaline pH, usually higher than 8, commonly required to approach the pKa of the lysine residue (pKa 10.54²⁸) and necessary to provide a significant amount of deprotonated amino groups.



Scheme 1: Lysine modification with a) anhydride, b) NHS ester, c) isothiocyanate and d) aldehyde¹²

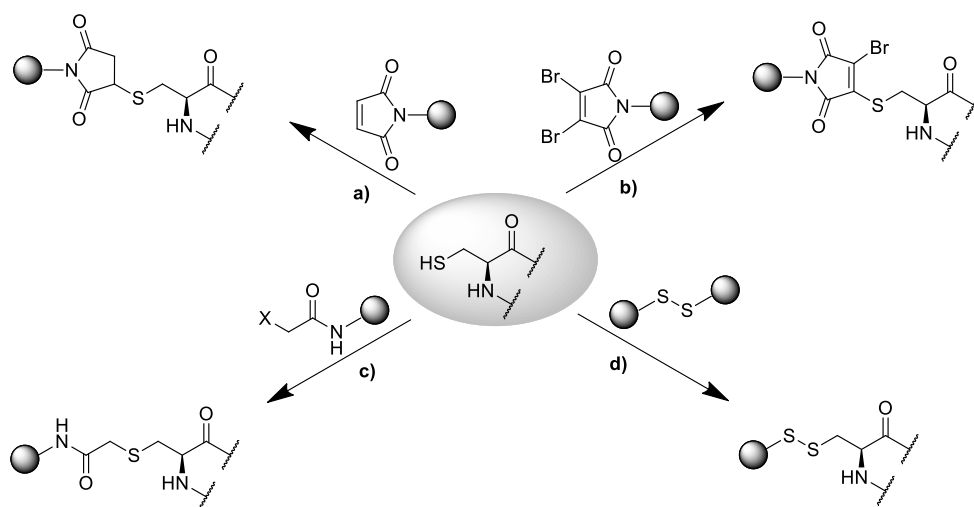
Chapter 1: Introduction

NHS ester, the most reactive and widely used lysine modification reagent, has limited storage stability and must be often used in large excess due to its moisture sensitivity, thus increasing the chances of unselective reactivity with other amino acids²⁹. An additional major disadvantage is the high abundance of lysine residues on protein surfaces that always gives a statistical mixture of heterogeneous reaction products¹². A high number of modifications can rise problems such as product stability, due to the surface charge loss, which can increase the clearance rate from the patient blood, or as altered activity due to labelled lysines in or near the protein binding site³⁰. Consequently, although lysine modification has been extensively used and many chemically modified biological products available bare a lysine modification, lysine labelling is not considered ideal nowadays.

1.1.3 Cysteine modification

Among the 20 natural amino acids, cysteine is the most exploited residue for site-selective protein modification due to its numerous advantages. Cysteine has a low natural abundance among proteins, ranging between 2.26 % in mammals and 0.5 % in some members of the Archaea bacteria order³¹ and, furthermore, it is also the most nucleophilic amino acid. These characteristics make cysteine an ideal residue for targeted site-selective modification of a few and controlled sites, avoiding unwanted side reactions and heterogeneous products. In addition, single cysteine residues can be site-selectively introduced via mutagenesis thus expanding the application field³² or, alternatively, native disulfide bonds can be reduced in order to exploit the thiolate reactivity for subsequent modification³³. The high nucleophilic nature of cysteine is due to its sulfhydryl side chain, which has a pKa of

8.37²⁸ and allows the residue to be present as a partially deprotonated thiolate at neutral pH, while the lysine's amine will be mostly protonated. Thus, by carefully controlling the buffer pH, the nucleophilic character of the residue can be subtly tuned and, together with the accurate choice of the electrophilic nature of the reactive probe, preferential reactivity can be achieved. For these numerous reasons, cysteine labelling has been widely investigated and exploited and it will be further employed in this thesis, proving once again its versatility and site-selective reactivity.



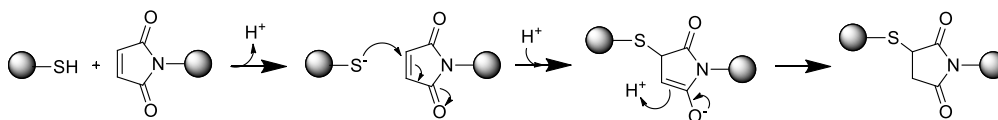
Scheme 2: Cysteine modification with a) maleimide, b) NGM, c) α -halocarbonyl and d) disulfide¹²

A selection of the most common chemical cysteine modifications is displayed in Scheme 2 and briefly explained below.

Chapter 1: Introduction

1.1.3.1 Maleimides

Maleimides (maleic acid imides) are the most widely employed electrophiles for cysteine modification and were first introduced by Friedmann in 1949 as the product of the reaction between maleic anhydride and amine derivatives^{13,34}. Maleimide is an α,β -unsaturated 5-member ring, containing an imide group in which the two carbonyls are conjugated with the C=C double bond. The reagent acts as the Michael acceptor in a Michael addition reaction with the cysteine thiolate, forming a thiosuccinimide as reaction product as shown in Scheme 3.



Scheme 3: Schematic mechanism of a Michael addition reaction between thiol and maleimide

The strong electrophilic nature of maleimides is the key to the great success of these compounds in the bioconjugation field and is mainly ascribable to two features. The first is the fact that the molecule bears electron withdrawing groups (EWG) that lower the energy of the lowest unoccupied molecular orbital (LUMO), while the second is the straining of the double bond that decreases the energetic gap between the highest occupied molecular orbital (HOMO) and the LUMO. Both of these effects contribute to the decrease of the LUMO energy of the alkene and, consequently, to the increase of the compound reactivity¹³. Maleimides, therefore, offer rapid reactions under physiological conditions, giving conjugation products in

Chapter 1: Introduction

nearly quantitative yields without the need for a large molar excess of reagent, thus being widely applicable to several conditions and biological molecules.

Despite the numerous advantages, maleimides have also some limitations that must be considered in order to properly use these reagents. The biggest restraint is their susceptibility to undergo spontaneous hydrolysis in aqueous buffers at pH above 8 either making the compound unreactive towards thiols or, if already conjugated, affording a mixture of isomeric succinamic acid adducts by ring-opening^{11,13,35}. Temperature, pH and the presence of electron withdrawing substituents strongly influence hydrolysis rates. A linear relationship between pH and hydrolysis rate was found, reducing the half-life of maleimides from 42 h at 30 °C and pH 7 to less than 24 h at pH 8.5³⁶, while Fontaine et al.³⁷ studied the ring-opening acceleration by electron withdrawing N-substituents introduction. Additionally, if a reactive lysine is proximal to the cysteine-maleimide conjugate, crosslinked products can be formed by nucleophilic attack of the primary amine onto the maleimide imide moiety thus irreversibly opening the ring in a process called aminolysis^{38,39}. A third issue, which has emerged only over time, is the maleimide leaking witnessed especially in strongly reducing environments, even though the reaction was at first thought to be irreversible. As a matter of fact, the conjugation product was found to be susceptible to a retro-Michael reaction in which the maleimide ring is released and is able to subsequently react with other thiols in the environment, thus potentially realising toxic drugs or probes before reaching their target^{13,40}. Nevertheless, these numerous issues, once investigated and understood, could also turn out to be an advantageous resource for linker stability tuning and controlled drug release, and indeed several research groups have explored these opportunities^{30,40}. For instance,

hydrolysis or aminolysis could both promote the ring opening thereby preventing a retro-Michael reaction and increasing the stability and therapeutic activity of the conjugate^{30,41}. Deliberate acceleration of the ring-opening hydrolysis reaction can be catalysed by incorporation of basic functional groups adjacent to the thiol-maleimide conjugate to afford a stable product³⁰, or by designing the maleimide N-substituent in order to favour basic catalysed hydrolysis^{41,42}. On the other hand, the Michael reaction reversibility, could also be exploited for controlled delivery, for instance in reducing environments such as cell cytoplasm, where the glutathione concentrations can reach approximately 10 mM thus favouring the consequent drug release⁴³. In conclusion, these issues do not diminish maleimide importance in the bioconjugation field, but instead this class of compounds has shown to be a complex and versatile platform.

1.1.3.2 Next generation maleimides

Recently a new class of maleimide derivatives, called next generation maleimides (NGMs), has been introduced by Baker et al. expanding the abilities of this set of reagents^{44,45}. NGMs are maleimides that can be substituted either in only the 3- position or both in the 3- and 4- positions with two good leaving groups, such as bromines, named mono-bromo and di-bromo maleimide respectively. The incorporation of a leaving group enables an addition-elimination reaction sequence with a first thiolate addition on the maleimide double bond, following the subsequent elimination of the bromide forming a thiomaleimide, with the retained double bond, as the product. If a second leaving group is present, the reaction sequence can be repeated a second time, always yielding a thiomaleimide product which, in contrast to

the saturated thiosuccinimide product obtained in a thiol-maleimide reaction, can further react. In total, di-bromo maleimides can offer three points of attachment or, otherwise, can be used for reversible cysteine modification as the thiomaleimide conjugate is cleaved by TCEP treatment⁴⁴. But, above all, their major interest is in the capability of re-bridging reduced disulfide bonds by a 2-carbon bridge insertion which does not alter protein stability and structure, whilst functionalising the protein and retaining the cleavable ability in reducing environments by an addition-elimination mechanism^{33,46}. These reactions are fast, efficient, high yielding and generate robust products that can either release their cargo in reducing environments such as cell cytoplasm or be “locked” by hydrolysis in a highly homogeneous and stable conjugate with retained biological activity⁴².

1.1.3.3 α -Halocarbonyls

Alkylation of cysteine is an alternative common reaction that exploits α -halocarbonyls such as iodoacetamides or chloroacetamides in a SN2 (nucleophilic substitution 2) reaction in which the α -halocarbonyl acts as the electrophile and the cysteine thiolate acts as the nucleophile that displaces the halogen atom forming a stable covalent bond. Although the use of maleimides is often preferred because of their higher reaction rates, α -halocarbonyls represent a valid alternative especially in applications where the stability of the product is crucial¹³. The reaction is commonly carried out under slightly basic conditions, at pH between 8 and 9, to generate a fast reaction and avoid iodoacetamide undesired reactions with other nucleophilic side chains, especially common when a high excess of reagent is required. Cross reactivity can also be eluded using the less reactive chloroacetamides,

which exhibit a greater specificity due to their slower reaction rate and diminished electrophilic nature. In addition, chloroacetamides are also preferred over the iodoacetamides to limit free iodine generation, a reagent capable of reaction with residues such as tyrosine, histidine or triptophane.^{13,47}

1.1.3.4 *Disulfides*

Cysteine oxidation is a reaction often exploited by nature to create disulfide bonds to stabilize the tertiary and quaternary protein assembly and is, therefore, a crucial reaction in post-translational modifications and protein folding³. Inspired by nature, scientists have also extensively exploited thiol-disulfide exchange reactions for cysteine modification, a reversible reaction in which a cysteine thiolate breaks a disulfide bond attacking one of the sulphur atoms, releasing a new thiolate and forming a new mixed disulfide bond. The reaction is highly selective and can be carried out in mild conditions but, unfortunately, due to its reversible nature, it is susceptible to thiols and reducing agents and this aspect strongly limits its application. The most important example of thiol-disulfide exchange reaction is the Ellman's assay reaction, used to quantify free reduced thiols in solution, exploiting the so-called Ellman's reagent (5,5-dithiobis(2-nitrobenzoic acid) or DTNB) properties⁴⁸. The TNB (2-nitro-5-thiobenzoate) is an optimal leaving group, with the ability to shift the equilibrium toward the mixed disulfide product and, in addition, its formation can be monitored by UV-Vis spectroscopy thanks to TNB distinct absorption at 412 nm^{49,50}. However, if the thiol-disulfide exchange equilibrium can not be strongly shifted toward a preferred product, labelling with non activated-disulfides can require a large reagent

molar excess, with the risk of unwanted side reactions. An ultimate issue in using this set of reagents in protein conjugation is the lack of control over the possible disulfide scrambling that can eventually bring to aggregation.

1.2 Ferritins

Ferritins have been first identified in 1894, in horse liver, by the pharmacologist O. Schmieberg and have been later isolated for the first time in 1937, from horse spleen, by V. Laufberger^{51,52}. Since then, ferritins have been ubiquitously found in all life kingdoms, from bacteria and archaea to plants and animals, and have never failed to attract scientists' interest for various purposes. Ferritins are large proteins of 480 kDa, composed of 24 subunits that assemble together to form a highly symmetrical and spherical hollow cage (Figure 1A), with an external diameter of 12 nm and an internal one of 8 nm (Figure 1B).

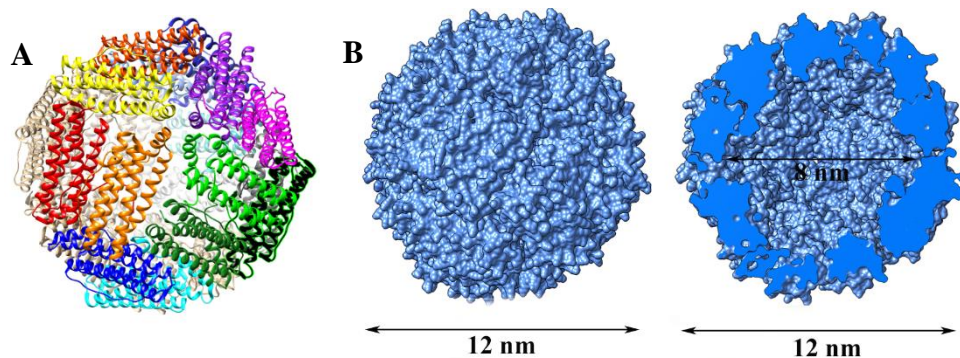


Figure 1: A) Ferritin structure in which each subunit is depicted in a different colour;
B) Schematic depiction of ferritin cavity dimensions

The building block subunits that participate in the ferritin structure self-assembly are not always identical in ferritins of different species. While

plants and bacterial ferritins are homopolymers, mammalian ferritins are made of two different kinds of subunits: heavy (H) and light (L) of 21 and 19 kDa respectively in human ferritin.

Ferritins are biologically designed to oxidise and store iron within their cavity, accommodating up to 4500 atoms as a microcrystalline hydrated ferric oxide named ferrihydrite. Despite a significant effort to define the events that take place during the catalytic cycle, the mechanism is still not fully understood⁵³. However, even though there are many contrasting indications, the majority of the studies agree that the iron atoms enter through eight hydrophilic channels, about 4-6 Å in diameter, located at the 3-fold symmetry axis, thanks to an electrostatic gradient generated by the negative electrostatic potential of the three-fold channels and the ferroxidase sites together with the positive electrostatic potential of the 3-fold channel surrounding regions, which can guide the cations inside the cavity toward the ferroxidase centre⁵⁴. One catalytic centre has been identified in the middle of each ferritin subunit and is made of three distinct metal binding sites, except for L subunit which lacks ferroxidase activity and serves as nucleation and mineralization site⁵⁵. Among the three ferroxidase centre sites, two sites, called A and B, are located in the middle of each subunit while a third metal binding site is just a bit further and closer to the inner ferritin surface (Figure 2). The third site C, does not have a catalytic activity, but might be involved in the nucleation process⁵³. Each iron atom in the ferroxidase centre is five-coordinated. In site A, the site with the strongest iron affinity, the metal coordinates three oxygen atoms, one nitrogen atom and a water molecule. Four oxygen atoms and a water molecule coordinate the metal in site B. Amino acids in the ferroxidase centres are highly conserved among the different species and include glutamates, glutamines and histidines⁵³. When

Chapter 1: Introduction

ferritins are loaded with iron, they are commonly addressed as ferritins, or *holo*-ferritin, while a cage empty ferritin, with no iron in its cavity, is addressed as *apo*-ferritin.

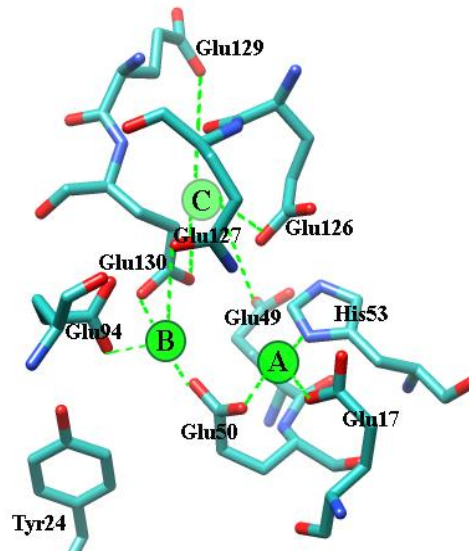


Figure 2: Ferroxidase centre from *Pyrococcus furiosus* (PDB 2X17) in which the A, B and C sites are presented as green spheres and the residues involved in iron coordination are highlighted in cyan

Living organisms have developed this peculiar protein machine, not only to store iron, but also to protect themselves from free circulating iron cations, which can form free radicals by reaction with reactive oxygen species (ROS), and ultimately cause oxidative stress and cell damage⁵³. Despite the main iron-storage and antioxidant functions, recent studies are underlying the importance of ferritin's involvement in many other biological roles⁵⁶ such as inflammation, cancer⁵⁷, immunity and autoimmunity⁵⁸, Parkinson's and Alzheimer's diseases^{59,60}.

1.2.1 Ferritin uptake

Ferritin has been located into the blood stream and in multiple cell compartments, from the cytosol to the nucleus, as it can easily bind and enter into a variety of cell types. Unfortunately, despite the long time spent on ferritin studies, only recently, a few ferritin receptors have been identified. The most important ferritin receptor, the transferrin receptor-1 (TfR1, also known as CD71), has been known for a long time as the transferrin receptor, but only recently, in 2010, it has been recognised also as the H-ferritin receptor⁶¹. This newly discovered TfR1 dual function underlines the important role of this receptor in iron homeostasis. TfR1 is a dimeric transmembrane receptor composed of two 95 kDa subunits, linked by multiple disulphide bonds. Each subunit presents a short cytoplasmic domain, a hydrophobic transmembrane domain and a large extracellular domain^{62,63}. While the binding site of transferrin is known to be located in the cytoplasmic lobe, the ferritin binding site hasn't been yet identified, but ferritin's binding behaviour has been deeply investigated and interesting evidences have emerged. For instance, it is evident that TfR1 can specifically bind only H-ferritin polymers while it lacks any affinity for the L-polymers. In addition, the H-ferritin binding is only partially inhibited by transferrin treatment, suggesting the possibility that two distinct binding sites might exist for ferritin and transferrin⁶¹. It has also been demonstrated, by blocking the TfR1 receptor with a specific monoclonal antibody, that most of ferritin's uptake is actually regulated by TfR1 in many cells such as B cells, T cells, reticulocytes, macrophages, etc., as the ferritin uptake has been almost completely inhibited⁶¹.

After TfR1 binding the ferritin cellular internalization pathway shows a similar behaviour to that of transferrin, where the protein-receptor complex is uptaken by a clathrin mediated endocytosis process^{62,64,65}. Clathrin mediated endocytosis is a common internalization pathway composed of several steps. At first, the cell membrane slowly forms a vesicle around the receptor-protein complex, trapping both the ligand and the receptor within the vesicle cavity. Then, the vesicle is completely covered by clathrin molecules and delivers the protein ligand to its fate. Finally, the receptor is either recycled or degraded into the lysosomes⁶⁵.

A confocal microscopy study on ferritin internalization into HeLa cells by Bellini et al.⁶⁶ has shown that ferritin quickly interacts with the TfR1 on the cell membrane within 15 minutes, and is later completely internalized within 3 hours of incubation. By marking different endocytic compartments with fluorescent tags, it has been demonstrated that ferritin is already localised in the early endosome after only one hour, thereafter never reaching either the Golgi apparatus, the recycling endosome or the lysosomes. Consequently, the fate of ferritins once inside the cell is still unknown, but these evidences suggest that the protein is not immediately degraded and thus can be exploited as a long lasting nanocarrier⁶⁶. By investigating ferritin uptake in different kind of cells, a high ferritin internalization has been shown in several cancerous cells such as melanoma cells, breast cancer cells, erythroleukemia cells, HeLa cervical cancer cells, ovarian cancer cells, prostate cancer cells, glioblastoma cells, pancreatic cancer cells, etc.^{62,67}. This effect is probably due to the increased iron requirements necessary for the rapid tumour growth. Indeed the TfR1 expression level in cancerous cells can be up to 100 times higher than in normal healthy cells. This discovery suggests that ferritins may actually find application in the treatment of

several tumours, as they will be selectively highly uptaken and accumulated into tumour cells, where they can eventually selectively release encapsulated chemotherapeutic drugs.

Despite TfR1 is the most important ferritin receptor found up to now, the very first ferritin receptor discovered is TIM-2, the mouse T-cell immunoglobulin and mucin domain-2, a receptor overexpressed in mouse B-cells^{68,69}, kidneys^{68,69}, liver⁶⁹, oligodendrocytes⁷⁰. The TIM-2 receptor has been located only in mice and no analogue has been found in humans, in the same way as no corresponding murine TfR1 receptor has ever been found in mice. However, similarly to TfR1, TIM-2 lacks affinity for L-ferritin⁶¹ and is internalized via a clathrin mediated endocytosis pathway that will bring the TIM-2 receptor either into the endosomes or into the lysosomes⁶⁸.

The third and last ferritin receptor identified is the Scavenger Receptor Class A Member 5, SCARA-5⁷¹. This ferritin receptor is the first receptor identified that binds only the L-polymer, while it lacks any affinity for the H-polymer. SCARA-5, as well as the other known receptors, delivers ferritin inside the cell through the endocytic pathway and it has been found expressed in mouse liver, developing kidneys, bladder, lungs, trachea, retina, macrophages etc. but no orthologue has been found in humans yet^{57,71}.

To conclude, even if ferritins is usually considered a cytoplasmic protein, there have been reports locating H-ferritin into the nucleus of neurons, hepatocytes and cancer cells⁷². Bellini et al.⁶⁶, for instance, describes the nuclear internalization of a doxorubicin loaded H-ferritin. The research group proposes that ferritin might be uptaken inside the nucleus in response to oxidative stress. The uptaken ferritin, indeed, thanks to its known antioxidant action, would have a DNA protecting role against oxidative damage. Unfortunately, the nuclear ferritin uptake mechanism is still unknown, but

recent evidences suggest that an active transport mechanism is involved, which however does not require any nuclear localization sequence^{66,72,73}. In conclusion, ferritin nuclear uptake, if further explored and potentially controlled, could be an interesting feature for the development of nuclear selective drug delivery nanoplatforms.

1.2.2 Ferritin structure and assembly

All ferritin proteins display a highly conserved tertiary structure, in which each of the 24 subunits is composed of a four-helix bundle namely A, B, C, D, and a fifth additional short E helix at the C-terminus as shown in Figure 3A. A solvent exposed and flexible loop connects helices B and C and is involved in the stabilization of the dimer interface, in which two antiparallel monomers are oriented head to tail with respect to each other as shown in Figure 3B. Each dimer has many extended contacts and interactions which are polar between the loops and apolar between the helices.

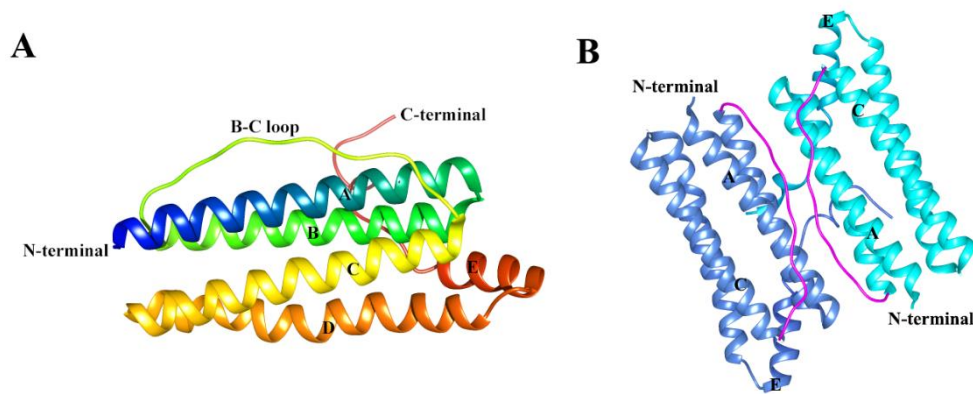


Figure 3: A) Ferritin monomeric subunit, B) ferritin dimer interface, with the interacting BC loops highlighted in magenta

The 24 monomers commonly assemble with an octahedral 4-3-2 symmetry, in a packing that results in the formation of several channels. At the 3-fold symmetry axis (C3), a total of eight negatively charged hydrophilic channels, which commonly mediate the iron entrance into the protein cage, are formed, while, at the 4-fold symmetry axis (C4) there are six hydrophobic channels (Figure 4). In addition, a small channel at the junction of three monomers, named B pore, can be found along the interface that connects the C3 and the C4 axes as shown in Figure 4⁷⁴. In total, each dimeric unit interacts with four adjacent dimers, with three main kind of contacts: the C3, along the 3-fold axis, the C4, along the 4-fold axis, and the C3-C4, the interface that connects the two symmetry axes covering the largest interaction area (Figure 4)⁷⁵.

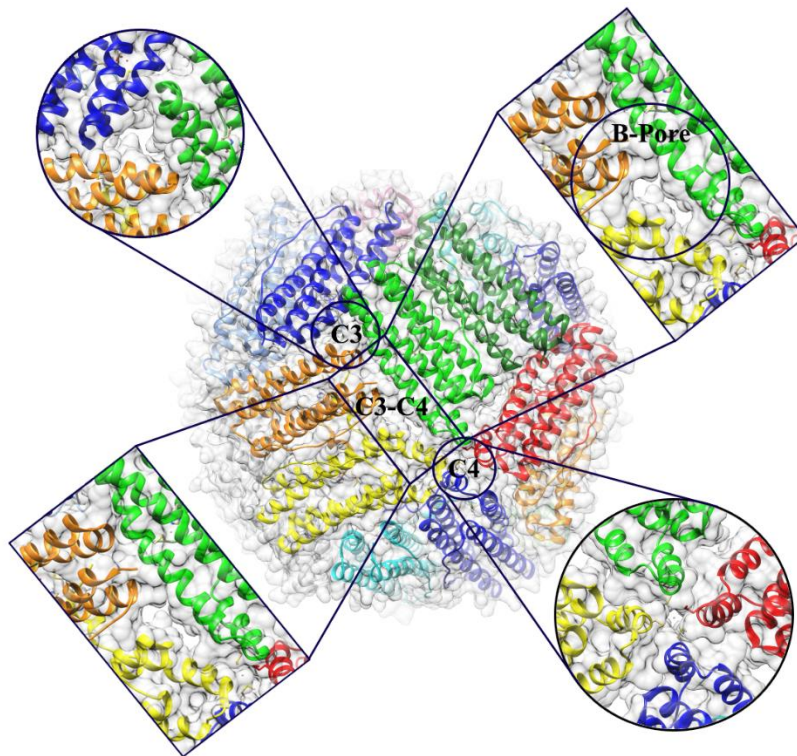


Figure 4: *Depiction of the main ferritin subunit contacts and channels*

Self-assembly of the 24 subunits is a spontaneous process driven by several non-covalent interactions including hydrogen bonding, hydrophobic and van der Waals interactions. Despite the single interactions are rather weak, the high amount of them synergistically create a highly stable quaternary structure⁷⁶. Site-directed mutagenesis studies have been widely employed to investigate the role of specific residues in ferritin self-assembly. Amino acid removal from the C-terminal E-helix or from the N-terminal does not alter ferritin assembly but only influences the cage stability^{76,77}. On the contrary, alterations of crucial contacts within the dimer interface or in the BC loop completely inhibit the self-assembly, providing only monomers incapable of any reciprocal interaction^{75,78}. Mutagenesis at the 3-fold and 4-fold channels affects protein stability, while leaving the 24-meric assembly intact⁷⁸. The understanding of these non-covalent interactions is essential in order to be able to externally control and manipulate the cage stability for biotechnological purposes.

Although the assembly of ferritin is a complex and not already fully understood process, it has already been widely exploited for different purposes. In 1973, horse spleen *apo*-ferritin was for the first time disassembled at pH 1.6 and then reversibly reassembled by bringing the buffer pH back to neutrality⁷⁹. Similarly, the protein cage can be disassembled by increasing the pH. Denaturants such as sodium dodecyl sulphate or guanidine hydrochloride, however, can only denature the protein, while treatment with 8 M urea does not alter the assembly state⁷⁹. The thermodynamic and kinetic aspects of this curious pH-triggered self-assembly behaviour have been studied during the 80's by fluorescence⁸⁰, CD spectroscopy⁸¹, sedimentation velocity centrifugation⁸¹, covalent cross-linking with glutaraldehyde⁸⁰, and more recently by SAXS^{82,83}.

Unfortunately, the results of these studies are confusing and incomplete, as the self-assembly oligomerization process of a highly symmetrical and oligomeric protein is hard to characterize, due to the many possible intermediates and pathways that can take place during the reaction⁷⁴. However, all these studies⁸⁰⁻⁸³, supported also by mutagenesis investigations⁷⁵, seem to agree on the fact that the very first stable assembly building block is the dimer. In addition, the existence of a significant population of oligomeric intermediates has been proposed and include mainly trimers, tetramers, hexamers, octamers and dodecamers. In conclusion, it is possible to speculate that in an acidic environment the protein disassembles into dimeric units which then, once the buffer is brought back to neutrality, will start to associate into different kinds of oligomers that eventually will form the 24-meric cage-like protein.

In recent years, the ferritin's cage pH induced reversible association/dissociation process has been widely exploited to load larger probes or drugs within the protein's cavity. The cage has been indeed disassembled in acidic conditions and reassembled by pH switch in a solution containing a high concentration of the selected cargo, in such a way that a high number of molecules would be statistically trapped inside the cage. These cargo-loaded ferritins have recently been employed for various biotechnological applications ranging from bioimaging to drug delivery. However, only recently, a SAXS study has demonstrated how this process is not entirely ideal and has instead some drawbacks⁸³. The *apo*-ferritin cage is quite stable in the pH range 3.4-10 but, outside this range, the dissociated subunits do not always reassemble correctly when brought back to neutral pH, leaving holes on the cage structure, corresponding to missing dimers. This evidence suggests that at pH 2, the pH commonly employed in probe

encapsulation procedures into the ferritin cages, the protein is partially irreversibly denatured and therefore incapable of a completely reversible reassociation process⁸³. Afterwards, in an effort to improve and control the unclear but still useful pH-triggered assembly/disassembly process, the protein cage has been willingly destabilised by removing amino acids from the C-terminal sequence⁷⁶ or by adding a pH sensitive peptide⁸⁴, in order to cause the disassembly at milder pH. The necessity to have a flawless, easy and completely reversible assembly mechanism is indeed highly important. To this end, thanks to the knowledge gained on the ferritin structure and assembly and the will to shape this structure accordingly to every possible necessity, researchers have been able to design and produce ferritins with unexpected shapes and properties such as an oval ferritin with 16 monomers⁸⁵ or a bigger cavity with 48 subunits⁸⁶. In conclusion, the widely explored ferritin's cage versatility and stability are the key ingredients that make this scaffold incredibly useful and resourceful for any imaginable biotechnological application. However, the thermodynamic and kinetic characterization of the reversible assembly/disassembly mechanism is an underestimated but even more important goal, as the success of the ferritin based drug delivery system relies on the effective design and control of the process.

1.2.2.1 Archaeoglobus fulgidus ferritin structure and assembly

One of the most peculiar ferritin structure is the one from the hyperthermophilic archaea *Archaeoglobus fulgidus* (AfFt)⁸⁷. In AfFt the 24 subunits, instead of the typical octahedral 4-3-2 symmetry, assemble with a tetrahedral 2-3 symmetry, causing the formation of four wide triangular pores

on the protein cage surface with a height of 45 Å as shown in Figure 5A. Up to date, this is the only ferritin found that presents such a unique assembly, as even other archaea ferritins show the typical octahedral symmetry.

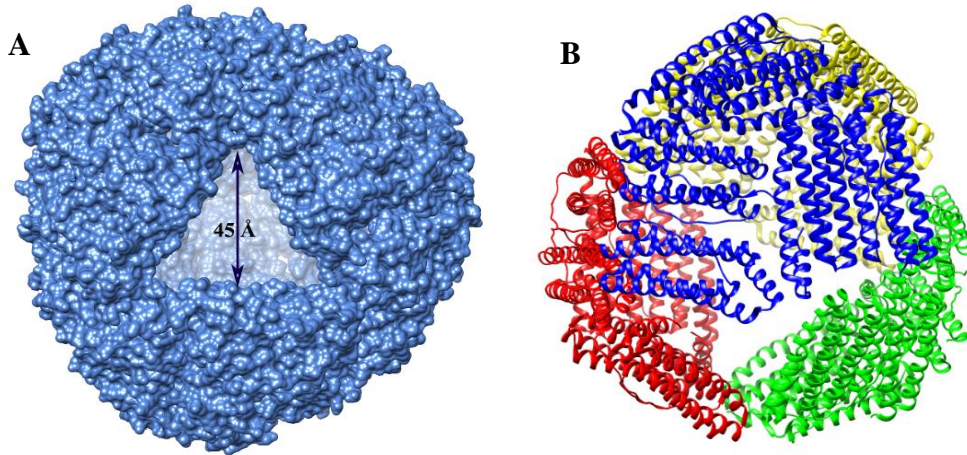


Figure 5: *Archaeoglobus fulgidus* ferritin structure with A) the typical triangular pore and B) the hexamers depicted with different colours

In this peculiar tetrahedral assembly, hexamers are the highest oligomers with extended interactions and four hexamers assemble to form the spherical cage-like protein with the characteristic holes (Figure 5B). The large pores may allow for entry of large molecules, especially if negatively charged, as along the pore apices there are cluster of positive surface potential that may attract anions. Despite these large pores, iron cations apparently always enter the internal cavity through the 3-fold channels⁸⁸. The novel protein packing, indeed, leaves the 3-fold channels intact, even though there are only four C3 channels instead of eight, but completely destroys the 4-fold channels that are no longer present on the AfFt structure.

An additional unique feature of the AfFt protein is its ionic strength driven assembly. The ferritin is indeed present in its dimeric state in low ionic

strength buffers (e.g. 20 mM NaCl), while it assembles into 24-mers only at high ionic strength (e.g. 500 mM NaCl), as demonstrated by gel filtration chromatography at increasing NaCl concentrations^{87,89}. This effect is probably due to the extended hydrophobic interactions between dimers that are enhanced at high ionic strength, bringing the subunits closer together, forcing them to assemble into the 24-meric state, to minimize the solvent exposure^{87,88,90}. Successively, Sana et al. have also described a successful attempt of iron-triggered self-assembly of the dimeric AfFt subunits⁸⁸. In addition, the reversible dissociation process induced by dissolving the iron core with reducing agents has also been characterised. As the complete assembly is reached by addition of only 20 ferrous iron per subunit, Sana et al. has proposed an additional active role of iron binding to the ferroxidase centre in the stabilization of the inter-subunits interactions that eventually favours the self-assembly process⁸⁸.

Overall, this newly discovered archaea ferritin has unique features such as its peculiar pore structure, that can facilitate the entrance of cargos inside the ferritin's cavity, and as its sodium- or iron- induced assembly, that offer a new set of association/dissociation molecular triggers, opening new possibilities for the encapsulation of molecular cargoes into a mild neutral environment. Indeed, with AfFt there is no need to reach extreme acid conditions that endanger the protein stability and limit the possibility of cargos encapsulation to only strong, stable and acid-resistant molecules.

By analysing the AfFt amino acidic sequence and structure, Sana et al. located two critical non-conserved residues, Lys-150 and Arg-151, as probably involved in the protein's unique assembly. The two positive residues, that are located at the big pore's apices, might indeed create strong repulsive electrostatic interactions that destabilise the classical octahedral

assembly. With the aim of investigating the possible role of these two amino acids, an *Archaeoglobus fulgidus* mutant, where Lys-150 and Arg-151 are replaced by two hydrophobic alanine residues, has been designed, expressed, purified and crystallized. The substitutions, as expected, remove the repulsive destabilizing forces and, unexpectedly, the mutant's assembly switches back to the typical octahedral one, with no pores, thus demonstrating the crucial involvement of the two residues. Surprisingly, the K150A-R151A AfFt mutant, despite the cage closure, has maintained intact the ability to assemble with increasing salt concentration, with a slightly higher preference for the assembled state at comparable ionic strength⁹⁰.

Overall the peculiar structural features of this archaea ferritin have opened new horizons for drug delivery and, at the same time, allow for an easy and controlled switch between two different cage architectures⁹⁰.

1.2.3 Ferritin in drug delivery and imaging

In the last years, nanoparticles have displayed their great potential as versatile tools for many biotechnological applications spanning from nanoreactors and nanosensors to nanoplatforms for bioimaging and drug delivery. Nanoparticles have several advantages including dimensions and versatility, as they can acquire new functionalities by genetic engineering or chemical modification of their external surface, inner cavity or interface between the subunits. Usually, metals, drugs or any kind of probe are loaded inside the interior cavity, hidden from the outside, while the external surface is variously functionalised with the introduction of tags, fluorophores, peptides, antibodies or other moieties for selective targeting⁹¹.

Ferritin is an interesting and ideal nanoparticle for its numerous peculiar features. It has a regular, uniform and homogeneous shape that grants a narrow size distribution. Being an endogenous protein, it is biocompatible, soluble and stable in the blood stream, as well as biodegradable. It has the right size to avoid rapid clearance through kidneys while granting a long circulation half-life. From a synthetic point of view, it is easily produced as a recombinant protein in *E. coli* cells yielding high amounts ranging between 100-200 mg l⁻¹ of ferritin on a laboratory scale. Its stability to a wide range of temperatures and pH conditions facilitate its purification procedure, as unwanted *E. coli* endogenous proteins can be denatured and precipitated by heat shock and finally removed by simple centrifugation. This simple and clean production and purification protocol might also be ideal for a future easy and low-cost industrial scale-up. In addition, the protein has an intrinsic versatility and can be variously functionalised on the surface or in the inner cavity where the hollow cage can host hundreds of molecules. As each ferritin has 24 identical subunits, by genetic engineering of a single amino acid, 24 sites can be easily site-selectively introduced and customised thus easily amplifying the desired effect. At last, the most important feature is the already mentioned ability to be selectively uptaken by cancerous cells thanks to the higher expression level of the TfR1 receptor. These several crucial and remarkable features, all available in one unique device, make ferritin an amenable scaffold for the design of bioimaging and drug delivery nanoplatforms.

Relevant examples of ferritins in the bioimaging field include their use in magnetic resonance imaging (MRI), fluorescence optical imaging or positron emission tomography (PET). For instance, the ferromagnetic iron oxide core trapped inside the cavity can be detected by MRI, a powerful diagnostic

technique with high sensitivity and accuracy used for tumour diagnosis^{92,93}. Indeed this technique, exploiting ferritin iron core and ferritin uptake by cancerous cells, was able to detect micro-tumours at early stage *in vivo* in the brain, proving at the same time the ferritin's ability to cross the blood brain barrier (BBB)^{94,95}. In fluorescence optical imaging, instead, ferritins can either be conjugated on the external surface with fluorescent dyes or loaded with fluorescent rare earth atoms inside the cavity⁹⁶, while the encapsulation with radioactive compounds is used to produce ferritins for positron emission tomography (PET)⁹⁷.

Regarding the drug delivery field, ferritins are exploited either for their ability to attract metal cations inside their cavity or for their reversible association/dissociation assembly induced by a pH switch, or by a ionic strength switch in the case of *Archaeoglobus fulgidus* ferritin. The first examples of encapsulation involved atoms such as silver⁹⁸, gold^{89,99}, uranium¹⁰⁰, gadolinium¹⁰¹ and platinum derivative as cisplatin, carboplatin or oxaliplatin¹⁰²⁻¹⁰⁵. Following these first approaches, molecules with positive charges or with the ability to bind metals such as desferrioxamine B¹⁰⁶, ferrocene¹⁰⁷ or doxorubicin in complex with copper(II)¹⁰⁸, have been encapsulated into the ferritin cavity. The complexation with metal cations provides a driving force that guide the passage of a molecule through the 3-fold axis which, otherwise, would not be accessible. However, several studies reported the successful encapsulation of cation free doxorubicin into the ferritin's cage by simple pH-triggered disassembly/assembly^{66,109-111}. These protein complexes showed a minor cardiotoxicity compared to free doxorubicin, as well as a higher tumour uptake, a longer half-life, a diminished drug resistance and a stronger tumour inhibition.

Further encapsulation experiments of probes with no preferential affinity for the internal ferritin surface can be rather challenging, due to the limited interaction between the protein and the molecules. Any encapsulated probe with low or no affinity will slowly pass through the protein pores causing a potentially dangerous leak. Indeed, only a few lipophilic molecules have been encapsulated into the ferritin cage such as curcumin¹¹², β -carotene¹¹³ and aminoanthracene¹¹⁴. However, the molecules low hydrosolubility strongly affects the encapsulation yield and this is the reason why only a few studies have been published on the matter.

Ultimately, the ability to offer a new approach to concomitant therapy by encapsulation of different drugs in the same cage, or the ability to create multifunctional nanodevices for both imaging and drug delivery^{97,111,115,116}, has opened a new stimulating and promising field in which ferritins have a decisive role in the battle of many diseases with a particular regard for the tumour targeted delivery.

2. AIM

Chemical modification of biological entities has widespread in the recent years leading to the creation of novel biochemical investigation approaches and innovative biological systems for therapeutic and diagnostic purposes. Among the novel nanoscaffolds for biotechnological application, ferritins have been gaining increasing attention due to their remarkable properties. Ferritin proteins are indeed stable, biocompatible, versatile, easily produced and modified, but most of all they present a unique uniform and homogenous spherical shape with an internal cavity of 8 nm diameter suitable for cargo loading and delivery. Most protocols for the encapsulation of large molecules in ferritin envisage, however, a controversial pH-induced assembly/disassembly of the ferritin cage that commonly involves drastic pH values (pH 2) which may be harmful to both the protein structure and the loaded cargo. The work presented in this thesis has thus the aim of exploiting chemical modification procedures to investigate the ferritin oligomerization process and the entrapment of endogenous molecules within the protein nanocage in a mild physiological environment.

The *Pyrococcus furiosus* (PfFt) ferritin, a model for the human ferritin nanocage, has been engineered and chemically modified on the surface with an azobenzene moiety, a molecular photoswitch which, upon light-induced *trans-cis* isomerizations, can promote the opening and reclosure of the protein scaffold. The permeability of the canonical close PfFt 24-meric cage was compared with the unique *Archaeoglobus fulgidus* ferritin (AfFt), the only known ferritin cage displaying four wide triangular pores on the surface, by exploiting the thiol chemistry by means of a disulfide exchange reaction with Ellman's reagent. Subsequently my thesis research work has focused on

Chapter 2: Aim

the study of the peculiar AfFt oligomerization properties, which bring the protein into its associated state upon salt increase while dissociating it into dimers with chelating agents. AfFt has been chemically engineered by introducing two pyrene moieties on key cysteine residues at the protein dimer interface and the assembly process has been investigated thermodynamically and kinetically by observing the pyrene fluorescence changes upon oligomerization. Once the salt-induced assembly features were assessed, in order to exploit the AfFt architecture for *in vitro* applications in mammalian cells, a surface mutant (HumAfFt) with a “humanized” external loop mimicking the human ferritin recognition motif for the human ferritin receptor TfR1 has been designed and produced. A new pyrene-HumAfFt conjugate was synthesised and the pyrene fluorescence emission has been exploited to compare the oligomerization process with the AfFt mechanism and to follow HumAfFt uptake into human cancerous cells by TfR1 recognition. At last, the HumAfFt mutant has been variously functionalised with different linkers and a small nucleic acid sequence with the aim of exploring the potential biotechnological application of this protein in drug delivery.

Various chemical modifications techniques were further explored during a training semester at the University College of London where I studied different bioconjugation approaches for the improvement of new antibody-drug conjugates (ADCs) which, however, were not discussed in the thesis but resulted in a publication (see Attachment 3).

3. MATERIALS AND METHODS

3.1 Ferritin production and characterization

3.1.1 *Pyrococcus furiosus* ferritin

The gene encoding for *Pyrococcus furiosus* (PfFt) wild type ferritin was already available in our laboratory (PDB 2X17). Three different mutants were designed for different experiments but all with the aim of introducing cysteine residues within the protein amino acid sequence in site-specific positions. In the first variant PfFt P77C, a mutation on the solvent exposed protein surface was introduced, while in the PfFt G52C mutant, a cysteine residue was placed on the internal cavity surface. In the third mutant PfFt I124C/K135C, two different residues on the D helix were substituted by two cysteines. All these single point mutations were introduced in the wild type gene, cloned into the expression vector pET22b (Novagen), by using a PCR QuickChange Mutagenesis kit (Stratagene) with customised primers. The mutated plasmids were then transformed into *E. coli* TOP 10 cells and the resulting colonies were screened by DNA sequencing. The successfully mutated plasmids were transformed into BL21 (DE3) *E. coli* cells for further protein expression.

All PfFt mutants were overexpressed and purified according to the same procedure. Each mutant was inoculated in 1 l of LB broth medium, containing 100 mg of ampicillin, with 5 ml of an overnight culture grown from one single colony. The overexpression was induced with 1 mM IPTG at an optical density at 600 nm (OD₆₀₀) of 0.6 verified by UV-Vis spectroscopy. Cells were grown over night at 37 °C and, the morning after, were harvested

by centrifugation at 10000 rpm for 30 minutes. The pellet was then resuspended in 20 ml of lysis buffer (20 mM TRIS pH 7.4, 300 mM NaCl) containing a cOmplete™ Mini Protease Inhibitor Cocktail EDTA-free Tablet (Roche). Cells were disrupted by sonication, the insoluble fraction was eliminated by centrifugation (10000 rpm, 30 min) while the soluble fraction was further purified by heat shock (80 °C, 10 min). The denatured *E. coli* proteins were removed by centrifugation (10000 rpm, 30 min) and the remaining solution was purified by ammonium sulphate treatment. PfFt ferritin was found as a pure fraction in the 70 % ammonium sulphate precipitate and was resuspended in 5-6 ml of buffer (20 mM HEPES pH 7.4, 50 mM MgCl₂) and dialysed against the same buffer. At last, ferritin was further purified by gel filtration chromatography (AKTA-Prime system, HiLoad 26/600 Superdex 200 pg column, eluent 20 mM HEPES pH 7.4, 50 mM MgCl₂). The highly pure protein was then concentrated by ultrafiltration (100 kDa MWCO, Millipore) and the concentration was calculated by measuring the UV absorbance at 280 nm using an extinction molar coefficient of 31400 M⁻¹cm⁻¹. Protein yield was approximately of 100 mg per litre of culture for all ferritin mutants PfFt P77C, PfFt G52C and PfFt I124C/K135C.

3.1.2 *Archaeoglobus fulgidus* ferritin

The gene encoding for the archaea ferritin *Archaeoglobus fulgidus* (AfFt) was already available in our laboratory (PDB 1S3Q). At first the AfFt M54C mutant was produced in order to introduce a cysteine residue on the ferritin interior cavity surface. The AfFt M54C mutant was subsequently mutated to introduce two alanine residues in positions 150 and 151 in order to obtain the

AfFt M54C/K150A/R151A mutant, with an octahedral symmetry instead of the typical AfFt tetrahedral one⁹⁰. All the single point mutations were introduced one by one in the wild-type gene in the expression vector pET22b (Novagen), using a PCR QuickChange Mutagenesis kit (Stratagene) with customised primers. The DNAs were transformed into *E. coli* TOP 10 cells, the resulting colonies were screened by DNA sequencing and the plasmid bearing the correct mutation was transformed into BL21 (DE3) *E. coli* cells for further protein expression. Each *Archaeoglobus fulgidus* mutant was grown at 37 °C by inoculating a solution of 1 l of LB broth medium and 100 mg of ampicillin, with 5 ml of an overnight culture grown from one single colony. The protein overexpression was then induced with 1 mM IPTG at OD₆₀₀ 0.6 and cells were grown over night at 37 °C, to be later harvested by centrifugation at 10000 rpm for 30 minutes. The pellet was then resuspended in 20 ml of lysis buffer (20 mM TRIS pH 7.4, 300 mM NaCl) containing a cOmplete™ Mini Protease Inhibitor Cocktail EDTA-free Tablet and the bacterial cells were disrupted by sonication. After centrifugation, the soluble fraction was further purified by heat shock at 80 °C for 10 minutes and the denatured *E. coli* proteins were removed by centrifugation (10000 rpm, 30 min). The soluble fraction was further purified by ammonium sulphate treatment, the precipitated fraction at 70 % ammonium sulphate containing the ferritin, was resuspended in 5-6 ml of buffer (20 mM HEPES pH 7.4, 50 mM MgCl₂) and dialysed against the same buffer. Gel filtration chromatography onto a HiLoad 26/600 Superdex 200 pg column mounted on an AKTA-Prime system (GE Healthcare) finally purified the protein, that was obtained in high purity with a yield varying up to 100 mg l⁻¹. The concentration was calculated by measuring the UV absorbance at 280 nm using an extinction molar coefficient of 33900 M⁻¹cm⁻¹.

3.1.3 Humanized *Archaeoglobus fulgidus* ferritin

The gene encoding for the “Humanized” mutant of *Archaeoglobus fulgidus* (HumAfFt) ferritin was synthesised by GeneArt (ThermoFisher), subcloned into a pET22b vector (Novagen) by introduction between the restriction sites NdeI and HindIII at the 5’ and 3’ positions respectively, and then transformed into BL21(DE3) *E. coli* cells for protein expression. The *E. coli* cells were grown in 1 l LB broth medium and ampicillin (100 mg), where 10 ml of overgrown inoculum were added. The protein overexpression was induced at OD₆₀₀ 0.6 by addition of 1 mM IPTG and the cells were grown at 37 °C over night. The pellet obtained by centrifugation at 10000 rpm for 30 minutes was resuspended in 20 ml of lysis buffer (20 mM TRIS pH 7.4, 300 mM NaCl), with a cOmplete™ Mini Protease Inhibitor Cocktail EDTA-free Tablet (Roche). The cells were disrupted by sonication, centrifuged at 10000 rpm for 30 minutes and the soluble fraction was further purified by heat shock at 80 °C for 10 minutes. Denatured *E. coli* proteins were removed by centrifugation (10000 rpm, 30 min) and the soluble fraction was purified by ammonium sulphate precipitation. The precipitated fraction at 70 % ammonium sulphate containing the ferritin, was resuspended in 5-6 ml of buffer (20 mM HEPES pH 7.4, 50 mM MgCl₂) and dialysed versus the same buffer. A final purification step by gel filtration chromatography (HiLoad 26/600 Superdex 200 pg column, AKTA-Prime system, eluent 20 mM HEPES pH 7.4, 50 mM MgCl₂) allowed to obtain a highly pure ferritin with a yield ranging between 50-100 mg l⁻¹. The protein concentration was calculated by measuring the UV absorbance at 280 nm using an extinction molar coefficient of 32400 M⁻¹cm⁻¹.

3.1.3.1 Self-assembly assessment

Magnesium-triggered self-assembly in solution was studied by size exclusion chromatography (SEC) using a Superdex 200 26/600 GL Column (GE Healthcare) mounted on an AKTA-Prime system (GE Healthcare). The size of HumAfFt was determined in different conditions (mobile phase: 20 mM HEPES pH 7.4 and various $MgCl_2$ concentrations) by comparison with the elution volumes of known standard proteins. HumAfFt elution profiles were in agreement with the AfFt gel filtration chromatograms in all conditions (Figure 6).

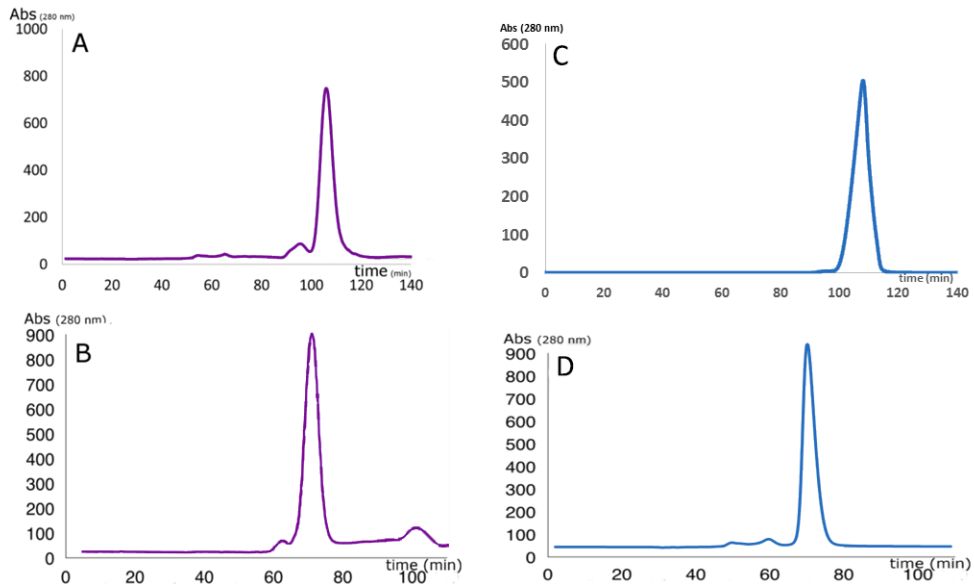


Figure 6: Gel filtration chromatograms on Superdex 200 26/600 GL column. A) HumAfFt and C) AfFt in 20 mM HEPES pH 7.4. B) HumAfFt and D) AfFt in 20 mM HEPES pH 7.4 and 20 mM $MgCl_2$

3.1.4 Ellman's assay

All sulfhydryl moieties introduced in the ferritin mutants listed above were tested by Ellman's assay. Each ferritin was incubated with TCEP (10 eq.) for 1 hour at room temperature. Excess reducing agent was removed by gel filtration chromatography (Desalting column, GE Healthcare) and, immediately after, the protein was reacted with the Ellman's reagent. DTNB (stock 100 mM in ethanol, 20 eq.) was added to the protein solution and allowed to react at room temperature for 5-15 minutes, until no further changes were observed by UV-Vis spectroscopy at 412 nm. The absorbance at 280 nm and 412 nm were recorded using as blank a sample containing the same amount of Ellman's reagent in buffer. The protein concentration was estimated with the appropriate ferritin extinction coefficient at 280 nm, and the TNB concentration was estimated by using a molar extinction coefficient at 412 nm of $14150 \text{ M}^{-1}\text{cm}^{-1}$. The sulfhydryl per protein ratio (SPR) was calculated from the ratio between the Ellman's reagent concentration and the protein concentration. Every experiment was repeated 3 times and the results were calculated based on the average of the 3 experiments. All cysteines in the numerous mutants were demonstrated to be accessible and reactive toward the DTNB reagent. Control reactions were carried out with AfFt and PfFt wild type proteins mixed with DTNB reagent in the same conditions previously described, to confirm that there is no DTNB reactivity, as both the wild type proteins do not contain any cysteine residue within their sequence.

3.2 Archaea ferritin permeation study

3.2.1 DTNB-ferritin labelling reaction

The four ferritin mutants PfFt P77C, PfFt G52C, AfFt M54C and AfFt M54C/K150A/R151A in buffer 20 mM HEPES pH 7.4 and 20 mM MgCl₂ were all reduced with 3 mM TCEP for 1 h at room temperature. The TCEP was removed by gel filtration chromatography on a desalting column (GE Healthcare, AKTA Start system) washing with 20 mM HEPES pH 7.4 and 20 mM MgCl₂. The reduced ferritin samples were immediately reacted with a 40-fold molar excess of DTNB (stock 50 mM in ethanol) for 3 hours at room temperature. The UV-Vis absorbance at 412 nm and 280 nm were measured to determine the SPR value as previously described, confirming the sulfhydryl accessibility of all cysteine residues in every ferritin mutant. The unreacted reagent was then removed by ultrafiltration (100 kDa MWCO, Millipore) washing with a 20 mM HEPES pH 7.4 and 20 mM MgCl₂ buffer. The conjugation percentage was determined by mass spectrometry as described below.

3.2.2 TNB-labelled ferritin mass spectrometry analysis

All the four ferritin mutants (PfFt P77C, PfFt G52C, AfFt M54C, AfFt M54C/K150C/R151C) reacted with DTNB as previously described were analysed by LC-MS. Each sample was desalted by extensive dialysis in distilled water and in 100 µM EDTA and filtered before analysis. LC-MS measurements were performed on a Waters AcquityUPLC connected to Waters Acquity Single Quad Detector. A Hypersil Gold C4 column was used

(1.9 μm , 2.1 \times 50 mm). Each sample was eluted with a gradient from 95:5 to 5:75 water (0.1 % formic acid) : MeCN (0.1 % formic acid) over 6 min, with a 0.4 ml min⁻¹ flow rate. The eluted product was observed at 254 nm, in a mass range between 250–2000 (ES+) m/z, with a scan time of 0.25 s. Data were obtained in continuum mode by setting the electrospray source of the MS with a capillary voltage of 3.5 kV and a cone voltage of 50 V. N₂ gas was used as nebulizer and desolvation gas at a total flow of 300 l h⁻¹. Ion series were generated by integration of the UV absorbance at 254 nm chromatogram over 1.2–1.8 min range. Mass spectra were subsequently reconstructed from the ion series using the MaxEnt 1 algorithm on MassLynx software program.

3.2.3 Stopped-flow experiments

Kinetic measurements were carried out on a thermostated Applied Photophysics stopped-flow apparatus (Leatherhead, UK). Each protein sample was initially incubated with 3 mM TCEP for 1h at room temperature. The reducing agent was removed by gel filtration chromatography using a Desalting column (GE Healthcare, eluent 20 mM HEPES pH 7.4 and 20 mM MgCl₂) and the protein was then immediately used for stopped-flow measurements. Each ferritin mutant (8-10 μM before mixing (b.m.) in 20 mM HEPES pH 7.4 and 20 mM MgCl₂) was mixed with DTNB solutions at different concentration (from 0.4 to 1.4 mM before mixing (b.m.) in 20 mM HEPES pH 7.4 and 20 mM MgCl₂). The reaction was monitored by observing the UV-Vis absorbance at 430 nm, instead of the classical wavelength used for DTNB measurements (412 nm), in order to avoid interference of the instrument phototube from the high concentrations of

DTNB. While the unreacted DTNB in excess has a significant contribution at 412 nm, it does not have a high molar extinction coefficient at 430 nm ($\epsilon_{430}(\text{DTNB})=77.8 \text{ M}^{-1}\text{cm}^{-1}$) where the TNB has instead a significant absorption. The TNB extinction coefficient at 430 nm was calculated to be $12205 \text{ M}^{-1}\text{cm}^{-1}$, as determined from the $14150 \text{ M}^{-1}\text{cm}^{-1}$ extinction coefficient at 412 nm¹¹⁷. The collected data were analysed by using a Matlab software and the experimental traces were fitted to exponential or bi-exponential functions using a Levenberg-Marquardt algorithm.

3.3 Azobenzene-ferritin conjugate for self-assembly photocontrol

3.3.1 4,4'-Dichloroacetamido-azobenzene synthesis

A solution of 4,4'-diaminoazobenzene (40 mg, 188 μmol) in dry tetrahydrofuran (THF) was placed in an ice bath and trimethylamine (Et_3N , 79 μl , 565 μmol , 3 eq.) was slowly added. After a few minutes, chloroacetyl chloride (45 μl , 565 μmol , 3 eq.) was added to the reaction mixture and the solution was stirred at 0 °C for 1 hour. An orange precipitate was slowly formed and, after 1 hour, the precipitate formation was favoured by cold water addition. The precipitate was filtered *in vacuo*, washed with additional cold water, in order to remove any Et_3N or chloroacetyl chloride excess, and with diethyl ether (Et_2O) in order to remove any possible 4,4'-diaminoazobenzene left. The orange precipitate was dried *in vacuo* and the pure product was obtained in 80 % yield (55 mg, 151 μmol). The absence of any unreacted 4,4'-diaminoazobenzene was confirmed by ninhydrin staining and the purity of the product was checked by NMR spectroscopy and GC-MS analysis. Compounds were dissolved in deuterated DMSO (Sigma), poured

Chapter 3: Materials and Methods

into small tubes with a 5 mm diameter and NMR spectra were recorded with a Bruker Advance 400 operating at 400 MHz and 100 MHz respectively for the ^1H and ^{13}C nuclei (Figure 7 and 8). The spectra were elaborated with the MestReNova program, the chemical shifts were reported in ppm and the coupling constants in Hertz.

^1H NMR (400 MHz, DMSO) δ : 10.728-10.632 (d, $J=38.4$, 2H, CONH); 8.249-8.226-8.207-8.184 (dd, $J_1=16.8$, $J_2=9.2$, 4H, Ph); 7.826-7.803-7.774-7.752 (dd, $J_1=20.4$, $J_2=9.2$, 4H, Ph); 4.321-4.304 (d, $J=6.8$, 4H, COCH_2Cl)

^{13}C NMR (100 MHz, DMSO) δ : 164.984; 142.829; 139.583; 126.465; 122.946; 43.592

GC-MS(-): $m/z = 364$ [M-H] $^-$; 168 [$\text{M}_{1/2}$ -N] $^-$

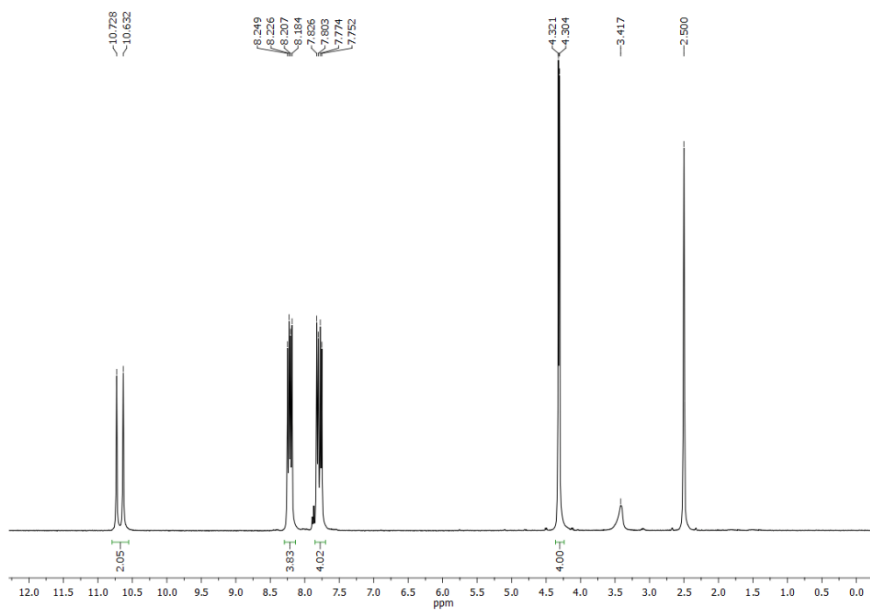


Figure 7: ^1H NMR spectrum in DMSO of 4,4'-dichloracetamido-azobenzene

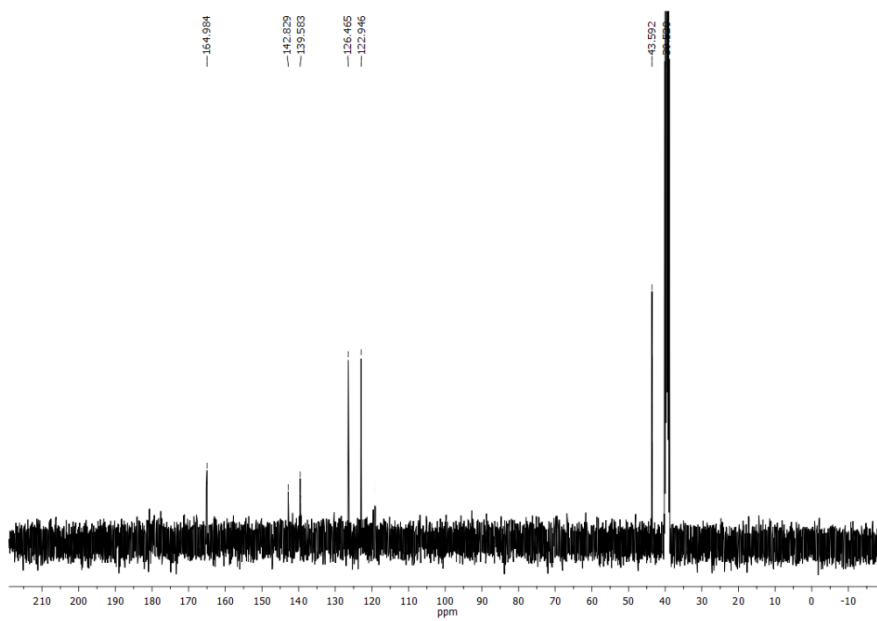


Figure 8: ^{13}C NMR spectrum in DMSO of 4,4'-dichloracetamido-azobenzene

3.3.2 Azobenzene-labelled ferritin preparation

A solution of PfFt I124C/K135C (4 mg ml⁻¹, in buffer 20 mM HEPES pH 8 and 150 mM NaCl) was reduced with TCEP (30 eq. per ferritin subunit, 15 eq. per sulfhydryl moiety, stock 250 mM in buffer) and then incubated at room temperature for 1 hour. The reduced ferritin solution was preheated at 37 °C and 1-butyl-2,3-dimethyl-imidazolium tetrafluoroborate in 20 % v/v was added to favour 4,4'-dichloroacetamido-azobenzene solubility. The 4,4'-dichloroacetamido-azobenzene (stock 100 mM in DMSO, 5 eq.) was then slowly added in 5 additions every 30 minutes (1 eq. per addition). After the last addition the reaction was continued for 2 hours at 37 °C under shaking. The solution mixture was then centrifuged (14000 rpm, 15 min), the precipitate was removed and the supernatant was further purified by gel filtration chromatography (G25, eluent 20 mM HEPES pH 8, AKTA Start system). The protein was recovered in 82 % yield and the labelling percentage was determined by Ellman's assay to be around 40 %.

The same reaction condition were used on PfFt wild type and the lack of any unspecific 4,4'-dichloroacetamido-azobenzene binding was verified by UV-Vis spectroscopy by the absence of any peak at 370 nm.

3.3.3 Azobenzene-labelled ferritin mass spectrometry analysis

The azobenzene-PfFt sample was analysed by MALDI-TOF mass spectrometry by Cogentech s.r.l.. The conjugate sample was desalted on C8 Empore Disk (3M, Minneapolis, MN) home-made stage tip and resuspended in 3 µl formic acid 1 %. 1 µl was spotted on a MALDI sample plate and allowed to air dry. Recrystallized sinapinic acid (SA matrix from Thermo

Fisher Scientific) was prepared at a concentration of 5 mg ml⁻¹ in 50:50 acetonitrile/water (0.1 % FA) and spotted directly prior to insertion into the mass spectrometer. Matrix-assisted laser desorption ionization (MALDI) mass spectra were acquired on 4800 MALDI-TOF/ TOF mass spectrometer (Applied Biosystems, Foster City, CA) equipped with a nitrogen laser operated at 336 nm laser. Acquisitions were performed in linear mode averaging 2500 laser shots in a random, uniform pattern. Ions were accelerated with a 20 kV pulse, with a delayed extraction period of 860 ns. Spectra were generated by averaging between 500 and 2000 laser pulses in a mass range from 4 kDa to 50 kDa. Laser intensity was set to optimize the signal-to-noise ratio and the resolution of mass peaks of the analyte. All spectra were externally calibrated and processed via Data Explorer (version 4.7) software¹¹⁸.

3.3.4 Photoinduced isomerization reaction

The azobenzene-labelled PfFt I124C/K135C solution (170 µM, 100 µl in 20 mM HEPES pH 8) was placed in a quartz cuvette (1 cm path length) and the sample was irradiated with a Sutter Lambda XL lamp, with a 300 W Xe light source and a 16 nm band pass filter, at 370 nm and 430 nm (Sutter VF5 tuneable filter wheel). The *trans-cis* isomerization was accomplished by irradiation at 370 nm for 1 hour, until no further changes in the UV-Vis spectra were verified. The isomerised sample turned from pale yellow (*trans*) to a strong yellow (*cis*). The solution was then irradiated at 430 nm for different amounts of time up to 24 hours to achieve the *cis-trans* conversion. UV-Vis spectra were recorded either with a UV5600 Spectrophotometer in a

0.1 cm path length quartz cuvette or with a NanoDrop™ 2000c spectrophotometer (ThermoFisher).

Circular dichroism (CD) spectra were recorded with a Jasco J-810 spectropolarimeter. Measurements were performed in a thermostated quartz cuvette (0.1 cm path length) at 20 °C. The azobenzene-labelled ferritin (25 µM in 5 mM HEPES pH 8) spectra were acquired as an average of 5 individual scans and the background recorded with the only buffer was subtracted. The wavelength were scanned in continuous mode in the 190-300 nm range, with a scan speed of 200 nm min⁻¹ and a bandwidth of 2 nm.

3.4 Pyrene-ferritin conjugate for protein oligomerization study and imaging in living cells

3.4.1 Pyrene-labelled ferritin preparation

HumAfFt and AfFt M54C (4 mg ml⁻¹, in 20 mM HEPES pH 7.4, 50 mM MgCl₂) were reduced with TCEP (10 eq.) for 1h at room temperature under mild agitation. The conjugation reaction was carried out in 15 % v/v acetonitrile to favour N-(1-pyrenyl)maleimide (NPM) solubility. The NPM linker (5 eq.) was slowly added to the protein solution and the reaction mixture was left under stirring for 4 hours at 37 °C. NPM excess was removed by gel filtration chromatography (G25 Desalting, eluent 20 mM HEPES pH 7.4, 15 % v/v acetonitrile), cosolvent was removed by dialysis against 20 mM HEPES pH 7.4 and, in order to remove excess MgCl₂ and maintain the protein in its dimeric state 5 mM EDTA was added to the dialysis buffer. Extensive dialysis against 20 mM HEPES pH 7.4 was then performed to get rid of any trace of MgCl₂, EDTA or acetonitrile that could

alter the following analysis. Determination of free sulfhydryl was performed by Ellman's assay according to standard procedure as previously described. The pyrene-labelled ferritins were obtained in 85 % yield and the labelling percentage reached was 75 %, as determined by Ellman's assay.

An additional control to assess any possible unspecific interaction of NPM with ferritin hydrophobic cavities was carried out. NPM was added to AfFt wild type, not bearing any cysteine residue, in the same reaction conditions previously described. The unspecific hydrophobic interaction was approximately 5 %.

3.4.2 Pyrene-labelled ferritin mass spectrometry analysis

The pyrene-labelled ferritin samples was analysed by MALDI-TOF mass spectrometry by Cogentech s.r.l.. Each ferritin sample was desalted on C8 Empore Disk (3M, Minneapolis, MN) home-made stage tip and resuspended in 3 μ l formic acid 1 %. 1 μ l was spotted on a MALDI sample plate and allowed to air dry. Recrystallized sinapinic acid (SA matrix from Thermo Fisher Scientific) was prepared at a concentration of 5 mg ml⁻¹ in 50:50 acetonitrile/water (0.1 % FA) and spotted directly prior to insertion into the mass spectrometer. Matrix-assisted laser desorption ionization (MALDI) mass spectra were acquired on 4800 MALDI-TOF/TOF mass spectrometer (Applied Biosystems, Foster City, CA) equipped with a nitrogen laser operated at 336 nm laser. Acquisitions were performed in linear mode averaging 2500 laser shots in a random, uniform pattern. Ions were accelerated with a 20 kV pulse, with a delayed extraction period of 860 ns. Spectra were generated by averaging between 500 and 2000 laser pulses in a mass range from 4 kDa to 50 kDa. Laser intensity was set to optimize the

signal-to-noise ratio and the resolution of mass peaks of the analyte. All spectra were externally calibrated and processed via Data Explorer (version 4.7) software¹¹⁸. The pyrene-labelled ferritin mass spectra were compared to the unlabelled ferritin mass spectra and a high percentage of conjugate was found, while only a small amount of unreacted ferritin was detected.

3.4.3 Dynamic light scattering measurements

DLS experiments were carried out with a Zetasizer Nano S (Malvern Instruments, Malvern, U.K.) equipped with a 4 mW He-Ne laser (633 nm). Measurements were performed at 25 °C, at an angle of 173° with respect to the incident beam. All ferritin samples were prepared at 2 mg ml⁻¹ in HEPES 20 mM pH 7.4 and various MgCl₂ concentrations, and were filtered with a 0.2 µm filter before analysis. Peak intensity analysis was used to determine the average hydrodynamic diameters (Z-average diameter) of the scattering particles.

3.4.4 Fluorescence spectroscopy measurements

Fluorescence measurements were carried out with a FluoroMax 4 (Horiba) spectrofluorimeter with a Haake D8 refrigerated bath at 25 °C and at equilibrium. Fluorescence emission spectra of pyrene-labelled samples (30 µM in 20 mM HEPES pH 7.4) were recorded by 342 nm excitation and fluorescence data were collected from 350 to 650 nm. The association process dependence on ionic strength was investigated varying concentrations of MgCl₂ and NaCl, while the dissociation mechanism was studied by EDTA treatment. Emission spectra were normalized with respect

to the maximum absorption peak of a single pyrene molecule and the excimer/monomer ratio (e/m) was used as a relative indicator of the extent of excimer formation.

3.4.5 Stopped-flow measurements

Kinetic measurements were carried out on a single mixing stopped-flow apparatus (Applied Photophysics, Leatherhead, UK) at 4 °C and 25 °C. Samples were excited at 342 nm (6 nm slits) and total emission fluorescence was collected with a 360 nm long-pass filter. Association kinetic experiments were performed at 5 µM protein b.m. in 20 mM HEPES pH 7.4, increasing concentrations of MgCl₂ or NaCl, and at constant salt concentration (either 20 mM MgCl₂ or 2 M NaCl b.m.) increasing protein concentrations (5 to 100 µM ferritin b.m.). Dissociation kinetic experiments were performed at 5 µM protein b.m. in 20 mM HEPES pH 7.4 and MgCl₂ increasing EDTA/Mg²⁺ molar ratios or, at a fixed EDTA concentration (20 mM b.m.) increasing protein concentrations (5 to 100 µM ferritin in 20 mM MgCl₂ b.m.). Experimental traces were fitted by using Matlab software, employing a double exponential function for magnesium association curves and for EDTA dissociation curves. For the NaCl-induced association process, a Gompertz function was used to fit the lag phase, while the remaining phases were fitted with a quadruple exponential function.

3.4.6 FITC-labelled ferritin preparation

HumAfFt, AfFt and *holo*-transferrin as controls (2 mg ml⁻¹ in 20 mM HEPES pH 7.4 and 50 mM MgCl₂) were labelled with fluorescein-isothiocyanate

(FITC, 1 mg ml⁻¹ in DMSO, 10 eq.) for 2 hours at room temperature. The excess reagent was removed by gel filtration chromatography (Desalting column, GE Healthcare, 20 mM HEPES pH 7.4 and 50 mM MgCl₂ eluent) and the fluorescent dye to protein ratio was determined to be around 60 % by UV-Vis spectroscopy using a FITC extinction coefficient of 68000 M⁻¹cm⁻¹ at 494 nm and a 0.3 correction factor at 280 nm. Labelling percentage was confirmed by LC-MS analysis where the Humanized protein was compared to the FITC-labelled HumAfFt ferritin. Protein samples were diluted in distilled water and 1 mM EDTA, and were loaded on a Waters Acquity UPLC connected to Waters Acquity Single Quad Detector. A BEH300 C4 column (1.7 μm, 2.1×150 mm) was used. The observation wavelength was set at 220 nm. The protein was eluted with water (0.1 % TFA) : MeCN (0.1 % TFA) gradient from 20 to 65 % over 60 min and a flow rate of 0.25 ml min⁻¹. MS mode was set at a scan range of m/z from 200 to 2,000 (ES+), a scan time of 0.5 s, electrospray source with a capillary voltage of 3.0 kV and a cone voltage of 45 V. N₂ gas was used as nebulizer and desolvation gas at a total flow of 200 l h⁻¹. Ion series were generated by integration of the UV-absorbance chromatogram over 2.4–2.8 min range. Mass spectra were reconstructed from the ion series by using MassLynx software program. The spectra confirmed an approximate 60 % labelling percentage of FITC-HumAfFt. The FITC-HumAfFt ferritin showed a small amount of unreacted protein at 20372 Da (39 %), a first peak corresponding to the mono-labelled protein at +389 ± 4 Da (52 %) and a second peak corresponding to the bi-labelled protein at +778 ± 4 Da (9 %) (Figure 9).

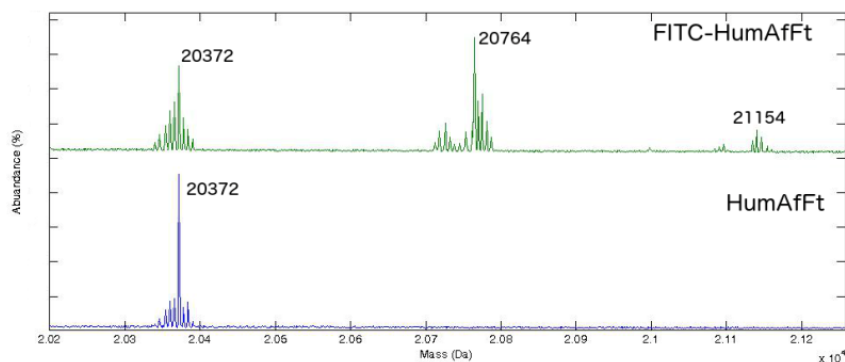


Figure 9: LC-MS spectrum of FITC-labelled Humanized ferritin (green) in comparison with Humanized ferritin (blue) spectrum

3.4.7 FITC-labelled ferritin internalization and visualization into HeLa cells

HeLa cells were grown at 37 °C in Eagle's MEM supplemented with 10 % v/v FBS, Glutamax (Invitrogen) and penicillin-streptomycin solution (Sigma). The cells were then incubated with FITC-proteins (FITC-HumAfFt, FITC-AfFt and FITC-Tf) at the final concentration of 30 $\mu\text{g ml}^{-1}$ for various time (1 h, 3 h, 20 h).

3.4.7.1 Flow cytometry analysis

For flow cytometry analysis HeLa cells were seeded on multiwell plates. Cells were incubated with FITC-labelled proteins as described previously, washed two times with PBS, detached with trypsin-EDTA (Euroclone), washed again with PBS and resuspended in BD-FACS flow buffer. Half of each sample was treated with Trypan Blue (TB, Sigma) to quench the FITC signal from not internalized membrane-bound nanoparticles. The quenching was performed with 0.04 % TB for 10 min on ice. Control cells were treated

in the same way but without FITC-labelled proteins incubation. Internalization before and after TB treatments was measured at the BD LSFORTESSA (BD Biosciences, San Jose, CA, USA) equipped with a 488 nm laser and FACSDiva software (BD Biosciences version 6.1.3). Live cells were first gated by forward and side scatter area (FSC-A and SSC-A) plots, then detected in the green channel for FITC expression (530/30 nm filter) and side scatter parameter. The gate for the final detection was set in the control sample. Data were analysed using FlowJo9.3.4 software (Tree Star, Ashland, OR, USA).

3.4.7.2 Confocal microscopy measurements

To visualize protein internalization into living cells by confocal microscopy, HeLa TagRFP cells were seeded on a μ -slide 8-well ibiTreat (ibidi) and induced with $0.2 \mu\text{g ml}^{-1}$ of doxycycline. Cells were then incubated with FITC-labelled proteins at the final concentration of $30 \mu\text{g ml}^{-1}$ for 20 h. Before imaging, cells were washed two times with an imaging medium (DMEM without phenol red, 10 % FBS, 10 mM HEPES, Glutamax and penicillin–streptomycin solution) to eliminate the unbound FITC-nanoparticles. The confocal laser-scanning microscope used was an Olympus FV10i platform equipped with a built-in incubator. Images were acquired with a 60 \times /1.2NA water-immersion objective, LD lasers, 473 nm and 559 nm, and filter sets for FITC and TRITC. Phase-contrast images were acquired simultaneously.

3.4.7.3 TfR1 silencing in HeLa cells

HeLa cells were transfected with Lipofectamine® RNAiMAX (Life Technologies) following standard procedure. The siRNA against TfR1 was purchased from Sigma (siRNA ID: SASI_Hs01_00059217). Cells were then incubated with 30 $\mu\text{g ml}^{-1}$ FITC-HumAfFt. After 3 h cells were collected, washed and analysed at the cytometer for the FITC fluorescent intensity. The FITC intensity was normalized for the FITC intensity of the control (scr) samples.

3.4.8 Two-photon fluorescence spectroscopy measurements

Preliminary two-photon fluorescence spectroscopy measurements were carried out on pyrene-labelled PfFt P77C, pyrene-labelled HumAfFt and the unlabelled proteins as control, at a 416 μM concentration and in 20 mM HEPES pH 7.4 and 50 mM MgCl_2 . Each sample was injected into the channels (90.9 μm thick and 90.9 μm wide) of a polymethylsiloxane microfluidic device¹¹⁹ and analysed by two-photon fluorescence microscopy.

3.4.8.1 Excitation

Microscope images were acquired through an inverted Olympus IX83 microscope (Olympus Europe, Hamburg, Germany), equipped with an UPLSAPO 10X2 objective (NA 0.4), with a confocal aperture of 80 micron for a corresponding theoretical resolution of 680x680 nm (HxV). The collinear light beams from a 559 nm laser diode light source and a 690-1040 nm tuneable Spectra-Physics Mai Tai DeepSee Ti:Sapphire pulsed laser

source were injected into the microscope via a FV1200 MPE laser scanning confocal device. The samples were illuminated with the tuneable IR light from the pulsed source at a constant integrated power of 500 mW over the entire range of frequencies. A set of adjusted dichroic mirrors and a 405-540 nm emission filter (for the non-descanned photon detection) deflected the fluorescence emitted radiation into photomultiplier (PMT) detectors for integrated light intensity measurements. An optical condenser (0.55 NA) collected the transmitted radiation to the bright-field image detector. The PMT high-voltages were adjusted such that no pixels were saturated in the images. The 1024x1024 pixel fluorescence images (1270.6x1270.6 nm, 10X2 objective) were collected in line sequential mode. The emitted fluorescence from the separated channel device was integrated in the 405-540 nm interval and elaborated with Fiji software. Fluorescence emission of pyrene-labelled HumAfFt and PffFt P77C were recorded using the unlabelled ferritin signal as blank.

3.4.8.2 Emission

The pyrene-labelled ferritin samples were excited at a 755 nm multi-photon excitation wavelength with the IR pulsed source at a constant integrated power of 500 mW, as previously described. The spectral distribution of the fluorescence signal in the UV-Vis range was collected with a PI Acton SpectraPro SP-2300 spectrometer equipped with a 150 gr mm⁻¹ horizontal diffraction grating and a PI Pixis 256 CCD camera. The emitted radiation was collected by a 665 nm cut dichroic mirror placed in a NDD adapter from PicoQuant and coupled to the spectrometer by a liquid light guide and collection optics. A further short pass filter (Omega Optical 630SP

RapidEdge) next to the spectrometer entrance slit reduced the IR excitation line by about 7 orders of magnitude. The spectral images onto the CCD camera were vertically rebinned and integrated for 100 s. Eventually, the background from unlabelled ferritin emission was subtracted to provide the two-photon fluorescence emission spectra.

3.4.9 TRITC-labelled pyrene-ferritin preparation

A solution of pyrene-labelled ferritin (4 mg ml⁻¹ in 20 mM HEPES pH 7.4 and 50 mM MgCl₂) was brought to a more basic pH by addition of a carbonate solution pH 9 (final concentration 0.1 M). A solution of TRITC (tetramethylrhodamine isothiocyanate, Thermofisher, 2.5 mM in DMSO, 1 eq.) was added to the protein solution and left to react for 4 h at room temperature under agitation. The solution was purified by gel filtration chromatography (Desalting column, AKTA Start system, GE Healthcare, eluent 20 mM HEPES pH 7.4 and 50 mM MgCl₂) and a 60 % labelling was obtained as determined by UV-Vis spectroscopy, with a protein recovery of 80 %.

3.4.10 Pyrene-Humanized ferritin internalization and visualization into HeLa cells

HeLa cells were grown at 37 °C in DMEM without phenol red and supplemented with 10 % (v/v) FBS, Glutamax (Invitrogen) and penicillin-streptomycin solution (Sigma). Cells were seeded on the 8-well μ -slide ibiTreat (ibidi) and after 24 h, TRITC-labelled pyrene ferritins (pyrene-HumAfFt-TRITC and HumAfFt-TRITC as control) and pyrene-labelled

HumAfFt were added at the final concentration of $300 \mu\text{g ml}^{-1}$ and incubated for 48 h. Just before imaging, cells were washed to eliminate the unbound ferritin and then acquired by confocal laser-scanning microscopy.

Microscope images were acquired through an inverted Olympus IX83 microscope, equipped a built-in incubator. Images were acquired with an UPLSAPO 60X/1.2NA water immersion objective. Confocal aperture was 120 micron for a corresponding theoretical resolution of $220 \times 220 \text{ nm}$ (HxV). The images were acquired by both two- or one- photon fluorescence confocal microscopy. The collinear light beams from a 559 nm laser diode light source and a 690-1040 nm tuneable Spectra-Physics Mai Tai DeepSee Ti:Sapphire pulsed laser source were injected into the microscope via a FV1200 MPE laser scanning confocal device and used at an excitation wavelength of 755 nm with a constant integrated power of 500 mW. A set of adjusted dichroic mirrors plus a band-pass grating filter (for the TRITC channel) and a 405-540 nm emission filter (for the non-descanned photon detection) deflected the fluorescence emitted radiation into photomultiplier (PMT) detectors for integrated light intensity measurements. An optical condenser (0.55 NA) collected the transmitted radiation to the bright-field image detector. The PMT high-voltages were adjusted such that no pixels were saturated in the images. The 1024×1024 pixel fluorescence images ($70.7 \times 70.7 \text{ nm}$, 60X objective) were collected in line sequential mode. Z-stacks were collected at 200 nm slice interval, for a total counting time of about 300 s per series.

3.5 DNA encapsulation into Humanized ferritin

3.5.1 DNA-labelled Humanized ferritin preparation

A solution of HumAfFt (6 mg ml⁻¹ in buffer 20 mM HEPES pH 7.4 and 50 mM MgCl₂) was incubated with TCEP (10 eq., stock 250 mM in buffer) for 1 hour at room temperature. The reductive agent was then removed by gel filtration chromatography (Desalting column, GE Healthcare). To the reduced protein (4 mg ml⁻¹ in buffer 20 mM HEPES pH 7.4 and 50 mM MgCl₂) a solution of 1,8-bismaleimido-diethyleneglycol (BM(PEG)₂) or dithiobismaleimidoethane (DTME) or N-(2-aminoethyl)maleimide (NAEM) (stock 50 mM in DMSO, 10 eq.) was added and the reaction took place at room temperature, under mild agitation for 1 hour. The excess reagent was then washed away by gel filtration chromatography (Desalting column, GE Healthcare) eluting in HEPES 20 mM pH 7.4. Meanwhile, a solution of Ro-DNA-SH (1 mM in TRIS 10 mM pH 8, DNA sequence from 5'-3' [ChR6G]GTGTAACACGTCTATACGCCCA[ThiC3], Sigma) was incubated with TCEP (10 eq., stock 250 mM) for 1 h at room temperature and the excess TCEP was removed with an Oligo Clean & ConcentratorTM kit, ZymoResearch. The BM(PEG)₂-labelled, the DTME-labelled and the NAEM-labelled HumAfFt, all 2 mg ml⁻¹ in buffer 20 mM HEPES pH 7.4, were incubated with the previously reduced Ro-DNA-SH (10 eq.) for 1 h at room temperature. At the end of the reaction, 50 mM MgCl₂ was added to the protein solution from a 2 M MgCl₂ stock and the mixture was left under agitation for additional 30 min. The unreacted Ro-DNA-SH was then removed by ultrafiltration (100 kDa MWCO, Millipore) washing with 20 mM HEPES pH 7.4 and 50 mM MgCl₂ until no further Ro-DNA-SH was

observed in the flow-through. The conjugated products were then analysed by UV-Vis spectroscopy and the labelling percentage was determined by the ratio between the Ro-DNA-SH concentration ($\epsilon_{530}=116000 \text{ M}^{-1}\text{cm}^{-1}$) and the protein concentration ($\epsilon_{280}=32400 \text{ M}^{-1}\text{cm}^{-1}$). A 160 % labelling per ferritin 24-mer was found for the Ro-DNA-SH-DTME-HumAfFt conjugate, meaning that almost 2 DNA molecules have been successfully encapsulated within the ferritin cavity. The Ro-DNA-SH-BM(PEG)₂-HumAfFt conjugate showed a labelling yield of 22 % per 24-mer and similarly only a 13 % per 24-mer of Ro-DNA-SH interacted non-covalently with the interior cavity of NAEM-HumAfFt conjugate.

The reaction was performed, in the same conditions previously reported, on the HumAfFt where the sulfhydryl reactive moieties were unavailable due to a prior reaction with N-methylmaleimide (NMM, 10 eq., 1 h, r.t.) and the absence on any unspecifically bound nucleic acid fragment was confirmed.

3.5.2 DNA-labelled Humanized ferritin mass spectrometry analysis

Due to the low percentage of DNA-labelling per monomeric ferritin unit, mass spectra of the final conjugates failed to show the peak corresponding to the conjugate. However, the linker-HumAfFt conjugate were analysed by mass spectrometry analysis to verify the successful first step of the conjugation. Samples were analysed by MALDI-TOF mass spectrometry by Cogentech s.r.l.. Each ferritin sample was desalted on C8 Empore Disk (3M, Minneapolis, MN) home-made stage tip and resuspended in 3 μl formic acid 1 %. 1 μl was spotted on a MALDI sample plate and allowed to air dry. Recrystallized sinapinic acid (SA matrix from Thermo Fisher Scientific) was prepared at a concentration of 5 mg ml^{-1} in 50:50 acetonitrile/water (0.1 %

FA) and spotted directly prior to insertion into the mass spectrometer. Matrix-assisted laser desorption ionization (MALDI) mass spectra were acquired on 4800 MALDI-TOF/TOF mass spectrometer (Applied Biosystems, Foster City, CA) equipped with a nitrogen laser operated at 336 nm laser. Acquisitions were performed in linear mode averaging 2500 laser shots in a random, uniform pattern. Ions were accelerated with a 20 kV pulse, with a delayed extraction period of 860 ns. Spectra were generated by averaging between 500 and 2000 laser pulses in a mass range from 4 kDa to 50 kDa. Laser intensity was set to optimize the signal-to-noise ratio and the resolution of mass peaks of the analyte. All spectra were externally calibrated and processed via Data Explorer (version 4.7) software¹¹⁸.

3.5.3 DNA-labelled FITC-Humanized ferritin preparation

The HumAfFt was labelled with FITC as previously described. The DTME and BM(PEG)₂ linkers were then added to the FITC-HumAfFt and ultimately the Ro-DNA-SH were added as described in paragraph 3.5.1.

3.5.4 DNA-labelled FITC-Humanized ferritin cellular uptake

HeLa cells were incubated with Ro-DNA-SH-DTME-HumAfFt-FITC, Ro-DNA-SH-BM(PEG)₂-HumAfFt-FITC at the final concentration of 300 µg ml⁻¹. The proteins were then treated and analysed by flow cytometry analysis by using the same protocol previously used for HumAfFt-FITC visualization, extensively described in paragraph 3.4.7.

4. RESULTS AND DISCUSSION

4.1 Archaea ferritin permeation study

In view of the relevance of ferritin as nanocarrier for metals, drugs and fluorescent probes, the incorporation of molecules inside the protein cavity is an important and challenging step. Commonly employed encapsulation techniques exploit the pH-induced cage disassembly to open the ferritin cavity and to trap various molecules inside it upon reclosure⁷⁹. However, as previously mentioned, the reassembly is not always complete and hence new innovative methods are needed⁸³. In this framework, the recently discovered *Archaeoglobus fulgidus* ferritin has emerged thanks to its unique salt-induced assembly properties⁸⁸. In addition, another archaea ferritin from *Pyrococcus furiosus* has lately emerged as a promising nanodevice⁹⁸. The success of these archaea ferritins is ascribable to their high thermal stability and easiness of expression and purification, features that have contributed to their increasing use as ferritin versatile scaffolds for various aims¹²⁰.

Up to now, several molecules have been encapsulated inside the ferritin cavity either by simple diffusion, or by physical entrapment after ferritin induced dissociation and reassociation. Simple permeation through the ferritin cage would be ideal but, apart from cations encapsulation, only a few more reports concerning larger molecules have been described, all regarding uniquely mammalian ferritins¹²¹. This is due to the restricted channels dimensions as even solvated cations (6.5 Å diameter) would need a partial dehydration or a ferritin rearrangement in order to penetrate the 3-fold ferritin channel (15 Å long and 5-6 Å wide). However, Yang et al. successfully reported the charge-selective ferritin uptake of positively charged nitroxide

derivatives through the 3-fold channels. The entrance could occur for positively charged or polar molecules, while was restricted for negatively charged substrates, until anionic residues in the 3-fold channel were replaced by histidines (HuHF D131H/E134H) by site-directed mutagenesis¹²². The charge-selective passage could be explained in light of the electrostatic potential originated by the positive cluster near the 3-fold entrance and the negative amino acid residues along the 3-fold channel that guide the positive molecules entrance¹²³. Therefore, while mammalian ferritins have been studied and the molecular diffusion inside the cage is known to take place through the 3-fold channel and to be restricted to positively charged molecules, little is still known about the more recently discovered archaea ferritins, in particular concerning the molecular diffusion in and out of the protein cavity. A study by Sana et al.⁸⁸ on the ferroxidase activity of AfFt established that the iron cations enter via the same mammalian ferritin pathway, the three fold symmetry channels, and not through the peculiar *Archaeoglobus fulgidus* triangular aperture. Indeed, no difference in the iron binding and oxidation rates was found comparing AfFt bearing the peculiar triangular pores and AfFt K150A/R151A, the “closed” form with the classical octahedral symmetry without the 45 Å wide holes. Aside from this study on the iron entry, the entrance of larger molecules permeating the archaea ferritin cavity has never been investigated and, as *Pyrococcus furiosus* and *Archaeoglobus fulgidus* ferritins are both emerging as unique biological scaffolds, their permeation properties must be explored. Indeed, their difference in nature and shape can provide novel possible routes for the entry and the encapsulation of molecules, thus expanding the scope of possible biotechnological applications.

4.1.1 *Archaea ferritin mutants design*

To investigate the permeation ability of the newly discovered archaea ferritins, a set of four different mutants from AfFt and PfFt, in which cysteine residues were placed in topological specific positions, were designed expressed and purified¹²⁴. The set of ferritins included two mutants from *Pyrococcus furiosus* and two mutants from *Archaeoglobus fulgidus* ferritin. The first PfFt mutants, PfFt P77C and PfFt G52C, displayed a reactive cysteine residue on the external surface and in the inner cavity respectively, while both *Archaeoglobus fulgidus* mutants, AfFt M54C and AfFt M54C/K150A/R151A showed a cysteine facing the inner cavity (Figure 10). However, while the AfFt M54C maintained the typical triangular wide pores, the AfFt M54C/K150A/R151A mutant displayed the “closed” octahedral shape with no pores, common to all ferritins. The internal cysteine modification was introduced in a topologically equivalent position inside the protein cavity of both PfFt and AfFt.

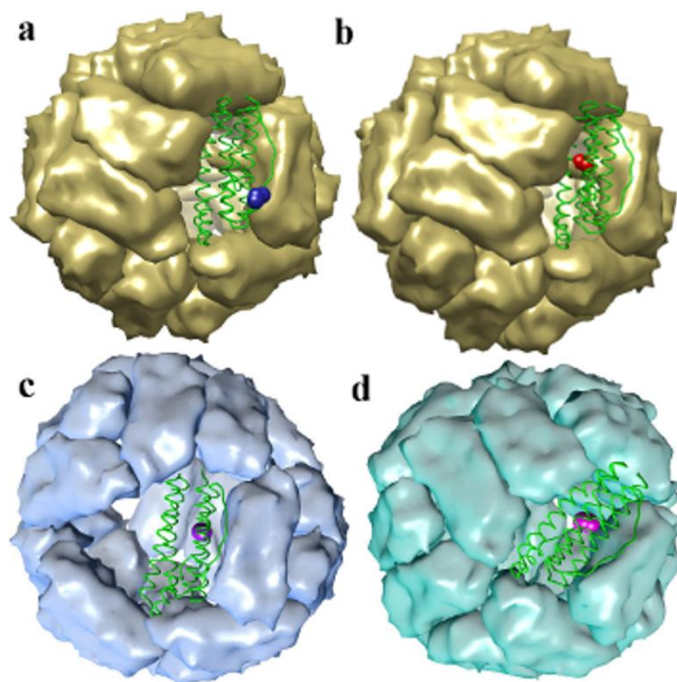


Figure 10: 3D structures of the ferritin mutants in which one monomer is depicted as green ribbon and the cysteine residues are represented in CPK style for clarity. a) PjFt P77C with the external cysteine shown as blue spheres, b) PjFt G52C with the internal cysteine depicted in red, c) AfFt M54C, with the internal cysteine depicted in purple, d) AfFt M54C/K150A/R151A with the internal cysteine in magenta

By exploiting the newly introduced sulfhydryl moieties, the ferritin permeability was investigated by reaction with a bulky and negatively charged molecule such as DTNB (Figure 11) which, with a 5-6 Å diameter and a 8-10 Å length, should be incapable of penetrating the ferritin cavity.

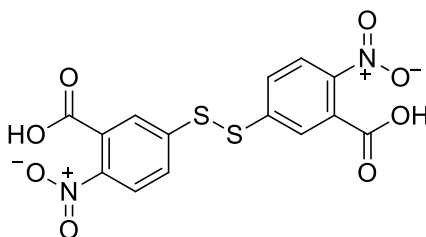


Figure 11: DTNB molecular structure

4.1.2 DTNB-ferritin reaction

By analysing the cysteine accessibility and the cage structure of the four ferritin mutants, the thiol-disulfide exchange reaction rates between DTNB and the cysteine sulfhydryl moieties could be predicted. The solvent exposed cysteine on the protein surface of PfFt P77C, would show a complete and fast reactivity, while the internal cysteine in AfFt M54C, although accessible because of the big triangular pores, would be partially hindered due to its internal position. On the contrary, absolutely no reactivity should be observed in PfFt G52C and AfFt M54C/K150A/R151A. Surprisingly, however, all ferritin mutants were reactive towards DTNB and the cysteine moieties were all quantitatively bound as confirmed by UV-Vis spectroscopy by observing the TNB absorbance at 412 nm. Sulfhydryl per protein ratios (SPR) found were all close to 1, indicating a complete reaction. This evidence was also confirmed by LC-MS analysis, where the mass spectra of the four ferritin mutants were compared with the ones after DTNB treatment. The mass spectra correctly displayed the peak corresponding to the monomeric unit at around 20 kDa for the unlabelled protein and a $+198\pm 2$ Da shifted peak corresponding to the TNB molecule for the DTNB reacted ferritins, in agreement with the predicted molecular weights (Figure 12). In all samples the reaction produced a pure mono-labelled product with the only exception of the PfFt G52C mutant, where a 18 % unlabelled protein was found as demonstrated by both Ellman's assay and LC-MS measurements. In conclusion, by simple diffusion, a negatively charged and bulky molecule such as DTNB was easily uptaken in all archaea ferritin cavities demonstrating the more tolerant and permeable nature of the cavity compared to the impermeable and selective mammalian ferritin cage.

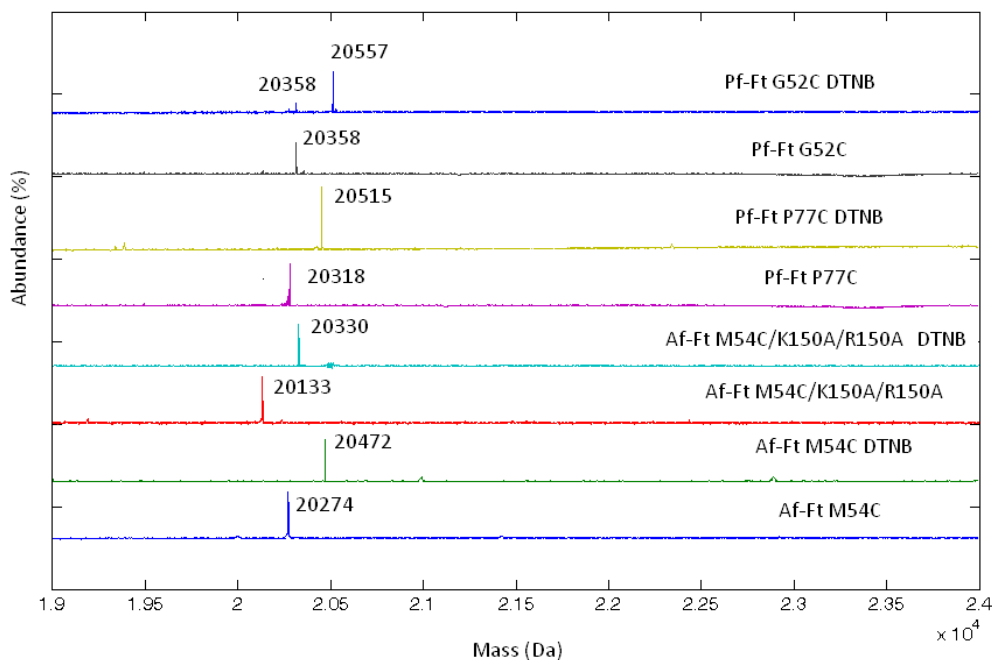


Figure 12: LC-MS spectra of the four ferritin mutants before and after DTNB reaction

4.1.3 Kinetics of DTNB binding

Kinetics of the thiol-disulfide exchange reaction between the cysteine sulfhydryl moiety and the DTNB disulfide were studied by following the TNB UV-Vis time-dependent absorbance increase at 430 nm with a stopped-flow apparatus. The experiments were carried out under pseudo-first order conditions, therefore mixing ferritins with different DTNB concentrations in large excess and acquiring a complete set of curves for each protein. The reactions were followed either to their end or to the instrumental limit of 1000 s, and the exponential traces were acquired to be further analysed. Curiously, while all ferritins were correctly fitted by a mono-exponential function, the AfFt M54C traces could be fitted only by a bi-exponential function (Figure 13).

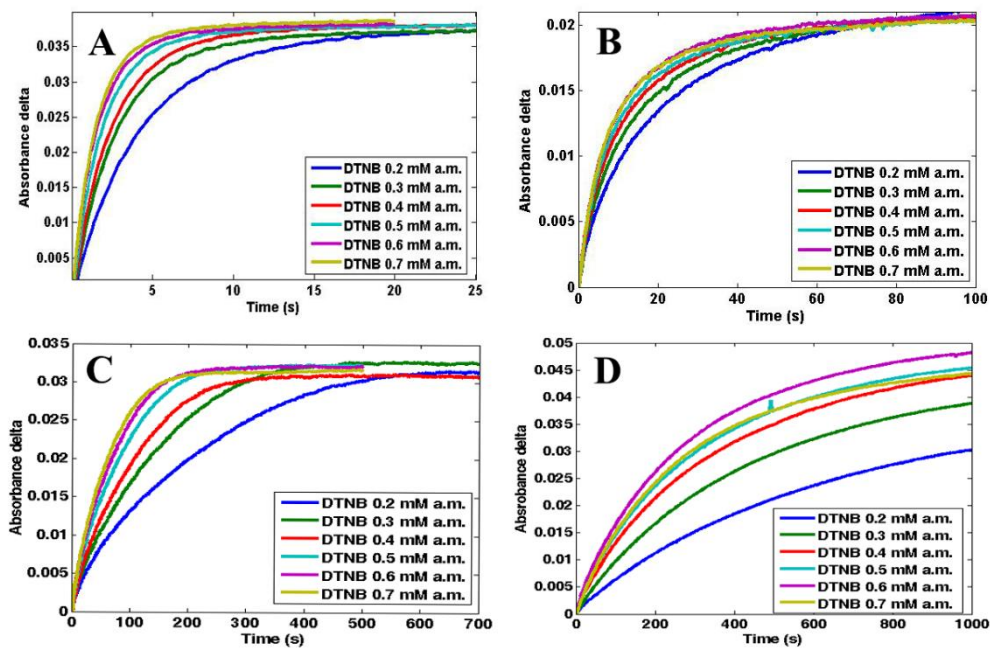


Figure 13: Kinetic traces of ferritin mutants as a function of DTNB concentrations: A) mono-exponential traces of PfFt P77C, B) bi-exponential traces of AfFt M54C, C) mono-exponential traces of AfFt M54C/K150A/R151A, D) mono-exponential traces of PfFt G52C

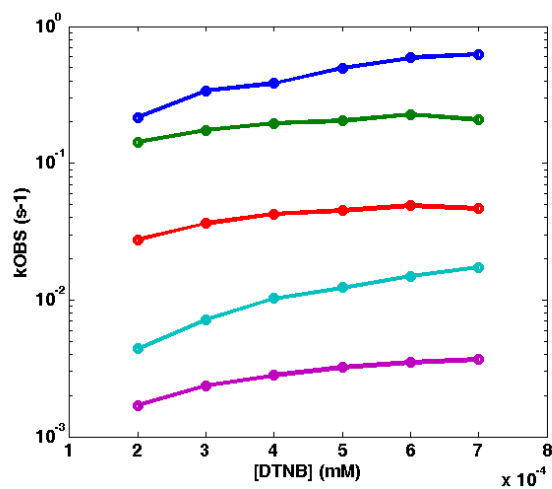


Figure 14: Pseudo-first order plot of the observed rate constants as a function of DTNB concentration of PfFt P77C (blue), AfFt M54C (green for the fast phase and red for the slow phase), AfFt M54C/K150A/R151A (cyan), PfFt G52C (purple). All reported concentrations are after mixing

Chapter 4: Results and Discussion

Each set of kinetic traces was fitted and the observed rate constants were plotted in a pseudo-first order plot as a function of increasing DTNB concentrations (Figure 14).

A linear dependence of the reaction rates on DTNB concentration was found and the apparent second order rate constants for each ferritin were calculated from the slopes and are listed in Table 1.

Ferritin	k_{OBS} ($M^{-1}s^{-1}$)
PfFt P77C	908 ± 122
PfFt G52C	5 ± 1
AfFt M54C	198 ± 65 (k fast) 51 ± 21 (k slow)
AfFt M54C/K150A/R151A	26 ± 2

Table 1: Apparent pseudo-first order rate constants for the DTNB-ferritin reactions in the various ferritin mutants

The reaction time scale varied considerably among the mutants and, while the PfFt P77C reaction was complete within 20 seconds, the PfFt G52C reaction was not even complete after 1000 s. As expected, the PfFt P77C mutant with the external cysteine displayed the fastest kinetics, almost 200 times faster than the PfFt G52C mutant bearing an internal cysteine. The AfFt M54C displayed, instead, an intermediate behaviour as, even though the cysteine is facing the internal cavity, the DTNB had a facilitated access via the wide triangular pores. Curiously, however, this process could only be fitted by a bi-exponential function, in which the fastest rate constant was of the same order of magnitude determined for PfFt P77C, just 4.5 times lower, and the slow rate constant was comparable in magnitude to the rates found for the two closed mutants, PfFt G52C and AfFt M54C/K150A/R151A, bearing cysteines in the inner cavity. A strong quenching effect on the reaction rates

in the last mutants was then observed, with PfFt G52C as the most inaccessible protein barrier with a rate constant five times slower than the rate of the closed Archaeoglobus mutant with no pores AfFt M54C/K150A/R151A. In addition, from this study, the importance of the AfFt M54C triangular pores as a preferential entrance to large negatively charged molecules emerged, as the rate constant of the “open” AfFt M54C was 8 times higher than the “closed” AfFt M54C/K150A/R151A with no pores. The negatively charged molecule entrance could indeed also be favoured by the positive clusters at the triangular pore apices.

Overall these data showed that the diffusion rates of molecules through the protein cage barrier could be accurately measured and that the archaea ferritin shell was more permeable than the mammalian one, as even bulky negatively charged molecules as DTNB could easily pass through it. Interestingly, by comparing the uptake of positively charged molecules by mammalian ferritins and the permeation of negatively charged molecules in closed archaea ferritins, the same time range was observed, suggesting a different uptake mechanism or a different packing that alter the cavity permeability. The presented evidence sheds light on the archaea ferritin cavity access mechanism and will be of relevance for ligand encapsulation and drug delivery applications.

4.1.4 DTNB entrance route

Possible entrance routes through the ferritin cage barrier and toward the ferritin internal cavity had been examined by structural analysis (PDB: 2JD6 for PfFt, 1SQ3 and 3KX9 for AfFt with and without triangular pores respectively, 2FHA for HuHF). As the 3-fold channels represented the

privileged route for iron and molecules entry in both archaea and mammalian ferritin a similar route could be proposed for the DTNB entrance. Indeed, while the 8 mammalian ferritin 3-fold channels formed by the interaction of three adjacent monomers were negatively charged and contained 6 highly conserved residues (Asp131 and Glu134 two for each monomer) located at the end of the channel (Figure 15C)¹²³, the archaea 3-fold channels presented a diminished hydrophilic character. PfFt, similarly to HuHF displayed some negative residues on the channel entrance (Asp109, Asp110, Asp111), but differed in the hydrophilic character of the central part of the channel, where polar and positively charged residue as Tyr114 and Arg117 were found, and in the terminal part, where Ala118 and Glu121 were located (Figure 15B)¹²⁵. On the contrary, in the three fold channels of AfFt a mixture of hydrophilic and hydrophobic residues along all the channel length was identified. Only one negative amino acid was located at the channel entrance (Glu113), while the Asp131 and Glu134 in HuHF were replaced by a neutral (Tyr119) and a positively charged residue (Asn120) (Figure 15A).

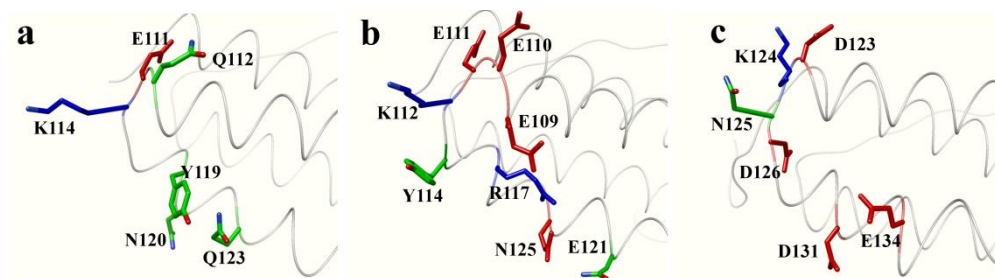


Figure 15: Profile view of the amino acid lining in the three fold channel in a) AfFt and b) PfFt with respect to c) HuHF. The exterior of the shell lies on the left side and the inner cavity on the right side of each cartoon as shown schematically. Positive, negative and polar residues are depicted as blue, red and green sticks, respectively

The reduced negative charge in the three fold axes of archaea ferritins might explain the facilitated entrance of negatively charged molecules, in

agreement with the high rate constants reported in the data previously shown. In addition, the comparison between AfFt and PfFt 3-fold channels and the slightly higher negatively charge of PfFt might also explain the difference between the observed rate constants between AfFt M54C/K150A/R151A and PfFt G52C, as a 5 times higher rate constant was found in the first protein although both ferritins displayed the typical octahedral closed conformation.

Finally, the 4-fold channel should also be considered as possible route to enter the cavity. Indeed, by structural analysis the 4-fold channels of PfFt and AfFt M54C/K150A/R151A showed a more polar and hydrophilic character than the respective channels in mammalian ferritins. In addition, structural evidences identified cations within the 4-fold channels, suggesting a hypothetical alternative cation entrance pathway⁵⁴. Nevertheless, the dimensions of the 4-fold channels, being smaller compared to the 3-fold channels (4-5 Å vs. 5-6 Å respectively), could not justify the entrance of large molecules as they would barely accommodate the entrance of cations. Therefore the passage of organic molecules through the 4-fold channels would seem even more unlikely than the 3-fold channel hypothesis¹²³.

Overall, excluding 4-fold channels as possible entrance route due to the restricted dimensions and having obtained data in support of the 3-fold channel permeation hypothesis, the 3-fold channel pathway was proposed as preferred route to encapsulate negatively charged molecules such as DTNB within the ferritin cavity. However, as the molecular dimensions of DTNB slightly exceeded the 3-fold channel size, rotameric adjustments of relevant amino acid side chains must take place during the molecule entrance, thus implying a high degree of plasticity of the channel. The flexibility of the protein barrier, however, might cause leaking of molecules trapped within the

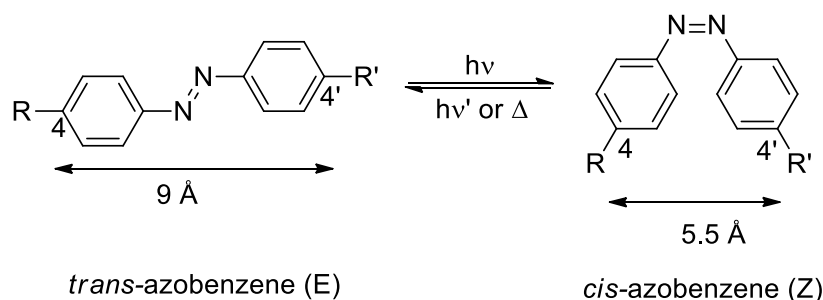
protein cavity and, as the ferritin has shown to be less rigid than predicted by the only structural analysis, further investigations will be needed.

In conclusion, archaea ferritins, with their improved permeability, could be employed as new scaffolds for the encapsulation of negative molecules, thus widening the potential biotechnological applications of ferritins as nanocarriers.

4.2. Azobenzene-ferritin conjugate for self-assembly photocontrol

As the aforementioned encapsulation by permeation, although useful, is restricted to molecules with limiting characteristics and the pH-induced association/dissociation method is not completely reversible, new methods for convenient and reversible encapsulation of any molecule are still needed. The last decades have witnessed significant advances in the ability to control, manipulate or alter molecular motion of small chemical objects and of complex biological molecules. In particular, among various stimuli to discipline biological systems, light has been found to be the most appealing and outstanding one for numerous reasons. Light can be switched on and off quickly, easily and reversibly, and its intensity and wavelength can be simply modulated. The light ray can be focused onto a small area and can be controlled in remote thus being less invasive. In conclusion, light can offer spatially and temporally control over a wide variety of processes¹²⁶. The most remarkable example in nature is the photoreceptive protein rhodopsin which can be activated by light-induced isomerization of a covalently attached chromophore¹²⁷. By imitating nature, scientists made an effort to covalently link light-responsive molecules to proteins in order to be able to induce conformational changes upon photoisomerization of the compounds. Among

a variety of molecules, one in particular has emerged for its remarkable properties: azobenzene. Azobenzenes are a unique class of chromophores, with a peculiarly efficient and clean photochemistry, characterised by two aromatic rings linked by a central azo group (N=N) that extend the aromatic conjugation. Azobenzenes are ideal molecular switches as they can exist as two different isomers, namely the *trans* (E) isomer and the *cis* (Z) isomer, that are able to photochemically or thermally interconvert rearranging their geometry around the azo bond as shown in Scheme 4¹²⁸.



Scheme 4: Schematic azobenzene isomerization process

Usually, the more stable *trans* isomer is converted by irradiation with a wavelength between 320-380 nm into its *cis* state, which in turn can either thermally relax to the more stable *trans* isomer or be photoisomerized by irradiation at 400-450 nm. The photoinduced switch proceeds by absorption of a photon that generates an excited state with a decreased energy barrier between the two isomeric states and, consequently, the isomers can more easily interconvert one into each other. The isomerization yields of the process are outstandingly high, thus allowing for the use of low intensity lights, and the isomerisation kinetics are remarkably fast, while thermal relaxation time is strongly dependent on the specific system^{126,129,130}. All

these excellent features make azobenzenes incredibly photostable and many photoswitching cycles can be repeated without any degradation or side effect. The only disadvantage is the impossibility to have a full and complete conversion from the *trans* isomer into the *cis* one, as only a 75 % *trans-cis* conversion is commonly reached while 100 % conversion is always verified from *cis* to *trans*. From a molecular point a view, the isomerisation leads to a strong molecular movement that causes large geometrical and conformational changes, reducing the distance between the two carbon atoms in position 4 and 4' from 9 Å to 5,5 Å as shown in Scheme 4¹³⁰. In addition the two aromatic rings from a planar geometry in the *trans* isomer, are brought closer together as one of the rings rotates, twisting at an angle of around 90° to minimize steric hindrance thus creating a dipole moment that wasn't present before in the symmetrical *trans* molecule¹²⁹. These geometrical changes strongly affect the UV-Vis absorption of this class of compounds making possible to easily study the interconversion reaction by UV-Vis spectroscopy, helped also by the high characteristic extinction coefficients of azobenzene molecules that are therefore detectable even at low physiologically relevant concentrations¹²⁶.

Substitution with reactive functional groups is necessary in order to cross-link the photoswitch to a biological substrate in one or two attachments sites. Chemical modification with a mono-functional azobenzene derivative counts on its sterical hindrance interference whereas bi-functional azobenzenes are usually chemically linked to two strategic positions and can induce strong conformational changes. Once again, cysteine is the most exploited amino acid for cross-linking as it is easily introduced via site-directed mutagenesis in key sites at a precise distance avoiding side reactions with other residues. Despite maleimides are the most commonly used cysteine reagents,

haloacetamides are often preferred for azobenzene functionalization because of the improved stability and robustness of the covalent bond and because of the decreased flexibility of the linker. The light-induced isomerization of azobenzene molecules covalently attached to biomolecules has been widely used in a variety of systems in order to photocontrol peptide structures¹³¹⁻¹³⁴, DNA helicity¹³⁵, or even protein structures and complex proteic machines such as ATP machines¹³⁶ or protein-folding machines¹³⁷. Enzymatic activity can easily be controlled with azobenzene based light-switches¹³⁸⁻¹⁴⁰ as well as receptors such as glutamate receptors which regulate ion channels, therefore offering a tool to control the opening and closure of cellular membrane pores¹⁴¹⁻¹⁴³. Azobenzenes can also be incorporated into proteins, by exploiting *E. coli* variants expressly designed for this purpose, in the form of an unnatural amino acid phenylalanine-azobenzene significantly extending the scope of the technique¹⁴⁴ or even be useful in gene transcription regulation by interfering with the RNA-polymerase¹⁴⁵. In addition, the stability and efficacy of azobenzenes was also proved in *in vivo* tests on zebrafish where the molecule showed almost comparable photochemistry *in vivo* and *in vitro*¹⁴⁶. In conclusion, any biochemical pathway, no matter how much complex, can be potentially controlled by photoregulation just with a simple key molecule positioned in the right spot. As several successful reports of azobenzene-controlled motion of proteic units have been described, the same method could possibly be applied to ferritins in order to photocontrol their assembly/disassembly equilibrium. To site-selectively introduce an azobenzene molecular switch onto the ferritin surface in a topologically selected position, the ferritin and the azobenzene designs must be carefully chosen.

4.2.1 Ferritin mutant design

The chosen ferritin cage used as a model to test the photoinduced disassembly/assembly equilibrium is the *Pyrococcus furiosus* ferritin. PfFt was selected because of its high stability, easiness of production and the octahedral symmetry of its cage, similar to the human ferritin packing. Indeed PfFt is always assembled as a tetraicosameric cage and its dissociation can only be induced by extreme pH values. In addition, the close packing originated from the octahedral symmetry does not allow any large molecule to penetrate the cage barrier, as the substance should be small enough to be able to cross the 3-fold symmetry channels. Therefore, the only chance to encapsulate large or pH-sensitive drugs into such ferritins is by means of a controlled and completely reversible dissociation/association equilibrium such as the photoisomerization.

As wild type PfFt did not contain any cysteine residue within its amino acidic sequence, two cysteines were introduced by site-directed mutagenesis, offering new sites for site-selective conjugation. However, several particular conditions were required for an efficient azobenzene cross-linking. Certainly, the distance of the side chain sulphur atoms of the engineered cysteines must match the end-to-end distance of the azobenzene derivative linker in its *trans* state. Fortunately, the 16 Å length of a *trans* di-haloacetamide azobenzene derivative matched exactly the distance between two parallel amino acids on the i^{th} and $i+4^{\text{th}}$ helical turns of an α -helical structure. The chosen two amino acids on the α -helix must be exposed and accessible to the solvent in order to correctly react with the azobenzene derivative in solution. Lastly, the azobenzene must be placed in a key spot for the 24-meric assembly involving a crucial subunit-subunit interface. By analyzing ferritin crystal structure, 4

main interactions were identified as responsible for the cage-like assembly (Figure 16): i) the dimer interface at C2 where the A and B helices of one monomer interact with the corresponding A' and B' helices of a second monomer, ii) the three fold channels at C3 where three couples of C and D helices form a triangular entrance, iii) the four fold channels at C4 where four E helices interact, and iv) the extended area between the three and the four fold axes C3-C4 involving several residues of three different monomers. As known from several mutagenesis studies, any modification at the C2 interface on the A or B helices (respectively in blue and green in Figure 16) would only destroy the dimeric building block, while alteration at the C3 and C4 channels would hardly alter the protein assembly^{75,78}. Even the complete rupture of the E helices (red in Figure 16) would probably not be enough to destroy the ferritin assembly as several residues had already been removed without any consequence for the cage packing⁷⁶. Therefore, excluding the helices A, B and E, the mutations could only be inserted either on the helix C or D. The choice fell on the solvent exposed part of the D helix (orange in Figure 16) as the C helix (yellow in Figure 16), despite being more accessible, established fewer contacts with the interfacing dimers and, due to the central position within the monomeric unit, it would hardly drag the hole α -helical bundle with it upon azobenzene isomerization. On the contrary, the C-terminal part of the D-helix was accessible by the solvent, was involved in hydrophobic contacts and hydrogen bonds with the interfacing dimer, and was located close to the terminal E-helix. Thus the D helix could more easily cause the monomeric unit destabilization by breaking of the 4 terminal helical turns.

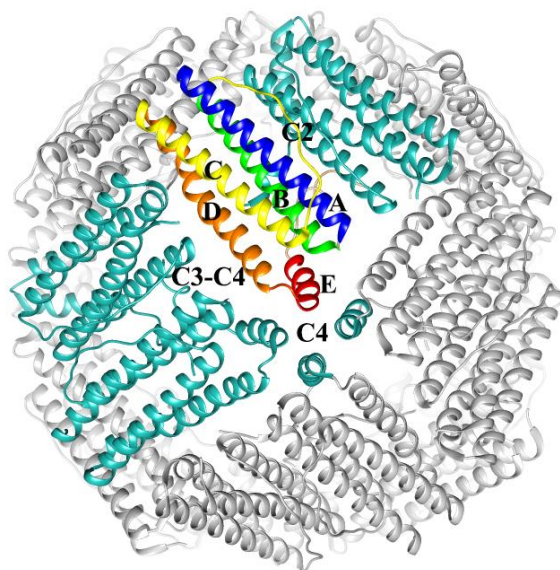


Figure 16: *PfFt* structure with the α -helical units in the monomer highlighted in blue (A), green (B), yellow (C), orange (D) and red (E). The monomer main interactions with others subunits are highlighted in cyan

Once identified helix D as the most suited structural motif to introduce the two cysteine residues, two amino acids must be carefully chosen for site-directed mutagenesis. A sequence analysis was carried out to identify the conserved key residues among archaea ferritins, as the mutations should not be introduced on conserved residues not to alter protein crucial interactions. The *PfFt* D-helix amino acid sequence was compared to the ones from the archaea ferritins *Thermotoga maritima* (TmFt) and *Archaeoglobus fulgidus* (AfFt) (Figure 17). Keeping in mind all the aforementioned criteria three possible mutants were explored: i) *PfFt* K142C/E131C (Figure 18A), ii) *PfFt* I143C/A132C (Figure 18B), iii) *PfFt* K135C/I124C (Figure 18C).

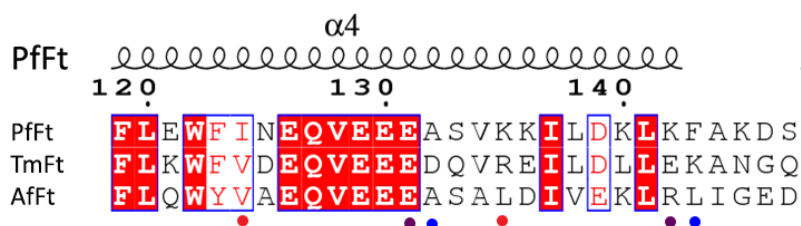


Figure 17: D-helix sequence alignment among PfFt, TmFt, AfFt archaea ferritins. Highly conserved residues are highlighted in red squares and the possible 3 set of mutations are indicated by colored dots (purple E131/K142, blue A132/F143, red I124/K135)

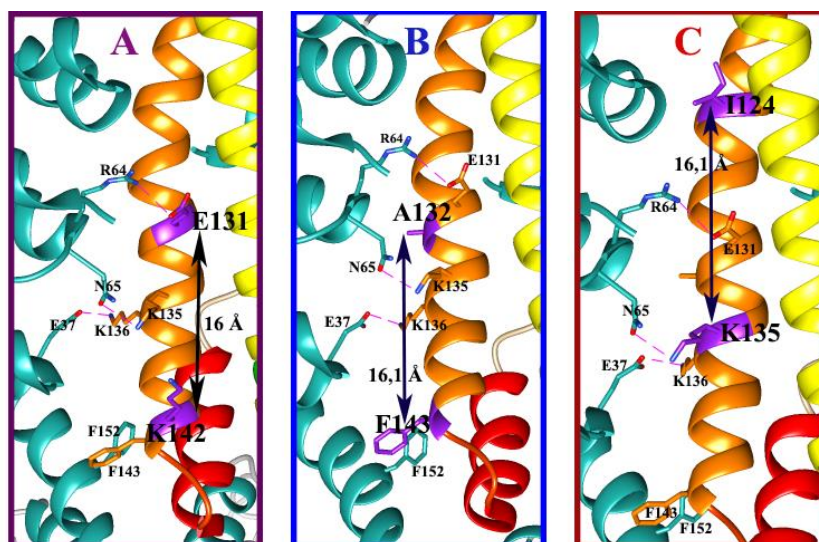


Figure 18: Schematic views of the three possible mutations set on the D helix (orange) of PfFt. The possible mutated residues are depicted in purple and the interactions between D helix residues and the vicinal dimer (cyan) residues are highlighted

Among the three possible choices, the first proposal (Glu131/Lys142, Figure 18, panel A), would mutate the conserved residue Glu131 and would destroy a crucial hydrogen bond between Glu131 and Arg64. Two non-conserved residues were instead involved in the second option (Ala132/Phe143, Figure 18, panel B) although both were buried within the dimer interface, thus being less exposed to the solvent. The third and last option (I124/K135, Figure 18, panel C), would involve residues on the more buried third and seventh helical

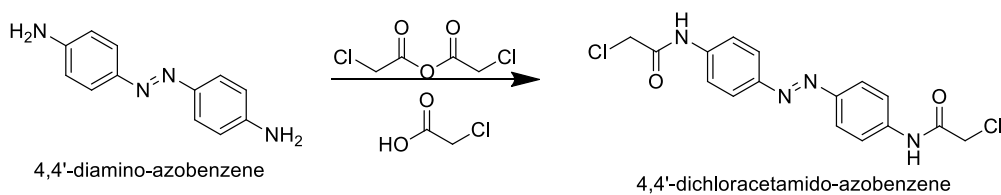
turns from the C-terminal of the D-helix, instead of the first and fourth helical turns of the other proposals, but would not alter any conserved residue. Taking into accounts all these considerations, the third mutant was selected as first choice, not to alter any conserved residue and preferring solvent exposed residues to the hydrophobic buried residues of the second option. The chosen mutations were then introduced one by one, by site-directed mutagenesis onto the wild type *Pyrococcus furiosus* ferritin gene. The ferritin was overexpressed in *E. coli* cells and purified in high yields, similarly to the wild type ferritin. The accessibility of the newly introduced cysteine residues was tested by Ellman's assay demonstrating a high reactivity.

4.2.2 Azobenzene derivative synthesis

Two cysteine reactive moieties were introduced at the ends of the 4,4'-diaminoazobenzene molecule, the azobenzene selected as building block. As the linkers introduced between the azobenzene molecule and the protein must be stable and strong enough to induce the molecular motion, a chloroacetamide reactive moiety was preferred to a maleimide group.

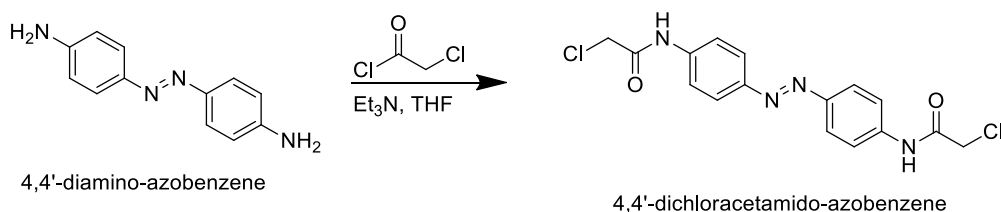
Initially, an acid catalysed synthetic pathway was attempted in which the 4,4'-diaminoazobenzene was reacted with chloroacetyl chloride and with chloroacetic acid as shown in Scheme 5. Unfortunately, the reaction always yielded a mixture of multi-functionalised products with 2, 3 or 4 chloroacetyl moieties, even by varying several reaction conditions such as temperature, solvent, molar equivalents of reagent and catalyst.

Chapter 4: Results and Discussion



Scheme 5: Acid catalyzed synthesis of 4,4'-dichloroacetamido-azobenzene

Therefore, the reaction conditions were completely changed and a base-catalysed reaction was attempted, as shown in Scheme 6. Gladly, the base-catalysed reaction yielded the desired pure bi-functional product in high yield (80 %) as confirmed by NMR analysis.



Scheme 6: Base catalyzed synthesis of 4,4'-dichloroacetamido-azobenzene

4.2.3 Azobenzene-labelled ferritin preparation

Having obtained both the azobenzene derivative by chemical synthesis and the PfFt I124C/K135C ferritin mutant by site-directed mutagenesis, the cross-linking bioconjugation reaction between the two was attempted. Unfortunately, a first issue emerged with the high insolubility of the 4,4'-dichloroacetamido-azobenzene. The compound was indeed extremely insoluble in hydrophilic environments and could only be dissolved in organic solvents such as DMSO or DMF. Several reaction attempts at different DMSO percentages up to 30 % v/v DMSO were then performed, but the

immediate precipitate formation could never be avoided, even by slow reagent addition or by increasing the temperature to favour the compound solubility. In these conditions the cross linking reaction always yielded a very poor labelling percentage. The breakthrough came from the employment of 1-butyl-2,3-dimethyl-imidazolium tetrafluoroborate (Figure 19), a water soluble ionic liquid that was able to solubilise the compound in the protein hydrophilic environment. Briefly, ionic liquids are salts found in the liquid state at room temperature, often made of at least an organic component with delocalised charge, which causes poor ion coordination thus preventing the formation of a crystal lattice.

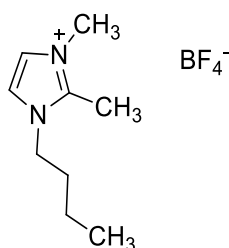


Figure 19: *1-Butyl-2,3-dimethyl-imidazolium tetrafluoroborate*

The ionic liquid was thus employed as cosolvent and its percentage was adjusted to find the right balance between protein stability and reagent solubility. Finally, by varying reaction conditions such as temperature and reagent equivalents and by introducing the reagent slowly over time, the crosslinked product was obtained with the best labelling yield achievable (40 % by Ellman's assay) and a high protein recovery (82 %). In particular, slow reagent addition was crucial in order to give time to the two reactive chloroacetyl moieties of the azobenzene to react with both cysteine residues. A first chloroacetyl moiety will presumably react with the more exposed C135 and the second reactive moiety will meet by rotation the C124 to only later

Chapter 4: Results and Discussion

react with it. An excessive reagent addition would instead saturate all the cysteine residues with one azobenzene molecule for each amino acid yielding a 1:1 cysteine/azobenzene ratio, instead of the desired 2:1 ratio with an azobenzene molecule bridging two cysteine residues.

The bioconjugate obtained showed a characteristic pale yellow colour, observable by UV-Vis spectroscopy in which a wide band centred at 370 nm, typical of azobenzene compounds, was found (Figure 20).

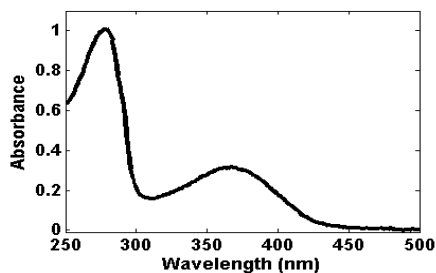


Figure 20: Azobenzene-PfFt conjugate UV-Vis spectrum

Unfortunately, the labelling percentage (40 % determined by Ellman's assay) was not high enough to observe the azobenzene conjugate by mass spectrometry analysis. The MALDI-TOF spectrum obtained showed the main unlabelled protein peak with a second broad noisy peak, probably corresponding to the azobenzene conjugate, too low to be analysed (Figure 21).

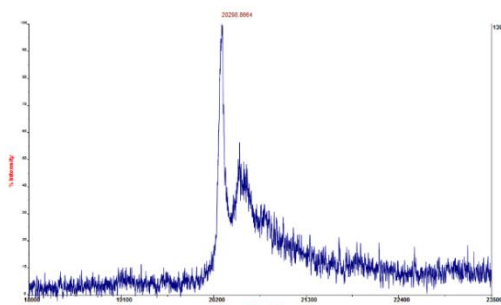


Figure 21: Azobenzene-PfFt conjugate MALDI-TOF spectrum

The PfFt wild type, without any cysteine residues, was reacted in the same conditions of PfFt I124C/K135C as control and, after purification, no trace of azobenzene derivative was found confirming the binding of the molecule on the cysteine residues and excluding any unspecific hydrophobic interaction.

4.2.4 Photoinduced isomerization

Finally, the photoinduced isomerization reaction was performed on the azobenzene-PfFt conjugate in collaboration with the Italian Institute of Technology (IIT). The sample was irradiated at 370 nm and UV spectra were recorded over time showing a decrease in the 370 nm peak and a smaller red-shifted peak increase at 430 nm as shown in Figure 22A. The isomerization proceeded with a mono-exponential trend (Figure 22B) and was complete in 60-90 minutes, as verified by the absence of further changes in the UV-Vis spectra. The isomerised sample containing the *cis* azobenzene isomer clearly presented a stronger yellow colour as indication of the successful isomerization.

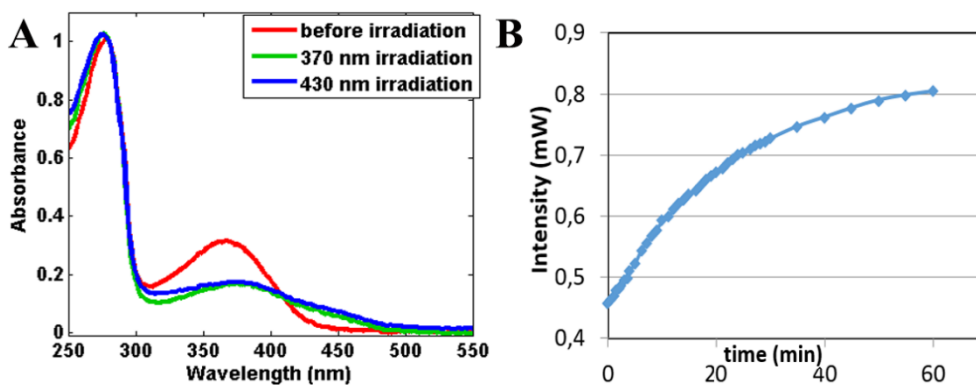


Figure 22: *Trans-cis* isomerization of the azobenzene-PfFt conjugate observed by A) UV-Vis spectroscopy and by B) kinetic measurement

Isomerization from the *cis* back to the *trans* isomer was attempted by irradiation at 430 nm, the UV-Vis maximum corresponding to the *cis* isomer identified by subtracting the UV-Vis spectra before and after isomerization. Unfortunately, the *cis* isomer was never able to isomerize back to its *trans* state neither by irradiation at 430 nm or by thermal relaxation, and no changes were ever verified by UV-Vis spectroscopy even after over night irradiation (Figure 22A, blue spectrum). The lack of success may be due to the insufficient power of the 430 nm irradiating lamp. Indeed, a higher amount of energy might be needed to bring the unstructured protein segment back to its native helical structure. Unfortunately, additional powerful light sources available in the laboratory, such as laser sources, did not irradiate at the correct 430 nm wavelength required.

The bioconjugate samples before and after irradiation were analysed by CD spectroscopy to observe any appreciable alteration in the α -helical structure. However, only tiny alterations were found in the CD profiles of the conjugate before irradiation, after 370 nm irradiation and after 430 nm irradiation (Figure 23). The low conjugation percentage together with the incompleteness of the *trans-cis* isomerization would probably alter only a few helical motifs over 120 α -helices on one single ferritin cage, thus resulting in a small alteration not detectable by CD spectroscopy. Therefore, only an indirect measure of the azobenzene isomerization state from the UV-Vis analysis might suggest the success or failure of the isomerization reaction, as the protein structural state could not be directly observed by CD spectroscopy.

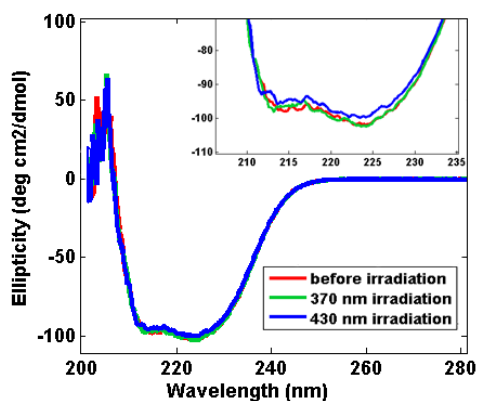


Figure 23: Azobenzene-PfFt conjugate CD spectra before and after irradiation

4.2.5 Conclusion and future perspectives

Disappointingly, the impossibility to perform the *cis-trans* isomerization prevented the successful conclusion of the ferritin photoinduced assembly-disassembly in one of the last steps of the project. Hopefully, in the future, a stronger 430 nm irradiating source could be capable of inducing the azobenzene isomerization thus reversibly closing the ferritin cage. The success of this process would open new perspectives for the encapsulation of various molecules inside the ferritin cavity and the eventual site-selective photo-triggered release *in vitro* or *in vivo*.

4.3 Pyrene-ferritin conjugate for protein oligomerization study and imaging in living cells

Pyrene is a unique fluorescent probe with peculiar spectral features, and its *N*-(1-pyrenyl)maleimide (NPM, Figure 24) derivative has been widely employed to label proteins or nucleic acids for various biological applications¹⁴⁷⁻¹⁵⁴. Any biological scaffold that can populate two distinct conformational states can be labelled in key positions with two pyrene moieties, in order to study the process involved in the shift between the two states by simply observing pyrene spectral changes. With this method it is possible to study protein oligomerization, protein folding-misfolding, conformational changes¹⁴⁷⁻¹⁴⁹, visualization of intracellular RNA¹⁵⁰, biomolecule signaling¹⁵¹, design of aptamer sensors^{152,153} and pH sensors in cellular organelles¹⁵⁴.

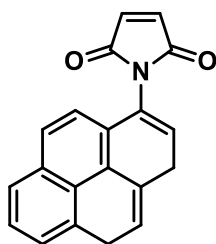


Figure 24: *N*-(1-pyrenyl)maleimide, NPM

Pyrene versatility is due to a spatially sensitive fluorescence emission that displays an ensemble of monomer emission peaks (375-405 nm) and an easily distinguishable red shifted broad peak (centred between 440-450 nm) corresponding to the excited state dimer called excimer, as shown in Figure 25^{155,156}.

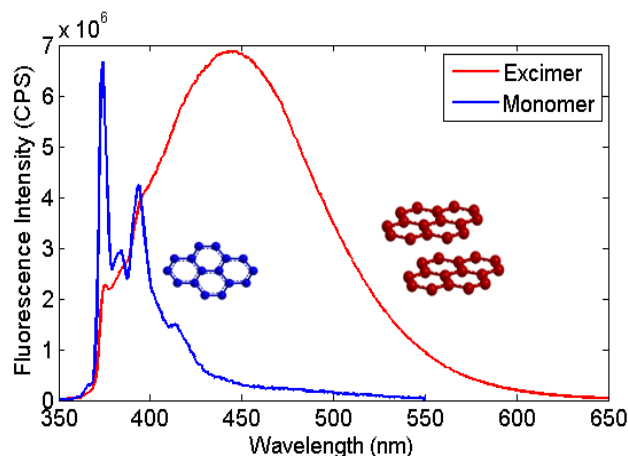
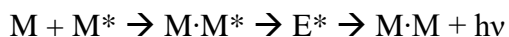


Figure 25: Pyrene monomer (blue) and excimer (red) fluorescence emission spectra

Excimer formation arises when two pyrene molecules, one in the ground state and the other one in the excited state, are located in close proximity ($\sim 10\text{-}15$ Å) and are involved in a non-covalent $\pi\text{-}\pi$ stacking interaction¹⁴⁷. For an efficient excimer formation, the two pyrene molecule must be close and parallel-oriented, in a slightly rotated sandwich geometry, at an interplanar distance of 3-4 Å^{155,156}. As the two molecules are close but sufficiently separated, light can be absorbed by only one of the two moieties, giving two pyrene monomers, one in its ground state (M) and one in its excited state (M*). The two pyrenes will then interact generating the excited excimer (E*), which will then decay, as shown below, giving rise to the peculiar fluorescence emission spectra¹⁵⁶.



Excimer formation is facilitated both by the long pyrene excited state lifetime (>100 ns) and its energy-accepting properties¹⁵⁷. Any change in the

excimer/monomer (e/m) ratio, determined by the fluorescence intensity ratio between the excimer band maximum at 445 nm and the monomer peak at 375 nm, gives information regarding the distance and the orientation between the two pyrene molecules. Therefore, if a protein is labelled with two pyrene moieties in two proximal positions in a way that an excimer can be formed, any subtle structural change will strongly affect the stacking interactions and therefore result in a clear shift in the fluorescence emission^{147,148,155}. The correlation between the e/m ratio and the distance of two pyrene molecules in a half-helical structure has been studied by Bains et al. and an inverse correlation has been found, with an additional contribution from the probe mobility and the helix flexibility¹⁴⁷.

Another important information is contained within the pyrene monomer emission profile as the so-called “Py value”, given by the intensity ratio between the first peak at 375 nm and the third peak at 385 nm, is used as a polarity index. The Py value changes with the environment’s polarity and is higher in polar solvents where the peak at 375 nm is the predominant one, or lower in hydrophobic environments, where the 385 nm peak increases^{157,158}.

In conclusion, pyrene fluorescence properties are ideal for biological investigations as the probe’s high molar extinction coefficient of the probe allows studies of proteins in solution at physiologically relevant concentrations and its high stability and long fluorescent lifetime give it resistance to photodamage and photobleaching¹⁵⁹.

4.3.1 Humanized archaea ferritin design

Cargo encapsulation within the ferritin cavity is a crucial step that still suffers the drawbacks of the most commonly used techniques. Cavity permeation is restricted by the molecule charge and dimension, even in the more tolerant archaea ferritins, while the pH-triggered encapsulation submits the protein to harsh conditions from which the ferritin not always recovers and limits the procedure application to pH resistant molecules. Recently, *Archaeoglobus fulgidus* ferritin has emerged as a possible solution to these issues thanks to its unique salt-induced self-assembly properties in mild neutral conditions. However, archaea ferritin uptake into mammalian cells has never been reported up to now, as the only H-homopolymer from human ferritin (HuHF) uptake, mediated by the TfR1 receptor, has been described¹⁶⁰. Nonetheless, the H-homopolymer TfR1 receptor binding site has not been yet identified. However, by analysing the three dimensional ferritin structure, with a particular regard to the ferritin surface, the most significant accessible areas highlighted are the external BC loop with its 19 amino acidic residues and the N-terminal segments. The N-terminal and C-terminal fragments are known to be not necessary for the TfR1 mediated ferritin uptake, as even by deletion of several residues the human ferritin could still be internalised¹⁶⁰, suggesting that the TfR1 interacts with other ferritin portions to recognize and uptake the protein.

In light of these evidences, to favour the archaea ferritin uptake, an engineered archaea ferritin named “Humanized” *Archaeoglobus* ferritin (HumAfFt) was produced, in which the external BC loop was substituted with the H-homopolymer human analogue loop. This chimeric protein should indeed maintain the salt-induced assembly/disassembly properties typical of

Archaeoglobus fulgidus ferritin while being successfully internalised into human cells by TfR1 recognition.

At first, the 3D structure and the amino acid sequence alignment of HuHF and AfFt were analysed. From a structural point of view, both human and archaea loops were similarly arranged in an antiparallel orientation, while from the sequence alignment several differences emerged, as among the central portion of the 19 residues loop (from residue 70 to 83, AfFt numbering) only 3 residues of the HuHF BC-loop were conserved in the AfFt one. Thus, 9 amino acid residues in the centre of the AfFt loop were substituted with the residues typical of the human H-homopolymer as shown in Figure 26.

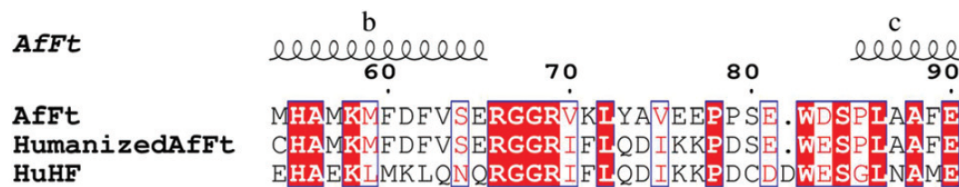


Figure 26: Sequence alignment between AfFt, HumAfFt and HuHF. Elements of the secondary structure are shown on the top and the conserved residues are highlighted in red squares

The chimeric protein was then expressed in *E. coli* cells. The overexpression and the purification protocols were optimised starting from the AfFt procedure until the pure protein was obtained with a yield between 50-100 mg per litre of culture. The protein was then crystallized and its structure, determined by X-ray crystallography at a 2.87 Å resolution (PDB 5L69) and by cryo-electron microscopy at a 33 Å resolution (Figure 27), confirmed the existence of the wide triangular pores and of the correct 24-meric assembly.

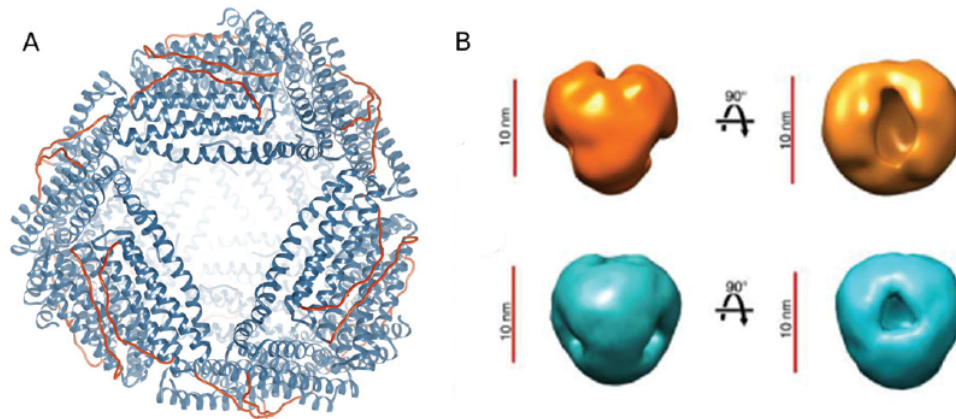


Figure 27: 3D structure of HumAfFt determined by A) X-ray crystallography with the external mutated BC loops in red and B) by cryo-electron microscopy where the HumAfFt (orange) is compared with AfFt (cyan)

The salt-induced assembly properties of the chimeric ferritin were verified by size exclusion chromatography (SEC), confirming identical association properties to the native AfFt. The protein was assembled as a dimer at 20 mM HEPES pH 7.4, while it eluted as a 480 kDa 24-mer at 20 mM HEPES pH 7.4 and 20 mM MgCl₂ (Figure 6). The mutations on the loop did not affect the assembly properties and the chimeric Humanized ferritin was thus able to open and reclose by tuning the buffer ionic strength.

4.3.2 Pyrene-ferritin conjugate design

In order to explore and investigate thermodynamically and kinetically the HumAfFt assembly/disassembly mechanism from the dimeric to the cage-like 24-meric state, a conservative mutation M54C was introduced in the middle of the B helix and the protein was selectively labelled with N-(1-pyrenyl)maleimide (NPM), a fluorescent pyrene derivative. The NPM

molecule was inserted in a topologically selected position inside the protein cavity, at the two-fold axis of the dimer, far from any inter-subunit contacts or loop regions in order to avoid any interference with the cage assembly. As shown in Figure 28, the distance between two β -carbons of two C54 is approximately 14 Å, enough to allow for the excimer formation by π -stacking interaction between two pyrene molecules. Any subtle rearrangement or structural change in the pyrene-labelled ferritin should affect the reciprocal orientation and distance of the two pyrene molecules involved in the excimer, thus altering the excimer stacking interaction and therefore resulting in a shift in the fluorescence emission. The pyrene fluorescence emission sensitivity could thus be used to investigate the assembly/disassembly process.

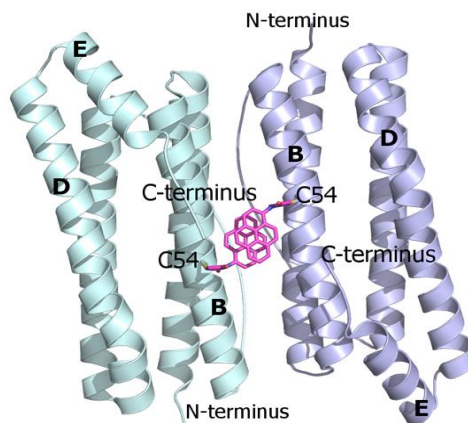


Figure 28: Ribbon diagram of the antiparallel homodimer structure of HumAfFt (PDB 5LS9). Two NPM molecules are depicted in magenta sticks bound to C54, establishing a π - π stacking interaction, at the dimer interface

4.3.3 Pyrene-ferritin conjugate preparation

Optimization of the ferritin-NPM bioconjugation reaction was extensively carried out by screening a set of various reaction conditions such as temperature, time, reagent equivalents, protein concentration, buffer ionic strengths and cosolvent presence. The difficulties met in finding the optimal reaction conditions were mainly attributable to the NPM hydrophobic nature. Indeed, due to its aromatic pyrene core, NPM was hardly suited for biological conjugation in hydrophilic environments. The presence of a cosolvent in the reaction mixture was the key ingredient for the success of the reaction, and several cosolvents such as DMSO or acetonitrile in different percentages were tested. The best results were obtained by employing 15 % v/v acetonitrile, the highest amount tolerated by HumAfFt ferritin, and by increasing the temperature to 37 °C to favour compound solubilisation. Unfortunately, however, even with the cosolvent employment, the NPM amount could never be risen above 5 molar equivalents due to precipitate formation and consequent protein loss. The labelling yields were then improved by longer reaction times and higher protein concentrations. Finally, with the best optimised conditions the pyrene-ferritin bioconjugate was obtained with a 85 % protein recovery and a 75 % labelling. The labelling percentage was determined by Ellman's assay and MALDI-TOF mass spectrometry analysis, since a UV-Vis determination was not reliable due to red-shift and hypochromic effect of the pyrene absorption peaks caused by micro-environment changes¹⁵⁶. As shown in Figure 29A, the mass spectrometry spectrum of the conjugate confirmed the presence of two species, the unlabelled HumAfFt (observed mass 20248 Da, expected mass 20243 Da for HumAfFt after the loss of the first methionine residue from its

Chapter 4: Results and Discussion

sequence) as the first minor peak and the pyrene-HumAfFt conjugate (observed mass 20545 Da, expected mass 20540 Da) with an additional mass of 297 Da, proper of the NPM molecule, as the main peak.

The conjugation reaction was performed in the same conditions on AfFt M54C, in order to compare the behaviour of the two proteins in their “humanized” and “non-humanized” versions to verify if the 9 mutations inserted altered somehow the assembly behaviour. The protein yield and labelling percentage were approximately the same as in HumAfFt, as confirmed by Ellman’s assay and MALDI-TOF mass spectrometry analysis (Figure 29B). Again a first small peak corresponding to the AfFt M54C unlabelled protein was found (observed mass 20152 Da, expected mass 20157 Da for AfFt after the loss of the first methionine residue from its sequence) together with the main peak corresponding to the NPM-AfFt conjugate (observed mass 20458 Da, expected mass 20454 Da).

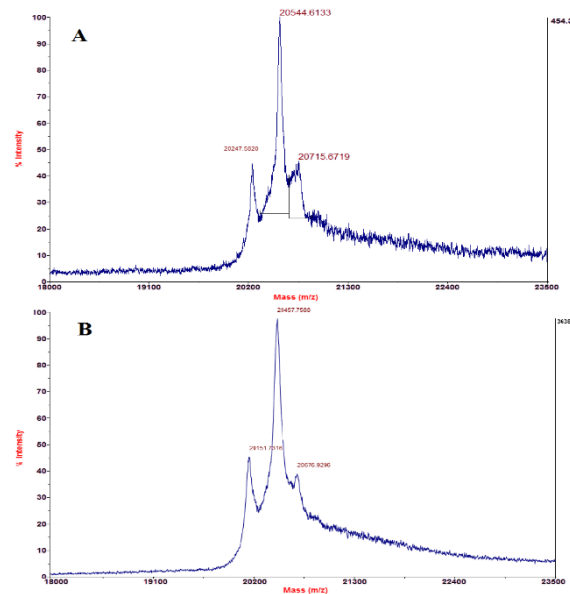


Figure 29: MALDI-TOF mass spectra of A) NPM-HumAfFt conjugate and of B) NPM-AfFt M54C conjugate

In addition, a control to assess the absence of any unspecific interaction with ferritin hydrophobic regions was carried out by adding NPM to AfFt wild type, with no reactive sulfhydryl moieties, under identical reaction conditions. A partial unspecific binding was initially verified and the purification conditions were then adjusted to remove any unbound molecule. To this end, and once more, the cosolvent turned out to be crucial and by optimising the purification protocol the unspecific hydrophobic binding was reduced to approximately 5 %.

4.3.4 Ferritin assembly assessment by DLS

In order to verify that the overall oligomerization process had not been altered by pyrene-labelling, a DLS study on the ferritin assembly was carried out. All ferritins were found to be monodispersed in solution when assembled into their 24-meric state, while they were slightly polydispersed when dissociated into dimers, an effect probably due to the low signal of the dimer (Figure 30).

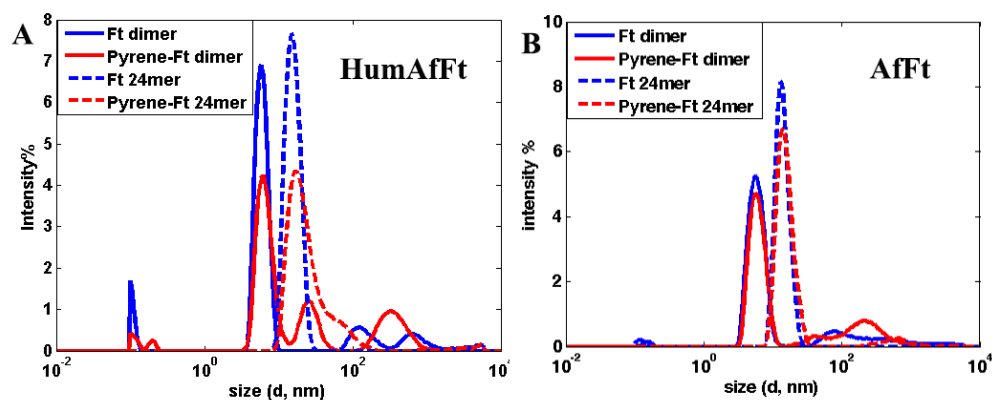


Figure 30: DLS intensity by size distribution of A) HumAfFt and of B) AfFt M54C both pyrene-labelled (red) and unlabelled (blue) in their dimeric (line) and 24meric association state (dotted line)

Chapter 4: Results and Discussion

The DLS intensities were reported as a function of the size distribution and the average hydrodynamic diameters were extrapolated from the peak maxima. The calculated hydrodynamic diameters are listed in detail in Table 2 and showed an average 5.8 nm diameter for the dissociated state in the absence of MgCl₂, in agreement with the predicted theoretical value for a dimer⁵³, and an approximate 14 nm diameter for the associated state in 20 mM MgCl₂. Both pyrene-labelled HumAfFt and pyrene-labelled AfFt M54C ferritins showed similar sizes to the respective unlabelled proteins within the error and, in both labelled and unlabelled ferritins, a slightly larger diameter was found for HumAfFt compared to AfFt M54C.

	AfFt M54C	Pyrene-AfFt M54C	HumAfFt	Pyrene-HumAfFt
<i>20 mM HEPES</i>	5,6 Å	5,6 Å	5,9 Å	6,2 Å
<i>20 mM HEPES, 20 mM MgCl₂</i>	12,9 Å	14,1 Å	14,8 Å	17 Å

Table 2: *Calculated hydrodynamic diameters of both pyrene labelled and unlabelled ferritins in absence or presence of magnesium cations*

The magnesium dependent DLS titrations confirmed the comparable self-assembly properties of AfFt and HumAfFt, with and without pyrene, and showed a complete transition within 5 mM MgCl₂ (Figure 31).

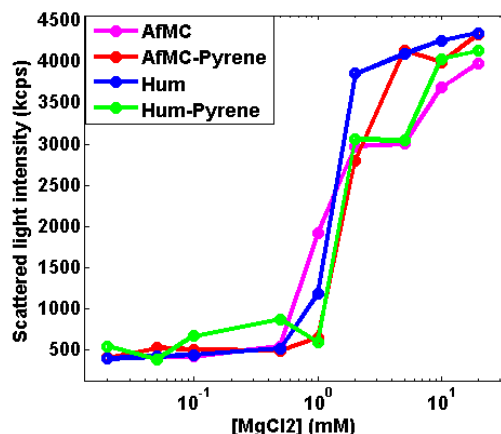


Figure 31: DLS scattered light intensity as a function of $MgCl_2$ concentration of HumAfFt and AfFt M54C both pyrene-labelled and unlabelled

4.3.5 Ferritin assembly/disassembly assessment by fluorescence spectroscopy

The HumAfFt salt-induced self-assembly process was extensively studied in comparison with the AfFt M54C oligomerization process, by exploiting the pyrene sensitive fluorescence emission and by employing PfFt P77C as standard. *Pyrococcus fulgidus* ferritin was chosen as standard as it is uniquely found as 24-meric assembled cage in solution, thus being an ideal assembled cage standard independent of salt concentrations. In addition, the pyrene molecules linked to the PfFt P77C external cysteines were placed at a 24 Å distance, too far from each other to form an excimer by stacking interaction, but ideal to represent a pyrene monomer standard.

The set of three pyrene-labelled ferritins (pyrene-HumAfFt, pyrene-AfFt M54C, pyrene-PfFt P77C) were analysed by fluorescence spectroscopy at 25 °C (excitation at 342 nm). As reported in Figure 32, only the pyrene monomer fluorescence emission was present in PfFt P77C, while in AfFt

M54C and HumAfFt an additional broad band centred at 445 nm appeared, thus confirming the predicted excimer formation.

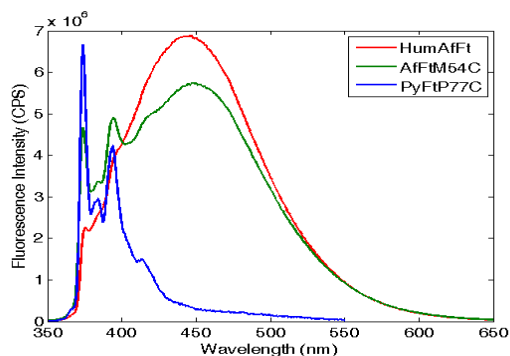


Figure 32: Fluorescence emission spectra of the pyrene-labelled ferritins obtained by excitation at 342 nm

Surprisingly a higher amount of excimer was found in HumAfFt although the protein differed from AfFt M54C by only 9 residues on the loop between helices B and C and the superposition of the two structures did not highlight any significant repositioning in the residue 54. For an efficient excimer formation, two pyrene molecules must be stacked in a parallel orientation allowing for a π - π interaction to take place, and these mutations on the loop could possibly slightly affect the relative orientation and distance between the two pyrene moieties¹⁴⁷.

The AfFt wild type, bearing no cysteines, was also analysed by fluorescence spectroscopy to investigate the possible contribution of the 5 % unspecific hydrophobic labelling. As NPM alone is fluorescent only when reacted with a sulfhydryl moiety, due to a quenching effect of the maleimide double bond, no pyrene fluorescence spectra was observed, confirming the absence of any contribution to the conjugate fluorescence spectra from the unspecifically bound molecules. The unlabelled protein contribution to the fluorescence spectra was also analysed and found to be inexistent as expected.

An additional control to verify that the excimer arose from the intermolecular interaction of two close pyrene molecules and not from intramolecular interactions of pyrene aggregates from different cages was carried out and the fluorescence spectra were recorded at different dilutions both with and without magnesium cations. While the total fluorescence decreased the excimer/monomer ratio, an index of the total excimer amount, remained constant demonstrating that the excimers were formed by intermolecular pyrene stacking (data not shown).

Remarkably, in the tetraeicosameric state, upon cation-triggered oligomerization, the overall amount of excimer decreased in both pyrene-HumAfFt and pyrene-AfFt M54C, as shown in Figure 33, probably due to movements at the dimer interface that caused a destabilization of π - π stacking interactions between the two pyrene moieties.

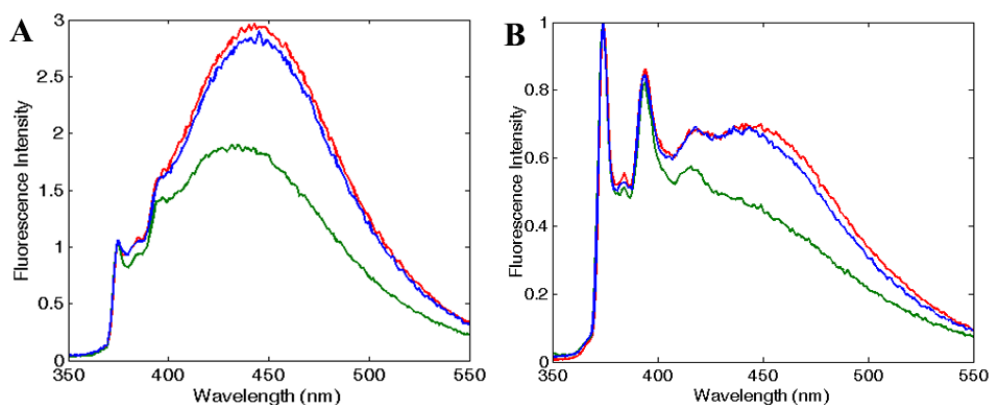


Figure 33: Reversibility assessment of the assembly-disassembly mechanism. Fluorescence spectra of A) pyrene-HumAfFt and B) pyrene-AfFt M54C in the absence of salts (red), in the presence of 50 mM MgCl₂ (green) and after 50 mM EDTA addition (blue)

Moreover, the excimer amount was successfully restored after EDTA addition (equimolar to the MgCl₂ in solution), suggesting that the chelating agent ability could promote protein disassembly by removal of magnesium

cations and that the excimer content could be related to the association state of ferritin (Figure 33).

To corroborate that the fluorescence excimer band variation was related to the oligomerization process and was independent of the ionic strength, the fluorescence emission was measured at fixed ionic strength using different amounts of either MgCl_2 or NaCl . According to the Debye–Hückel model, the experiment was carried out at two different ionic strength conditions: at low salt concentrations (i.e. 150 mM NaCl or 50 mM MgCl_2), where the protein was associated in the 24-meric state only in MgCl_2 , and at high salt concentrations (i.e. 600 mM NaCl or 200 mM MgCl_2), where the protein was associated in both salts. As shown in Figure 34, the excimer content without salt and in the first condition at 150 mM NaCl were similar, in agreement with a dissociated state. In contrast, at 50 mM MgCl_2 , therefore at an equal ionic strength as above, the excimer content revealed the presence of an associated state for both proteins (Figure 34). Moreover, the pyrene monomer emission profile of PffFt P77C did not change at various salt concentrations, excluding any ionic strength influence on the pyrene fluorescence emission (data not shown).

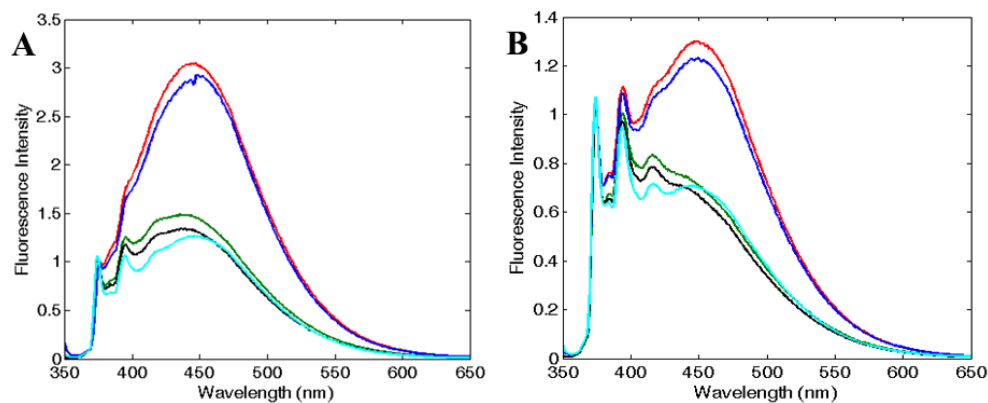


Figure 34: Assessment of the correlation between oligomerization state and excimer fluorescence. Fluorescence emission spectra of A) HumAfFt and B) AfFt, without any salt and at two different fixed ionic strengths for either $MgCl_2$ or NaCl. Spectra in the absence of any salt (red) and 150mM NaCl (blue) correspond to a dimeric state, while the profiles at 600 mM NaCl (cyan), 50 mM (green) and 200 mM (black) $MgCl_2$, correspond to the associated state

The fluorescence emission dependence on the protein oligomerization state was thus investigated by monitoring magnesium-induced association at equilibrium. By exploiting the excimer/monomer ratio (e/m) as an index of the extent of excimer formation, the association process was investigated as a function of $MgCl_2$ concentration. A sigmoidal curve was found, suggesting a high cooperativity within the oligomerization process, with a transition between 0.5 and 2 mM $MgCl_2$ and a complete assembly at about 5 mM $MgCl_2$ in both ferritins (Figure 35). Apart from small differences between AfFt M54C and HumAfFt profiles, the overall assembly process was not drastically altered by mutation of the 9 residues on the BC loop in HumAfFt.

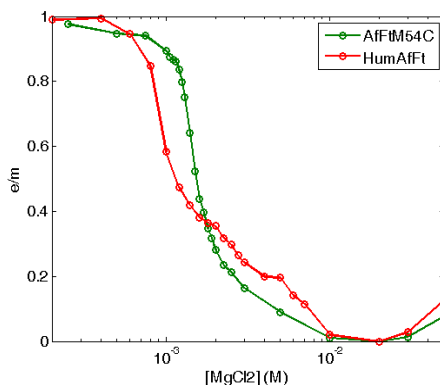


Figure 35: Thermodynamic study of Mg^{2+} -triggered oligomerization process. Fluorescence e/m ratio is shown as a function of magnesium concentration. The curves were obtained at equilibrium at 25 °C for both pyrene-labeled HumAfFt (red) and AfFtM54C (green) and show a highly cooperative transition

By comparing the sigmoidal curves obtained by fluorescence measurements and dynamic light scattering analysis, the overall shapes of the curves perfectly matched (Figure 36), confirming that the indirect pyrene fluorescence changes observed were actually representative of the protein assembly state, thus validating the fluorescence method employed.

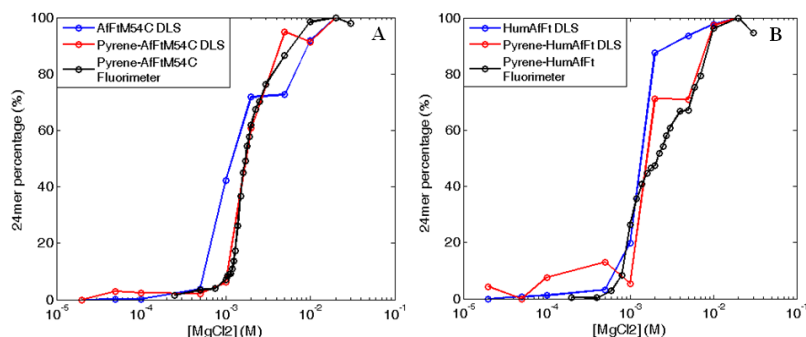


Figure 36: DLS titration compared with fluorescence titration as a function of $MgCl_2$ concentration. DLS measurements for (A) AfFtM54C and (B) HumAfFt, native (blue) and pyrene-labeled (red), are compared with fluorescence measurements on pyrene-labeled ferritins (black). All the measurements show a cooperative association not altered by pyrene labelling

Despite being an indirect method, the fluorescence investigation has the advantage to be faster and to require smaller amounts of sample than DLS. In addition, by observing the fluorescence signal, fast kinetics could be observed that were otherwise not detectable by DLS analysis.

In light of the surprisingly strong effect observed by employing Mg^{2+} cations, the subunits assembly was analysed in terms of possible contributions to specific binding within the three-dimensional crystallographic structure (PDB 5LS9) by using PISA software (CCP4 suite). No significant evidence of Mg^{2+} presence at the interface between dimers was observed. In fact, as it was previously reported by Sana et al.^{88,90}, it was evident that the hydrophobic network connecting the dimer interface played a key role in stabilizing the cage structure in high ionic strength buffers. In turn, divalent cations were found to occupy the AfFt ferroxidase centre under conditions of iron deficiency, through explicit coordination provided by Asp52, Glu19 and His55, according to AfFt numbering⁸⁷, and several metal cations as Mg(II), Mn(II), Cd(II), Zn(II), Tb(III) were also observed in the three sites of the ferroxidase centre of several other proteins^{54,60,161,162}. In the light of these observations, it might be hypothesized that coordination of Mg^{2+} in the ferroxidase centre can assist the assembly process by exerting some subtle conformational rearrangement within the dimeric species, thus explaining the different behaviour respect to a monovalent cation.

4.3.6 Ferritin assembly/disassembly kinetics

By monitoring the pyrene fluorescence changes over time with a stopped-flow apparatus, the kinetics of the salt-induced oligomerization process were studied. The fluorescence emission was observed as total fluorescence with a 360 nm cut-off. The areas under the curve (AUC) were thus calculated for the fluorescence profiles of the dimeric and 24-meric ferritin states at equilibrium and the highest AUC was found in the protein with a higher excimer content, the ferritin dimer (Figure 33). Therefore, a fluorescence decrease over time was expected upon protein oligomerization. Initial measurements revealed a surprisingly fast time course with a magnesium-triggered assembly complete within 10 ms, which is quite close to the dead-time of the stopped-flow apparatus (1-2 ms) and therefore impossible to follow by stopped-flow measurements at 25 °C. However, by lowering the temperature to 4 °C a clear decaying exponential curve was recorded. Despite being always close to the instrumental time limit and despite the loss of the initial data due to the impossibility to observe the processes under 10 ms, some semi-quantitative estimates on Mg^{2+} -induced association could still be obtained.

Fluorescence emission decreased upon Mg^{2+} addition with a double exponential trend and the reaction was complete within 25 ms, as shown in Figure 37. Reaction rates increased proportionally with both Mg^{2+} and protein concentration with a major contribution from the protein concentration (Figure 37B). The pyrene-HumAfFt and pyrene-AfFt kinetics were comparable, and as an example the only pyrene-HumAfFt kinetic traces were reported in Figure 37. Control experiments in which the protein dissolved at very low ionic strength (i.e. buffer alone, 20 mM HEPES pH 7.4) was injected against an identical sample or against the only buffer

confirmed the absence of any time-dependent changes in the fluorescence signal (data not shown).

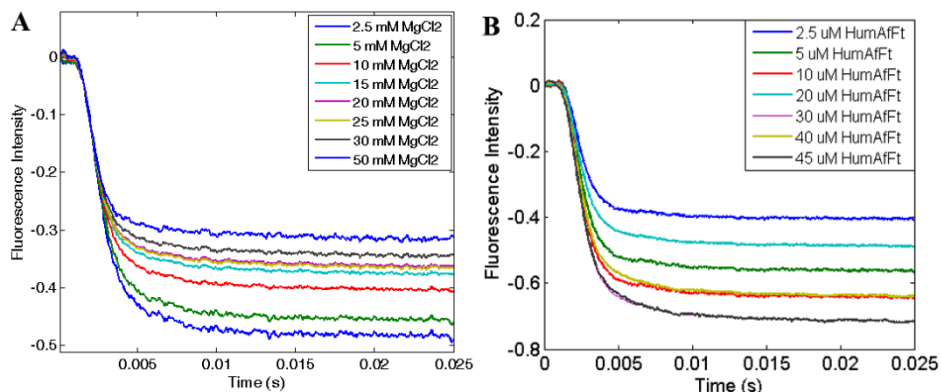


Figure 37: Association kinetics as a function of (A) $MgCl_2$ concentration and (B) ferritin concentration recorded at 4 °C showing a fast bi-exponential behavior complete in 25 ms

The EDTA-triggered dissociation process was slower than the assembly and was measured both at 25 and 4 °C. Faster dissociation rates were observed at higher temperatures, with completeness reached in 0.1 s at 25 °C and in 0.25 s at 4 °C. The dissociation kinetics showed a biphasic time profile, dependent on EDTA concentration but independent of protein concentration (Figure 38), as expected. Once more there were no appreciable differences between the pyrene-HumAfFt and the pyrene-AfFt M54C profiles.

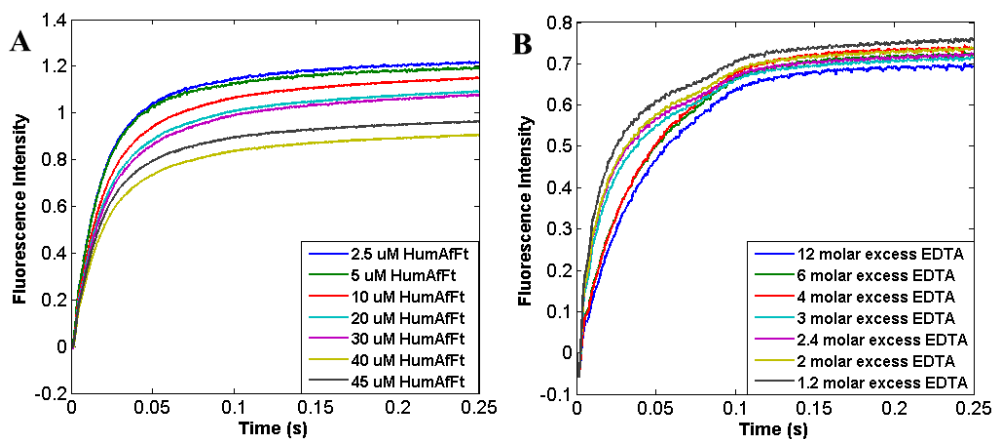


Figure 38: Dissociation kinetics as a function of (A) ferritin concentration (B) EDTA/Mg²⁺ molar ratio, recorded at 4 °C showing a fast bi-exponential behavior complete in 250 ms

Since the kinetic reaction in the presence of magnesium cations appeared to be too fast to be properly studied, the slower Na⁺-induced association process was also investigated. In comparison with magnesium, higher salt concentrations were required to monitor Na⁺-triggered association as the oligomerization was complete only at 500 mM NaCl⁸⁹. The assembly showed much slower rates and a multiphasic kinetic profile (Figure 39) with an initial lag phase (Figure 39A' and 39B'), typical of a nucleation process commonly found in protein oligomerization^{163,164}, that evolved in four exponential phases towards the end of the reaction, which was reached only after 20-30 minutes at 25 °C. These changes in the total fluorescence emission over time, could be due to multiple pyrene rearrangements during the assembly. Additionally, while the association rates were proportionally increasing with NaCl concentration, at fixed NaCl concentration and varying protein concentration the reaction rates were approximately constant.

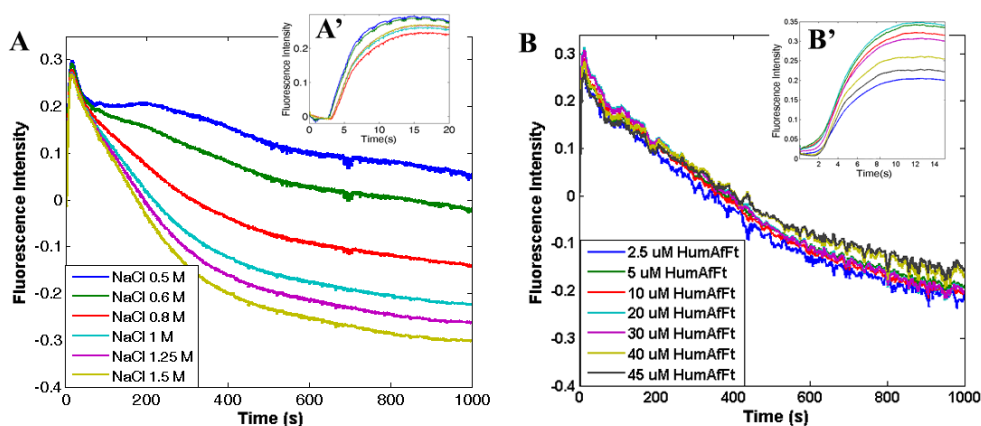


Figure 39: Association kinetics as a function of (A) NaCl concentration (B) ferritin concentration, recorded at 25 °C showing a multi-exponential behavior not complete in 1000 s. In the close up views A' and B' the initial lag phases respectively as a function of NaCl and ferritin concentration were shown

Sodium-triggered association showed a markedly different behaviour with respect to the magnesium-induced process, not only because of the higher amount of salt required but also because of the longer times and the different influence of protein or salt concentration on the reaction rates. This evidence, although difficult to interpret and analyse due to the complexity of the aggregation mechanism, seem to suggest that a different mechanism might be involved in the magnesium-triggered association compared to the sodium-triggered one. Unfortunately, even though the curves had been mathematically fitted by multi-exponential functions, due to the complexity of the mathematical analysis and the intrinsic difficulty in extracting a mechanistic meaning from the data without a supporting kinetic model¹⁶⁵, it was impossible to deeply understand the meaning of these findings. However, the data reported in this thesis are a first step in unravelling the

details of the aggregation process of ferritins, by using a simple spectroscopic technique such as fluorescence spectroscopy (as opposed to more sophisticated methodologies, i.e. DLS and small-angle X-ray scattering) that hopefully, in the future, will be of help in disclosing the single steps of the process. In addition, these evidences will offer new insights for the controlled assembly/disassembly crucial for cargo encapsulation in mild physiological conditions of both AfFt and HumAfFt. Indeed magnesium-triggered assembly represents a convenient alternative to the NaCl-induced process as Mg^{2+} can induce a faster cage closure with lower salts amounts, thus potentially representing a marked improvement for the synthesis of drug delivery nanodevices.

4.3.7 Humanized ferritin cellular uptake

HumAfFt was expressly designed with the aim of creating a protein cage with the peculiar characteristics of AfFt ferritin, which were assessed as previously described, and with the TfR1-recognition motive typical of the human ferritin H-homopolymer. Indeed, as TfR1 is overexpressed in several tumour cell lines, the successful recognition of HumAfFt would open new possibilities in exploiting the ferritin nanocages for cell-targeted delivery of probes for diagnostic or therapeutic purposes. Thus the humanized ferritin HumAfFt cellular uptake was studied both by flow cytometry analysis and by confocal microscopy in collaboration with the Italian Institute of Technology (IIT).

4.3.7.1 Flow cytometry analysis

HeLa cells, with their high level of TfR1 expression, were chosen as tumour cell line testers for the HumAfFt uptake receptor. A set of three different proteins, AfFt, HumAfFt, and transferrin (Tf, as control for TfR1 uptake), were labelled with a FITC fluorophore. The proteins were incubated with HeLa cells for different amounts of time (1, 3, 20 h) and were then analysed by flow cytometry (Figure 40A). As expected, transferrin was highly internalised in all cells, while AfFt ferritin was excluded (5 % uptake at 1 h, less than 20 % at 20 h). However, the engineered chimeric ferritin HumAfFt was actively uptaken already after 1h of incubation at a much higher percentage (81 % at 1 h and 90 % at 20 h) than the native AfFt. The increased uptake after 20 h, as it involved both AfFt and HumAfFt, might be due to an unspecific uptake by pinocytosis, while the initial uptake would probably involve a specific receptor-mediated internalization.

In addition, to confirm that the internalization was actively mediated by TfR1, the cellular uptake was analysed by FACS after blocking the receptor expression by siRNA transfection. Cells were transfected with a scrambled RNA sequence (scr) as control and with a specific anti-TfR1 siRNA for 24 or 48 h, and the HumAfFt internalization percentage was analysed by FACS, confirming the involvement of TfR1 in HumAfFt uptake, as a 50 % decrease was recorded after anti-TfR1 siRNA transfection for 48 hours (Figure 40B).

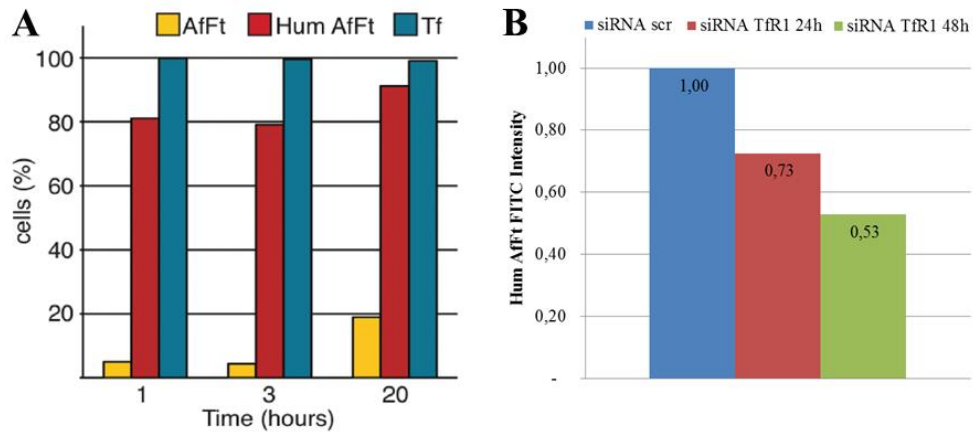


Figure 40: A) FITC labelled-proteins uptake by HeLa cells measured by flow cytometry analysis and reported as percentage of cells internalizing the nanoparticle, B) HumAfFt uptake decrease in HeLa cells by TfR1 silencing measured by flow cytometry

4.3.7.2 Confocal microscopy measurements

FITC-HumAfFt internalization by HeLa cells was also studied by confocal microscopy, where the HeLa cell line used was the TagRFP HeLa, HeLa cells with a red labelled nucleus. Both FITC-HumAfFt and control FITC-Tf as control were incubated for 20 h with the HeLa cells and the non internalised proteins were washed away just before imaging. The confocal images confirmed a high internalization of HumAfFt and highlighted a cellular distribution both in the cytoplasm and in the perinuclear space with a spherical pattern that might suggest a clathrin-coated endocytosis pathway, typical of TfR1 uptake (Figure 41).

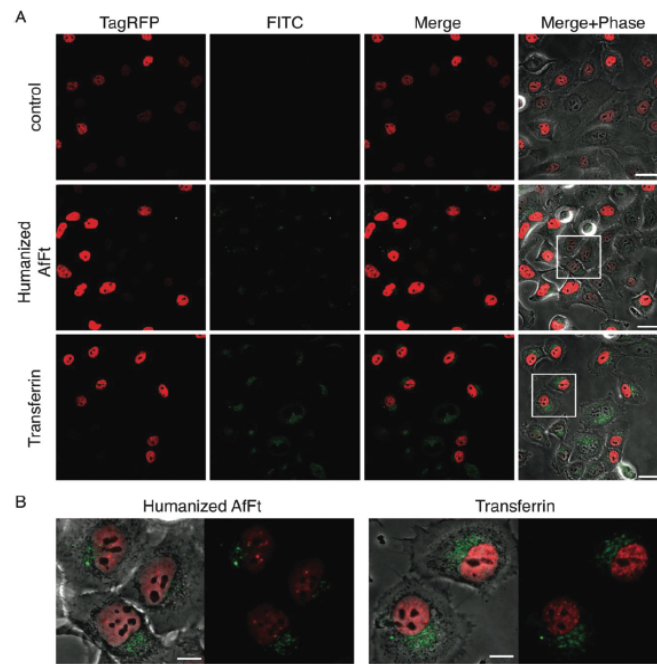


Figure 41: Protein internalization into living HeLa cells observed by confocal microscopy. A) FITC-protein internalized in HeLa TagRFP cells were shown as single, merged channels and overlay images (scale bar 40 μm). B) Magnified views of the white squares highlighted regions in panel A showing the merged channels and the overlay for transferrin and HumAfFt (scale bar 10 μm)

4.3.8 Two-photon absorption and emission spectroscopy measurements on pyrene-HumAfFt

HumAfFt TfR1-mediated uptake into mammalian cells might facilitate the site-selective delivery of selected cargos within tumour cells such as HeLa cells. The already available pyrene-HumAfFt ferritin was thus employed for ferritin visualization into HeLa cells, in order to test this new nanoscaffold as potential bioimaging diagnostic tool for two-photon fluorescence microscopy (TPFM). Two-photon excitation is a fluorescence technique involving the excitation of a fluorophore by the simultaneous absorption of two low energy

photons, commonly infrared (IR) photons. TPFM has several advantages over the canonical one-photon fluorescence confocal microscopy among which are: i) the IR light with a longer penetration depth due to the decreased absorption by biological samples and ii) the minimized photobleaching and photodamage, useful for non invasive biological studies.¹⁶⁶ In this framework, molecules with extensive π -conjugation such as pyrene, have emerged as ideal systems for two-photon fluorescence microscopy, thanks to their long fluorescence lifetime and electronic stability providing more sensitive microscopic images than currently used dyes^{166,167}.

Preliminary two-photon measurements were then carried out, in collaboration with the Italian Institute of Technology, on pyrene-labelled HumAfft and pyrene-labelled PfFt P77C in order to study the behaviour of the pyrene fluorophore in its excimeric and monomeric states respectively by two-photon fluorescence microscopy. All measurements were performed by employing the corresponding unlabelled ferritins as blanks. The conventional single photon absorption spectra (Figure 42A) were then compared with the spectra acquired by measuring the total fluorescence emission as a function of the excitation wavelength (Figure 42B). As expected, the overall shape of the two- and one- photon spectra were in good agreement except for small differences due to the diverse absorption/emission cross sections of the electronic processes involved, a common feature observed in numerous experimental studies^{168,169}. The frequency shift occurring between the half of the two-photon and the one-photon excitation wavelengths could also be ascribed to the different excitation cross-sections.

The two-photon total fluorescence spectra reported in Figure 42D were then acquired by excitation at a 755 nm wavelength, the maximum in both pyrene monomer and excimer excitation spectra. The comparison between the two-

photon fluorescence spectrum at 755 nm (Figure 42D) and the one-photon fluorescence spectrum at 342 nm (Figure 42C) showed similar excimer profile shapes and a slightly different shape for the monomer profile.

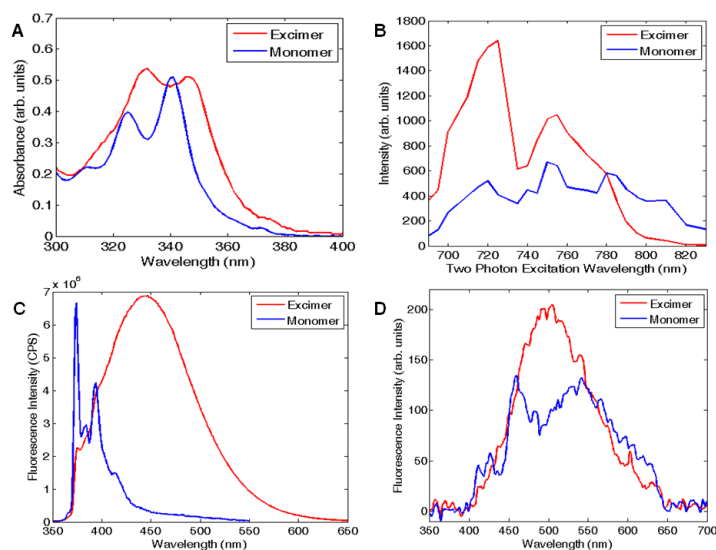


Figure 42: Pyrene excimer and monomer absorption and emission curves. In all panels, pyrene-labeled PyFtP77C and pyrene-labeled HumAfFt corresponding to monomer and excimer pyrene are shown in blue and red respectively: A) UV-Vis absorption spectra, B) Spectral integrated fluorescence as a function of the two-photon exciting wavelength, C) Fluorescence emission spectra recorded exciting at 342 nm, D) Two-photon fluorescence emission spectra recorded exciting at 755 nm

In addition, both two-photon fluorescence spectra presented a red shifted signal possibly due to non-radiative decays.

The overall spectral behaviour of pyrene monomer and excimer was mostly preserved in the single and two-photon approach, with a maintained remarkable difference between the pyrene monomeric profiles and the pyrene excimer profiles typical of the pyrene-labelled HumAfFt.

4.3.9 Pyrene-HumAfFt cellular uptake and visualization by two-photon fluorescence microscopy

Finally, to evaluate the performance of this novel nanodevice as active fluorescent probe for two-photon confocal microscopy, live HeLa cells expressing high levels of TfR1 receptor and capable of HumAfFt ferritin uptake were incubated with pyrene-labelled HumAfFt-TRITC and imaging studies were carried out by TPFM. HumAfFt internalization process was not altered by pyrene-labelling as confirmed by TRITC signal, detected with one-photon excitation (Figure 43A, A'). Once more the ferritin was found localised within the cytoplasm and the perinuclear space.¹⁷⁰ By observing the same cells, but switching to TPFM imaging, the pyrene excimer emission was detected in the same locations where the TRITC signal was recorded (Figure 43B, B') and a partial co-localization was highlighted (Figure 43C, C' and 43D, D'). Unfortunately, only a partial overlap between pyrene and TRITC signals was found due to differences attributable to the diverse techniques employed. Indeed the two imaging acquisitions had intrinsic different integrated z-section, smaller in the TPFM compared to confocal imaging with a minor total number of visible particles in a single plane. In addition, as to switch from the one-photon to the two-photon mode there was an intrinsic delay time and as the HeLa cells observed were alive and not fixed, intracellular compartments moved and rearranged. However from the same spherical pattern of both pyrene and TRITC emission and from the vicinal localization it could be confirmed that the emission corresponded to the ferritin fluorophore thus successfully reporting the employment of the excimer-based pyrene functionalised nanoparticle for TPFM imaging. In the future these findings could enable the creation of a novel and versatile set of

pyrene-excimer based ferritin probes for diagnostic and biomedical application based on the high intensity excimer fluorescence and on the ability of HumAfFt to target the overexpressed TfR1 receptor in human cancer cells.

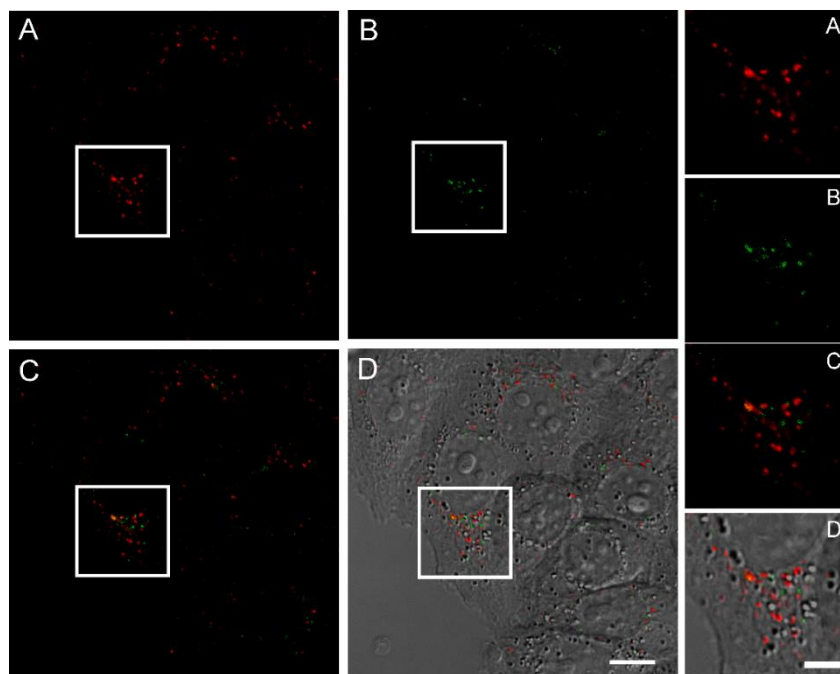


Figure 43: Confocal imaging of live HeLa cells incubated with pyrene-HumAfFt-TRITC. Images were acquired at one and two-photon excitations to detect respectively the TRITC (A) and the pyrene excimer emission (B). Merged signals and the overlay with the DIC image are shown in C and D, respectively (scale bar is $10\mu\text{m}$). Magnified images of the highlighted regions are showed in corresponding panels A', B', C' and D' (scale bar is $5\mu\text{m}$)

4.4 DNA encapsulation into Humanized ferritin

The remarkable structure together with the peculiar assembly properties of the chimeric Humanized ferritin nanocage and the successful recognition by the TfR1 receptor make HumAfFt an appealing and ideal nanoscaffold for incorporation, site-selective delivery and release of any payload in the cytoplasm of cancerous cells overexpressing TfR1. With its 8 nm cavity, ferritin can host both small and large cargos, shielding them from degradation and rapid clearance until the target is reached. Nucleic acid sequences, for instance, often need a delivery vehicle to be transported through the blood stream and to be delivered site-selectively into the cell, as they are easily subjected to enzymatic degradation and are too negatively charged to cross the cellular membrane¹⁷¹. Despite these issues, drugs based on the use of DNA or RNA sequences are emerging for their remarkable efficacy in the treatment of several diseases¹⁷² as they are selective and versatile drugs which could potentially target any gene with high specificity. Therefore, the future success of nucleic acid based therapies lies in the research for well suited delivery vehicles, capable of protecting the short sequences from degradation both *in vitro* and *in vivo* until the target is specifically reached. Commonly employed vehicles are the viral or non-viral systems^{173,174} but, despite the high transfection efficiency of viral vectors, non-viral vectors are often preferred due to immunological issues¹⁷⁵. In this framework Li et al. successfully described the encapsulation of a small interfering RNA (siRNA) into a non-viral vector like the human ferritin cage¹⁷¹. However, the encapsulation procedure employed is not ideal as the molecules are entrapped by pH-induced dissociation and reassociation of the ferritin cavity, thus possibly damaging both the protein and a sensitive molecule such as a nucleic

acid sequence by lowering the pH down to 2. On the contrary, Humanized archaea ferritin with its unique triangular pores might facilitate the nucleic acid entrance by electrostatic attraction of the positive clusters on the triangular pore apices or, otherwise, it could trap the molecule inside the cavity by dissociation and reassociation at neutral pH by a mild salt jump.

4.4.1 DNA-labelled Humanized ferritin preparation

The HumAfFt ferritin ability to encapsulate a large molecule such as a nucleic acid sequence was thus tested. However, due to the potential leak from the triangular pore, the DNA sequence should preferably be covalently bound to the internal ferritin cavity. Despite the apparent simple idea, various parameters concerning the linker should be considered, as the successful delivery and release rely on the choice of the molecule. Indeed the linker should be sufficiently stable to enable the conjugate to circulate in the bloodstream without premature release of the cargo which could potentially cause toxicity to normal tissues. On the other hand, the linker should also be cleavable at the target site where it should actively release the free drug. Among the most commonly employed linkers in this field, glutathione sensitive linkers have emerged for selective cargo release in the cytosol¹⁷⁶. Indeed, any disulfide bond is generally stable in the blood stream while it is easily cleaved once inside the cell, due to the higher glutathione concentration in the cytosol⁴³. The linker should therefore bear a disulfide moiety and, in order to selectively crosslink both the protein and the nucleic acid sequence, it must bear two additional reactive groups. The already available Cys54 in the HumAfFt inner cavity can be exploited as a unique site-selective attachment site, and a thiol moiety can be introduced at the end

of the DNA sequence for crosslinking. Thus, a sulfhydryl to sulfhydryl crosslinker containing a disulfide group will be needed. The commercially available DTME linker (Figure 44A) was chosen because of its disulfide cleavable bond and the two reactive maleimide moieties for the protein and DNA crosslinking. The similar BM(PEG)₂ linker (Figure 44B), resistant to glutathione cleavage due to the absence of any disulfide moiety, was used as negative release control agent.

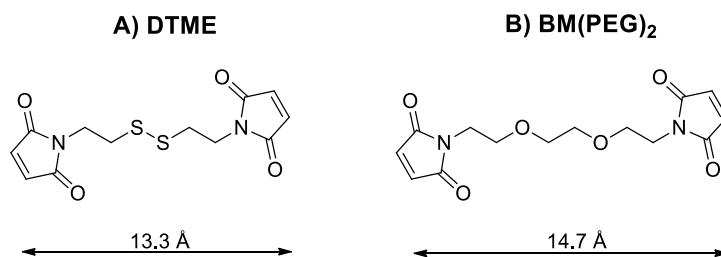
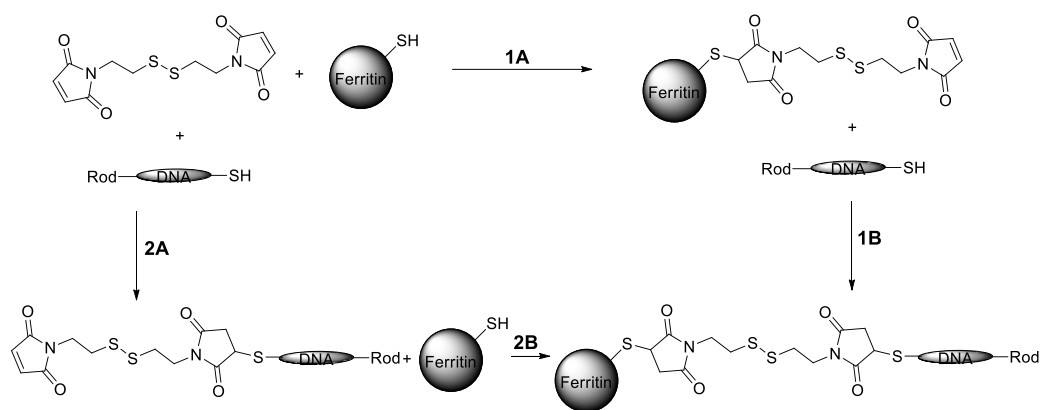


Figure 44: A) DTME cleavable bifunctional linker, B) BM(PEG)₂ uncleavable bifunctional linker. The distance between the two reactive functional moieties are reported under the molecule in Å units

A simple 22 base DNA sequence (Ro-DNA-SH), with no apparent active target or effect, was purchased from Sigma Aldrich and was modified with a thiol moiety at the 3' end and a rhodamine fluorophore at the 5' end to easily detect the molecule by UV-Vis and fluorescence spectroscopy.

The crosslinking bioconjugation reaction between the three species, the ferritin, the linker and the DNA sequence, can take place according to two possible reaction sequences that must be tested and compared (Scheme 7).



Scheme 7: Ferritin-linker-DNA crosslinking reaction pathways A and B

The first pathway envisaged a first reaction between the ferritin and the linker (Scheme 7-1A) and a second conjugation between the second reactive maleimide moiety of the linker and the thiol group on the DNA sequence (Scheme 7-1B). On the other hand, the linker could first be reacted with the DNA segment (Scheme 7-2A) and only later crosslinked to the ferritin Cys54 (Scheme 7-2B). Both pathways were explored with the first pathway showing an increased reliability and higher yields, while the second reaction sequence presented several limitations due to the possible multiple reactions between the linker and the DNA. Indeed, even though the reagents were reacted in a 1:1 molar ratio, both the mono- and double- labelled (i.e. DNA-linker-DNA) products could be produced, and a purification step to isolate the mono-labelled conjugate would be difficult. On the contrary, in Scheme 7-1A a high molar ratio of linker (10 eq.) could be mixed with ferritin, and easily removed by gel filtration chromatography, yielding a high labelling percentage as confirmed by mass spectrometry analysis (Figure 45).

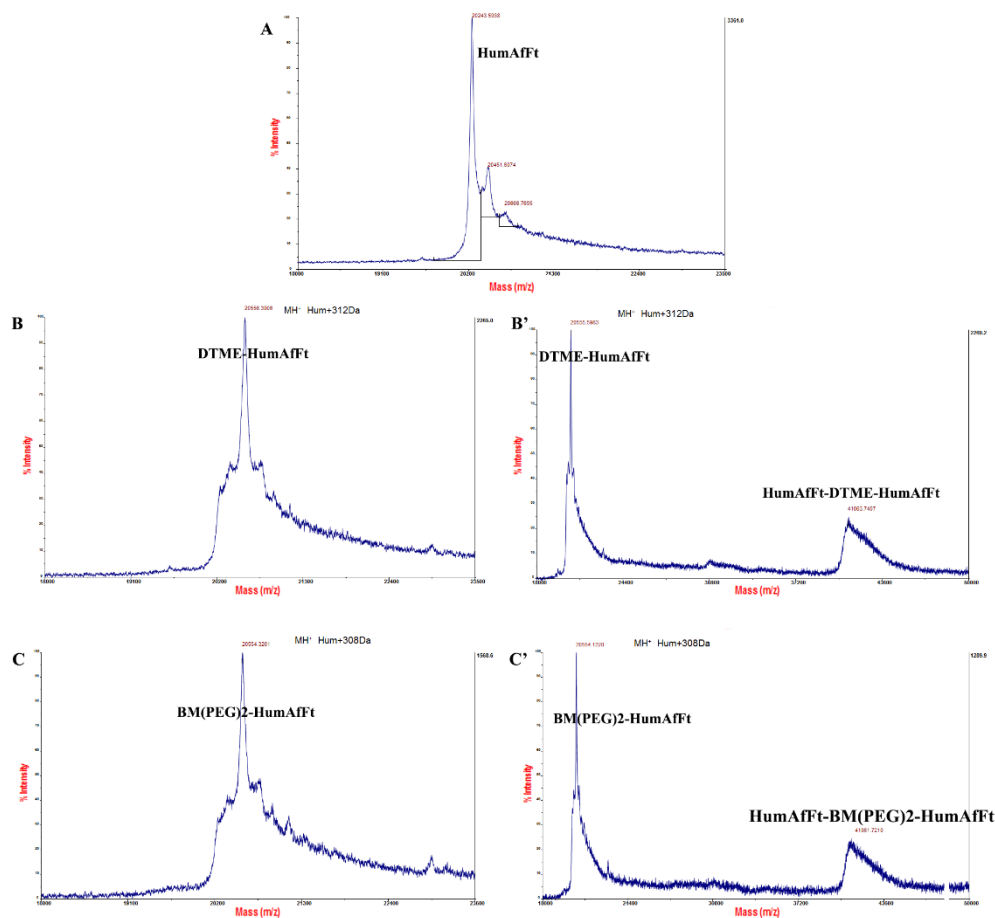


Figure 45: MALDI-TOF mass spectra of A) HumAfFt, B) DTME-labelled HumAfFt monomer, B') DTME-labelled HumAfFt crosslinked dimer, C) BM(PEG)₂-labelled HumAfFt monomer, C') BM(PEG)₂-labelled HumAfFt crosslinked dimer

As shown in Figure 45B' and 45C', however, an encountered inconvenient was the crosslinking between two cysteines at the ferritin dimer interface as the two residues are located at a 14 Å distance, unfortunately matching the linker length. Thus, the two maleimide groups at the linker extremes reacted with the two Cys54 on two adjacent monomers preferring a linker to cysteine ratio of 1:2 instead of the correct 1:1 that left the second maleimide moiety

available for further DNA conjugation. Nonetheless, this side reaction was minimized by fast addition of a high amount of linker, as verified both by denaturing SDS-PAGE and MALDI-TOF mass spectrometry analysis, resulting in a small amount of crosslinked dimers (approximately 15 %). After the first reaction step was optimised, the reaction and purification conditions of the crosslinking between linker-labelled ferritin and Ro-DNA-SH were adjusted. The highest labelling yields were reached by dissociating the protein into dimers before the reaction between the ferritin and the DNA fragment. In this way, the available maleimide of the linker was more exposed to the solvent and accessible to the DNA segment thus yielding higher labelling percentages. The best labelling yields achieved per 24-meric cage were 160 % (i.e. 1.6 molecules of DNA per ferritin 24-mer) employing the DTME linker and 22 % (i.e. 1 molecule of DNA every 5 ferritin 24-meric cage) using the BM(PEG)₂ linker. All the yields were determined by UV-Vis spectroscopy by calculating the ratio between the rhodamine fluorophore concentration at 530 nm, corresponding to the DNA concentration, and the protein concentration at 280 nm. Mass analysis could not highlight the ferritin-DNA conjugate since only a small percentage of DNA was bound with respect to the ferritin monomeric unit detected by mass spectroscopy. Therefore only the main ferritin-linker peak was detected due to the fact that the DNA-ferritin conjugate was under the instrumental detection limit. However, and surprisingly, although the two linkers were very similar, the BM(PEG)₂ linker afforded lower labelling yields than the DTME reaction and the origin of this curious discrepancy is still under investigation.

A control reaction was performed by mixing the ferritin with N-methyl maleimide (NMM), a small linker incapable of further reaction with the DNA segment. Correctly, nonspecific DNA binding to the ferritin cavity was not

found in the control reaction demonstrating both the effectiveness of the purification procedure and the successful encapsulation in the previously described experiments.

4.4.2 DNA-labelled Humanized ferritin cellular uptake

Despite the still improvable labelling yields, preliminary cytofluorimetry tests on HeLa cells were nevertheless carried out, in collaboration with the Italian Institute of Technology, to verify the DNA ferritin-mediated internalization in living cells. The protein was thus first labelled on the external surface with a fluorescein fluorophore and later labelled on the internal cavity with the DNA fragment crosslinked with the DTME and BM(PEG)₂ linkers. The ferritins were then internalised by HeLa cells according to the standard conditions and analysed by flow cytometry by using a control sample with plain cells not incubated with the protein. As shown in Figure 46, the percentage of FITC positive cells was high for both ferritins (99.7 % and 90.3 % for the ferritin crosslinked with DTME and BM(PEG)₂ respectively), while it was different for the rhodamine positive cells (99.6 % and 50.3 % respectively) reflecting the minor labelling degree of the Ro-DNA-SH-BM(PEG)₂-HumAfFt. These data show that DNA encapsulation did not alter the TfR1 mediated HumAfFt internalization into HeLa cells.

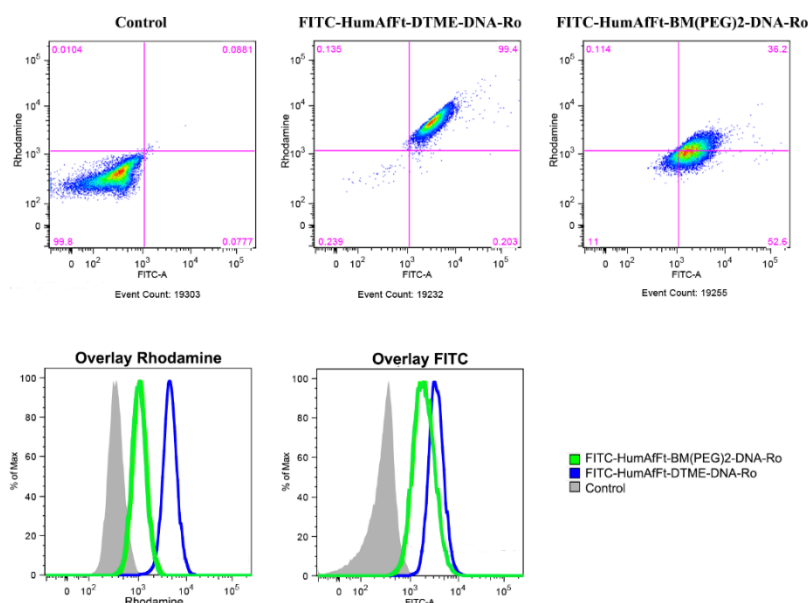


Figure 46: DNA-HumAfFt complex internalization analysis by flow cytometry

4.4.3 DNA encapsulation by electrostatic interaction

Following these first encouraging results, a third linker called NAEM (Figure 47), bearing an amine group which will be mostly protonated in physiological buffers, was also examined. This linker was chosen with the aim of introducing 24 additional positive charges within the ferritin internal cavity that might promote a non-covalent electrostatic interaction with the negatively charged nucleic acid sequence and thus promote the DNA uptake without the need of a covalent DNA labelling.

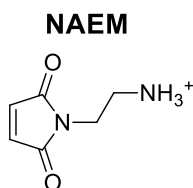


Figure 47: NAEM linker molecular structure

Chapter 4: Results and Discussion

The reaction was carried out according to the reaction scheme used for the two covalent linkers and a 13.5 % labelling yield per ferritin 24mer was obtained. Overall, the NAEM yield was the lowest yield obtained, far from the high yield reached with the DTME linker but not too much lower than the BM(PEG)₂ yield. Although the DTME and BM(PEG)₂ covalent strategies were superior with respect to the NAEM linker, the small amount of entrapped DNA that was found suggests that the introduction of 24 positive charges into the inner ferritin cavity may actually favour the DNA uptake compared to the control. Thus, in the future, the introduction of a high number of positive charges within the protein cavity could enable the encapsulation of various negatively charged molecules stabilised by non-covalent electrostatic interactions.

4.4.4 Conclusion and future perspectives

In conclusion, even though the BM(PEG)₂ crosslinking and encapsulation reaction must still to be improved, the reaction employing the DTME linker allowed the encapsulation of 1.6 DNA molecules per HumAfFt ferritin in its 24-meric cage assembly, shielding and transporting the DNA into HeLa cells by TfR1 mediated internalization. Further FACS and confocal microscopy experiments will be needed to verify the cleavage of the disulfide linker and the consequent DNA release. In the future, eventually, the transport of active nucleic acid sequences such as siRNAs could eventually be attempted to evaluate their potential effect. Indeed, the use of HumAfFt as a transfecting agent and as carrier of active nucleic acid fragments would represent a marked improvement with respect to the ferritin pH-induced encapsulation,

Chapter 4: Results and Discussion

considerably expanding the potential biotechnological application of this proteic nanodevice.

5. CONCLUSIONS

The work described in this thesis is focused on ferritins and their remarkable properties. In particular, archaea ferritin proteins and the novel chimeric humanized archaea ferritin HumAfFt were investigated in detail and their potential as nanoplateforms for the encapsulation and the targeted cellular delivery of drugs or diagnostic probes has been explored. The versatility of the ferritin cage allowed the insertion of various key modifications within the amino acid sequence, which had been further chemically functionalised for various applications, with the main objective to study ferritin self-assembly and encapsulation ability for the delivery of a wide variety of molecules.

The protein matrix permeability and the diffusion of molecules through various archaea protein cages were investigated, highlighting an unexpected flexibility, even within apparently impermeable closed ferritin structures such as *Pyrococcus fulgidus* ferritin, and a facilitated entrance through the *Archaeoglobus fulgidus* ferritin (AfFt) which bears characteristic wide triangular pores. The possibility to encapsulate various molecules within the peculiar AfFt cage either by diffusion through the large openings or by assembly/disassembly entrapment in a physiological environment is of outstanding importance for biotechnological applications envisaging a mild cargo encapsulation strategy, alternative to the canonical procedure requiring drastic pH values. Thanks to a newly synthesised pyrene-ferritin conjugate the thermodynamic and kinetic aspects of the AfFt self-assembly were deeply characterised by observing the shifts in the pyrene excimer fluorescence emission upon protein oligomerization, which strongly reflected the protein assembly state. The magnesium- and the sodium- triggered assembly were compared, with the magnesium-induced process being superior in all aspects.

Indeed, magnesium cations were able to induce a faster cage closure at lower salt concentrations, thus potentially representing a marked improvement for the controlled encapsulation of molecules and a convenient alternative to the classical sodium-triggered self-assembly, which takes place on a considerably longer time scale. In addition, the extremely cooperative magnesium-induced process is also completely reverted by EDTA treatment, offering an easy means to control the entire oligomerization process.

Archaea ferritins can not be recognised by the human ferritin receptor TfR1, a receptor which is found to be overexpressed in several cancerous cells. Thus, to investigate archaea ferritins *in vitro*, a humanized chimeric ferritin HumAfFt, which combined the AfFt structure and assembly properties with the human H-ferritin recognition motif for the TfR1 receptor, was designed and successfully purified in our laboratory with high yields.

Both the oligomerization properties and the TfR1 mediated internalization of HumAfFt into human cancerous HeLa cells were investigated by conjugating the protein with a pyrene molecule and by exploiting pyrene excimer fluorescence emission. These experiments confirmed both the assembly properties comparable to AfFt ferritin and the active internalization into mammalian cells. In particular, as the pyrene excimer intense emission was observed in living cells by two-photon fluorescence confocal microscopy, the pyrene-HumAfFt conjugate could represent the first example of a set of novel TfR1-selective pyrene-ferritin probes for TPFM bioimaging, which could be further expanded by pyrene derivatization.

In order to further explore the HumAfFt versatility and ability to specifically target the overexpressed TfR1 receptor in human cancerous cells, a set of novel conjugates were designed and employed for delivery of small nucleic acids, a technique nowadays widely employed in cancer treatment. A small

Chapter 5: Conclusions

DNA sequence was covalently bound or physically entrapped within the internal cavity of the ferritin by mildly dissociating and reassociating the protein cage at neutral pH. The modified ferritin was able to stabilize the DNA sequence, shielding it from degradation and carrying it inside HeLa cells as confirmed by FACS analysis. These encouraging results, might widen the scope of HumAfFt as a transfecting agent and as a carrier of active nucleic acid sequences, considerably expanding the biotechnological application of this protein biotherapeutic nanodevice.

Overall, the several experiments discussed in this thesis support the importance of ferritins as optimal and unique nanoparticles which, thanks to their widely explored versatility together with the TfR1 selective targeting, can transport a variety of molecules spanning from imaging probes to therapeutically active molecules for bioimaging and drug delivery applications.

REFERENCES

1. Meanst, G. E. & Feeney, R. E. Chemical Modifications of Proteins: History and Applications. *Bioconjugate Chem.* **1**, 2–12 (1990).
2. Spicer, C. D. & Davis, B. G. Selective chemical protein modification. *Nat. Commun.* **5**, 4740 (2014).
3. Walsh, C. T., Garneau-Tsodikova, S. & Gatto, G. J. Protein posttranslational modifications: The chemistry of proteome diversifications. *Angew. Chemie - Int. Ed.* **44**, 7342–7372 (2005).
4. Seet, B. T., Dikic, I., Zhou, M. M. & Pawson, T. Reading protein modifications with interaction domains. *Nat. Rev. Mol. Cell. Biol.* **7**, 473–483 (2006).
5. Leader, B., Baca, Q. J. & Golan, D. E. Protein therapeutics: a summary and pharmacological classification. *Nat. Rev. Drug Discov.* **7**, 21–39 (2008).
6. Harris, J. M. & Chess, R. B. Effect of pegylation on pharmaceuticals. *Nat. Rev. Drug Discov.* **2**, 214–21 (2003).
7. Crivat, G. & Taraska, J. W. Imaging proteins inside cells with fluorescent tags. *Trends Biotechnol.* **30**, 8–16 (2012).
8. Steiner, M. & Neri, D. Antibody-radionuclide conjugates for cancer therapy: Historical considerations and new trends. *Clin. Cancer Res.* **17**, 6406–6416 (2011).
9. Piston, D. W. & Kremers, G.-J. Fluorescent protein FRET: the good, the bad and the ugly. *Trends Biochem. Sci.* **32**, 407–414 (2007).
10. Lue, R. Y. P., Chen, G. Y. J., Hu, Y., Zhu, Q. & Yao, S. Q. Versatile Protein Biotinylation Strategies for Potential High-Throughput Proteomics. *J. Am. Chem. Soc.* **126**, 1055–1062 (2004).
11. Kalia, J. & Raines, R. T. Advances in Bioconjugation. *Curr. Org. Chem.* **14**, 138–147 (2010).
12. Baslé, E., Joubert, N. & Pucheault, M. Protein Chemical Modification on Endogenous Amino Acids. *Chem. Biol.* **17**, 213–227 (2010).
13. Koniev, O. & Wagner, A. Developments and recent advancements in the field of endogenous amino acid selective bond forming reactions for bioconjugation. *Chem. Soc. Rev.* **44**, 5495–551 (2015).
14. Lang, K. & Chin, J. W. Bioorthogonal reactions for labeling proteins. *ACS Chem. Biol.* **9**, 16–20 (2014).
15. Gao, Y. & Wang, Y. Site-selective modifications of arginine residues in human hemoglobin induced by methylglyoxal. *Biochemistry* **45**, 15654–15660 (2006).
16. Gauthier, M. A. & Klok, H. A. Arginine-specific modification of proteins with polyethylene glycol. *Biomacromolecules* **12**, 482–493 (2011).
17. Okamoto, M. & Morino, Y. Selective Modification of the Mitochondrial Isozyme of Aspartate Aminotransferase by beta-Bromopropionate. *Biochemistry* **11**, 3188–3195 (1972).

References

18. Chalker, J. M., Bernardes, G. J. L., Lin, Y. A. & Davis, B. G. Chemical modification of proteins at cysteine: Opportunities in chemistry and biology. *Chem. Asian J.* **4**, 630–640 (2009).
19. Schlick, T. L., Ding, Z., Kovacs, E. W. & Francis, M. B. Dual Surface Modification of the Tobacco Mosaic Virus. *J. Am. Chem. Soc.* 3718–3723 (2005).
20. Chen, G. *et al.* Reactivity of functional groups on the protein surface: Development of epoxide probes for protein labeling. *J. Am. Chem. Soc.* **125**, 8130–8133 (2003).
21. Chen, X., Muthoosamy, K., Pfisterer, A., Neumann, B. & Weil, T. Site-selective lysine modification of native proteins and peptides via kinetically controlled labeling. *Bioconjug. Chem.* **23**, 500–508 (2012).
22. Joshi, N. S., Whitaker, L. R. & Francis, M. B. A three-component Mannich-type reaction for selective tyrosine bioconjugation. *J. Am. Chem. Soc.* **126**, 15942–15943 (2004).
23. Nagaraj, R. H. *et al.* Acetylation of alfaA-crystallin in the human lens: Effects on structure and chaperone function. *Biochim. Biophys. Acta* **1822**, 120–129 (2012).
24. Zhou, T., Chung, Y. H., Chen, J. & Chen, Y. Site-Specific Identification of Lysine Acetylation Stoichiometries in Mammalian Cells. *J. Proteome Res.* **15**, 1103–1113 (2016).
25. Nakamura, T., Kawai, Y., Kitamoto, N., Osawa, T. & Kato, Y. Covalent modification of lysine residues by allyl isothiocyanate in physiological conditions: Plausible transformation of isothiocyanate from thiol to amine. *Chem. Res. Toxicol.* **22**, 536–542 (2009).
26. Metz, B. *et al.* Identification of Formaldehyde-induced Modifications in Proteins. *J. Biol. Chem.* **279**, 6235–6243 (2004).
27. Cai, X. *et al.* Reversible PEGylation and Schiff-base linked imidazole modification of polylysine for high-performance gene delivery. *J. Mater. Chem. B* **3**, 1507–1517 (2015).
28. Voet, D., Voet, J. G. & Pratt, C. W. *Fondamenti di biochimica.* (Zanichelli, 2013).
29. Kalkhof, S. & Sinz, A. Chances and pitfalls of chemical cross-linking with amine-reactive N-hydroxysuccinimide esters. *Anal. Bioanal. Chem.* **392**, 1–8 (2008).
30. Shen, B.-Q. *et al.* Conjugation site modulates the in vivo stability and therapeutic activity of antibody-drug conjugates. *Nat. Biotechnol.* **30**, 184–189 (2012).
31. Miseta, A. & Csutora, P. Relationship between the occurrence of cysteine in proteins and the complexity of organisms. *Mol. Biol. Evol.* **17**, 1232–9 (2000).
32. Davis, B. G., Lloyd, R. C. & Jones, J. B. Controlled site-selective glycosylation of proteins by a combined site-directed mutagenesis and chemical modification approach. *J. Org. Chem.* **63**, 9614–9615 (1998).

References

33. Schumacher, F. F. *et al.* Next generation maleimides enable the controlled assembly of antibody-drug conjugates via native disulfide bond bridging. *Org. Biomol. Chem.* **12**, 7261–7269 (2014).
34. Friedmann, E. & Marrian, D. H. *Br. J. Pharmacol.* 105–108 (1949).
35. Knight, P. Hydrolysis of p-NN'-phenylenebismaleimide and its adducts with cysteine. Implications for cross-linking of proteins. *Biochem. J.* **179**, 191–197 (1979).
36. Machida, M., Machida, M. I. & Kanaoka, Y. Hydrolysis of N-substituted Maleimides: Stability of Fluorescence Thiol Reagents in Aqueous Media. *Chem. Pharm. Bull.* **25**, 2739–2743 (1977).
37. Fontaine, S. D., Reid, R., Robinson, L., Ashley, G. W. & Santi, D. V. Long-term stabilization of maleimide-thiol conjugates. *Bioconjug. Chem.* **26**, 145–152 (2015).
38. Khan, M. N. Intramolecular General Acid-Base Catalysis and the Rate-determining Steps in the Nucleophilic Cleavage of Maleimide with Primary Amines. *J. Chem. Soc. Perkin Trans. II* 1977–1984 (1985).
39. Wu, C.-W., Yarbrough, L. R. & Wu, F. Y.-H. N-(1-Pyrene)maleimide: a fluorescent cross-linking reagent. *Biochemistry* **15**, 2863–2868 (1976).
40. Baldwin, A. D. & Kiick, K. L. Tunable degradation of maleimide-Thiol adducts in reducing environments. *Bioconjug. Chem.* **22**, 1946–1953 (2011).
41. Ryan, C. P. *et al.* Tunable reagents for multi-functional bioconjugation: reversible or permanent chemical modification of proteins and peptides by control of maleimide hydrolysis. *Chem. Commun.* **47**, 5452–5454 (2011).
42. Morais, M. *et al.* Optimisation of the dibromomaleimide (DBM) platform for native antibody conjugation by accelerated post-conjugation hydrolysis. *Org. Biomol. Chem.* **15**, 2947–2952 (2017).
43. Smith, C. V., Jones, D. P., Guenther, T. M., Lash, L. H. & Lauterburg, B. H. Compartmentation of glutathione: implications for the study of toxicity and disease. *Toxicol. Appl. Pharmacol.* **140**, 1–12 (1996).
44. Smith, M. E. B. *et al.* Protein modification, bioconjugation, and disulfide bridging using bromomaleimides. *J. Am. Chem. Soc.* **132**, 1960–1965 (2010).
45. Tedaldi, L. M., Smith, M. E. B., Nathani, R. I. & Baker, J. R. Bromomaleimides: new reagents for the selective and reversible modification of cysteine. *Chem. Commun.* 6583 (2009).
46. Nunes, J. P. M. *et al.* Functional native disulfide bridging enables delivery of a potent, stable and targeted antibody-drug conjugate (ADC). *Chem. Commun.* **51**, 10624–10627 (2015).
47. Nielsen, M. L. *et al.* Iodoacetamide-induced artifact mimics ubiquitination in mass spectrometry. *Nat. Methods* **5**, 459–460 (2008).
48. Ellman, G. L. Tissue Sulphydryl Groups. *Arch. Biochem. Biophys.* **82**, 70–77 (1959).
49. Riener, C. K., Kada, G. & Gruber, H. J. Quick measurement of protein sulfhydryls with Ellman's reagent and with 4,4'-dithiodipyridine. *Anal. Bioanal. Chem.* **373**, 266–276 (2002).

References

50. Winther, J. R. & Thorpe, C. Quantification of thiols and disulfides. *Biochim. Biophys. Acta* **1840**, 838–846 (2014).
51. Laufberger, V. Sur la cristallisation de la ferritine. 1575–1582 (1937).
52. Crichton, R. R. Structure and Function of Ferritin. *Angew. Chemie Int. Ed.* **12**, 57–65 (1973).
53. Honarmand Ebrahimi, K., Hagedoorn, P. L. & Hagen, W. R. Unity in the biochemistry of the iron-storage proteins ferritin and bacterioferritin. *Chem. Rev.* **115**, 295–326 (2015).
54. Bou-Abdallah, F. The iron redox and hydrolysis chemistry of the ferritins. *Biochim. Biophys. Acta* **1800**, 719–731 (2010).
55. Santambrogio, P., Levi, S., Cozzi, A., Corsi, B. & Arosio, P. Evidence that the specificity of iron incorporation into homopolymers of human ferritin L- and H-chains is conferred by the nucleation and ferroxidase centres. *Biochemistry* **314**, 139–144 (1996).
56. Watt, R. K. The many faces of the octahedral ferritin protein. *BioMetals* **24**, 489–500 (2011).
57. Alkhateeb, A. A. & Connor, J. R. The significance of ferritin in cancer: Anti-oxidation, inflammation and tumorigenesis. *Biochim. Biophys. Acta* **1836**, 245–254 (2013).
58. Recalcati, S., Invernizzi, P., Arosio, P. & Cairo, G. New functions for an iron storage protein: The role of ferritin in immunity and autoimmunity. *J. Autoimmun.* **30**, 84–89 (2008).
59. Jellinger, K., Paulus, W., Grundke-Iqbal, I., Riederer, P. & Youdim, M. B. H. Brain iron and ferritin in Parkinson's and Alzheimer's diseases. *J. Neural Transm. - Park. Dis. Dement. Sect.* **2**, 327–340 (1990).
60. Carmona, F. *et al.* Ferritin iron uptake and release in the presence of metals and metalloproteins: Chemical implications in the brain. *Coord. Chem. Rev.* **257**, 2752–2764 (2013).
61. Li, L. *et al.* Binding and uptake of H-ferritin are mediated by human transferrin receptor-1. *Proc. Natl. Acad. Sci.* **107**, 3505–3510 (2010).
62. Tortorella, S. & Karagiannis, T. C. Transferrin receptor-mediated endocytosis: A useful target for cancer therapy. *J. Membr. Biol.* **247**, 291–307 (2014).
63. Cheng, Y. *et al.* Structure of the Human Transferrin Receptor-Transferrin Complex. *Cell* **116**, 565–576 (2004).
64. Aisen, P. Transferrin receptor 1. *Int. J. Biochem. Cell Biol.* **36**, 2137–2143 (2004).
65. McMahon, H. T. & Boucrot, E. Molecular mechanism and physiological functions of clathrin-mediated endocytosis. *Nat. Rev. Mol. Cell. Biol.* **12**, 517–533 (2011).
66. Bellini, M. *et al.* Protein nanocages for self-triggered nuclear delivery of DNA-targeted chemotherapeutics in Cancer Cells. *J. Control. Release* **196**, 184–196 (2014).
67. Fan, K. *et al.* Magnetoferritin nanoparticles for targeting and visualizing

References

- tumour tissues. *Nat. Nanotechnol.* **7**, 459–464 (2012).
68. Han, J. *et al.* Iron uptake mediated by binding of H-ferritin to the TIM-2 receptor in mouse cells. *PLoS One* **6**, 1–9 (2011).
69. Chen, T. T. *et al.* TIM-2 is expressed on B cells and in liver and kidney and is a receptor for H-ferritin endocytosis. *J. Exp. Med.* **202**, 955–65 (2005).
70. Todorich, B., Zhang, X., Slagle-Webb, B., Seaman, W. E. & Connor, J. R. Tim-2 is the receptor for H-ferritin on oligodendrocytes. *J. Neurochem.* **107**, 1495–1505 (2008).
71. Li, J. Y. *et al.* Scara5 Is a Ferritin Receptor Mediating Non-Transferrin Iron Delivery. *Dev. Cell* **16**, 35–46 (2009).
72. Alkhateeb, A. A. & Connor, J. R. Nuclear ferritin: A new role for ferritin in cell biology. *Biochim. Biophys. Acta - Gen. Subj.* **1800**, 793–797 (2010).
73. Surguladze, N., Patton, S., Cozzi, A., Fried, M. G. & Connor, J. R. Characterization of nuclear ferritin and mechanism of translocation. *Biochem. J.* **388**, 731–40 (2005).
74. Zhang, Y. & Orner, B. P. Self-assembly in the ferritin nano-cage protein superfamily. *Int. J. Mol. Sci.* **12**, 5406–5421 (2011).
75. Bernacchioni, C. *et al.* Loop electrostatics modulates the intersubunit interactions in ferritin. *ACS Chem. Biol.* **9**, 2517–2525 (2014).
76. Chen, H. *et al.* Engineering protein interfaces yields ferritin disassembly and reassembly under benign experimental conditions. *Chem. Commun.* **52**, 7402–7405 (2016).
77. Kim, S. W., Kim, Y. H. & Lee, J. Thermal stability of human ferritin: concentration dependence and enhanced stability of an N-terminal fusion mutant. *Biochem. Biophys. Res. Commun.* **289**, 125–9 (2001).
78. Santambrogio, P. *et al.* Effects of modifications near the 2-, 3- and 4-fold symmetry axes on human ferritin renaturation. *Biochem. J.* **322**, 461–468 (1997).
79. Crichton, R. R. & Bryce, C. F. Subunit interactions in horse spleen apoferritin. Dissociation by extremes of pH. *Biochem. J.* **133**, 289–299 (1973).
80. Gerl, M. & Jaenicke, R. Mechanism of the self-assembly of apoferritin from horse spleen - Cross-linking and spectroscopic analysis. *Eur. Biophys. J.* **15**, 103–109 (1987).
81. Stefanini, S., Vecchini, P. & Chiancone, E. On the mechanism of horse spleen apoferritin assembly: a sedimentation velocity and circular dichroism study. *Biochemistry* **26**, 1831–1837 (1987).
82. Sato, D. *et al.* Ferritin Assembly Revisited: A Time-Resolved Small-Angle X-ray Scattering Study. *Biochemistry* **55**, 287–293 (2016).
83. Kim, M. *et al.* pH-Dependent Structures of Ferritin and Apoferritin in Solution : Disassembly and Reassembly. *Biomacromolecules* **12**, 1629–1640 (2011).
84. Choi, S. H., Choi, K., Chan Kwon, I. & Ahn, H. J. The incorporation of GALA peptide into a protein cage for an acid-inducible molecular switch.

References

- Biomaterials* **31**, 5191–5198 (2010).
85. Zhang, S. *et al.* Conversion of the Native 24-mer Ferritin Nanocage into Its Non-Native 16-mer Analogue by Insertion of Extra Amino Acid Residues. *Angew. Chemie - Int. Ed.* **55**, 16064–16070 (2016).
 86. Zhang, S. *et al.* ‘silent’ Amino Acid Residues at Key Subunit Interfaces Regulate the Geometry of Protein Nanocages. *ACS Nano* **10**, 10382–10388 (2016).
 87. Johnson, E., Cascio, D., Sawaya, M. R., Gingery, M. & Schröder, I. Crystal Structures of a Tetrahedral Open Pore Ferritin from the Hyperthermophilic Archaeon *Archaeoglobus fulgidus*. *Structure* **13**, 637–648 (2005).
 88. Sana, B., Johnson, E. & Lim, S. The unique self-assembly/disassembly property of *Archaeoglobus fulgidus* ferritin and its implications on molecular release from the protein cage. *Biochim. Biophys. Acta - Gen. Subj.* **1850**, 2544–2551 (2015).
 89. Swift, J., Butts, C. A., Cheung-Lau, J., Yerubandi, V. & Dmochowski, I. J. Efficient Self-Assembly of *Archaeoglobus fulgidus* ferritin around metallic cores. *Langmuir* **25**, 5219–5225 (2009).
 90. Sana, B. *et al.* The role of nonconserved residues of *archaeoglobus fulgidus* ferritin on its unique structure and biophysical properties. *J. Biol. Chem.* **288**, 32663–32672 (2013).
 91. MaHam, A., Tang, Z., Wu, H., Wang, J. & Lin, Y. Protein-based nanomedicine platforms for drug delivery. *Small* **5**, 1706–1721 (2009).
 92. Li, K. *et al.* Multifunctional ferritin cage nanostructures for fluorescence and MR imaging of tumor cells. *Nanoscale* **4**, 188 (2012).
 93. Nandwana, V. *et al.* Engineered ferritin nanocages as natural contrast agents in magnetic resonance imaging. *RSC Adv.* **7**, 34892–34900 (2017).
 94. Cao, C. *et al.* Targeted in vivo imaging of microscopic tumors with ferritin-based nanoprobes across biological barriers. *Adv. Mater.* **26**, 2566–2571 (2014).
 95. Fisher, J. *et al.* Ferritin: a novel mechanism for delivery of iron to the brain and other organs. *Am J Physiol Cell Physiol* **293**, C641-9 (2007).
 96. Harada, T. & Yoshimura, H. Ferritin protein encapsulated photoluminescent rare earth nanoparticle. *J. Appl. Phys.* **114**, (2013).
 97. Lin, X. *et al.* Chimeric Ferritin Nanocages for Multiple Function Loading and Multimodal Imaging. *Nano Lett.* **11**, 814–819 (2011).
 98. Kasyutich, O. *et al.* Silver Ion Incorporation and Nanoparticle Formation inside the Cavity of *Pyrococcus furiosus* Ferritin: Structural and Size-Distribution Analyses. *J. Am. Chem. Soc.* **132**, 3621–3627 (2010).
 99. Fan, R., Chew, S. W., Cheong, V. V. & Orner, B. P. Fabrication of Gold Nanoparticles Inside Unmodified Horse Spleen Apoferritin. *Small* 1483–1487 (2010).
 100. Hainfeld, J. F. Uranium-loaded apoferritin with antibodies attached: molecular design for uranium neutron-capture therapy. *Proc. Natl. Acad. Sci. U. S. A.* **89**, 11064–8 (1992).

References

101. Aime, S. & Frullano, L. Compartmentalization of a Gadolinium Complex in the Apoferritin Cavity : A Route To Obtain High Relaxivity Contrast Agents for Magnetic Resonance Imaging. **521**, 2001–2003 (2002).
102. Falvo, E. *et al.* Antibody–drug conjugates: targeting melanoma with cisplatin encapsulated in protein-cage nanoparticles based on human ferritin. *Nanoscale* **5**, 12278 (2013).
103. Xing, R. *et al.* Characterization and cellular uptake of platinum anticancer drugs encapsulated in apoferritin. *J. Inorg. Biochem.* **103**, 1039–1044 (2009).
104. Yang, Z. *et al.* Encapsulation of platinum anticancer drugs by apoferritin. *Chem. Commun.* **7345**, 3453–3455 (2007).
105. Ji, X., Huang, L. & Huang, H. Construction of nanometer cisplatin core-ferritin (NCC-F) and proteomic analysis of gastric cancer cell apoptosis induced with cisplatin released from the NCC-F. *J. Proteomics* **75**, 3145–3157 (2012).
106. Domínguez-Vera, J. M. Iron(III) complexation of Desferrioxamine B encapsulated in apoferritin. *J. Inorg. Biochem.* **98**, 469–472 (2004).
107. Niemeyer, J. *et al.* Noncovalent insertion of ferrocenes into the protein shell of apo-ferritin. *Chem. Commun.* **1**, 6519–6521 (2008).
108. Zhen, Z. *et al.* RGD-Modified Apoferritin Nanoparticles for Efficient Drug Delivery to Tumors. 4830–4837 (2013).
109. Gumulec, J. *et al.* Modulation of Induced Cytotoxicity of Doxorubicin by Using Apoferritin and Liposomal Cages. *Int. J. Mol. Sci.* **15**, 22960–22977 (2014).
110. Zhang, L. *et al.* H-Chain Ferritin : A Natural Nuclei Targeting and Bioactive Delivery Nanovector. *Adv. Healthc. Mater.* **4**, 1305–1310 (2015).
111. Damiani, V., Falvo, E., Fracasso, G., Federici, L. & Pitea, M. Therapeutic Efficacy of the Novel Stimuli-Sensitive Nano-Ferritins Containing Doxorubicin in a Head and Neck Cancer Model. *Int. J. Mol. Sci.* **18**, 1555 (2017).
112. Chen, L. *et al.* Encapsulation of curcumin in recombinant human H-chain ferritin increases its water-solubility and stability. *Food Res. Int.* **62**, 1147–1153 (2014).
113. Chen, L. *et al.* Encapsulation of β -carotene within ferritin nanocages greatly increases its water-solubility and thermal stability. *Food Chem.* **149**, 307–312 (2014).
114. Butts, C. A. *et al.* Identification of a fluorescent general anesthetic , 1-aminoanthracene. *Proc. Natl. Acad. Sci.* **106**, 6501–6506 (2009).
115. Yao, H. *et al.* Multifunctional ferritin nanocages for bimodal imaging and targeted delivery of doxorubicin into cancer cells. *RSC Adv.* **6**, 109322–109333 (2016).
116. Vannucci, L. *et al.* In Vivo Targeting of Cutaneous Melanoma Using an Melanoma Stimulating Hormone-Engineered Human Protein Cage with Fluorophore and Magnetic Resonance Imaging Tracers. *J. Biomed. Nanotechnol.* **11**, 81–92 (2015).

References

117. Riddles, P. W., Blakeley, R. L. & Zerner, B. Ellman 's Reagent: 5,5'-Dithiobis(2-nitrobenzoic Acid)-a Reexamination. **81**, 75–81 (1979).
118. Rappsilber, J., Ishihama, Y. & Mann, M. Stop and Go Extraction Tips for Matrix-Assisted Laser Desorption / Ionization , Nanoelectrospray , and LC / MS Sample Pretreatment in Proteomics. *Anal. Chem.* **75**, 663–670 (2003).
119. Deosarkar, S. P. *et al.* A novel dynamic neonatal blood-brain barrier on a chip. *PLoS One* **10**, 1–21 (2015).
120. Tatur, J., Hagedoorn, P. L., Overeijnder, M. L. & Hagen, W. R. A highly thermostable ferritin from the hyperthermophilic archaeal anaerobe *Pyrococcus furiosus*. *Extremophiles* **10**, 139–148 (2006).
121. Yang, X. & Chasteen, N. D. Molecular Diffusion into Horse Spleen Ferritin : A Nitroxide Radical Spin Probe Study. *Biophys. J.* **71**, 1587–1595 (1996).
122. Yang, X., Arosio, P. & Chasteen, N. D. Molecular Diffusion into Ferritin : Pathways , Temperature Dependence , Incubation Time , and Concentration Effects. *Biophys. J.* **78**, 2049–2059 (2000).
123. Douglas, T. & Ripoll, D. R. Calculated electrostatic gradients in recombinant human H-chain ferritin. 1083–1091 (1998).
124. Calisti, L. *et al.* Probing bulky ligand entry in engineered archaeal ferritins. *Biochim. Biophys. Acta* **1861**, 450–456 (2017).
125. Tatur, J., Hagen, W. R. & Matias, P. M. Crystal structure of the ferritin from the hyperthermophilic archaeal anaerobe *Pyrococcus furiosus*. *J. Biol. Inorg. Chem.* **12**, 615–630 (2007).
126. Fehrentz, T., Schönberger, M. & Trauner, D. Optochemical genetics. *Angew. Chemie - Int. Ed.* **50**, 12156–12182 (2011).
127. Schoenlein, R. W., Peteanu, L. A. L. A., Mathies, R. A. & Shank, C. V. The first step in vision: femtosecond isomerization of rhodopsin. *Science* **254**, 412–415 (1991).
128. Mart, R. J. & Allemann, R. K. Azobenzene photocontrol of peptides and proteins. *Chem. Commun.* **52**, 12262–12277 (1226).
129. Yager, K. G. & Barrett, C. J. Novel photo-switching using azobenzene functional materials. *J. Photochem. Photobiol. A Chem.* **182**, 250–261 (2006).
130. Merino, E. & Ribagorda, M. Control over molecular motion using the cis-trans photoisomerization of the azo group. *Beilstein J. Org. Chem.* **8**, 1071–1090 (2012).
131. Renner, C. & Moroder, L. Azobenzene as conformational switch in model peptides. *ChemBioChem* **7**, 868–878 (2006).
132. Zhang, F., Sadowski, O. & Woolley, G. A. Synthesis and characterization of a long, rigid photoswitchable cross-linker for promoting peptide and protein conformational change. *ChemBioChem* **9**, 2147–2154 (2008).
133. Behrendt, R. *et al.* Photomodulation of the conformation of cyclic peptides with azobenzene moieties in the peptide backbone. *Angew. Chemie - Int. Ed.* **38**, 2771–2774 (1999).
134. Burns, D. C. *et al.* Origins of helix-coil switching in a light-sensitive peptide.

References

- Biochemistry* **43**, 15329–15338 (2004).
135. Deiana, M. *et al.* Photochromic switching of the DNA helicity induced by azobenzene derivatives. *Sci. Rep.* **6**, 28605 (2016).
 136. Hoersch, D., Roh, S., Chiu, W. & Kortemme, T. Reprogramming an ATP-driven protein machine into a light-gated nanocage. *Nat. Nanotechnol.* **8**, 928–32 (2013).
 137. Muramatsu, S., Kinbara, K., Taguchi, H., Ishii, N. & Aida, T. Semibiological Molecular Machine with an Implemented ‘AND’ Logic Gate for Regulating Protein Folding. *J. Am. Chem. Soc.* **128**, 3764–3769 (2006).
 138. Schierling, B. *et al.* Controlling the enzymatic activity of a restriction enzyme by light. *Proc. Natl. Acad. Sci. U. S. A.* **107**, 1361–6 (2010).
 139. Nakayama, K., Endo, M. & Majima, T. A hydrophilic azobenzene-bearing amino acid for photochemical control of a restriction enzyme BamHI. *Bioconjug. Chem.* **16**, 1360–1366 (2005).
 140. Inada, T., Terabayashi, T., Yamaguchi, Y., Kato, K. & Kikuchi, K. Modulation of the catalytic mechanism of hen egg white lysozyme (HEWL) by photochromism of azobenzene. *J. Photochem. Photobiol. A Chem.* **175**, 100–107 (2005).
 141. Kienzler, M. *a et al.* A red-shifted , fast-relaxing azobenzene photoswitch for visible light control of an ionotropic glutamate receptor. *J. Am. Chem. Soc.* **135**, 17683–17686 (2013).
 142. Volgraf, M. *et al.* Allosteric control of an ionotropic glutamate receptor with an optical switch. *Nat. Chem. Biol.* **2**, 47–52 (2006).
 143. Banghart, M., Borges, K., Isacoff, E., Trauner, D. & Kramer, R. H. Light-activated ion channels for remote control of neuronal firing. *Nat. Neurosci.* **7**, 1381–6 (2004).
 144. Bose, M., Groff, D., Xie, J., Brustad, E. & Schultz, P. G. The Incorporation of a Photoisomerizable Amino Acid into Proteins in *E. coli* The Incorporation of a Photoisomerizable Amino Acid into Proteins in *E. coli*. **128**, 388–389 (2006).
 145. Liu, M., Asanuma, H. & Komiyama, M. Azobenzene-tethered T7 promoter for efficient photoregulation of transcription. *J. Am. Chem. Soc.* **128**, 1009–1015 (2006).
 146. Beharry, A. A., Wong, L., Tropepe, V. & Woolley, G. A. Fluorescence imaging of azobenzene photoswitching in vivo. *Angew. Chemie - Int. Ed.* **50**, 1325–1327 (2011).
 147. Bains, G. K., Kim, S. H., Sorin, E. J. & Narayanaswami, V. The extent of pyrene excimer fluorescence emission is a reflector of distance and flexibility: Analysis of the segment linking the LDL receptor-binding and tetramerization domains of apolipoprotein E3. *Biochemistry* **51**, 6207–6219 (2012).
 148. Bains, G., Patel, A. B. & Narayanaswami, V. Pyrene: A probe to study protein conformation and conformational changes. *Molecules* **16**, 7909–7935 (2011).

References

149. Betcher-Lange, S. L. & Lehrer, S. S. Pyrene Excimer Fluorescence in Rabbit Skeletal α Tropomyosin Labeled with N-(1-Pyrene)maleimide. *J. Biol. Chem.* **253**, 3757–3760 (1978).
150. Krasheninina, O. A., Lomzov, A. A., Fishman, V. S., Novopashina, D. S. & Venyaminova, A. G. Rational design and studies of excimer forming novel dual probes to target RNA. *Bioorganic Med. Chem.* **25**, 2244–2250 (2017).
151. Wu, C., Wang, C., Yan, L. & Yang, C. J. Pyrene excimer nucleic acid probes for biomolecule signaling. *J. Biomed. Nanotechnol.* **5**, 495–504 (2009).
152. Ma, C., Huang, H. & Zhao, C. An aptamer-based and pyrene-labeled fluorescent biosensor for homogeneous detection of potassium ions. *Anal. Sci.* **26**, 1261–1264 (2010).
153. Freeman, R. *et al.* Self-assembly of supramolecular aptamer structures for optical or electrochemical sensing. *Analyst* **134**, 653–6 (2009).
154. Faggi, E. *et al.* Pseudopeptidic fluorescent on-off pH sensor based on pyrene excimer emission: Imaging of acidic cellular organelles. *Sensors Actuators, B Chem.* **234**, 633–640 (2016).
155. Birks, J. B. Excimers. *Rep. Prog. Phys.* **38**, 903–974 (1975).
156. Winnik, F. Photophysics of preassociated pyrenes in aqueous polymer solutions and in other organized media. *Chem. Rev.* **93**, 587–614 (1993).
157. Bichenkova, E. V *et al.* Exciplex fluorescence emission from simple organic intramolecular constructs in non-polar and highly polar media as model systems for DNA-assembled exciplex detectors. *Org. Biomol. Chem.* **4**, 367–78 (2006).
158. Karpovich, D. & Blanchard, G. Relating the Polarity-Dependent Fluorescence Response of Pyrene To Vibronic Coupling - Achieving a Fundamental Understanding of the Py Polarity Scale. *J. Phys. Chem.* **99**, 3951–3958 (1995).
159. Conlon, P. *et al.* Pyrene excimer signaling molecular beacons for probing nucleic acids. *J. Am. Chem. Soc.* **130**, 336–342 (2008).
160. Levi, S. *et al.* Mechanism of ferritin iron uptake: Activity of the H-chain and deletion mapping of the ferro-oxidase site. A study of iron uptake and ferro-oxidase activity of human liver, recombinant H-chain ferritins, and of two H-chain deletion mutants. *J. Biol. Chem.* **263**, 18086–18092 (1988).
161. Ha, Y., Shi, D., Small, G. W., Theil, E. C. & Allewell, N. M. Crystal structure of bullfrog M ferritin at 2.8 Å resolution: analysis of subunit interactions and the binuclear metal center. *JBIC* **4**, 243–256 (1999).
162. Santambrogio, P. *et al.* Crystal Structure and Biochemical Properties of the Human Mitochondrial Ferritin and its Mutant Ser144Ala. *J. Mol. Biol.* **340**, 277–293 (2004).
163. Morris, A. M., Watzky, M. A. & Finke, R. G. Protein aggregation kinetics, mechanism, and curve-fitting: a review of the literature. *Biochim. Biophys. Acta* **1794**, 375–97 (2009).
164. Arosio, P., Knowles, T. P. J. & Linse, S. On the lag phase in amyloid fibril formation. *Phys. Chem. Chem. Phys.* **17**, 7606–7618 (2015).

References

165. Bernacki, J. P. & Murphy, R. M. Model discrimination and mechanistic interpretation of kinetic data in protein aggregation studies. *Biophys. J.* **96**, 2871–2887 (2009).
166. Kim, H. M., Lee, Y. O., Lim, C. S., Kim, J. S. & Cho, B. R. Two-Photon Absorption Properties of Alkynyl-Conjugated Pyrene Derivatives. *J. Org. Chem.* 5127–5130 (2008).
167. Niko, Y. *et al.* A novel pyrene-based two-photon active fluorescent dye efficiently excited and emitting in the ‘tissue optical window (650–1100 nm)’. *J. Mater. Chem. B* **3**, 184–190 (2015).
168. Xu, C. & Webb, W. W. Measurement of two-photon excitation cross sections of molecular fluorophores with data from 690 to 1050 nm. *J. Opt. Soc. Am. B* **13**, 481 (1996).
169. Makarov, N. S., Drobizhev, M. & Rebane, A. Two-photon absorption standards in the 550-1600 nm excitation wavelength range. *Opt. Express* **16**, 4029 (2008).
170. de Turrís, V. *et al.* Humanized archaeal ferritin as a tool for cell targeted delivery. *Nanoscale* **9**, 647–655 (2017).
171. Li, L. *et al.* Ferritin-mediated siRNA delivery and gene silencing in human tumor and primary cells. *Biomaterials* **98**, 143–151 (2016).
172. Davidson, B. L. & McCray, P. B. Current prospects for RNA interference-based therapies. *Nat. Rev. Genet.* **12**, 329–340 (2011).
173. Lee, E. J. *et al.* Engineered Proteinticles for Targeted Delivery of siRNA to Cancer Cells. *Adv. Mater.* 1–8 (2015).
174. Whitehead, K. A., Langer, R. & Anderson, D. G. Knocking down barriers: advances in siRNA delivery. *Nat. Rev. Drug Discov.* **8**, 129–138 (2009).
175. Zhang, Y., Satterlee, A. & Huang, L. In Vivo Gene Delivery by Nonviral Vectors: Overcoming Hurdles? *Mol. Ther.* **20**, 1298–1304 (2012).
176. Perez, H. L. *et al.* Antibody-drug conjugates: Current status and future directions. *Drug Discov. Today* **19**, 869–881 (2014).

ATTACHMENTS

As a result of my PhD work the following publications were published or have been submitted for publication.

- **Attachment 1:** Lorenzo Calisti, Irene Benni, Matilde Cardoso Trabuco, Paola Baiocco, Barbara Ruzicka, Alberto Boffi, Elisabetta Falvo, Francesco Malatesta, Alessandra Bonamore, “Probing bulky ligand entry in engineered archaeal ferritins”, *Biochimica et Biophysica Acta*, 1861, 450-456 (2017).
- **Attachment 2:** Valeria de Turrís, Matilde Cardoso Trabuco, Giovanna Peruzzi, Alberto Boffi, Claudia Testi, Beatrice Vallone, Linda Celeste Montemiglio, Amédée Des Georges, Lorenzo Calisti, Irene Benni, Alessandra Bonamore, Paola Baiocco, “Humanized archaeal ferritin as a tool for cell targeted delivery”, *Nanoscale*, 9, 647–655 (2017).
- **Attachment 3:** Mauricio Morais, João P. M. Nunes, Kersti Karu, Nafsika Forte, Irene Benni, Mark E. B. Smith, Stephen Caddick, Vijay Chudasama, James R. Baker, “Optimisation of the dibromomaleimide (DBM) platform for native antibody conjugation by accelerated post-conjugation hydrolysis”, *Organic & Biomolecular Chemistry*, 15, 2947-2952 (2017).
- **Attachment 4:** Irene Benni, Matilde Cardoso Trabuco, Enrico Di Stasio, Alessandro Arcovito, Alberto Boffi, Francesco Malatesta, Alessandra Bonamore, Simone De Panfilis, Valeria de Turrís, Paola Baiocco, “Excimer based fluorescent pyrene-ferritin conjugate for protein oligomerization studies and imaging in living cells”, submitted.



Contents lists available at ScienceDirect

Biochimica et Biophysica Acta

journal homepage: www.elsevier.com/locate/bbagen

Probing bulky ligand entry in engineered archaeal ferritins

Lorenzo Calisti ^a, Irene Benni ^a, Matilde Cardoso Trabuco ^a, Paola Baiocco ^b, Barbara Ruzicka ^c, Alberto Boffi ^{a,d}, Elisabetta Falvo ^d, Francesco Malatesta ^a, Alessandra Bonamore ^{a,*}^a Department of Biochemical Sciences "Alessandro Rossi Fanelli", Sapienza University of Rome, P.le Aldo Moro 5, I-00185 Rome, Italy^b Center for Life Nano Science@Sapienza, Istituto Italiano di Tecnologia, V.le Regina Elena 291, Rome I-00185, Italy^c Istituto dei Sistemi Complessi del Consiglio Nazionale delle Ricerche (ISC-CNR) Sede Sapienza and Dipartimento di Fisica, Sapienza University of Rome, P.le Aldo Moro 5, I-00185 Rome, Italy^d Istituto di Biologia e Patologia Molecolari, Consiglio Nazionale delle Ricerche (IBPM-CNR) Sede Sapienza University of Rome, P.le Aldo Moro 5, I-00185 Rome, Italy

ARTICLE INFO

Article history:

Received 31 May 2016

Received in revised form 1 September 2016

Accepted 11 October 2016

Available online 15 October 2016

Keywords:

Self-assembly
Binding kinetics
Nano-scaffold
Ferritin

ABSTRACT

Background: A set of engineered ferritin mutants from *Archaeoglobus fulgidus* (AF-Ft) and *Pyrococcus furiosus* (PF-Ft) bearing cysteine thiols in selected topological positions inside or outside the ferritin shell have been obtained. The two apo-proteins were taken as model systems for ferritin internal cavity accessibility in that AF-Ft is characterized by the presence of a 45 Å wide aperture on the protein surface whereas PF-Ft displays canonical (three-fold) channels.

Methods: Thiol reactivity has been probed in kinetic experiments in order to assess the protein matrix permeation properties towards the bulky thiol reactive DTNB (5,5'-dithiobis-2-nitrobenzoic acid) molecule.

Results: Reaction of DTNB with thiols was observed in all ferritin mutants, including those bearing free cysteine thiols inside the ferritin cavity. As expected, a ferritin mutant from PF-Ft, in which the cysteine thiol is on the outer surface displays the fastest binding kinetics. In turn, also the PF-Ft mutant in which the cysteine thiol is placed within the internal cavity, is still capable of full stoichiometric DTNB binding albeit with an almost 200-fold slower rate. The behaviour of AF-Ft bearing a cysteine thiol in a topologically equivalent position in the internal cavity was intermediate among the two PF-Ft mutants.

Conclusions and general significance: The data thus obtained indicate clearly that the protein matrix in archaeal ferritins does not provide a significant barrier against bulky, negatively charged ligands such as DTNB, a finding of relevance in view of the multiple biotechnological applications of these ferritins that envisage ligand encapsulation within the internal cavity.

© 2016 Elsevier B.V. All rights reserved.

1. Introduction

Ferritins from a variety of species have emerged as versatile scaffolds for a number of diverse nanotechnological applications spanning from the synthesis of metal nanoparticles to drugs or diagnostics delivery. The most notable property of ferritins resides in their ability to sequester metals as well as small molecules within their internal cavities. Ferritin proteins are by far the best-studied biomineralisation scaffolds in that these proteins are able to accommodate up to 4500 iron atoms in an iron (III) oxide form within the central cavity. Iron (II) is oxidised within the ferroxidase centers located at the entrance of ferritin pores (threefold channels on the protein surface) and subsequently transferred to the central cavity and mineralised as iron (III) oxide nanocrystals. Thereafter, under physiological reducing conditions, the iron (III) oxide can be reverted to iron (II) and diffuses out of the cavity,

most likely through negatively charged pores in the ferritin shell, formed between subunits [1]. These channels allow for the entry and exit of cations during mineralisation and demineralisation and display a relatively broad selectivity thus allowing for the accumulation of a variety of metal ions, with a preference for divalent cations. These properties have been used to develop ferritin as a drug delivery platform [2]. At physiological pH ferritin exists as a stable 24-mer, whereas in highly acidic or basic solutions it disassembles reversibly thereby spontaneously reassembling as neutral pH is restored. The reversible subunit assembly has been used to trap molecules in solution within its cavity simply by changing pH in the presence of the desired molecule. This property has been used to load the cavity with metal containing drugs, such as the cancer drug cisplatin [3,4], and the iron chelator desferrioxamine B [5,6], as well as a variety of organic and inorganic compounds, including metal nanoparticles.

The incorporation of non-metal-containing drugs within ferritin is however challenging due to the limited interactions with the ferritin shell, and the diffusion of these molecules through the surface pores. Strategies to overcome these problems have focused on complexing

* Corresponding author.

E-mail addresses: alessandra.bonamore@uniroma1.it, alessandra.bonamore@gmail.com (A. Bonamore).

drugs with transition metals, such as Cu(II), prior to their internalisation [7], or the addition of charged accessory molecules such as poly-L-aspartic acid to optimise loading of ferritin with drugs [8]. By combining the loading of ferritin with drugs and surface modification with peptide epitopes and labels, ferritin can be specifically targeted to particular cell types and tumours for efficient delivery of therapeutic agents [9]. Thus far, ferritins and other protein nanocages show a great deal of promise that will hopefully transfer to a clinical setting.

Nevertheless, molecular diffusion in and out of the ferritin cavity appears to be a complex phenomenon that is only partially understood. The pathway of iron entry inside the ferritin cavity is characterized by the presence of eight protein ion channels positioned around the three-fold symmetry axes of the cage and delimited by three proximal subunits. Such ion channels are about 15 Å in length and 5–6 Å in diameter. Because hydrated ions have diameters of about 6.5 Å, partial dehydration is thought to occur for ion passage through the channel. On this basis, possible entry of larger ligands of physiological interest (e.g. iron III reductants) or other small organic molecules may seem unlikely. However, a large number of experimental observations, mostly carried out on mammalian ferritins heteropolymers or recombinant H and L homopolymers, pointed out that small organic molecules can permeate the protein shell, possibly through the same negatively charged three-fold channels that govern metal ions fluxes [10–12]. The permeation of small molecules into ferritins at physiological temperature and pH has been shown to be a charge-selective process in both native, H and L-chains of several mammalian proteins having similar channel structures [13]. A number of studies thus supported the hypothesis that the threefold channels are indeed the primary avenues of entry into the protein cavity of small molecules endowed with cationic properties [14]. The complete exclusion of the negatively charged probes from the interior of these proteins has been elegantly demonstrated by means of spin labeled molecules [11]. At the same time, the permeability of the same molecules in mutated proteins bearing positively charged groups along the three fold channels has been demonstrated [15,16]. More recently, however, many different ferritins from phylogenetically distinct trees have been identified and characterized. Among these, highly thermostable ferritins from Archaea emerged as privileged scaffolds in view of their remarkable thermal stability, easy expression in high yields in common *E. coli* cells and, at least in a few examples, uncommon association-dissociation properties. In particular, archaeal ferritins from *Archaeoglobus fulgidus* (Af-Ft) and *Pyrococcus furiosus* (Pf-Ft) emerged as most interesting tools for diverse applications. In spite of the high sequence similarity (50 and 70% amino acid sequence identity and similarity, respectively), Pf-Ft and Af-Ft do not share the same quaternary assembly. In fact, whereas the Pf-Ft 24-mer has the canonical 432 point-group symmetry, the Af-Ft 24-mer displays a 23 point-group symmetry typical of smaller 12-mer ferritin-like proteins. This unusual assembly does not display the 4-fold channels and constrains the quaternary structure thus leading to the appearance of four large triangular openings about 45 Å wide in the protein shell [17]. To date, Af-Ft assembly, here referred to as an “open” structure, is considered unique among all other known structures of tetraicosameric ferritins. The stability of this tetrahedral configuration is governed by two critical residues in the helix E of the 4-helices bundle, namely K150 and R151. Indeed, the structure of Af-Ft K150A/R151A mutant reported by Sana et al. [18], shows a typical “closed” octahedral symmetry.

However, diffusion of small molecules within archaeal ferritins have been little investigated. Differences in the nature, shape and properties of open pores within these ferritins thus provide novel possible routes for small molecules entry/incorporation thus expanding the scope of possible biotechnological applications of these proteins. In the present work, we have engineered a set of Pf-Ft, Af-Ft (“open”) and Af-Ft K150A/R151A (“closed”) mutants by placing reactive cysteine residues in the same topological positions either inside or outside the internal cavity. The reactivity of the bulky, negatively charged DTNB molecule has been probed in the set of available mutants.

2. Materials and methods

2.1. Point mutations and protein expression

The genes encoding for bacterial ferritin from Af-Ft and Pf-Ft were cloned into the expression vector pET22b (Novagen). Point mutants Af-FtM54C, Af-FtM54C/K150A/R151A, Pf-FtG52C and Pf-FtP77C were obtained by PCR using QuickChange Mutagenesis kit (Stratagene). The recombinant plasmids were transformed into *E. coli* TOP 10 cells and the resulting colonies were screened by DNA sequencing. Plasmids bearing the desired mutations were transformed into BL21(DE3) *E. coli* strain for protein expression. For each mutant, protein over-expression was obtained as follows: 1 L LB broth medium was inoculated with 2 ml overnight culture of a single colony and the gene expression was induced with 1 mM IPTG when the absorbance at 600 nm reached 0.6. Cells were harvested by centrifugation after overnight induction at 37 °C and the cell pellets were stored at –20 °C.

2.2. Protein purification

Harvested cells from 1 l culture over-expressing Af-FtM54C and Af-FtM54C/K150A/R151A mutants were resuspended in 20 ml buffer A (25 mM HEPES pH 7.5, 20 mM MgCl₂) containing a cComplete™ Mini Protease Inhibitor Cocktail Tablet (Roche) and disrupted by sonication. The soluble fraction was thermally purified by heating at 85 °C for 10 min followed by removal of denatured proteins by centrifugation at 14000 rpm for 30 min at 4 °C. The supernatant was fractionated by ammonium sulfate precipitation. 70% ammonium sulfate pellet containing highly purified protein was resuspended in buffer A, dialysed versus the same buffer, sterile filtered and stored at 4 °C. Cells over-expressing Pf-FtG52C and Pf-FtP77C were sonicated in 25 mM HEPES buffer at pH 7.5 containing 0.5 mM EDTA, 0.3 M NaCl and cComplete™ Mini Protease Inhibitor Cocktail Tablet. After sonication, the crude bacterial extract was digested with DNase for 1 h at 37 °C, heated at 55 °C for 10 min and then at 80 °C for 8 min. Heat treatment was followed by centrifugation to remove insoluble material and ammonium sulfate precipitation. 70% ammonium sulfate pellet was resuspended in 20 mM HEPES pH 7.5 plus 150 mM NaCl, dialysed versus the same buffer and loaded onto a HiLoad 26/600 Superdex 200 pg column (GE Healthcare). Fractions containing highly purified protein were pooled, sterile filtered and stored at 4 °C.

2.3. Preparation of ferritin-DTNB adducts

All mutants were reduced with 3 mM TCEP (tris(2-carboxyethyl)phosphine) in their storage buffers and then loaded onto a desalting column (GE Healthcare) to remove the reducing agent. Each mutant was reacted with 40-fold molar excess of Ellman's Reagent, (DTNB) per cysteine for 3 h at room temperature. Stock DTNB solutions were prepared in ethanol. The excess (non-reacted) reagent was removed by ultra-filtration using 100 kDa Amicon Ultra-15 centrifugal devices (Millipore Corporation). The Ferritin-DTNB samples were analyzed by mass spectrometry as described below.

2.4. Stopped flow experiments

Kinetic measurements were carried out on a thermostated Applied Photophysics stopped-flow apparatus (Leatherhead, UK) by mixing 8–10 μM protein solutions, previously reduced with TCEP, with solutions containing different concentrations of DTNB (from 0.2 to 0.7 mM after mixing) in 20 mM HEPES, 20 mM MgCl₂ pH 7.5. In order to avoid interference of the instrument phototube from the high concentrations of DTNB and the released chromophore 5-thio-2-nitro-benzoic acid (TNB), the reaction was followed at 430 nm and the extinction coefficient calculated to be 12205 mM⁻¹ cm⁻¹, as determined from the extinction coefficient of 14150 mM⁻¹ cm⁻¹ at 412 nm [19]. All fitting

procedures were carried out by using the Matlab software (Mathworks, USA). Experimental traces were fitted by non-linear regression to either exponential or biexponential processes by using an Levenberg-Marquardt algorithm.

2.5. Self-assembly study

MgCl₂-mediated self-assembly of ferritin mutants was studied by incubating aliquots of proteins (1 mg/ml) with different salt concentrations in 25 mM HEPES buffer, pH 7.5. Molecular sizes of AF-FtM54C, AF-FtM54C/K150A/R151A, PF-FtG52C and PF-FtP77C was determined by size exclusion chromatography (SEC) using HiPrep 16/60 Sephacryl S300 column (GE Healthcare). The column was equilibrated with 25 mM HEPES, pH 7.5, containing MgCl₂ at the same concentration in which the protein was pre-incubated and the same buffer was used as mobile phase. Molecular weight of each mutant were determined by comparing their elution volumes with the elution volumes of standard proteins in the same salt concentration.

Dynamic light scattering measurements (DLS) were performed using an ALV-5000 logarithmic correlator in combination with a standard optical set-up based on a He-Ne ($\lambda = 632.8$ nm) 10 mW laser and a photomultiplier detector. The intensity autocorrelation functions were directly obtained as $g_2(q, t) = \langle I(q, t)I(q, 0) \rangle / \langle I(q, 0) \rangle^2$, where q is the modulus of the scattering vector defined as $q = (4\pi n/\lambda) \sin(\theta/2)$ ($\theta = 90^\circ$ in the present experiment). The raw measurements as directly obtained, without any data corrections are shown in Fig. 1 for different samples without added salt (black symbols) and at different MgCl₂ concentrations between 5 and 30 mM (colored symbols as described in the legend). Quantitative analysis of the measurements was obtained through a fit of the data with a single exponential expression: $g_2(q, t) = 1 + b e^{-t/\tau}$ where b is the coherence factor and τ is the relaxation time related to the motion of the particles, specifically to the diffusion coefficient [20].

2.6. Protein LC-MS

LC-MS was performed on protein samples before and after DTNB titration, after dialysis in distilled water in the presence of 0.1 mM EDTA, using a Waters AcquityPLC connected to Waters Acquity Single Quad Detector. A Hypersil Gold C4 column was used: 1.9 μ m, 2.1 \times 50 mm at 254 nm observation wavelength; mobile phase: 95:5 water (0.1% formic acid):MeCN (0.1% formic acid); gradient over 6 min (to 5:75 water (0.1% formic acid):MeCN (0.1% formic acid)); flow rate: 0.4 ml min⁻¹; MS mode was set at a scan range: $m/z = 250$ –2,000 (ES+); scan time: 0.25 s. Data were obtained in continuum mode by setting the electrospray source of the MS with a capillary voltage of 3.5 kV and a cone voltage of 50 V. N₂ gas was used as nebulizer and desolvation gas at a total flow of 300 l/h. Ion series were generated by integration of the ultraviolet-absorbance (at 254 nm) chromatogram over 1.2–1.8 min range. Mass spectra were subsequently reconstructed for proteins from the ion series using the MaxEnt 1 algorithm on Masslynx software program.

3. Results

3.1. Assessment of ferritin mutants assembly

In order to assess the association state of the engineered ferritin mutants AF-FtM54C, AF-FtM54C/K150A/R151A, PF-FtG52C and PF-FtP77C, all proteins were studied by DLS and SEC as a function of MgCl₂ concentration. A full characterization of AF-FtM54C association state is reported in Fig. 1. Data relative to the other mutants are reported as Supplementary materials (Figs. S1, S2 and S3). Fig. 1 clearly shows that the shape of the curve without added salt is significantly different from that observed in the presence of added salt. This behavior is confirmed by data fitting obtained as described under Methods section. The fitting

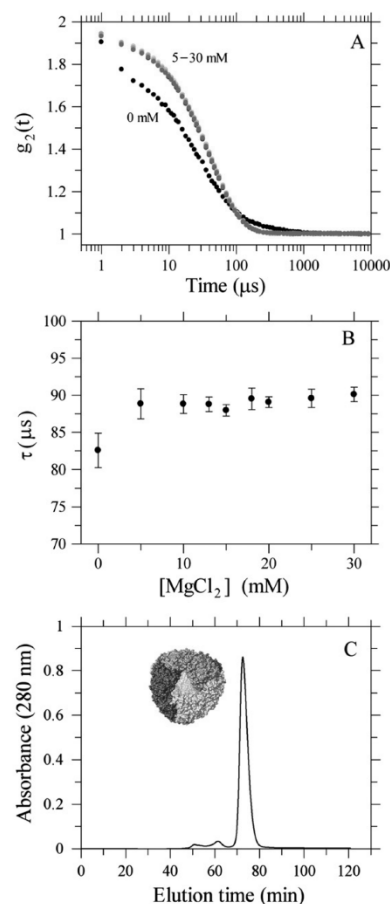


Fig. 1. Polymeric assembly of *Archaeoglobus fulgidus* ferritin mutants. A) Dynamic Light Scattering intensity correlation functions of AF-FtM54C at different MgCl₂ concentrations indicated in the legend. The curves at different MgCl₂ are all superimposed. B) Dynamic Light Scattering relaxation time of AF-FtM54C as a function of MgCl₂ concentration. C) Gel filtration profiles of AF-FtM54C at 20 mM MgCl₂.

curves appears to interpolate very well experimental data in presence of salts whereas are less accurate for samples without added salt, where the addition of polydispersity is necessary.

PF-Ft mutants are stable 24-mers (~490 kDa) independent of salt concentration, whereas the self-assembly of AF-Ft mutants was strongly dependent on ionic strength. MgCl₂ was used as polymerizing salt at variance with previous reports [18] in which NaCl was used. As a result, it appeared that at our working concentration (20 mM MgCl₂) all the proteins are structured as a stable 24-meric cage. It is noticeable that the 24-mer to dimer ratio increases with increasing MgCl₂ concentration from 0 to 20 mM, whereas at least 100 mM NaCl concentration of NaCl are needed to reach full polymerization (data not shown). Thus, it appears that divalent cations such as Mg²⁺ and Ca²⁺ are more effective in promoting the 24-mer association with respect to NaCl. The

comparison between SEC and DLS data on Af-FtM54C and Af-FtM54C/K150A/R151A however need further comments. First of all, the heterogeneous, polydisperse population observed in the absence of divalent cations is manifest in the presence of both low molecular weight species (presumably dimers as reported in refs. [16–18]) and distributed high molecular weight polymers (present in much lower amount), apparently in a proportion even higher than the canonical 24-mers. Addition of $MgCl_2$ at 5–10 mM concentration brings about a very sharp transition in both Af-Ft mutants resulting in the formation of homogeneous and stable 24-mer species. At 20 mM $MgCl_2$ concentration, all proteins investigated are consistent with a stable 24-mer assembly.

3.2. Kinetics of DTNB binding to Pf-Ft and Af-Ft mutants

The kinetics of the disulfide exchange reaction of DTNB with cysteine residues on ferritin mutants were carried out by stopped-flow spectroscopy. The kinetics, determined under pseudo-first order conditions, appeared to be multiexponential and were followed to the maximum time possible with the instrument (1000 s). Independent experiments performed by using UV-visible absorption spectroscopy and LC-MS (see below) confirmed the essentially complete cysteine reactivity. As Fig. 2A shows, the time scales of the four ferritin mutants are significantly different. As expected, the Pf-Ft P77C mutant bearing the cysteine residue on the convex outer surface displayed the fastest reactivity as compared to Pf-Ft G52C which carries the mutation inside the ferritin tetraicosamer. A complete set of time courses of the Pf-Ft P77C mutant has been carried out increasing DTNB concentration and reported in Supplementary Materials (Fig. S4). Within the observed time frame all traces could be fit to a simple relaxation process with apparent second-order rate constants of ca. $900 M^{-1} cm^{-1}$ (see also Table 1). The Af-Ft mutants had an intermediate behaviour in the reaction with DTNB. Quite unexpectedly the Af-Ft M54C mutant, in which the internal cysteine reacts with DTNB in a facilitated way through the four 45-Å large triangular openings in the protein shell, could only be fit by a biexponential process in which the fastest second-order rate constant was of the same order of magnitude determined for the Pf-Ft P77C mutant (Table 1). Finally, closure of the openings by introduction of the K150A/R151A mutations in Af-M54C brought about a significant quenching of the ligand binding rate. The complete set of kinetic traces for each mutant were also fit by either exponential or biexponential relaxations with second-order rate constants as reported in Supplementary materials (Fig. S5). Overall these results indicate that the diffusion of molecules across the proteinaceous barrier of closed ferritin 24-mers can be accurately measured and secondly that contrary to intuition and reported data (see discussion section) the protein shell

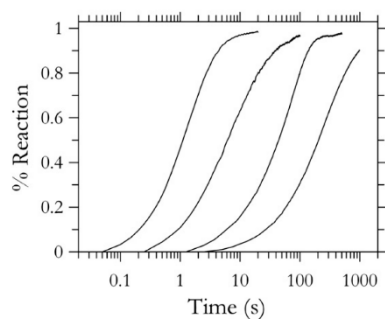


Fig. 2. Kinetics of DTNB binding to Af-Ft and Pf-Ft mutants. A. Comparison of the reaction time scales of all mutants; from left to right, Pf-FtP77C, Af-FtM54C, Af-FtM54C/K150A/R151A, and Pf-FtG52C. All mutants were 5 μM except Af-FtM54C which was 4 μM , and DTNB was 0.7 mM.

Table 1
Apparent second-order constants for ferritin mutants as determined by the DTNB reaction.

Protein	Cysteine position	$k_{OBS} (M^{-1} s^{-1})$
Pf-FtP77C	External	908 ± 122
Pf-FtG52C	Internal	5 ± 1
Af-FtM54C open	Internal	Fast: 198 ± 65 Slow: 51 ± 21
Af-FtM54C/K150A/R151A closed	Internal	26 ± 2

permeability to bulky molecules such as DTNB is much higher than expected. These results bear relevant implications discussed below in so far as ligand encapsulation and delivery is concerned.

3.3. LC/MS data

LC-MS measurements were performed on the selected point mutants Af-FtM54C, Af-FtM54C/K150A/R151A, Pf-FtG52C and Pf-FtP77C after titration with DTNB in comparison with unreacted proteins. In all samples, ferritins were eluted as monomers of molecular weight of about 21 kDa, and DTNB reacted proteins showed a shifted peak of $+198 \pm 2$ Da, in agreement with the expected molecular weight of the thio-nitrobenzoic moiety. In all samples reaction was complete with the exception of Pf-Ft G52C protein in which 18 % of unreacted protein was present (Supplementary materials, Fig. S6).

4. Discussion

The present data highlight notable properties related to bulky ligands penetration through prototypic archaeal ferritin homopolymers that are relevant both to the general ligand entry/escape mechanism and to the widespread nanotechnological applications of these proteins [21,22].

The experimental set up was designed around four mutants of Pf-Ft and Af-Ft bearing a cysteine residue per subunit either in topologically equivalent positions inside the 24-mer cavity (Af-FtM54C, Af-FtM54C/K150A/R151A, Pf-FtG52C) or outside the 24-mer cage in the Pf-FtP77C mutant (see Fig. 3). In this framework, access to the reactive sulfidryls is totally unhindered on the protein external surface in Pf-FtP77C, partially hindered in the internal cavity in Af-FtM54C and totally hindered in the internal cavity in Af-FtM54C/K150A/R151A and Pf-FtG52C. The overall picture that emerges from the body of experimental results is that even fully assembled, closed Af-FtM54C/K150A/R151A and Pf-FtG52C structures are capable of stoichiometric binding of the bulky, negatively charged, DTNB ligand. These results indicate that the permeation of negatively charged molecular species of 8–10 Å length and 5–6 Å diameter into archaeal ferritins does occur at variance with the reported exclusive entry of positively charged or neutral species only in vertebrate ferritins [13,14]. Charge selectivity was reported in the case of horse spleen ferritin (HoSF) and human H-chain ferritin (HuHF) and was correlated to the nature of threefold channels, endowed with hydrophilic, negatively charged tunnels involved in iron uptake [23]. Electron paramagnetic resonance spectroscopy and gel permeation chromatography studies with HoSF demonstrated that molecular charge and polarity of the diffusants play a critical role in their permeation into ferritin [14]. Kinetic studies of permeation using small nitroxide spin probes also confirmed the role of these channels as providing a charge-selective pathway for entry into the cavity [10]. A negatively charged nitroxide was completely excluded from the interior of the protein, whereas positively charged and polar nitroxide radicals penetrated the protein shell to interact with the iron core. Mutated HuHF (D131H/E134H), where the negatively charged glutamate and aspartate residues lining the threefold channels are replaced by histidines, partially allowed the entry of negatively charged species (4-carboxyTEMPO radical) thus providing strong evidence that the negatively charged threefold channels are the principal pathways for molecular

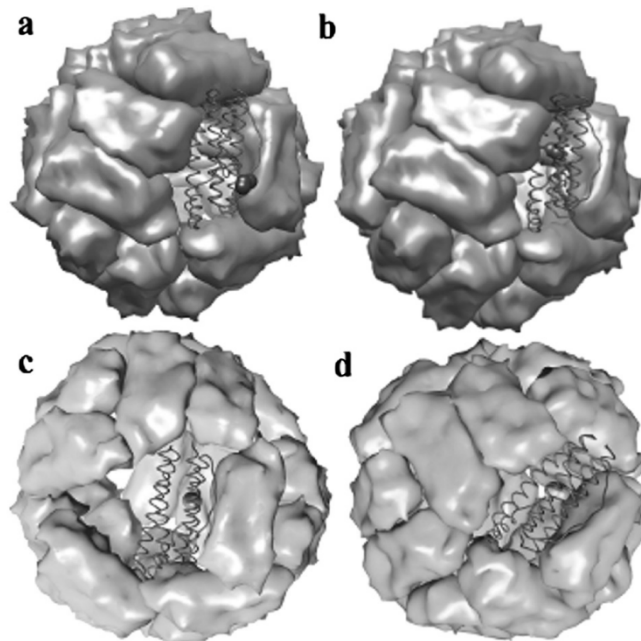


Fig. 3. Three-dimensional structures of the ferritin mutants. A monomer is depicted as green ribbon and the cysteine residues are represented in CPK style for clarity. a) Pf-FtP77C: the external cysteine is shown as blue spheres. b) Pf-FtC52C: the internal cysteine is depicted in red (models a) and b) built on Pf-Ft structure, (PDB ID: 2JD6). c) Af-Ft54C: the internal cysteine is depicted in purple. d) Af-FtM54C/K150A/R151A: the internal cysteine in magenta (models c) and d) built on Af-Ft structure, (PDB ID: 1SQ3). Molecular graphics and analyses were performed with the UCSF Chimera package [25].

diffusion into ferritin [10]. Interestingly, first-order half-lives for permeation of positively charged compounds in mammalian ferritins are in the same time range of those observed in DTNB uptake in fully closed Af-FtM54C/K150A/R151A and Pf-FtG52C archaeal ferritins although Af-Ft and Pf-Ft have been reported to show a different amino acid arrangement in the threefold channels that suggested a different ligand incorporation mechanism.

In particular, the eight threefold channels in each protein are shaped by the C-terminal segment of C helix and the N-terminus of D helix in the 4-helix bundle of three adjacent monomers [24]. Thus, C-terminal ends of helices C define the outer entrance to the channel and the N-termini of helices D define the inner entrance. In the case of Pf-Ft, channels are similar to those of HuHF in the outer side, that is rich in negative aminoacids (Glu109, Glu110 and Glu111), whereas they differ in the central region due to the presence of polar and positively charged residues (Tyr114 and Arg117). Lastly, the inner entrance of the channel is characterized by the presence of Ala118 and Glu121, in the topological position which is deemed essential for the transfer of iron (II) to the ferroxidasic center in mammalian ferritins [26].

In the case of Af-Fts, namely Af-FtM54C ("open" form) and Af-FtM54C/K150A/R151A ("closed" form), the threefold channels are lined by a mix of hydrophobic and hydrophilic aminoacids: only one glutamate (Glu113; PDB ID: 1SQ3 and 3KX9) is located to the entrance and two acidic residues lining HuHF channels (D131 and E134) (PDB ID: 2FHA) are replaced by neutral and positively charged residues (Tyr119 and Asn 120). Thus, in the case of Af-Ft, the cluster of negative charges characteristic of HuHF is not present, presumably because it is not necessary to drive iron (II) atoms towards the ferroxidasic site,

readily available through the large pores present in this protein. Hence, the threefold channels of archaeal ferritins are less negatively charged than the mammalian ones, possibly allowing the entrance of negatively charged compounds (see Fig. 4). Of course, the "open" Af-FtM54C, here investigated, displays the four 45 Å wide triangular pores, defined by C and D helices, characterized by the presence of a group of positive charged residues located at the three apices [17]. These large openings are most likely preferential paths for large ligand entry into the cavity as demonstrated by the 8 fold faster DTNB reaction rate with the internal thiol with respect to the closed Af-FtM54C/K150A/R151A mutant (see Table 1). In turn, the DTNB entry rate into Af-FtM54C/K150A/R151A mutant is 5 fold faster than in the Pf-FtG52C protein. Such difference is significant in view of the fact that the last two proteins are assimilated to closed cages with thiols in topologically equivalent positions.

As a last comment it is worth considering the possible role of the so-called fourfold channels. As matter of fact, the quaternary assembly of the closed Af-FtM54C/K150A/R151A mutant is similar to that of Pf-FtG52C and other mammalian Ft cages displaying a canonical octahedral conformation with fourfold channels of 4–5 Å size. The six fourfold channels of Pf-Ft (PDB ID: 2JD6) are polar and hydrophilic. Moreover, Lys145 in the DE loop (corresponding to Lys 150 in Af-Ft), which forms an outer gate to the fourfold channel, makes this entrance more polar and charged than that of HuHF, which is basically uncharged. Nevertheless, the dimensions of the fourfold channel in both mammalian and archaeal ferritins is found to be too small even to metal ions with the possible exception of protons and cannot be taken as a possible option for the entry of organic molecules.

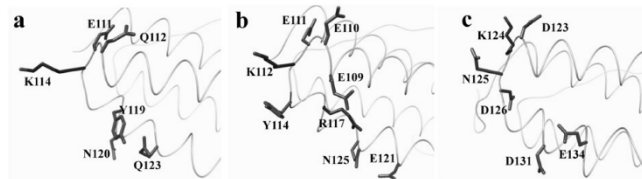


Fig. 4. Profile view of the lining amino acids in the threefold channel in a) Af-Ft (PDB ID: 1SQ3) and b) Pf-Ft (PDB ID: 2JD6) with respect to c) HuHF (PDB ID: 2FHA). The exterior of the shell lies on the left side and the inner cavity on the right side of each cartoon as shown schematically. Positive, negative and polar residues are depicted as blue, red and green sticks, respectively.

Thus, on the basis of the observed DTNB binding rates and available crystallographic structures we conclude that archaeal ferritins from *P. furiosus* and *A. fulgidus* are able to incorporate negatively charged, modestly sized diffusants, even in their fully “closed” forms, most likely through the threefold channels whose nature appears less restrictive with respect to that of vertebrate proteins. Possibly, the presence of positively charged residues in the middle of the threefold channel may favour entrance of negatively charged species in the archaeal proteins. As a last comment, it must also be pointed out that the dimensions of the currently used probe slightly exceed the diameter of the threefold channel as inferred from crystal structure coordinates. A mechanism of rotameric adjustment of relevant amino acid side chains is thus necessary in order to allow for the entry/exit of small organic molecules. Recent demonstration of multiple conformers in amino acids lining the inner entrance to the ferritin cavity may explain the necessary plasticity of the threefold channels in ferritins [26].

5. Conclusions

The results of the present work indicate that molecular diffusion into archaeal ferritin is a complex phenomenon and that even apparently closed, impermeable structures, ferritins do allow entry of 8–10 Å long organic molecules with no necessity of 24-mer disassembly. The data thus obtained indicate clearly that the protein matrix in archaeal ferritins does not provide a significant barrier against bulky, negatively charged ligands such as DTNB, a finding of relevance in view of the multiple biotechnological applications of these ferritins that envisage ligand encapsulation within the internal cavity. The potential impact of such engineered ferritins on the general topics related to their biotechnological application is wide. On the side of material science, the possibility of disposing of a cations dependent self-assembling cage provides the basis of unique “molecular carpentry” tools. On the side of biomedical applications, the use of archaeal proteins must still be explored. The entry of archaeal ferritins into mammalian cells is under investigation in order to clarify their receptor recognition properties, the pathways of intracellular trafficking, the impact on eukaryotic cell iron homeostasis and/or their toxic effects due to possible generation of oxidative stress under the widely different iron reductive mechanisms typical of eukaryotic cells.

Transparency document

The Transparency document associated with this article can be found, in the online version.

Acknowledgements

EU H₂₀₂₀ Project “X-Probe”, Grant N° 637295, to A. Bonamore and M.C.T. is gratefully acknowledged. Flagship project “Nanomax” from MIUR (Nanomax MIUR_J120062) to A. Boffi is also acknowledged.

Appendix A. Supplementary data

Supplementary data to this article can be found online at doi:10.1016/j.bbagen.2016.10.007.

References

- [1] K. Honarmand Ebrahimi, P.L. Hagedoorn, W.R. Hagen, Unity in the biochemistry of the iron-storage proteins ferritin and bacterioferritin, *Chem. Rev.* 115 (2015) 295–326.
- [2] Z. Zhen, W. Tang, H. Chen, X. Lin, T. Todd, C. Wang, RGD-modified apoferritin nanoparticles for efficient drug delivery to tumors, *ACS Nano* 7 (2013) 4830–4837.
- [3] N. Pontillo, F. Pane, L. Messori, A. Amoresano, A. Merlini, Cisplatin encapsulation within a ferritin nanocage: a high-resolution crystallographic study, *Chem. Commun. (Camb.)* 52 (2016) 4136–4139.
- [4] E. Falvo, E. Tremante, R. Fraioli, C. Leonetti, C. Zamparelli, A. Boffi, V. Morea, P. Ceci, P. Giacomini, Antibody-drug conjugates: targeting melanoma with cisplatin encapsulated in protein-cage nanoparticles based on human ferritin, *Nanoscale* 5 (2013) 12278–12285.
- [5] X.-T. Ji, L. Huang, H.-Q. Huang, Construction of nanometer cisplatin core-ferritin (NCC-F) and proteomic analysis of gastric cancer cell apoptosis induced with cisplatin released from the NCC-F, *J. Proteome* 75 (2012) 3145–3157.
- [6] J.M. Domínguez-Vera, Iron(III) complexation of desferrioxamine B encapsulated in apoferritin, *J. Inorg. Biochem.* 98 (2004) 469–472.
- [7] A. Maham, Z. Tang, H. Wu, J. Wang, Y. Lin, Protein-based nanomedicine platforms for drug delivery, *Small* 5 (2009) 1706–1721.
- [8] A. Maham, H. Wu, J. Wang, X. Kang, Y. Zhang, Y. Lin, Apoferritin-based nanomedicine platform for drug delivery: equilibrium binding study of daunomycin with DNA, *J. Mater. Chem.* 21 (2011) 8700–8708.
- [9] L. Vannucci, E. Falvo, C.M. Faila, M. Carbo, M. Fornara, R. Canese, S. Cecchetti, L. Rajsiglova, D. Stakheev, J. Krizan, A. Boffi, G. Carpinelli, V. Morea, P. Ceci, In vivo targeting of cutaneous melanoma using a melanoma stimulating hormone-engineered human protein cage with fluorophore and magnetic resonance imaging tracers, *J. Biomed. Nanotechnol.* 11 (2015) 81–92.
- [10] X. Yang, P. Arosio, N.D. Chasteen, Molecular diffusion into ferritin: pathways, temperature dependence, incubation time, and concentration effects, *Biophys. J.* 78 (2000) 2049–2059.
- [11] X. Yang, N.D. Chasteen, Molecular diffusion into horse spleen ferritin: a nitroxide radical spin probe study, *Biophys. J.* 71 (1996) 1587–1595.
- [12] B. Zhang, R.K. Watt, N. Gálvez, J.M. Domínguez-Vera, G.D. Watt, Rate of iron transfer through the horse spleen ferritin shell determined by the rate of formation of prussian blue and Fe-desferrioxamine within the ferritin cavity, *Biophys. Chem.* 120 (2006) 96–105.
- [13] R.R. Crichton, J.P. Declerck, X-ray structures of ferritins and related proteins, *Biochim. Biophys. Acta* 1800 (2010) 760–818.
- [14] T. Douglas, D.R. Ripoll, Calculated electrostatic gradients in recombinant H-chain ferritin, *Protein Sci.* 7 (5) (1998 May) 1083–1091.
- [15] P.M. Harrison, A. Treffy, T.H. Lilley, Ferritin as an iron-storage protein: mechanisms of iron uptake, *J. Inorg. Biochem.* 27 (1986) 287–293.
- [16] A. Treffy, P.M. Harrison, Spectroscopic studies on the binding of iron, terbium, and zinc by apoferritin, *J. Inorg. Biochem.* 21 (1984) 9–20.
- [17] E. Johnson, D. Cascio, M.R. Sawaya, M. Gingery, I. Schröder, Crystal structures of a tetrahedral open pore ferritin from the hyperthermophilic archaeon *Archaeoglobus fulgidus*, *Structure* 13 (2005) 637–648.
- [18] B. Sana, E. Johnson, P. Le Magueres, A. Criswell, D. Cascio, S. Lim, The role of nonconserved residues of *Archaeoglobus fulgidus* ferritin on its unique structure and biophysical properties, *J. Biol. Chem.* 288 (2013) 32663–32672.
- [19] P.W. Riddles, R.L. Blakeley, B. Zerner, Ellman’s reagent: 5,5'-dithiobis(2-nitrobenzoic acid) – a reexamination, *Anal. Biochem.* 94 (1979) 75–81.
- [20] B.J. Berne, R. Pecora, *Dynamic Light Scattering*, Wiley, New York, 1976.
- [21] M. Liang, K. Fan, M. Zhou, D. Duan, J. Zheng, D. Yang, J. Feng, X. Yan, H-ferritin-nanocaged doxorubicin nanoparticles specifically target and kill tumors with a single-dose injection, *Proc. Natl. Acad. Sci. U. S. A.* 111 (2014) 14900–14905.

- [22] M.A. Kostiaainen, P. Hiekkataipale, A. Laiho, V. Lemieux, J. Seitsonen, J. Ruokolainen, P. Ceci, Electrostatic assembly of binary nanoparticle superlattices using protein cages, *Nat. Nanotechnol.* 8 (2013) 52–56.
- [23] A. Desideri, S. Stefanini, F. Polizio, R. Petruzzelli, E. Chiancone, Iron entry route in horse spleen apoferritin. Involvement of the three-fold channels as probed by selective reaction of cysteine-126 with the spin label 4-maleimido-tempo, *FEBS Lett.* 287 (1991) 10–14.
- [24] J. Tatur, W.R. Hagen, P.M. Matias, Crystal structure of the ferritin from the hyperthermophilic archaeal anaerobe *Pyrococcus furiosus*, *J. Biol. Inorg. Chem.* 12 (2007) 615–630.
- [25] E.F. Pettersen, T.D. Goddard, C.C. Huang, G.S. Couch, D.M. Greenblatt, E.C. Meng, T.E. Ferrin, UCSF chimera—a visualization system for exploratory research and analysis, *J. Comput. Chem.* 25 (2004) 1605–1612.
- [26] R.K. Beheraa, E.C. Theil, Moving Fe^{2+} from ferritin ion channels to catalytic OH centers depends on conserved protein cage carboxylates, *Proc. Natl. Acad. Sci. U. S. A.* 111 (2014) 7925–7930.



Cite this: *Nanoscale*, 2017, 9, 647

Humanized archaeal ferritin as a tool for cell targeted delivery†

Valeria de Turris,^a Matilde Cardoso Trabuco,^b Giovanna Peruzzi,^a Alberto Boffi,^{a,c} Claudia Testi,^a Beatrice Vallone,^c Linda Celeste Montemiglio,^d Amédée Des Georges,^e Lorenzo Calisti,^d Irene Benni,^d Alessandra Bonamore^d and Paola Baiocco*^a

Human ferritins have been extensively studied to be used as nanocarriers for diverse applications and could represent a convenient alternative for targeted delivery of anticancer drugs and imaging agents. However, the most relevant limitation to their applications is the need for highly acidic experimental conditions during the initial steps of particle/cargo assembly, a process that could affect both drug stability and the complete reassembly of the ferritin cage. To overcome this issue the unique assembly of *Archaeoglobus fulgidus* ferritin was genetically engineered by changing a surface exposed loop of 12 amino acids connecting B and C helices to mimic the sequence of the analogous human H-chain ferritin loop. This new chimeric protein was shown to maintain the unique, cation linked, association–dissociation properties of *Archaeoglobus fulgidus* ferritin occurring at neutral pH values, while exhibiting the typical human H-homopolymer recognition by the transferrin receptor TfR1. The chimeric protein was confirmed to be actively and specifically internalized by HeLa cells, thus representing a unique nanotechnological tool for cell-targeted delivery of possible payloads for diagnostic or therapeutic purposes. Moreover, it was demonstrated that the 12 amino acids' loop is necessary and sufficient for binding to the transferrin receptor. The three-dimensional structure of the humanized *Archaeoglobus* ferritin has been obtained both as crystals by X-ray diffraction and in solution by cryo-EM.

Received 8th September 2016,
Accepted 23rd November 2016
DOI: 10.1039/c6nr07129e

www.rsc.org/nanoscale

Introduction

Ferritin proteins have been extensively used as nanocarriers for diverse applications due to their hollow cage-like structures and their unique, reversible, 24-mer assembly.^{1,2} In more detail, they represent the most convenient alternative to viral carriers for targeted delivery of anticancer drugs and imaging agents and have been successfully utilized as reaction nanovessels for the synthesis of non-native metallic nanoparticles in the inner core, with applications in nanoelectronic devices.^{3–5} The external and internal surfaces of ferritin are chemically and genetically modifiable allowing for the attach-

ment site for drugs, nucleic acids, fluorophores or magnetic moieties. Along this line, recent studies further established heavy (H) or light (L)-chain homopolymers as versatile multi-functional nanocarriers for targeted cancer diagnosis and therapy.^{6–10} In fact, human ferritins constitute biocompatible nanocarriers that stabilize and shelter the enclosed particles, thus preventing immunogenic responses. Moreover, ferritins are naturally targeted toward ubiquitously expressed TfR1 transferrin receptors (H-chain specific) or hepatic SCARA 5 receptors (L-chain specific). Such properties have been widely exploited for the efficient delivery of antitumor drugs to iron-avid, fast replicating, tumor cells overexpressing the TfR1 receptor.¹¹ Thus, ferritin based protein cages have been developed as versatile platforms for multiple applications in nanomedicine.

Current development of human ferritin based particle is however facing intrinsic limitations due to the experimental conditions linked to their assembly–disassembly equilibrium, whose control is a prerequisite in order to achieve encapsulation of the cargo within the internal cavity. In the conventional *in vitro* encapsulation procedures, ferritin must be disassembled at extreme pH values (pH = 2.0) and re-assembled in the presence of highly concentrated payload compounds.¹²

^aCenter for Life Nano Science@Sapienza, Istituto Italiano di Tecnologia, V.le Regina Elena 291, Rome 00161, Italy. E-mail: paola.baiocco@iit.it

^bMoltrion srl, via Ravenna 8, 00161 Rome, Italy

^cInstitute of Molecular Biology and Pathology, National Research Council, P.le A. Moro, 7, 00185, Rome, Italy

^dDepartment of Biochemical Sciences "Alessandro Rossi Panelli", Sapienza University of Rome, P.le A. Moro, 5, 00185, Rome, Italy

^eThe City University of New York Advanced Science Research Center 85 St. Nicholas Terrace, New York, NY 10031, USA

† Electronic supplementary information (ESI) available. See DOI: 10.1039/c6nr07129e

Such a procedure leads to a suboptimal load of cargo material, whose chemical structure is required to be pH resistant. Moreover, the pH jump procedure is only partially reversible and re-assembly may not be complete, depending on complex equilibrium and kinetic parameters.¹³ Currently, extensive research efforts are devoted to adjust the assembly properties of ferritin nanocages to the desired applications either by intersubunit interface mutagenesis¹⁴ or by genetic engineering of N- or C-terminal regions.¹⁵

Recently, novel ferritins from lower eukaryotes, bacteria and archaea, endowed with different polymer association–dissociation thermodynamic and kinetic features have emerged as possible alternatives to human ferritin homopolymers for several biotechnological applications requiring cargo material encapsulation.^{16,17} Despite low sequence similarity, these ferritins display a highly conserved quaternary structure consisting of a four-helix bundle namely A, B, C and D and a short E helix at the C-terminus. Helices B and C are connected by a 12 amino acid (aa) long loop involved in stabilizing interactions at the 2-fold dimer interface. Unlike most eukaryotic and prokaryotic ferritins, the archaeal ferritin from *Archaeoglobus fulgidus* (AfFt) is characterized by unique self-assembly properties. In fact, in neutral buffers it is present as dimeric species, easily combining into a non-canonical 24-mer cage in the presence of metal cations.¹⁸ AfFt assembles in a distinctive tetrahedral geometry as a result of particular packing between four hexameric units into a 24-mer structure different from those observed so far. Such unusual assembly results in the formation of four wide triangular pores (45 Å) on the protein shell.¹⁹ As demonstrated by Sana *et al.*,¹⁹ amino acid substitutions in the turn motif that connects D and E helices forming the 4-fold iron channels, namely K150A and R151A, are sufficient to restore the canonical octahedral symmetry observed in vertebrate and bacterial ferritins,^{18,19} thus providing a rationale for the atypical tetrahedral architecture of AfFt. Nevertheless, the low sequence similarity of AfFt with mammalian ferritins runs against the possibility of targeting AfFt onto the TfR1 receptors in mammalian cells.

Transferrin receptor TfR1, or CD71, has been reported to be a preferred target for human ferritin, due to the specific interaction of the receptor extracellular moiety with epitopes of the H-ferritin subunit.^{20,21} Inspection of the three-dimensional structure of the human H-homopolymer external surface indicates that the most significant accessible area is occupied by the external 12 aa long loop connecting B and C helices (up to 19 aa including the turn regions). Patches of a lesser extent exposed to solvent are formed by the N-terminal regions or by the iron channels within the threefold axis of the intersubunit assembly. However, it has been shown that N-terminal or C-terminal deleted human H-homopolymers are efficiently taken up by target cells, thus suggesting these regions are not required for receptor recognition or uptake.²² Therefore the BC loop, besides its structural role in stabilization of the interdimer interface,²³ appeared to be the best candidate for TfR1 receptor recognition of the ferritin molecule.

We decided then to engineer the archaeal ferritin to devise a chimeric construct, named humanized *Archaeoglobus* ferritin

(HumAfFt), in which the external 12 aa loop connecting the B and C helices was mutated to reproduce an analogous one in the corresponding region of the human H chain homopolymer (HuHF). It was observed that this chimeric protein (HumAfFt) was actively internalized by HeLa cells to an extent comparable to transferrin, the preferred ligand for TfR1.

Results and discussion

“Humanized” *Archaeoglobus* ferritin design

Heavy chain human ferritin and *Archaeoglobus* ferritin display 31% sequence identity. The structural alignment of HuHF and AfFt monomers (pdb code 3AJ0 and 1S3Q, respectively) reveals a shorter N-terminus and shorter loops between three of the four helices, with the notable exception of the long loop connecting B and C helices.

As shown in Fig. 1, the BC loops of two adjacent subunits run in an antiparallel fashion establishing significant, mutual interactions. Thus the BC loops of adjacent subunits display the same overall geometry in both HuHF and AfFt, though each couple of loops adopts a different symmetry along the spherical surface of the protein cage, given the different dimer–dimer positioning within each complete 24-mer structure.

In order to preserve the unique assembly properties of AfFt, while implementing a potential cellular uptake, we decided to exploit this external loop by mutating 9 residues into the corresponding residues found in HuHF, according to the sequence alignment shown in Fig. 2. In particular, the nine amino acids sequence IFLQDIKPP, typical of a human H ferritin homopolymer, located at the center of the 12 aa loop was inserted in place of VKLYAVEEP (from residue 70 to 79 in AfFt numbering, see Fig. 2). In addition, a cysteine residue in position 54 (AfFt numbering) has been introduced by point mutation in order to provide a conjugation site of potential thiol reactive derivatives into the cavity. As previously mentioned, we will refer to the chimeric protein described above as humanized *Archaeoglobus* ferritin (HumAfFt).

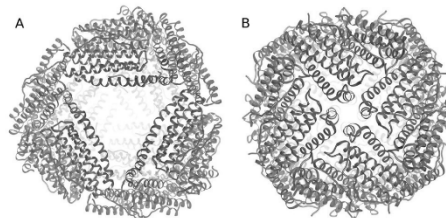


Fig. 1 Three-dimensional structures determined by X-ray crystallography. A cartoon representation of (A) HumAfFt and (B) HuHF (pdb code 3AJ0). Models are coloured in blue and green, respectively, and the external loop connecting the helices B and C of each monomer is shown as red ribbons. Molecular graphics were performed using a UCSF Chimera package.³⁵

ion is coordinated with both OE1 and OE2 of Glu19, (at 2.5 Å and 2.8 Å distance, respectively), with Glu52 (OE1) at 2.5 Å, with Gln129 (OE1) at 2.6 Å and with a water molecule at 2.6 Å distance. In the other chains, a water molecule has been modelled in the Fo–Fc map and successfully refined in the same position.

The loop region, including the conserved terminal turns, spans from amino acid 68 to amino acid 86. The sequence alignment and the structural superposition between HumAfFt and the human H-homopolymer, as well as between HumAfFt and AfFt, are shown in Fig. 2B and C. At the dimeric interface between the two antiparallel BC loops, the main interactions are a hydrogen bond between Arg69(NH2) and Ser80 (O) at 2.8 Å distance and two salt bridges, namely Lys71 (NZ)–Glu77 (OE1) at 3.0 Å distance and Glu81 (OE2)–Arg69 (NH1) at 2.7 Å distance. A weak salt bridge is established by Glu81 (OE2) and Arg69 (NH2), at a distance of 3.0 Å. The salt bridge between Lys71 and Glu77 observed in HuHF, is absent in HumAfFt since these positions were mutated into a phenylalanine (Phe71) and a lysine (Lys77). Other interactions are conserved between HuHF and HumAfFt and measured the same distances.

Cryo-electron microscopy confirms the canonical AfFt architecture in solution

Humanized AfFt samples were prepared in thin ice layer and analyzed by cryo-EM in order to assess the three-dimensional structure of the chimeric protein in a near-native environment. Particles were picked with a reference-based automated particle picking procedure. Single ferritin particles were visualized at a nominal resolution of 33 Å demonstrating that their shape and dimensions correspond to that of wild type AfFt in its 24-mer assembly (Fig. 3A). Moreover, the triangular apertures

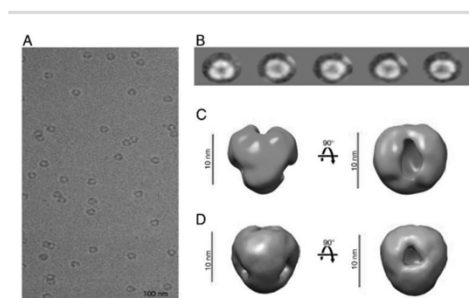


Fig. 3 Electron microscopy characterization of humanized *Archaeoglobus fulgidus* ferritin. (A) Sample micrograph of the HumAfFt data set. Scale bar: 100 nm. (B) Five representative 2D class averages obtained with RELION. (C) 3D reconstruction of HumAfFt obtained with RELION and visualized with UCSF Chimera³⁵. Map final resolution: 33.1 Å. Scale bars: 10 nm. Left: side view. Right: top view. (D) *Archaeoglobus fulgidus* ferritin crystal structure (from 16) filtered to 30 Å, shown for comparison. Scale bars: 10 nm. Left: side view. Right: top view.

on the protein surface were clearly observable in a bi-dimensional view (Fig. 3B) and better displayed in a three-dimensional reconstruction as shown in Fig. 3C.

Flow cytometry analysis shows HumAfFt cellular uptake

After we have demonstrated that our HumAfFt maintained its structure with large open pores and the self-assembly property characteristic of the original AfFt, we aimed to verify that the modified version also gained access to eukaryotic cancer cells such as HeLa cells. It is known that HuHF is recognized and internalized by the TfR1, which is overexpressed in many types of tumor cells but not in normal cells and healthy tissues.²¹ To validate the effect of our mutations on the external loop related to the uptake efficiency by HeLa cells, we performed time course experiments on cells treated with the same amount ($30 \mu\text{g ml}^{-1}$) of AfFt-FITC, HumAfFt-FITC and transferrin-FITC (Tf-FITC) and analyzed them by flow cytometry. As a baseline for FITC fluorescence, control cells not incubated with FITC-ferritins were used. Moreover, to exclude any signal generated from outside particles sticking on the cell membrane due to unspecific binding or remains from the washing steps, trypan blue quenching was performed before using FACS. In Fig. 4, the FACS analysis is summarized, shown as the percentage of cells internalizing the nanoparticles at different times. These data highlighted that HumAfFt nanoparticles are efficiently taken up by HeLa cells already after one hour incubation with a much higher percentage compared to AfFt (81% and 5% respectively). After a

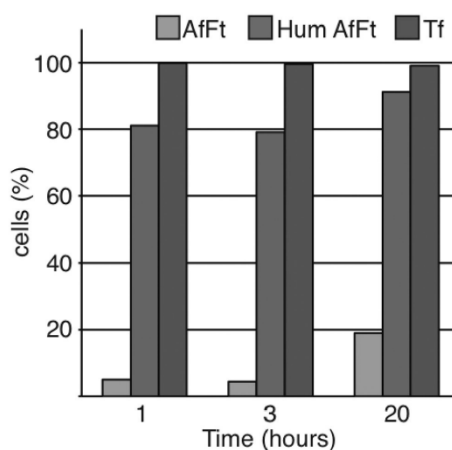


Fig. 4 Humanized AfFt is internalized with higher efficiency than the original ferritin. Ferritins taken up in HeLa cells have been quantified by flow cytometry. Cells have been treated with $30 \mu\text{g ml}^{-1}$ of AfFt-FITC, HumAfFt-FITC and transferrin-FITC (Tf). The percentage of cells internalizing the nanoparticles at the time indicated is shown. For each sample 30 000 events gated on live cells have been acquired.

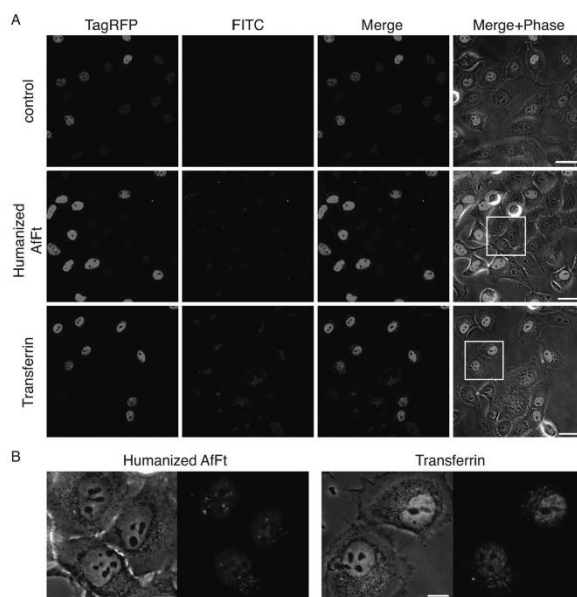


Fig. 5 Ferritin internalization observed at the confocal microscope. Cells were plated on an 8-well μ -slide (ibidi), induced with doxycycline to express TagRFP and then incubated with $30 \mu\text{g ml}^{-1}$ of humanized AfFt-FITC or transferrin-FITC for 20 h. After washing, cells were live-imaged using a confocal microscope. (A) Confocal images of live HeLa TagRFP cells are shown as single, merged channels and overlay images with the phase contrast. Scale bars: $40 \mu\text{m}$. (B) Images are a magnified view of the region highlighted by the white inset in panel A; merged channels and the overlay with the phase contrast images are shown. Scale bars: $10 \mu\text{m}$.

longer incubation time (20 hours), the FITC-positive cells for the humanized samples are increased to more than 90% whereas for native AfFt they are still less than 20%. The latter increment is possibly due to the unspecific uptake by pinocytosis. Each acquired plot is shown in Fig. S4.†

Moreover we performed the RNAi experiment against the transferrin receptor and analyzed the cellular uptake by FACS (Fig. S5†) obtaining around 50% HumAfFt uptake reduction after 48 hours of siRNA transfection, confirming the involvement of TfR1 in the internalization process.

Visualization of ferritin nanoparticles inside living cells by confocal microscopy

In order to visualize uptaken HumAfFt-FITC nanocages, we performed the internalization assay directly on an ibidi 8-well μ -slide and incubated the cells for 20 hours before confocal microscopy. We exploited the properties of the HeLa TagRFP cell lines available in the lab in order to have a reference fluorescence signal confirming that we were imaging inside the cell. This cell line contains a TagRFP-FUS protein under the control of a doxycycline-inducible promoter that allows for a controlled expression of the protein and hence permits visuali-

zation of the nucleus in the red channel. In this case the cells were not selected to eliminate the untransfected cells, allowing us to visualize different levels of expression and also unstained nuclei. Just before imaging, the cells were washed to eliminate the unbound FITC-nanoparticles and then acquired by confocal laser-scanning microscopy. Confocal representative images of the entire field of view of live HeLa TagRFP cells alone (control) or incubated with HumAfFt-FITC or TF-FITC are shown in Fig. 5A. A detailed view of the boxed region in panel A is shown in Fig. 5B. Images confirmed the high extent of HumAfFt internalization and highlight a cellular distribution in the cytoplasm and in the perinuclear space comparable to that observed in the case of transferrin, thus suggesting a typical clathrin-coated endocytosis pathway, mediated by TfR1.

Conclusion

The present data highlight the remarkable properties of a novel chimeric ferritin nanocage suitable for the design of efficient and versatile scaffolds for the intracellular delivery of bioactive small molecules and/or diagnostic probes.

Archaeoglobus fulgidus ferritin (AfFt) is a prominent example of this versatility due to its unique association/dissociation properties that lead to the presence of stable dimeric species at neutral pH and low ionic strength capable of associating into non-classical 24-mer species in the presence of either monovalent or divalent cations at physiological concentrations (*i.e.* higher than 0.5 M Na⁺ or 20 mM Mg²⁺). Moreover, AfFt also displays a unique subunit assembly, based on tetrahedral symmetry, which leads to the formation of four large openings in the protein shell. As such, AfFt represents a uniquely suitable scaffold for incorporating a wealth of diverse substructures inside the protein cavity, either by an assembly/disassembly process at neutral pH or by diffusion through the large triangular pores on the surface. Notable examples have been reported in recent literature.¹⁷ Nevertheless, one of the key properties of ferritin nanocages in biomedical applications is the possibility of targeting receptors on human cells, thus allowing the delivery of the desired payload within the cytoplasm. The engineered HumAfFt described here combines the versatility in assembly and cargo incorporation of AfFt by binding to TfR1 and by cellular uptake of HuHF. At present, further experiments with possible payloads for diagnostic or therapeutic applications are under development. However, *in vivo* applications will have to wait for the evaluation of possible immunological responses against non-human epitopes present on the protein surface. In fact, though the mutated loops appear to account for most of the solvent exposed surface, N-terminal and pore lining regions might still offer windows for non-self-recognition by the immune system.

Materials and methods

"Humanized" *Archaeoglobus* ferritin design

The gene encoding for a mutated ferritin from *Archaeoglobus fulgidus* was synthesised by GeneArt (ThermoFisher) and subcloned into a pET22b vector (Novagen) between the restriction sites NdeI and HindIII at 5' and 3' respectively. The recombinant plasmid was transformed into BL21(DE3) *E. coli* strain for protein expression.

Protein expression and purification

E. coli cells, containing the HumAfFt plasmid, were grown and induced with 1 mM IPTG (isopropyl- β -D-1-thiogalactopyranoside) at OD₆₀₀ = 0.6. Cells were harvested by centrifugation 3 hours post induction at 37 °C.

Cells harvested from 1 L culture were resuspended in 20 mM HEPES buffer, pH 7.5, containing 200 mM NaCl, 1 mM TCEP (tris(2-carboxyethyl)phosphine), and a cOmplete™ Mini Protease Inhibitor Cocktail Tablet (Roche). Cells were disrupted by sonication and the soluble fraction was purified by heat treatment at 78 °C for 10 minutes. Denatured *E. coli* proteins were removed by centrifugation at 15 000 rpm at 4 °C for 1 hour. The soluble protein was further purified by ammonium sulfate precipitation. The precipitated fraction at 70% ammonium sulfate was resuspended in 20 mM HEPES,

50 mM MgCl₂, pH 7.5 and dialyzed *versus* the same buffer. As a final purification step, the protein was loaded onto a HiLoad 26/600 Superdex 200 pg column previously equilibrated in the same buffer using an ÄKTA-Prime system (GE Healthcare). The purified protein was concentrated to obtain the final protein preparation of 1 mg mL⁻¹ and protein concentration was calculated by measuring the UV spectrum using an extinction coefficient of 32 400 M⁻¹ cm⁻¹. Protein yield was ~40 mg L⁻¹ culture.

Self-assembly assessment in solution

Size exclusion chromatography MgCl₂-mediated self-assembly was studied by size exclusion chromatography (SEC) using a Superdex 200 26/600 GL column (GE Healthcare). The molecular size of HumAfFt was determined under different conditions by comparing the elution volume with that of standard proteins. Composition of the mobile phase was 25 mM HEPES pH = 7.5 with different MgCl₂ concentrations accordingly to the composition of the protein buffer.

Crystallization and crystal structure determination

The purified protein was concentrated to 20 mg mL⁻¹ and initial crystallization screening was performed using a Phenix Robot. Crystals were obtained by mixing in a 2 μ L hanging drop 1 mM of the purified protein with a solution containing 22% (vol/vol) polyacrylic acid PAA, 0.1 M Tris, 0.02 M MgCl₂, pH 7.4, at 25 °C within a week, cryo-protected by increasing the precipitant concentration and flash-frozen in liquid nitrogen. Diffraction data have been collected at ID23-2 beamline at the European Synchrotron Radiation Facility (ESRF), Grenoble, France.

Data were processed with XDS²⁵ and scaled with Aimless (ccp4 suite) at a final resolution of 2.87 Å. The structure was solved by Molecular Replacement with MolRep (ccp4 suite) using the open pore structure AfFt (pdb code 1S3Q) as the search model. Model Building and refinement were done using Coot²⁶ and Refmac5, respectively. The final model was analyzed with PROCHECK²⁷ and Molprobit. The Ramachandran plot showed that 97.8% of residues are in preferred regions, 2.2% in allowed regions and no outlier is observed. The final atomic coordinates and structure factors were deposited with the PDB Data Bank (<http://www.rcsb.org>) with accession code: 5LS9. Complete data collection and refinement statistics are reported in Table S1.†

Cryo-Electron microscopy

Holey-gold grids were prepared as described by Russo and Passmore²⁹ from Quantifoil R1.2/1.3 (Quantifoil Micro Tools GmbH, Germany). 3 μ L of HumAfFt (12 μ M) was applied to the holey-gold grids after plasma cleaning with a mixture of H₂ and O₂. Grids were blotted for 4 seconds and vitrified by rapidly plunging into liquid ethane at -180 °C (ref. 30 and 31) with a Vitrobot (FEI).

Data acquisition was done using a FEI Titan Halo (FEI, Eindhoven) operating at 300 kV. Datasets were imaged with a Volta phase-plate (FEI, Eindhoven)³² and were collected with

the automated data collection system EPU (FEI, Eindhoven) at a nominal magnification of 59 000 \times on an FEI Ceta camera (FEI, Eindhoven) with a camera pixel size of 14 μm , corresponding to a calibrated pixel size of 1.49 \AA on the specimen scale and with a dose of 50 $\text{e}^{-}\text{\AA}^{-2}$.

Image processing. The particles were picked with the reference-based automated particle picking procedure implemented in RELION 1.3.^{33,34} CTF correction was not applied since the data were collected within 200 nm of focus and the first CTF zero crossing was well beyond the achievable resolution of the dataset. Those particles were subjected to 2D classification using RELION with $k = 100$ classes. Good particles were then subjected to 3D classification using RELION with the number of classes $K = 8$. Resulting classes were refined with the autorefine procedure in RELION.

Resolution estimation. Reported resolutions are based on the 'gold-standard' protocol with the FSC = 0.143 criterion using soft masks with an 8 pixel soft edge, and were corrected for the effects of the mask on the FSC curve using high-resolution noise substitution.³⁴

Maps were visualized using UCSF Chimera.³⁵

Cell line generation

The HeLa cell line stably expressing an inducible TagRFP-FUS protein (HeLaTagRFP) was generated by transfection with epB-Puro-TT-RFP-FUS wt plasmid and the piggyBac transposase vector. Plasmid construction is described in ref. 36.

Protein FITC labeling

HumAft, Aft and Olo-transferrin were labeled with fluorescein-isothiocyanide (FITC, ThermoFisher) according to the manufacturer's standard protocol. Briefly, 2 mg mL^{-1} of the purified protein was added with 10-fold molar excess of in protein storage buffer stirring for 2 hours at RT. The non-reacted dye was removed by gel filtration chromatography and the fluorescent dye to protein ratio was determined by UV-spectroscopy. LC-MS spectrometry measurements on HumAft-FITC confirmed that >60% of monomers are FITC labeled as reported in Fig. S6.†

Cell cultures and ferritin internalization

HeLa cells were grown at 37 $^{\circ}\text{C}$ in Eagle's MEM supplemented with 10% (v/v) FBS, Glutamax (Invitrogen) and penicillin-streptomycin solution (Sigma). When needed, the cells were induced with doxycycline 0.2 $\mu\text{g mL}^{-1}$. The internalization assay was performed as follows: after seeding the cells on the relevant substrate depending on the experiment, cells were left one day to attach and then incubated with FITC-ferritin nanoparticles (Aft-FITC, HumAft-FITC or Tf-FITC as specified in each experiment) at the final concentration of 30 $\mu\text{g mL}^{-1}$ for the time indicated (1 h, 3 h or 20 h).

Flow cytometry analysis

For flow cytometry analysis HeLa cells were seeded on multi-well plates. Cells were incubated with FITC-ferritin nanoparticles as described previously, then washed two times with

PBS, detached with trypsin-EDTA (Euroclone), washed with PBS and resuspended in BD-FACS flow buffer. Half of each sample was treated with Trypan Blue (TB; Sigma) to quench the FITC signal from membrane-bound nanoparticles that were not internalized. The quenching was performed with 0.04% TB for 10 min on ice. Control cells were treated in the same way but without FITC-ferritin incubation. Internalization of ferritins before and after TB treatments was measured at the BD LSFORTESSA (BD Biosciences, San Jose, CA, USA) equipped with a 488 nm laser and FACSDiva software (BD Biosciences version 6.1.3). Live cells were first gated by forward and side scatter area (FSC-A and SSC-A) plots, then detected in the green channel for FITC expression (530/30 nm filter) and side scatter parameter. The gate for the final detection was set in the control sample. Data were analyzed using FlowJo9.3.4 software (Tree Star, Ashland, OR, USA).

Confocal microscopy of live cells

To visualize ferritin internalization by live cells using a confocal microscope, HeLa TagRFP cells were seeded on a μ -slide 8-well ibiTreat (ibidi) and induced with 0.2 $\mu\text{g mL}^{-1}$ of doxycycline. Cells were then incubated with FITC-ferritin nanoparticles as previously described for 20 h and, before microscopy, cells were washed two times with an imaging medium (DMEM without phenol red, 10% FBS, 10 mM Hepes, Glutamax and penicillin-streptomycin solution) to eliminate the unbound FITC-nanoparticles. The confocal laser-scanning microscope used was an Olympus FV10i platform equipped with a built-in incubator. Images were acquired with a 60 \times /1.2NA water-immersion objective, LD lasers, 473 nm and 559 nm, and filter sets for FITC and TRITC. Phase-contrast images were acquired simultaneously.

Acknowledgements

We thank Alessandro Rosa and Riccardo De Santis for the HeLa TagRFP cell line. EU H₂₀₂₀ Project "X-Probe", Grant No. 637295, to A. B. and M. C. T. is gratefully acknowledged. Flagship Project "Nanomax" to A. B. is acknowledged. Regional project FILAS to B. V. is also acknowledged.

References

- 1 E. C. Theil, Ferritin protein nanocages use ion channels, catalytic sites, and nucleation channels to manage iron/oxygen chemistry, *Curr. Opin. Chem. Biol.*, 2011, **15**, 304–311.
- 2 L. Schoonen and J. C. van Hest, Functionalization of protein-based nanocages for drug delivery applications, *Nanoscale*, 2014, **6**, 7124–7141.
- 3 A. Prastaro, P. Ceci, E. Chiancone, A. Boffi, G. Fabrizi and S. Cacchi, Homocoupling of arylboronic acids and potassium aryltrifluoroborates catalyzed by protein-stabilized

- palladium nanoparticles under air in water, *Tetrahedron Lett.*, 2010, **51**, 2550.
- 4 F. Meng, B. Sana, Y. Li, Y. Liu, S. Lim and X. Chen, Bioengineered tunable memristor based on protein nanocage, *Small*, 2014, **10**, 277–283.
 - 5 M. A. Kostiainen, P. Hiekkataipale, A. Laiho, V. Lemieux, J. Seitsonen, J. Ruokolainen and P. Ceci, Electrostatic assembly of binary nanoparticle superlattices using protein cages, *Nat. Nanotechnol.*, 2013, **8**, 52–56.
 - 6 M. Liang, K. Fan, M. Zhou, D. Duan, J. Zheng, D. Yang, J. Feng and X. Yan, H-ferritin-nanocaged doxorubicin nanoparticles specifically target and kill tumors with a single-dose injection, *Proc. Natl. Acad. Sci. U. S. A.*, 2014, **111**, 14900–14905.
 - 7 L. Vannucci, E. Falvo, C. M. Failla, M. Carbo, M. Fornara, R. Canese, S. Cecchetti, L. Rajsiglova, D. Stakheev, J. Krizan, A. Boffi, G. Carpinelli, V. Morea and P. Ceci, In Vivo Targeting of Cutaneous Melanoma Using an Melanoma Stimulating Hormone-Engineered Human Protein Cage with Fluorophore and Magnetic Resonance Imaging Tracers, *J. Biomed. Nanotechnol.*, 2015, **11**, 81–92.
 - 8 E. Falvo, E. Tremante, R. Fraioli, C. Leonetti, C. Zamparelli, A. Boffi, V. Morea, P. Ceci and P. Giacomini, Antibody-drug conjugates: targeting melanoma with cisplatin encapsulated in protein-cage nanoparticles based on human ferritin, *Nanoscale*, 2013, **5**, 12278–12285.
 - 9 L. Vannucci, E. Falvo, M. Fornara, P. Di Micco, O. Benada, J. Krizan, J. Svoboda, K. Hulikova-Capkova, V. Morea, A. Boffi and P. Ceci, Selective targeting of melanoma by PEG-masked protein-based multifunctional nanoparticles, *Int. J. Nanomed.*, 2012, **7**, 1489–1509.
 - 10 S. Geninatti Crich, M. Cadenazzi, S. Lanzardo, L. Conti, R. Ruiu, D. Alberti, F. Cavallo, J. C. Cutrin and S. Aime, Targeting ferritin receptors for the selective delivery of imaging and therapeutic agents to breast cancer cells, *Nanoscale*, 2015, **7**, 6527–6533.
 - 11 K. Fan, C. Cao, Y. Pan, D. Lu, D. Yang, J. Feng, L. Song, M. Liang and X. Yan, Magnetoferritin nanoparticles for targeting and visualizing tumour tissues, *Nat. Nanotechnol.*, 2012, **7**, 459–464.
 - 12 Z. Zhen, W. Tang, T. Todd and J. Xie, Ferritins as nanoplat-forms for imaging and drug delivery, *Expert Opin. Drug Delivery*, 2014, **11**, 1913–1922.
 - 13 K. Mihee, R. Yecheol, S. J. Kyeong, A. Byungcheol, J. Sungmin, K. Heesoo and R. Moonhor, pH-dependent structures of ferritin and apoferritin in solution: disassembly and reassembly, *Biomacromolecules*, 2011, **12**, 1629–1640.
 - 14 H. Chen, S. Zhang, C. Xu and G. Zhao, Engineering protein interfaces yields ferritin disassembly and reassembly under benign experimental conditions, *Chem. Commun.*, 2016, **52**, 7402–7405.
 - 15 S. Kim, J. O. Jeon, E. Jun, J. Jee, H. K. Jung, B. H. Lee, I. S. Kim and S. Kim, Designing Peptide Bunches on Nanocage for Bispecific or Superaffinity Targeting, *Biomacromolecules*, 2016, **17**, 1150–1159.
 - 16 A. M. Sevcenco, M. Paravidino, J. S. Vrouwenvelder, H. T. Wolterbeek, M. C. van Loosdrecht and W. R. Hagen, Phosphate and arsenate removal efficiency by thermostable ferritinenzyme from *Pyrococcus furiosus* using radio-isotopes, *Water Res.*, 2015, **76**, 181–186.
 - 17 B. Sana, E. Johnson and S. Lim, The unique self-assembly/disassembly property of *Archaeoglobus fulgidus* ferritin and its implications on molecular release from the protein cage, *Biochim. Biophys. Acta*, 2015, **1850**, 2544–2551.
 - 18 E. Johnson, D. Cascio, M. R. Sawaya, M. Gingery and I. Schröder, Crystal structures of a tetrahedral open pore ferritin from the hyperthermophilic archaeon *Archaeoglobus fulgidus*, *Structure*, 2005, **13**, 637–648.
 - 19 B. Sana, E. Johnson, P. Le Magueres, A. Criswell, D. Cascio and S. Lim, The role of nonconserved residues of *Archaeoglobus fulgidus* ferritin on its unique structure and biophysical properties, *J. Biol. Chem.*, 2013, **288**, 32663–32672.
 - 20 Z. Heger, S. Skalickova, O. Zitka, V. Adam and R. Kizek, Apoferritin applications in nanomedicine, *Nanomedicine*, 2014, **9**, 2233–2245.
 - 21 L. Li, C. J. Fang, J. C. Ryan, E. C. Niemi, J. A. Lebrón, P. J. Björkman, H. Arase, F. M. Torti, S. V. Torti, M. C. Nakamura and W. E. Seaman, Binding and uptake of H-ferritin are mediated by human transferrin receptor-1, *Proc. Natl. Acad. Sci. U. S. A.*, 2010, **107**, 3505–3510.
 - 22 S. Levi, A. Luzzago, G. Cesareni, A. Cozzi, F. Franceschinelli, A. Albertini and P. Arosio, Mechanism of ferritin iron uptake: activity of the H-chain and deletion mapping of the ferro-oxidase site. A study of iron uptake and ferroxidase activity of human liver, recombinant H-chain ferritins, and of two H-chain deletion mutants, *J. Biol. Chem.*, 1988, **263**, 18086–18092.
 - 23 C. Bernacchioni, V. Ghini, C. Pozzi, F. Di Pisa, E. C. Theil and P. Turano, Loop electrostatics modulates the inter-subunit interactions in ferritin, *ACS Chem. Biol.*, 2014, **9**, 2517–2525.
 - 24 L. Calisti, I. Benni, M. Cardoso Trabuco, P. Baiocco, B. Ruzicka, A. Boffi, E. Falvo, F. Malatesta and A. Bonamore, Probing bulky ligand entry in engineered archaeal ferritins, *Biochim. Biophys. Acta*, 2016, DOI: 10.1016, [Epub ahead of print].
 - 25 W. Kabsch, Integration, scaling, space-group assignment and post-refinement, *Acta Crystallogr., Sect. D: Biol. Crystallogr.*, 2010, **66**, 133–144.
 - 26 P. Emsley and K. Cowtan, Coot: model-building tools for molecular graphics, *Acta Crystallogr., Sect. D: Biol. Crystallogr.*, 2004, **60**, 2126–2132.
 - 27 R. A. Laskowski, M. W. MacArthur, D. S. Moss and J. M. Thornton, PROCHECK - a program to check the stereochemical quality of protein structures, *J. Appl. Crystallogr.*, 1993, **26**, 283–29125.
 - 28 V. B. Chen, W. B. Arendall 3rd, J. J. Headd, D. A. Keedy, R. M. Immormino, G. J. Kapral, L. W. Murray, J. S. Richardson and D. C. Richardson, MolProbity: all-atom structure validation for macromolecular crystallo-

- graphy, *Acta Crystallogr., Sect. D: Biol. Crystallogr.*, 2010, **66**, 12–21.
- 29 C. J. Russo and L. A. Passmore, Ultrastable gold substrates for electron cryomicroscopy, *Science*, 2014, **346**, 1377–1380.
- 30 J. Dubochet, M. Adrian, J. J. Chang, J. C. Homo, J. Lepault, A. W. McDowell and P. Schultz, Cryo-electron microscopy of vitrified specimens, *Q. Rev. Biophys.*, 1988, **21**, 129–228.
- 31 T. Wagenknecht, R. Grassucci and J. Frank, Electron microscopy and computer image averaging of ice-embedded large ribosomal subunits from *Escherichia coli*, *J. Mol. Biol.*, 1988, **199**, 137–147.
- 32 R. Danev, B. Buijsse, M. Khoshouei, J. M. Plitzko and W. Baumeister, Volta potential phase plate for in-focus phase contrast transmission electron microscopy, *Proc. Natl. Acad. Sci. U. S. A.*, 2014, **111**, 15635–15640.
- 33 S. H. W. Scheres, Semi-automated selection of cryo-EM particles in RELION-1.3, *J. Struct. Biol.*, 2015, **189**, 114–122.
- 34 S. Chen, G. McMullan, A. R. Faruqi, G. N. Murshudov, J. M. Short, S. H. Scheres and R. Henderson, High-resolution noise substitution to measure overfitting and validate resolution in 3D structure determination by single particle electron cryomicroscopy, *Ultramicroscopy*, 2013, **135**, 24–35.
- 35 E. F. Pettersen, T. D. Goddard, C. C. Huang, G. S. Couch, D. M. Greenblatt and E. C. Meng, Ferrin TE. UCSF Chimera—a visualization system for exploratory research and analysis, *J. Comput. Chem.*, 2004, **25**, 1605–1612.
- 36 M. Morlando, S. Dini Modigliani, G. Torrelli, A. Rosa, V. Di Carlo, E. Caffarelli and I. Bozzoni, FUS stimulates microRNA biogenesis by facilitating co-transcriptional Drosha recruitment, *EMBO J.*, 2012, **31**, 4502.
- 37 X. Robert and P. Gouet, Deciphering key features in protein structures with the new ENDscript server, *Nucleic Acids Res.*, 2014, **42**, 320–324.



Cite this: DOI: 10.1039/c7ob00220c

Optimisation of the dibromomaleimide (DBM) platform for native antibody conjugation by accelerated post-conjugation hydrolysis†

Maurício Moraes, João P. M. Nunes, Kersti Karu, Nafsika Forte, Irene Benni, Mark E. B. Smith, Stephen Caddick, Vijay Chudasama* and James R. Baker*

Disulfide bridging offers a convenient approach to generate site-selective antibody conjugates from native antibodies. To optimise the reagents available to achieve this strategy, we describe here the use of dibromomaleimides designed to undergo accelerated post-conjugation hydrolysis. Conjugation and hydrolysis, which serve to 'lock' the conjugates as robustly stable maleamic acids, is achieved in just over 1 h. This dramatic acceleration is also shown to infer significant improvements in homogeneity, as demonstrated by mass spectrometry analysis.

Received 27th January 2017.

Accepted 3rd March 2017

DOI: 10.1039/c7ob00220c

rsc.li/obc

Introduction

Antibody bioconjugation is a key technological challenge in chemical biology, enabling a broad range of applications from targeted therapeutics (e.g. antibody–drug conjugates; ADCs) to radioimmunoconjugates and immunoassays.¹ Conjugation to antibodies is most readily achieved by exploiting the reactivity of lysine and cysteine residues to specific electrophilic reagents. There are >80 lysine residues in a typical antibody, and it has been estimated for ADCs that an average loading of 3–4 drugs per antibody leads to around 10⁶ molecular species present in the resulting heterogeneous conjugates.² The use of such complex mixtures in therapeutics is far from optimal, as each component will have a different pharmacological profile.^{2b,3} An alternative strategy is to release cysteine residues as sites for attachment by reduction of the interchain disulfide bonds, of which there are four in the major therapeutically relevant isotype (IgG1). Loading each of the cysteines with a reactive reagent, most commonly achieved using classical maleimides, still affords a heterogeneous mixture of products with drug-to-antibody ratios (DARs) of 0, 2, 4, 6 and 8 as the major components.⁴ The higher loaded species present have been identified as having reduced stability,⁵ and poorer outcomes *in vivo* due to their accelerated clearance.^{4,6}

There is significant evidence that increased homogeneity in conjugates will afford improved therapeutic windows,^{2b,6,7} and thus approaches for site-selective conjugation are gaining

momentum and can be expected to form a key component of future generations of ADCs.⁸ These include the use of genetic engineering to incorporate cysteine mutants, non-natural amino-acids or enzymatic recognition sequences as handles for controlled drug loading.^{7a,8,9} Site-selective methods which avoid this requirement for engineering can offer the further advantage of being directly applicable to native antibodies. To this end disulfide bridging is a highly promising strategy, in which the interchain disulfide bonds are targeted with reagents which reconnect the two cysteine residues.^{8b,10} This approach aims to generate antibody conjugates with a controlled loading of one drug per disulfide bond, and thus a DAR of 4 in IgG1s.

We have recently described the use of a class of modified maleimide reagents, known as next generation maleimides (NGMs),¹¹ which are able to achieve efficient disulfide bridging and thus represent a platform for site-selective ADC development (Fig. 1).¹² We have shown that dithiophenolmaleimide-monomethyl auristatin E (DTPM–MMAE) reagents can afford ADCs which offer potent and selective tumor cell killing activity *in vitro*^{12d} and *in vivo*.¹³ In addition to affording access to a narrow range of DAR species, with an average close to

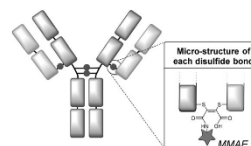


Fig. 1 NGM–ADC conjugates constructed by disulfide bridging.^{12d}

Department of Chemistry, UCL, 20 Gordon St, London, UK WC1H 0AJ.

E-mail: j.r.baker@ucl.ac.uk, v.chudasama@ucl.ac.uk

† Electronic supplementary information (ESI) available. See DOI: 10.1039/c7ob00220c

four, the NGMs provide a route to serum stable conjugates. This is achieved by hydrolysis of the maleimide ring to 'lock' the products as maleamic acids (see the structure shown in Fig. 1).^{12d}

Jackson *et al.* have also applied alternative NGMs, dibromomaleimides (DBMs), to generate analogous ADCs using MMAF as the payload, and have confirmed that the resultant ADCs offer improved *in vivo* efficacy compared to classical maleimide conjugates.¹⁴ Notably no hydrolysis step is included in this DBM-MMAF conjugation, and the resultant conjugates can be expected to cleave over several days in serum due to thiol exchange reactions.^{12d}

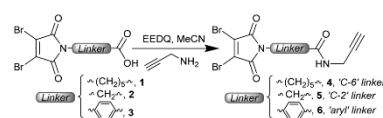
These approaches to NGM-ADCs, whilst highly promising, require optimisation. Post-conjugation hydrolysis is key to ensure robust serum stability, to prevent the loss of free drug leading to off-site toxicity; however the current prolonged conditions described, 72 h at pH 8.4,^{12d} are sub-optimal. This will serve to increase process times for downstream product development and can even introduce undesirable heterogeneity as shown herein. In this work we describe an investigation into accelerated hydrolysis, by means of linker design and conjugation conditions, and show that a dramatic increase in the rate of the reaction sequence is facilitated along with improved homogeneity. Whilst this optimisation is carried out in the context of ADCs, it also has implications on the design of NGM reagents for bioconjugation more widely, as these reagents are finding increasing application on diverse scaffolds ranging from peptides and proteins to polymers and surfaces.¹⁵

Results and discussion

Dibromomaleimide (DBM) reagent selection and synthesis

We chose to employ DBMs, which represent the simplest and most accessible disulfide bridging reagents, with varying linkers attached to the maleimide nitrogen. By varying from the C-6 (caproyl) linker which has been used in previous work to a C-2 (glycine derived) or an aryl linker, we expected to effect an increase in the rate of hydrolysis (due to increased electron withdrawal from the imide).¹⁶ Previous work has shown that aryl linkers on classical maleimides and DTPMs afford antibody conjugates which undergo accelerated hydrolysis.^{12c,17}

The synthesis of DBM reagents is commonly achieved by treatment of dibromomaleic anhydride (or commercially available diacid¹⁸) with an amine, refluxing in acetic acid to induce ring closure. Alternatively, an *N*-methoxy carbonyl activated DBM can be employed when a milder, room temperature, approach is required.¹⁹ Here we favoured a different strategy, in which the linker was pre-installed with the DBM, and an appended carboxylic acid could then be coupled with an amine. Notably the use of an NHS ester (comparable to ubiquitously employed heterobifunctional maleimide reagents) led to competing attack on the DBM to generate aminomaleimides. This highlights the increased electrophilicity of these substituted maleimides. To overcome this, a more active acylating agent is required, which can be achieved by the use of an



Scheme 1 Synthesis of dibromomaleimide reagents 4–6 with C-6, C-2 and aryl linkers.

EEDQ coupling (Scheme 1). Using readily synthesised acids **1–3** (see the ESI†) this strategy gave access to three model reagents **4–6**, incorporating an alkyne handle suitable for subsequent functionalisation if desired.

LC-MS validation and propensity of IgG1 to form disulfide isomers

We chose clinically relevant IgG1 trastuzumab²⁰ as a model antibody for our conjugation study, and sought to evaluate the LC-MS method that would be crucial to assessing the homogeneity of the conjugates. Trastuzumab was thus deglycosylated using PNGase F, and analysed by capillary electrospray ionisation on a Q-TOF LC-MS. The result was a single main species, corresponding to the deglycosylated full antibody (Fig. 2A, see the ESI† for raw data). Upon reduction with TCEP free heavy and light chains are observed (Fig. 2B), due to the denaturing conditions of the LC-MS. Finally we reoxidised this sample, using Ellman's reagent, to represent a control for the data that could be expected upon reformation of the covalent attachments between the chains (Fig. 2C). Intriguingly, whilst reoxidation was highly efficient, the product was formed as

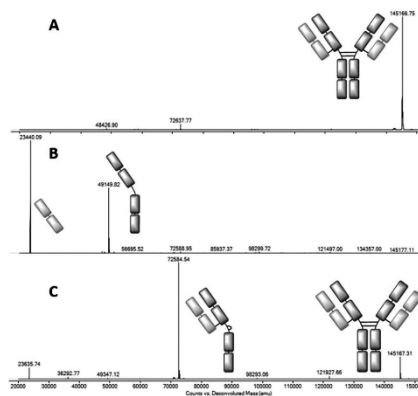


Fig. 2 Deconvoluted LC-MS data on: A – trastuzumab (mass observed 145 167, expected 145 167); B – reduced trastuzumab (mass observed 23 440 and 49 150, expected 23 440 and 49 150); C – reoxidised trastuzumab using Ellman's reagent (observed 72 585 and 145 167, expected 72 584 and 145 167).

two isomers; the full antibody (minor) and the 'half-antibody' (major). This half-antibody is simply the product in which the disulfides in the hinge region of the antibody have reformed in an intrachain, rather than interchain fashion, and is thus observed by the denaturing LC-MS method. This competitive inter- and intramolecular reactivity matches the outcome of disulfide bridging reagents^{12c,14} and suggests that IgG1s are susceptible to such disulfide scrambling. It should be noted that oxidation under other conditions, such as dehydroascorbic acid,²¹ is known to generate the native disulfide configuration. We postulate that the difference is due to Ellman's reagent's high reactivity, trapping the intrachain connectivity as a kinetic outcome. Indeed treatment of the isomeric mixture with an alkyl thiol (cysteamine, 10 equiv.) re-equilibrates the system to generate the native connectivity (ESI Fig. S8†).

Conjugation of DBM-linker reagents 4–6 with optimisation

This initial MS data served as a benchmark for our conjugation experiments. Thus trastuzumab was reduced with TCEP and treated with DBM reagent 4, which contains the C-6 linker and is expected to hydrolyse slowly post-conjugation. The LC-MS analysis (Fig. 3A) revealed that the conjugate was a mixture of species – the major components being the half antibody (with two attached NGM linkers), and non-crosslinked light and heavy chains. A closer inspection of the light chain mass reveals that the major species (23 361 Da) has undergone a decarboxylative cleavage of the C-terminal cysteine. This reaction, which has previously been observed to occur on trastuzumab-thiomaleimide conjugates under photochemical conditions,²² occurs even if light is excluded.

To preclude this undesirable heterogeneity, we proposed that rapid hydrolysis post-conjugation would be beneficial as it would remove the reactive dithiomaleimide functional group from the conjugate. Indeed the use of the C-2 and aryl linker (4 and 5) avoided this competing decarboxylative side-reaction, generating much improved homogeneity (ESI Fig. S11 and S13†). An additional improvement was achieved by switching the pH from 8.0 to 8.5, to further accelerate hydrolysis (Fig. 3B and C).

For both linkers the LC-MS data confirm that two isomeric products are formed almost exclusively, with one containing inter-heavy chain bridges and the other intrachain bridges; both represent antibody conjugates loaded with 4 DBMs. The raw data (see the ESI†) also give further insights, confirming this major improvement in homogeneity and showing that the half-antibody conjugate envelope (1400–2200 *m/z*) and the full antibody conjugate envelope (2600–3400 *m/z*) approach a 1 : 1 ratio in the optimised conjugates. SDS-PAGE analysis (ESI Fig. S2 and S3†) further confirms this improvement in homogeneity, and indicates that the full antibody conjugate now represents the major species. Overall these data reveal that these accelerated hydrolysis DBM reagents offer efficient and highly homogeneous conjugation with a loading of 4. Notably the LC-MS profile is similar to that obtained from the Ellman's reoxidation (Fig. 1C), indicating that the DBM bridging offers a comparably efficient mode of reactivity to disulfide reformation.

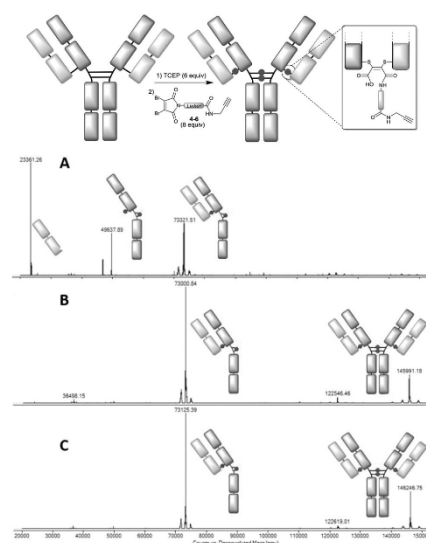


Fig. 3 Deconvoluted LC-MS data on the trastuzumab-NGM conjugates: A – using DBM-C₆-alkyne 4 at pH 8.0 (mass observed 73 119* and 73 322, expected 73 117); B – using DBM-C₂-alkyne 5 at pH 8.5 (mass observed 73 001 and 145 991, expected 73 005 and 146 008); C – using DBM-aryl-alkyne 6 at pH 8.5 (mass observed 73 125 and 146 247, expected 73 125 and 146 249). *See the ESI† for the expanded region in LC-MS.

Rate of hydrolysis post-conjugation

To investigate the rate of hydrolysis of these conjugates we exploited the convenient absorbance of the dithiomaleimides at ~400 nm²³ which is lost upon conversion to the corresponding maleamic acid (see the ESI†). The kinetic data at pH 8.5 confirm the dramatic acceleration inferred by the C-2 and aryl linkers (Fig. 4); the hydrolysis half-lives of 16–19 min (*cf.* 48 h for C-6 linker) are comparable to classical maleimides containing aryl linkers.¹⁷ These data confirmed that the conjugates using C-2 and aryl linkers are almost completely hydrolysed in an hour.

Rapid hydrolysis of DBM reagents

Given the acceleration in hydrolysis afforded the dithiomaleimide bridges by the electron withdrawing linkers, we were intrigued to compare the hydrolytic lability of the dibromomaleimide reagents themselves. Using a similar approach, we monitored the disappearance of absorbance associated with dibromomaleimide; in this case at 325 nm. The C-2 and C-6 linkers (reagents 4 and 5) were selected for the study, as they offered clearly distinguishable absorbances at this wavelength, which are again lost upon hydrolysis to generate the maleamic acids (see the ESI†). Intriguingly the dibromomaleimides were

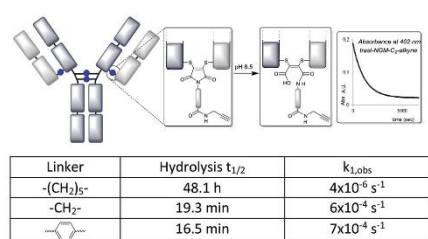


Fig. 4 Hydrolysis of antibody conjugates monitored by disappearance of dithiomaleimide absorbance ($\lambda_{max} = 402\text{--}406 \text{ nm}$).

found to hydrolyse extremely rapidly, with a half-life of under a minute for the C-2 linker, even at the slightly lower pH of 8.0 (Fig. 5). This reveals that bromines serve to further activate the imide to hydrolysis, through inductive electron-withdrawal. For comparison, dithiophenolmaleimides were found to hydrolyse much more slowly ($t_{1/2} = 30\text{--}60 \text{ min}$, ESI Fig. S25†), again highlighting the tuneable reactivity of NGMs.

The significance of this rapid reagent hydrolysis is that the DBM reagents must conjugate at sub-1 min timescales to affect efficient conjugation, which is clearly the case in the antibody conjugations reported herein. Indeed this is confirmed by the UV analysis of the conjugation, which reveals the maximum dithiomaleimide absorbance to be observed immediately upon taking the first reading (<1 min). It is also notable that any unreacted DBM reagent post-conjugation will be rapidly deactivated by hydrolysis. This suggests that there is unlikely to be any requirement to remove excess reagent post-conjugation. Indeed we trialled a one-pot conjugation and hydrolysis in 1 h using reagents 4 and 5, and found that the outcome by LC-MS was unchanged, efficient conjugation to generate DAR 4 conjugates.

Maleamic acid stability of C-2 and aryl linkers at low pH

Having previously shown that maleamic acid conjugates are robustly stable in serum,^{12d} we focused here on further profiling their known susceptibility to cleave at low pH.^{12a} We were keen to compare the C-2 and aryl linkers described in this work, in case the nature of the linker affected the rate of cleavage, and as a result the stability of the conjugates. Thus Alexa Fluor 488@

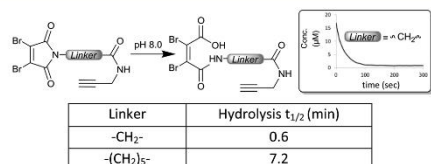


Fig. 5 Hydrolysis of the DBM reagents 4 and 5 monitored by the loss of absorbance at 325 nm.

was attached by a CuAAC reaction onto the pendant alkynes^{12d} and the conjugates monitored over 24 h by fluorescence SEC-HPLC (Fig. 6). We chose to compare pH 7.4 which would approximate the pH in circulation, with pH 5.5 representing acidic conditions approximating endosomal pH²⁴ (and thus the most acidic conditions a recycling antibody is likely to experience, prior to lysosomal degradation). The conjugates with C-2 and aryl linkers showed complete stability at pH 7.4 (even up to 10 days, see ESI Fig. S32†), whilst only the N-aryl conjugate showed a hint of cleavage at pH 5.5. Overall it can be summarised that maleamic acid antibody conjugates with various linkers will have robust stability in circulation *in vivo*.

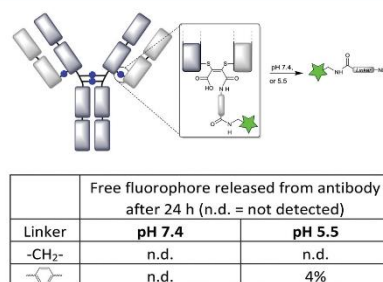


Fig. 6 Stability of the maleamic acid conjugates with C-2 and aryl linkers tested at pH 7.4 and 5.5, measured by fluorescence SEC-HPLC (see the ESI† for traces).

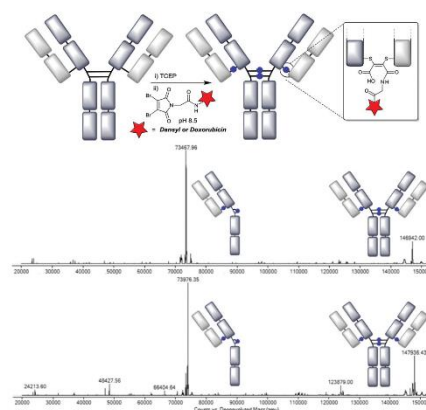


Fig. 7 Deconvoluted LC-MS data on the trastuzumab-NGM conjugates: A – using DBM-C₂-dansyl (mass observed 73 468 and 146 942, expected 73 480 and 146 959); C – using DBM-C₂-doxorubicin (mass observed 73 976 and 147 936, expected 73 980 and 147 959).

Functional DBM conjugation using optimised linkers and protocols

With improved linkers in hand, and robust stability further demonstrated, we constructed functionalised antibody conjugates using the optimised conditions. The C-2 linker was selected to avoid the unnecessary incorporation of extra hydrophobicity by an aryl ring, whilst dansyl and doxorubicin were chosen as a model fluorophore and drug respectively. The conjugations were carried out using the optimised protocol established, 5 min conjugation at pH 8.5 with a further 1 h for hydrolysis. The LC-MS analysis revealed that the two isomeric DAR 4 species were again successfully generated (Fig. 7). This was also consistent with the UV read-out for the doxorubicin conjugate, which indicated a DAR of 4.1.

Conclusions

Dibromomaleimides with electron-withdrawing C-2 linkers are demonstrated to offer an optimised bioconjugation platform for the construction of highly homogeneous and robustly stable antibody conjugates from native antibodies. These reagents enable a protocol which takes just over 1 hour for conjugation and 'locking' by hydrolysis, to generate an antibody loaded with a DAR of 4. This represents a substantial improvement in the 72 h protocol previously described for NGM reagents. By the combined use of these 'fast-hydrolysing' linkers and a pH of 8.5, we also show that improved homogeneity is inferred on the conjugates. This is due to the rapid hydrolysis of the dithiomaleimide bridges preventing undesired side-reactions, such as C-terminal decarboxylation of the light chain. It is notable that antibodies themselves are stable to such short exposure to alkaline conditions. Indeed they have been reported to only undergo degradation, by partial asparagine deamidation, under much harsher conditions (pH 9.2, 45 °C, 48 h), and even then full binding and structural integrity is retained.²⁵

Whilst other reports in the literature have focused on succinimide hydrolysis as a means to improve the stability of classical maleimide conjugates from native antibodies, the corresponding ADCs remain a heterogeneous mixture. The DBM technology combines stabilisation through hydrolysis with a significant improvement in homogeneity and controlled drug loading delivered by disulfide bridging, as demonstrated by LC-MS characterisation. We suggest that these readily available DBM reagents offer a convenient approach to antibody bioconjugation more widely, and can also be applicable to other peptide, protein and polymer scaffolds.

Acknowledgements

The authors gratefully acknowledge BBSRC, BRC, HEFCE, and EPSRC for funding. We also acknowledge Prof. Erik Arstad and Dr Kerstin Sanders for assistance with the fluorescence

SEC-HPLC and EPSRC UK National Mass Spectrometry Facility (NMSF), Swansea.

Notes and references

- (a) J. R. Adair, P. W. Howard, J. A. Hartley, D. G. Williams and K. A. Chester, *Expert Opin. Biol. Ther.*, 2012, **12**, 1191–1206; (b) A. M. Wu, *Methods*, 2014, **65**, 139–147.
- (a) L. T. Wang, G. Amphlett, W. A. Blattler, J. M. Lambert and W. Zhang, *Protein Sci.*, 2005, **14**, 2436–2446; (b) J. R. Junutula, H. Raab, S. Clark, S. Bhakta, D. D. Leipold, S. Weir, Y. Chen, M. Simpson, S. P. Tsai, M. S. Dennis, Y. M. Lu, Y. G. Meng, C. Ng, J. H. Yang, C. C. Lee, E. Duenas, J. Gorrell, V. Katta, A. Kim, K. McDorman, K. Flagella, R. Venook, S. Ross, S. D. Spencer, W. L. Wong, H. B. Lowman, R. Vandlen, M. X. Sliwkowski, R. H. Scheller, P. Polakis and W. Mallet, *Nat. Biotechnol.*, 2008, **26**, 925–932.
- J. R. Junutula, K. M. Flagella, R. A. Graham, K. L. Parsons, E. Ha, H. Raab, S. Bhakta, T. Nguyen, D. L. Dugger, G. M. Li, E. Mai, G. D. L. Phillips, H. Hiranagi, R. N. Fujii, J. Tibbitts, R. Vandlen, S. D. Spencer, R. H. Scheller, P. Polakis and M. X. Sliwkowski, *Clin. Cancer Res.*, 2010, **16**, 4769–4778.
- K. J. Hamblett, P. D. Senter, D. F. Chace, M. M. C. Sun, J. Lenox, C. G. Cervený, K. M. Kissler, S. X. Bernhardt, A. K. Kopcha, R. F. Zabinski, D. L. Meyer and J. A. Francisco, *Clin. Cancer Res.*, 2004, **10**, 7063–7070.
- (a) N. S. Beckley, K. P. Lazzareschi, H. W. Chih, V. K. Sharma and H. L. Flores, *Bioconjugate Chem.*, 2013, **24**, 1674–1683; (b) Y. T. Adem, K. A. Schwarz, E. Duenas, T. W. Patapoff, W. J. Galush and O. Esue, *Bioconjugate Chem.*, 2014, **25**, 656–664.
- C. A. Boswell, E. E. Mundo, C. Zhang, D. Bumbaca, N. R. Valle, K. R. Kozak, A. Fourie, J. Chuh, N. Koppada, O. Saad, H. Gill, B. Q. Shen, B. Rubinfeld, J. Tibbitts, S. Kaur, F. P. Theil, P. J. Fielder, L. A. Khawli and K. Lin, *Bioconjugate Chem.*, 2011, **22**, 1994–2004.
- (a) P. Denner, E. Fischer and R. Schibli, *Antibodies*, 2015, **4**, 197–224; (b) D. Jackson, J. Atkinson, C. I. Guevara, C. Y. Zhang, V. Kery, S. J. Moon, C. Virata, P. Yang, C. Lowe, J. Pinkstaff, H. Cho, N. Knudsen, A. Manibusan, F. Tian, Y. Sun, Y. C. Lu, A. Sellers, X. C. Jia, I. Joseph, B. Anand, K. Morrison, D. S. Pereira and D. Stover, *PLoS One*, 2014, **9**, 14.
- (a) P. Akkapeddi, S. A. Azizi, A. M. Freedy, P. Cal, P. M. P. Gois and G. J. L. Bernardes, *Chem. Sci.*, 2016, **7**, 2954–2963; (b) D. Y. Jackson, *Org. Process Res. Dev.*, 2016, **20**, 852–866.
- V. Chudasama, A. Maruani and S. Caddick, *Nat. Chem.*, 2016, **8**, 113–118.
- (a) S. L. Kuan, T. Wang and T. Weil, *Chem. – Eur. J.*, 2016, **22**, 17112–17129; (b) P. Bryant, M. Pabst, G. Badescu, M. Bird, W. McDowell, E. Jamieson, J. Swierkosz, K. Jurlewicz, R. Tommasi, K. Henseleit, X. B. Sheng,

- N. Camper, A. Manin, K. Kozakowska, K. Peciak, E. Laurine, R. Grygorash, A. Kyle, D. Morris, V. Parekh, A. Abhilash, J. W. Choi, J. Edwards, M. Frigerio, M. P. Baker and A. Godwin, *Mol. Pharm.*, 2015, **12**, 1872–1879;
- (c) G. Badescu, P. Bryant, M. Bird, K. Henseleit, J. Swierkosz, V. Parekh, R. Tommasi, E. Pawlisz, K. Jurlewicz, M. Farys, N. Camper, X. B. Sheng, M. Fisher, R. Grygorash, A. Kyle, A. Abhilash, M. Frigerio, J. Edwards and A. Godwin, *Bioconjugate Chem.*, 2014, **25**, 1124–1136;
- (d) A. Maruani, M. E. B. Smith, E. Miranda, K. A. Chester, V. Chudasama and S. Caddick, *Nat. Commun.*, 2015, **6**, 6645.
- 11 (a) L. M. Tedaldi, M. E. B. Smith, R. Nathani and J. R. Baker, *Chem. Commun.*, 2009, 6583–6585; (b) M. E. B. Smith, F. F. Schumacher, C. P. Ryan, L. M. Tedaldi, D. Papaioannou, G. Waksman, S. Caddick and J. R. Baker, *J. Am. Chem. Soc.*, 2010, **132**, 1960–1965; (c) C. P. Ryan, M. E. B. Smith, F. F. Schumacher, D. Grohmann, D. Papaioannou, G. Waksman, F. Werner, J. R. Baker and S. Caddick, *Chem. Commun.*, 2011, **47**, 5452–5454.
- 12 (a) L. Castaneda, A. Maruani, F. F. Schumacher, E. Miranda, V. Chudasama, K. A. Chester, J. R. Baker, M. E. B. Smith and S. Caddick, *Chem. Commun.*, 2013, **49**, 8187–8189; (b) F. F. Schumacher, V. A. Sanchania, B. Tolner, Z. V. F. Wright, C. P. Ryan, M. E. B. Smith, J. M. Ward, S. Caddick, C. W. M. Kay, G. Aeppli, K. A. Chester and J. R. Baker, *Sci. Rep.*, 2013, **3**, 1525; (c) F. F. Schumacher, J. P. M. Nunes, A. Maruani, V. Chudasama, M. E. B. Smith, K. A. Chester, J. R. Baker and S. Caddick, *Org. Biomol. Chem.*, 2014, **12**, 7261–7269; (d) J. P. Nunes, M. Morais, V. Vassileva, E. Robinson, V. S. Rajkumar, M. E. Smith, R. B. Pedley, S. Caddick, J. R. Baker and V. Chudasama, *Chem. Commun.*, 2015, **51**, 10624–10627.
- 13 E. Robinson, J. P. Nunes, V. Vassileva, A. Maruani, J. Nogueira, M. E. B. Smith, S. Caddick, J. R. Baker and V. Chudasama, *RSC Adv.*, 2017, **7**, 9073–9077.
- 14 C. R. Behrens, E. H. Ha, L. L. Chinn, S. Bowers, G. Probst, M. Fitch-Bruhns, J. Monteon, A. Valdiosera, A. Bermudez, S. Liao-Chan, T. Wong, J. Melnick, J.-W. Theunissen, M. R. Flory, D. Houser, K. Venstrom, Z. Levashova, P. Sauer, T.-S. Migone, E. H. van der Horst, R. L. Halcomb and D. Y. Jackson, *Mol. Pharm.*, 2015, **12**, 3986–3998.
- 15 (a) S. Y. Long, Q. Q. Tang, Y. Wu, L. X. Wang, K. Zhang and Y. M. Chen, *React. Funct. Polym.*, 2014, **80**, 15–20; (b) S. Ramesh, P. Cherkupally, T. Govender, H. G. Kruger, F. Albericio and B. G. de la Torre, *Org. Lett.*, 2015, **17**, 464–467; (c) A. Ross, H. Durmaz, K. Cheng, X. P. Deng, Y. W. Liu, J. Oh, Z. Chen and J. Lahann, *Langmuir*, 2015, **31**, 5123–5129; (d) Z. L. Li, L. H. Sun, J. M. Ma, Z. Zeng and H. Jiang, *Polymer*, 2016, **84**, 336–342; (e) M. P. Robin and R. K. O'Reilly, *Chem. Sci.*, 2014, **5**, 2717–2723; (f) M. W. Jones, R. A. Strickland, F. F. Schumacher, S. Caddick, J. R. Baker, M. I. Gibson and D. M. Haddleton, *J. Am. Chem. Soc.*, 2012, **134**, 1847–1852; (g) M. S. S. Palanki, A. Bhat, B. Bolanos, F. Brunel, J. Del Rosario, D. Dettling, M. Horn, R. Lappe, R. Preston, A. Sievers, N. Stankovic, G. Woodnut and G. Chen, *Bioorg. Med. Chem. Lett.*, 2013, **23**, 402–406.
- 16 (a) S. D. Fontaine, R. Reid, L. Robinson, G. W. Ashley and D. V. Santi, *Bioconjugate Chem.*, 2015, **26**, 145–152; (b) R. P. Lyon, J. R. Setter, T. D. Bovee, S. O. Doronina, J. H. Hunter, M. E. Anderson, C. L. Balasubramanian, S. M. Duniho, C. I. Leiske, F. Li and P. D. Senter, *Nat. Biotechnol.*, 2014, **32**, 1059.
- 17 R. J. Christie, R. Fleming, B. Bezabeh, R. Woods, S. Mao, J. Harper, A. Joseph, Q. L. Wang, Z. Q. Xu, H. Wu, C. S. Gao and N. Dimasi, *J. Controlled Release*, 2015, **220**, 660–670.
- 18 U. Muus, C. Hose, W. Yao, T. Kosakowska-Cholody, D. Farnsworth, M. Dyba, G. T. Lountos, D. S. Waugh, A. Monks, T. R. Burke Jr. and C. J. Michejda, *Bioorg. Med. Chem.*, 2010, **18**, 4535–4541.
- 19 L. Castaneda, Z. V. F. Wright, C. Marculescu, T. M. Tran, V. Chudasama, A. Maruani, E. A. Hull, J. P. M. Nunes, R. J. Fitzmaurice, M. E. B. Smith, L. H. Jones, S. Caddick and J. R. Baker, *Tetrahedron Lett.*, 2013, **54**, 3493–3495.
- 20 H. A. Burris III, H. S. Rugo, S. J. Vukelja, C. L. Vogel, R. A. Borson, S. Limentani, E. Tan-Chiu, I. E. Krop, R. A. Michaelson, S. Girish, L. Amler, M. Zheng, Y.-W. Chu, B. Klencke and J. A. O'Shaughnessy, *J. Clin. Oncol.*, 2011, **29**, 398–405.
- 21 J. R. Junutula, H. Raab, S. Clark, S. Bhakta, D. D. Leipold, S. Weir, Y. Chen, M. Simpson, S. P. Tsai, M. S. Dennis, Y. Lu, Y. G. Meng, C. Ng, J. Yang, C. C. Lee, E. Duenas, J. Gorrell, V. Katta, A. Kim, K. McDorman, K. Flagella, R. Venook, S. Ross, S. D. Spencer, W. L. Wong, H. B. Lowman, R. Vandlen, M. X. Sliwowski, R. H. Scheller, P. Polakis and W. Mallet, *Nat. Biotechnol.*, 2008, **26**, 925–932.
- 22 D. A. Richards, S. A. Fletcher, M. Nobles, H. Kossen, L. Tedaldi, V. Chudasama, A. Tinker and J. R. Baker, *Org. Biomol. Chem.*, 2015, **14**, 455–459.
- 23 L. M. Tedaldi, A. E. Aliev and J. R. Baker, *Chem. Commun.*, 2012, **48**, 4725–4727.
- 24 C. J. Choy, J. J. Geruntho, A. L. Davis and C. E. Berkman, *Bioconjugate Chem.*, 2016, **27**, 824–830.
- 25 L. N. Tumey, M. Charati, T. He, E. Sousa, D. S. Ma, X. G. Han, T. Clark, J. Casavant, F. Loganzo, F. Barletta, J. Lucas and E. I. Graziani, *Bioconjugate Chem.*, 2014, **25**, 1871–1880.

Excimer based fluorescent pyrene-ferritin conjugate for protein oligomerization studies and imaging in living cells

Authors: Irene Benni^a, Matilde Cardoso Trabuco^{a,b}, Enrico Di Stasio^c, Alessandro Arcovito^c, Alberto Boffi^{d,e}, Francesco Malatesta^a, Alessandra Bonamore^a, Simone De Panfilis^e, Valeria de Turris^e, Paola Baiocco^{e*}

Affiliations:

a) Department of Biochemical Sciences "Alessandro Rossi Fanelli", Sapienza University of Rome, P.le A. Moro 5, 00185 Rome, Italy

b) Molirom srl, via Ravenna 8, 00161 Rome, Italy

c) Institute of Biochemistry and Clinical Biochemistry, Catholic University, Largo Francesco Vito, 1, 00168 Rome, Italy

d) Institute of Molecular Biology and Pathology, National Research Council, P.le A. Moro 7, 00185 Rome, Italy

e) Center for Life Nano Science@Sapienza, Istituto Italiano di Tecnologia, V.le Regina Elena 291, 00161 Rome, Italy

Abstract

In the present work, the novel "humanized" chimeric Archaeal ferritin HumAfFt, displaying the recognition motifs typical of Human H homopolymer and the unique cation-triggered oligomerization properties of *Archaeoglobus fulgidus* (AfFt), was selectively labeled with N-(1-pyrenyl)maleimide on a topologically selected cysteine residue inside the protein cavity, next to the dimer interface. Pyrene characteristic fluorescence features were exploited to investigate the transition from a dimeric to a cage-like 24-meric state and to visualize the protein *in vitro* by two photon fluorescence microscopy.

The unique mono- and divalent-cation-triggered oligomerization properties of HumAfFt were explored thermodynamically and kinetically by studying the dramatic fluorescence emission changes observed during the subunits assembly due to the formation/release of excimers by stacking interaction of the two nearest pyrene molecules at the dimer interface. The magnesium induced oligomerization was faster than the monovalent cation-triggered process, highly cooperative, complete at low MgCl₂ concentrations, and reversed by treatment with EDTA.

Pyrene intense excimer fluorescence allowed to successfully visualize the protein uptake *in vitro* by two photon fluorescence microscopy. Pyrene-labeled HumAfFt was indeed actively uptaken into HeLa cells by human transferrin receptor TfR1 recognition thus representing a unique nano-device building block for two photon fluorescence cell imaging.

In conclusion, the present data highlight the remarkable fluorescence properties of a pyrene-HumAfFt conjugate as a versatile probe suitable for both oligomerization studies and for protein intracellular visualization by two photon fluorescence confocal microscopy.

Keywords: Pyrene, Excimer, Fluorescence, Self-assembly, Ferritin, Two photon fluorescence microscopy

1. Introduction

Ferritins are iron storage and transport proteins, found in most living organisms, characterized by a typical tetraicosameric subunits assembly.¹ Ferritin assembly results in the formation of a 8 nm diameter central cavity, which can be efficiently loaded with transition metals, drugs, fluorescent molecules or contrast agents.²⁻⁴ Thus, encapsulated molecules can be delivered through the ferritin nano-cages, to target the transferrin receptor (TfR1, or CD71), highly expressed in actively replicating cells such as tumour cells.⁵⁻⁷ These attributes make ferritins and their derivatives a powerful delivery system with potential application in nanomedicine. Recombinant mammalian ferritins, however, are difficult to disassemble into subunits as they can be dissociated only under extreme conditions, thus rendering the encapsulation of many substrates impractical. Commonly employed cargo encapsulation techniques involve the disassembly and re-assembly of ferritins cage by pH jump, reaching drastic pH values (pH 2)⁸ which cause a partial and incomplete re-assembly.⁹

Recently, the ferritin from *Archaeoglobus fulgidus* (AfFt) was engineered into a chimeric protein, named Humanized AfFt ferritin (HumAfFt), which maintained the unique cation-triggered association properties of AfFt at neutral pH, while capable of being recognized and internalized by human transferrin receptor TfR1 as human ferritin H homopolymer, thus representing a unique opportunity for a controlled cargo encapsulation for TfR1-targeted delivery.¹⁰

In the present paper, HumAfFt was site-specifically modified adding two overlapping pyrene molecules at the dimer interface in order to exploit the pyrene excimer fluorescence emission for HumAfFt association/dissociation equilibrium investigation and *in vitro* protein visualization by two-photon fluorescence microscopy. Pyrene fluorescence properties are ideal for biological and bioimaging investigations as the probe's high extinction coefficient allows studies of proteins in solution at physiologically relevant concentrations and its high stability and long fluorescent lifetime give it resistance to photodamage and photobleaching.¹¹ The pyrene probe, due to the high sensitivity to the protein microenvironment, was demonstrated to be a precious tool to investigate protein oligomerization, protein folding-misfolding, conformational changes¹²⁻¹⁴, visualization of intracellular RNA¹⁵, biomolecule signaling¹⁶, design of aptamer sensors^{17,18} and pH sensors in cellular organelles¹⁹. Pyrene versatility is due to a spatially sensitive fluorescence emission that displays an ensemble of monomer emission peaks and an easily distinguishable red shifted broad peak corresponding to the excited state dimer called excimer.^{20,21} Excimer formation

arises when two pyrene molecules, one in the ground state and the other one in the excited state, are located in close proximity (~ 10 Å) and are involved in a non-covalent π - π stacking interaction. Any subtle structural change in a pyrene-labeled protein could alter orientation and distance between the two pyrene molecules involved in the excimer, thus strongly affecting stacking interactions and therefore resulting in a clear shift in the fluorescence emission.^{12,20}

The sensitive excimer fluorescence emission in pyrene-HumAfFt conjugate enlightened new insights into the conformational changes that HumAfFt ferritin faces upon salt-induced oligomerization. A thermodynamic and kinetic analysis of the assembly process demonstrated a full and complete reversibility, and a surprising difference between the association rates of mono and divalent cations. The pyrene-labeled protein was also successfully visualized *in vitro* by using two-photon excimer-based fluorescence with the advantage to irradiate cells at low energy wavelengths thus ensuring a long penetration depth and reducing photodamage.²² HumAfFt uptake into HeLa cells was not altered by pyrene-labeling and was visualized through pyrene excimer fluorescence confirming the high extent of protein internalization and highlighting a cellular distribution typical of a clathrin-coated endocytosis pathway²³, mediated by TfR1.

2. Discussion

2.1 Ferritin design

Ferritins are cage-like proteins with a unique tetraicosameric (24-meric) assembly that usually displays a highly conserved basic unit, a monomer, composed of a four-helix bundle namely A, B, C and D, and a short E helix at the C-terminus. In high NaCl and MgCl₂ concentrations AfFt and chimeric ferritin HumAfFt assemble in their 24-meric cage-like shape while, in the absence of ions, the four-helix bundle of both ferritins assembles into a stable antiparallel dimer.^{10,24-26} At the two-fold axis of the dimer, in the middle of the B helix, a single point conservative mutation (M54C) was introduced for site-selective NPM labeling. The mutated residues were positioned far from any inter-subunit contacts or loop regions to avoid any interference with the cage assembly, at a 14 Å distance between two β -carbons of two C54, enough for a π -stacking interaction between two pyrene molecules (Figure 1). As previously demonstrated, the overall fold and function of HumAfFt, in comparison with AfFt, were not altered by the amino acid substitution.¹⁰ Hereafter, we will refer to HumAfFt and AfFt as both mutated at position 54.

A mutant of *Pyrococcus fulgidus* ferritin (PfFtP77C) with a cysteine residue on the external surface was labeled with NPM and used as pyrene monomer fluorescence standard, whereas a distance of 24 Å between two cysteines did not allow for excimer formation.¹² In addition, as PfFtP77C was

Attachment 4

uniquely found as a 24-meric assembled cage in solution, the protein could be used as a standard independent of the cation concentrations.²⁷

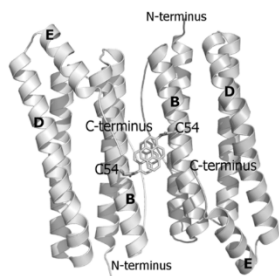


Figure1: Ribbon diagram of the antiparallel homodimer structure of HumAfFt (pdb 5LS9). Two NPM molecules are depicted in magenta sticks bound to C54, establishing a π - π stacking interaction, at the dimer interface.

2.2 Pyrene-labeled ferritin preparation

Best experimental conditions for the conjugation reaction between ferritin and NPM were described extensively in the SI and resulted in a 75% pyrene labeling as verified by Ellman's assay and MALDI-TOF Mass Spectrometry analysis. The expected molecular weights of 20458 Da for pyrene-labeled AfFt and 20545 Da for pyrene labeled-HumAfFt (Figure S1) were obtained. The percentage of labeling was determined by titration of the free-sulfhydryl groups according to the Ellman's assay, since a UV-Vis determination was not reliable due to red-shift and hypochromic effect of the pyrene absorption peaks caused by micro-environment changes.²¹

2.3 Ferritin's assembly assessment by DLS

The hydrodynamic diameters of both pyrene-labeled HumAfFt and AfFt proteins showed similar size to the respective native ferritins and were found to be monodispersed in solution. The hydrodynamic diameters measured by DLS experiments were 5.8 nm for the dissociated state in the absence of $MgCl_2$, in agreement with the predicted theoretical value for a dimer²⁸, and approximately 14 nm for the associated state in 20 mM $MgCl_2$.

The overall oligomerization process was not altered by pyrene-labeling as confirmed by DLS analysis. The Mg^{2+} -dependent titrations confirmed the comparable self-assembly properties of AfFt and HumAfFt, with and without pyrene, and showed a complete transition within 5 mM $MgCl_2$ (Figure S2).

2.4 Ferritin's assembly-disassembly assessment by fluorescence spectroscopy

Attachment 4

The self-assembly process of the previously described AfFt and HumAfFt ferritins was extensively studied by exploiting pyrene characteristic fluorescence emission, while PfFtP77C was employed as assembled 24meric cage and pyrene monomer standard. As shown in Figure 2, only the pyrene monomer fluorescence emission was present in PfFtP77C, while in AfFt and HumAfFt an additional broad band appeared, thus confirming the excimer formation. Surprisingly a higher amount of excimer was found in HumAfFt although this protein differed from AfFt by only 9 residues on the loop between helices B and C and the superposition of the two structures did not highlight any significant repositioning in the residue 54. For an efficient excimer formation, two pyrene molecules must be stacked in a parallel orientation allowing for a π - π interaction to take place, and these mutations on the loop could possibly slightly affect the relative orientation and distance between the two pyrene moieties.¹²

Remarkably, in the tetraicosameric state, the overall amount of excimer decreased, as shown in Figure 3 and Figure S3, probably due to movements at the inter-dimer interface that cause a destabilization of π -stacking interactions between the two pyrene moieties. Moreover, the excimer amount was successfully restored after EDTA addition, confirming that the chelating ability of this agent promote protein disassembly by removal of magnesium cations (Figure 3, Figure S3).

To corroborate that the fluorescence excimer broad band variation was related to the oligomerization process and was independent from the ionic strength, we measured fluorescence emission at fixed ionic strength using different concentrations of either MgCl_2 or NaCl . According to the Debye-Hückel model, the experiment was carried out at two different ionic strength conditions: at low salt concentrations (*i.e.* 150 mM NaCl or 50 mM MgCl_2), where the protein was associated in the 24-meric state only in MgCl_2 , and at high salt concentrations (*i.e.* 600 mM NaCl or 200 mM MgCl_2), where the protein was known to be associated in both salts.^{10,24-26} As shown in Figure 4 and Figure S4, in the first condition, the excimer content without salt and at 150 mM NaCl were similar, in agreement with a dissociated state, whereas at 50 mM MgCl_2 , therefore at equal ionic strength, the excimer content revealed the presence of an associated state for both proteins. Moreover, the pyrene monomer emission profile of PfFtP77C did not change at various salt concentration, excluding any ionic strength influence on the pyrene fluorescence emission (data not shown).

Fluorescence emission dependence on the protein oligomerization state was thus investigated by monitoring magnesium induced association at equilibrium. A sigmoidal curve was obtained by plotting excimer/monomer (e/m) ratio as a function of MgCl_2 concentration, suggesting a strong cooperativity within the association process, with a complete assembly at about 5 mM MgCl_2 in both ferritins (Figure 5).

The strong effect of Mg^{2+} ions on subunit assembly was then analyzed in terms of possible contributions to specific binding within the three-dimensional crystallographic structure (pdb 5LS9) by using PISA software (CCP4 suite). No significant evidence of Mg^{2+} presence at the interface between dimers was observed. In fact, as it was previously reported^{24,29}, it was evident that the hydrophobic network connecting the dimers' interface played a key role in stabilizing the cage structure in high ionic strength buffers. In turn, divalent cations were found to occupy the ferroxidase center under conditions of iron deficiency, through explicit coordination provided by Asp52, Glu19 and His55, according to AfFt numbering.³⁰ In the light of these observations, it might be hypothesized that coordination of Mg^{2+} in the ferroxidase center can assist the assembly process by exerting some subtle conformational rearrangement within the dimeric species, thus explaining the different behavior respect to a monovalent cation.

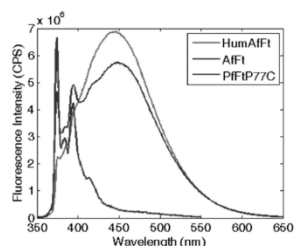


Figure 2: Fluorescence emission spectra of pyrene-labeled ferritins.

The characteristic pyrene-monomer peaks in PfFtP77C are shown in blue. In AfFt and in HumAfFt, the excimer emission profiles shown in green and red, respectively.

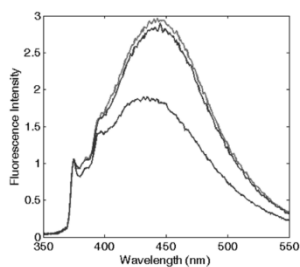


Figure 3: Reversibility assessment of the assembly-disassembly mechanism.

Fluorescence spectra of pyrene-HumAfFt in the absence of salts (red), in the presence of 50 mM $MgCl_2$ (green) and after 50 mM EDTA addition (blue). The excimer content difference in presence or absence of $MgCl_2$ reflects ferritin's association state.

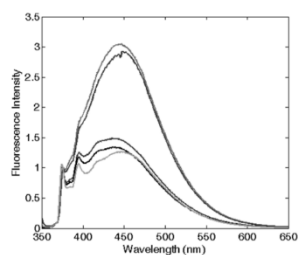


Figure 4: Assessment of the correlation between oligomerization state and excimer fluorescence.

Fluorescence emission spectra of HumAfFt, without any salt and at two different fixed ionic strengths for either MgCl_2 or NaCl. Spectra in the absence of any salt (red) and 150mM NaCl (blue) correspond to a dimeric state, while the profiles at 600 mM NaCl (cyan), 50 mM (green) and 200 mM (black) MgCl_2 , correspond to the associated state.

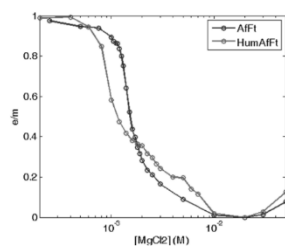


Figure 5: Thermodynamic study of Mg^{2+} -triggered oligomerization process.

Fluorescence e/m ratio is shown as a function of magnesium concentration, at equilibrium at 25 °C, for pyrene-labeled HumAfFt (red) and AfFt (green) highlighting a highly cooperative transition.

2.5 Ferritin's assembly kinetics

In order to determine the kinetics of the salt-induced oligomerization process, stopped-flow experiments were carried out by monitoring fluorescence changes over time. As the total fluorescence emission was higher for the disassembled ferritin, a fluorescence decrease over time was expected during protein oligomerization.

Magnesium-triggered assembly was too fast (time scale < 10 ms) to be followed by stopped-flow measurements at 25 °C. However, it was possible to single out a clear decay curve at lower temperature (4°C). Despite the assembly occurred close to the instrumental time limit, some semi-quantitative estimates on Mg^{2+} -induced association could still be obtained. Fluorescence emission decreased with a double exponential trend and the reaction was complete within 25 ms, as shown in Figure 6A. Reaction rates increased proportionally with both Mg^{2+} and protein concentration with a major contribution from the protein concentration, which showed an apparent second order rate constant of about $10^6 \text{ M}^{-1}\text{s}^{-1}$. In contrast, the EDTA-triggered dissociation process was slower than the assembly and was measured both at 25 and 4 °C. Faster dissociation rates were observed at

higher temperature, with completeness reached in 0.1 s at 25 °C and in 0.25 s at 4 °C. Dissociation showed a biphasic profile, dependent on EDTA concentration but independent of protein concentration (Figure S5), as expected.

Since the kinetic reaction in the presence of magnesium cations appeared to be too fast, we investigated the slower NaCl induced association process. In comparison with magnesium, higher salt concentrations were required to monitor Na⁺-triggered association as the oligomerization was complete only at 500 mM NaCl.²⁵ The assembly showed much slower rates and a multiphasic kinetic profile (Figure 6B) with an initial lag phase (Figure 6C), typical of a nucleation process commonly found in protein oligomerization³¹, that evolved in four exponential phases toward the end of the reaction, which was reached only after 20-30 minutes at 25°C. These changes in the total fluorescence emission over time, could be due to multiple pyrene rearrangement during the assembly. Additionally, while the association rates were proportionally increasing with NaCl concentration, at fixed NaCl concentration and varying protein concentration the reaction rates were approximately constant.

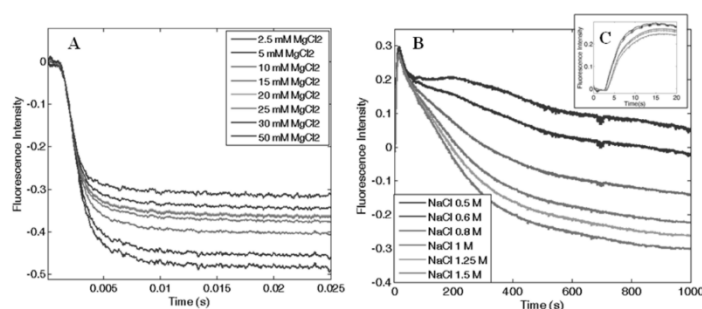


Figure 6: Association kinetics as a function of (A) MgCl₂ (B, C) and NaCl concentration. HumAfFt kinetic rates were recorded at A) 4 °C increasing MgCl₂ concentrations showing a fast biexponential behavior complete in 25 ms, and at B) 25 °C increasing NaCl concentrations showing a slow multi-phasic behavior barely complete after 1000 s. In the close-up view, C, the initial lag phase is shown (≤ 5 s).

2.6 Visualization of pyrene-labeled ferritins by two photon fluorescence microscopy.

The two photon spectral dependence of the pyrene excimer and monomer total fluorescence, respectively observed in pyrene-HumAfFt and pyrene-PfFtP77C, subtracted of the unlabelled ferritin signal, was reported in Figure S6B as a function of the excitation wavelength, together with the more conventional single photon absorption spectra (Figure S6A). As expected, the overall shape of the two and one photon spectra were in good agreement. The differences are due to the different absorption/emission cross sections of the electronic processes involved, and they are common feature observed in several experimental studies.³²⁻³³ The two photon total fluorescence

Attachment 4

spectra reported in Figure S6D did not exactly correspond to the two photon absorption, but they were qualitatively related to the absorption cross section in the generally valid assumption that non-radiative decay channels are independent of the excitation wavelength. The frequency shift occurring between the one and half of the two photon excitation wavelengths is also related to the different excitation cross-sections. An identical argument is valid when looking at the spectral distribution of the fluorescence signal at a given excitation wavelength as reported in Figure S6D. The overall spectral behavior was indeed preserved in the single and two photon approach, even in the presence of slight differences due to the discussed electronic features.

In conclusion, independently of the pyrene specific excitation or emission, spectra of monomer and excimer were remarkably different, as a further confirmation of the excimer formation in the ferritin cage-like structure.

2.7 Visualization of pyrene-HumAft-t-TRITC inside HeLa living cells by two photon fluorescence microscopy

To evaluate the performance of this novel nano-device as active fluorescent probe, living HeLa cells expressing high levels of TfR1 receptor, similar to many tumor cells, were incubated with pyrene-labeled HumAft-TRITC and imaging studies were carried out by TPFM. The HumAft internalization process was not altered by pyrene-labeling as confirmed by TRITC signal, detected with one photon excitation (Figure 7A, A'), distributed in the cytoplasm and in the perinuclear space as expected.¹⁰ In the same cells, switching to TPFM imaging, we were able to detect pyrene excimer emission in the same locations (Figure 7B, B') and a partial co-localization was highlighted (Figure 7C, C' and 7D, D'). The partial overlap between pyrene and TRITC signals could be explained by two main aspects. First, the two imaging techniques had intrinsic different integrated z-section, smaller in the TPFM compared to confocal imaging, meaning less particles visible in a single plane. Second, in the delay time during the switching mode between one and two photon excitation, the rearrangement in the intracellular compartments of living cells occurred.

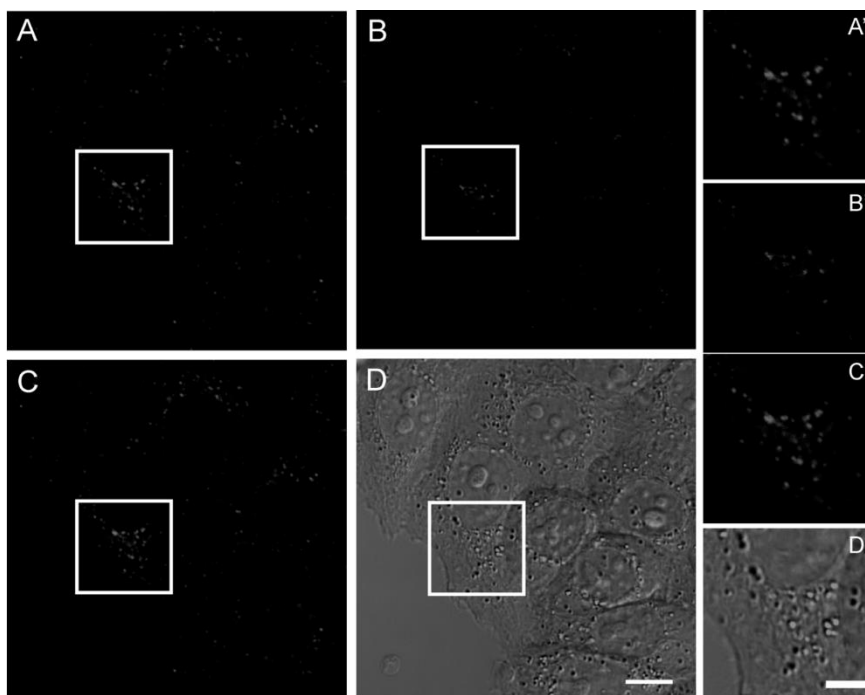


Figure 7: Confocal imaging of living HeLa cells incubated with pyrene-HumAfFt-TRITC. Images were acquired at one and two-photon excitations to detect respectively the TRITC (A) and the pyrene excimer emission (B). Merged signals and the overlay with the DIC image are shown in C and D, respectively (scale bar is 10 μ m). Magnified images of the highlighted regions are shown in corresponding panels A', B', C' and D' (scale bar is 5 μ m).

3. Experimental Section

3.1 Protein production

The chimeric HumAfFt ferritin was designed and produced as previously reported and its assembly properties were verified by size exclusion chromatography (SEC).¹⁰ The mutated ferritin from *Pyrococcus furiosus* PfFtP77C and *Archaeoglobus Fulgidus* AfFtM54C, already available in our lab, were purified as previously reported.^{26,34}

3.2 Pyrene-labeled ferritin preparation

Ferritins (4 mg ml⁻¹, in 20 mM HEPES pH 7.4, 50 mM MgCl₂) were reduced with TCEP (10 eq.) for 1h at room temperature under mild agitation. The conjugation reaction was carried out in 15% v/v acetonitrile to favor NPM solubility. The linker (5 eq.) was slowly added to the protein solution and the reaction mixture was left under stirring for 4 hours at 37 °C. NPM excess was removed by

Attachment 4

gel filtration chromatography (G25 Desalting, eluent 20 mM HEPES pH 7.4, 15% v/v acetonitrile), co-solvent was removed by dialysis against 20 mM HEPES pH 7.4 and, in order to remove excess MgCl_2 and maintain the protein in its dimeric state, 5 mM EDTA was added to the dialysis buffer. Extensive dialysis against 20 mM HEPES pH 7.4 was then performed.

Determination of free sulfhydryl was performed on a UV5600 Spectrophotometer using Ellman's assay according to standard procedure. Briefly, a stock solution of 5,5-dithio-bis-(2-nitrobenzoic acid) (Ellman's reagent) was mixed with the protein sample in a 20-fold molar excess. The solution was incubated for 5 minutes at room temperature and UV absorption was measured at 412 nm, using as blank, a sample containing the same amount of Ellman's reagent in buffer. A molar absorptivity of $14150 \text{ M}^{-1}\text{cm}^{-1}$ was used to estimate the sulfhydryl per protein ratio.

3.3 Dynamic light scattering measurements

DLS experiments were carried out with a Zetasizer Nano S (Malvern Instruments, Malvern, U.K.) equipped with a 4 mW He-Ne laser (633 nm). Measurements were performed at 25 °C, at an angle of 173° with respect to the incident beam. All samples were prepared at 2 mg ml^{-1} in HEPES 20 mM pH 7.4 and various MgCl_2 concentrations, and were filtered with a $0.2 \mu\text{m}$ filter before analysis. Peak intensity analysis was used to determine the average hydrodynamic diameters (Z-average diameter) of the scattering particles.

3.4 Fluorescence spectroscopy measurements

Fluorescence measurements were carried out with a FluoroMax 4 (Horiba) spectrofluorimeter with a Haake D8 refrigerated bath at 25°C and at equilibrium. Fluorescence emission spectra of pyrene-labeled samples ($30 \mu\text{M}$ in 20 mM HEPES pH 7.4) were excited at 342 nm and fluorescence data were collected from 350 to 650 nm. The association process dependence on ionic strength was investigated varying concentrations of MgCl_2 and NaCl, while the dissociation mechanism was studied by EDTA treatment. Emission spectra were normalized with respect to the maximum absorption peak of a single pyrene molecule and the excimer/monomer ratio, calculated as the fluorescence intensity of the excimer peak (445 nm)/monomer peak (375 nm) ratio, was used as a relative indicator of the extent of excimer formation.

3.5 Stopped-flow measurements

Kinetic measurements were carried out on a single mixing stopped-flow apparatus (Applied Photophysics, Leatherhead, UK) at 4°C and 25°C. Samples were excited at 342 nm (6 nm slits) and total emission fluorescence was collected with a 360 nm long-pass filter.

Attachment 4

Association kinetic experiments were performed at 5 μM protein before mixing (b.m.) in 20 mM HEPES pH 7.4, increasing concentrations of MgCl_2 or NaCl and, at constant salt concentration (either 20 mM MgCl_2 or 2 M NaCl b.m.) increasing protein concentrations (5 to 100 μM ferritin b.m.). Dissociation kinetic experiments were performed at 5 μM protein b.m. in 20 mM HEPES pH 7.4 and MgCl_2 increasing EDTA/ Mg^{2+} molar ratios or, at a fixed EDTA concentration (20 mM) increasing protein concentrations (5 to 100 μM ferritin in 20 mM MgCl_2 b.m.).

3.6 Pyrene-ferritin-TRITC preparation, cell culture, ferritin internalization and visualization into HeLa cells

Pyrene-ferritins were further labeled with TRITC (tetramethylrhodamine isothiocyanate, Thermofisher) following manufacturer's standard protocol. HeLa cells were grown at 37 °C in DMEM without phenol red and supplemented with 10% (v/v) FBS, Glutamax (Invitrogen) and penicillin-streptomycin solution (Sigma). The internalization assay was performed as follows: cells were seeded on the 8-well μ -slide ibiTreat (ibidi) and after 24 h, TRITC-ferritin nanoparticles (pyrene-HumAft-TRITC and HumAft-TRITC as control) were added at the final concentration of 300 $\mu\text{g ml}^{-1}$ and incubated for 48 h. Just before imaging, cells were washed to eliminate the unbound ferritin and then acquired by confocal laser-scanning microscopy.

4. Conclusions

In the present paper, a pyrene-based ferritin nano-device containing 0.75 pyrene molecule per monomer and capable of generating an intense excimer spectrum due to the juxtaposition of the pyrene aromatic rings along the dimer interface was characterized. The system was exploited to shed light on the cation-triggered ferritin oligomerization process and to visualize the ferritin uptake by HeLa cells for the first time by two photon fluorescence microscopy, thanks to the wide excimer emission band.

In this framework, HumAft represents a uniquely suitable scaffold for incorporating diverse substructures, including π -conjugated polyaromatic molecules, inside the protein cavity by a cation dependent assembly/disassembly process at neutral pH. As an example, a detailed study on the unique ferritin's association/dissociation properties at physiological concentrations was performed based on pyrene excimer formation which strongly reflects the oligomerization state. Dynamic light scattering studies confirmed the data from pyrene fluorescence emission thus validating the method employed. While both mono and divalent cations were capable of triggering ferritin association, divalent cations showed very fast kinetics, within a μsecond time scale, and were able to completely form the 24-meric cage at about 5 mM MgCl_2 concentrations. Magnesium therefore represents a

Attachment 4

convenient alternative to NaCl as it can trigger a faster cage closure with lower salt amounts, thus potentially representing a marked improvement for the synthesis of drug-delivery nano devices. The oligomerization process was also confirmed to be remarkably cooperative and fully reversible by EDTA treatment, causing the dissociation of ferritin into its dimeric state within microseconds.

We also report, for the first time, the application of pyrene-labeled proteins for a “two photon excimer based” intracellular visualization. Pyrene-HumAft was highly internalized by HeLa cells and pyrene excimer displayed effective fluorescence emission by two photon fluorescence confocal microscopy, which was comparable to common fluorophores emission, such as TRITC. The strategic use of pyrene excimer emission was confirmed to be an excellent building block for two photon fluorescent nano-particle design, which could be further explored by pyrene derivatization and optimization. We therefore believe that these findings will enable the creation of a novel and versatile set of pyrene-excimer based ferritin probes for diagnostic and biomedical application based on the ability of HumAft to target the overexpressed TfR1 receptor in human cancer cells.

Acknowledgments: MIUR Flagship Project “Nanomax” to A. Boffi is acknowledged. EU H2020 Project “X-Probe”, Grant No. 637295, to A. B. and M. C. T. is gratefully acknowledged. We thank the helpful staff of mass spectrometry service provided by Cogentech s.r.l.

Abbreviations: N-(1-pyrenyl)maleimide (NPM), two photon fluorescence microscopy (TPFM), tris(2-carboxyethyl)phosphine (TCEP), ethylenediaminetetraacetic acid (EDTA)

Supporting Information: Experimental procedures and characterizations (PDF)

References:

- (1) Munro, H. N.; Linder, M. C. *Physiol. Rev.* **1978**, 58, 317-396.
- (2) Zhen, Z.; Tang, W.; Guo, C.; Chen, H.; Lin, X.; Liu, G.; Fei, B.; Chen, X.; Xu, B.; Xie, J. *ACS Nano* **2013**, 7, 6988-6996.
- (3) Sun, C.; Yang, H.; Yuan, Y.; Tian, X.; Wang, L.; Guo, Y.; Xu, L.; Lei, J.; Gao, N.; Anderson, G. J.; Liang, X. J.; Chen, C.; Zhao, Y.; Nie, G. *J. Am. Chem. Soc.* **2011**, 133, 8617-8624.
- (4) Falvo, E.; Tremante, E.; Fraioli, R.; Leonetti, C.; Zamparelli, C.; Boffi, A.; Morea, V.; Ceci, P.; Giacomini, P. *Nanoscale* **2013**, 5, 12278-12285.
- (5) Truffi, M.; Fiandra, L.; Sorrentino, L.; Monieri, M.; Corsi, F.; Mazzucchelli, S. *Pharmacological Research* **2016**, 107, 57-65.
- (6) Zhen, Z.; Tang, W.; Chen, H.; Lin, X.; Todd, T.; Wang, G.; Cowger, T.; Chen, X.; Xie, J. *ACS Nano* **2013**, 7, 6, 4830-4837.

Attachment 4

- (7) Fan, K.; Cao, C.; Pan, Y.; Lu, D.; Yang, D.; Feng, J.; Song, L.; Liang, M.; Yan, X. *Nature Nanotechnology* **2012**, 7, 459-464.
- (8) Bellini, M.; Mazzucchelli, S.; Galbiati, E.; Sommaruga, S.; Fiandra, L.; Truffi, M.; Rizzuto, M. A.; Colombo, M.; Tortora, P.; Corsi, F.; Prosperi, D. *Journal of Controlled Release* **2014**, 196, 184-196.
- (9) Kim, M.; Rho, Y.; Jin, K. S.; Ahn, B.; Jung, S.; Kim, H.; Ree, M. *Biomacromolecules* **2011**, 12, 1629-1640.
- (10) de Turrís, V.; Cardoso Trabuco, M.; Peruzzi, G.; Boffi, A.; Testi, C.; Vallone, B.; Montemiglio, L. C.; Des Georges, A.; Calisti, L.; Benni, I.; Bonamore, A.; Baiocco, P. *Nanoscale* **2017**, 9, 647-655.
- (11) Conlon, P.; Yang, C. J.; Wu, Y.; Chen, Y.; Martinez, K.; Kim, Y.; Stevens, N.; Marti, A. A.; Jockusch, S.; Turro, N. J.; Tan, W. *JACS* **2008**, 130, 336-342.
- (12) Bains, G. K.; Kim, S. H.; Sorin, E. J.; Narayanaswami, V. *Biochemistry* **2012**, 51, 6207-6219.
- (13) Bains, G.; Patel, A. B.; Narayanaswami, V. *Molecules* **2011**, 16, 7909-7935.
- (14) Betcher-Lange, S. L.; Lehrer, S. S. *J. Biol. Chem.* **1978**, 253, 3757-3760.
- (15) Krasheninina, O. A.; Lomzov, A. A.; Fishman, V. S.; Novopashina, D. S.; Venyaminova, A. G. *Bioorganic & Medicinal Chemistry* **2017**, 25, 2244-2250.
- (16) Wu, C.; Wang, C.; Yan, L.; Yang, C. J. *Journal of Biomedical Nanotechnology* **2009**, 5, 495-504.
- (17) Ma, C.; Huang, H.; Zhao, C. *Analytical Sciences* **2010**, 26, 1261-1264.
- (18) Freeman, R.; Li, Y.; Tel-Vered, R.; Sharon, E.; Elbaz, J.; Willner, I. *Analyst* **2009**, 134, 653-656.
- (19) Faggi, E.; Serra-Vinardell, J.; Pandey, M. D.; Casas, J.; Fabrias, G.; Luis, S. V.; Alfonso, I. *Sensors and Actuators B* **2016**, 234, 633-640.
- (20) Birks J.B. *Rep. Prog. Phys.* **1975**, 38, 903-974.
- (21) Winnik F.M. *Chem. Rev.* **1993**, 93, 587-614.
- (22) Niko, Y.; Moritomo, H.; Sugihara, H.; Suzuki, Y.; Kawamata, J.; Konishi, G. *J. Mater. Chem. B* **2015**, 3, 184-190.
- (23) McMahon, H. T.; Boucrot, E. *Nature Reviews* **2011**, 12, 517-533.
- (24) Sana, B.; Johnson, E.; Le Magueres, P.; Criswell, A.; Cascio, D.; Lim, S. *JBC* **2013**, 288, 45, 32663-32672.
- (25) Swift, J.; Butts, C. A.; Cheung-Lau, J.; Yerubandi, V.; Dmochowski, I. J. *Langmuir* **2009**, 25, 9, 5219-5225.

Attachment 4

- (26) Calisti, L.; Benni, I.; Cardoso Trabuco, M.; Baiocco, P.; Ruzicka, B.; Boffi, A.; Falvo, E.; Malatesta, F.; Bonamore, A. *Biochim. Biophys. Acta* **2017**, 1861, 450-456.
- (27) Tatur, J.; Hagen, W. R.; Matias, P. M. *J. Biol. Inorg. Chem.* **2007**, 12, 615–630.
- (28) Ebrahimi, K. H.; Hagedoorn, P. L.; Hagen, W. R. *Chemical Reviews* **2015**, 290, 44, 26801-26810.
- (29) Sana, B.; Johnson, E.; Lim, S. *Biochim. Biophys. Acta.* **2015**, 1850, 2544-2551.
- (30) Johnson, E.; Cascio, D.; Sawaya, R. S.; Gingery, M; Schroder, I. *Structure* **2005**, 13, 637-648.
- (31) Morris, A. M.; Watzky, M. A.; Finke, R. G. *Biochimica et Biophysica Acta* **2009**, 1794, 375-397.
- (32) Xu, C.; Webb, W. W. *J. Opt. Soc. Am. B*, **1996**, 13, 3, 481-491.
- (33) Makarov, N. S.; Drobizhev, M.; Rebane, A. *Optics Express* **2008**, 16, 6, 4029-4047.
- (34) Kasyutich, O.; Ilari, A.; Fiorillo, A.; Tatchev, D.; Hoell, A.; Ceci, P. *JACS* **2010**, 132, 3621-3627.

Table of Content Figure

